



## City Research Online

### City, University of London Institutional Repository

---

**Citation:** Dasari, BhagyaLakshmi (2019). Production and characterisation of graphene oxide reinforced aluminium matrix composites. (Unpublished Doctoral thesis, City, University of London)

This is the accepted version of the paper.

This version of the publication may differ from the final published version.

---

**Permanent repository link:** <https://openaccess.city.ac.uk/id/eprint/22005/>

**Link to published version:**

**Copyright:** City Research Online aims to make research outputs of City, University of London available to a wider audience. Copyright and Moral Rights remain with the author(s) and/or copyright holders. URLs from City Research Online may be freely distributed and linked to.

**Reuse:** Copies of full items can be used for personal research or study, educational, or not-for-profit purposes without prior permission or charge. Provided that the authors, title and full bibliographic details are credited, a hyperlink and/or URL is given for the original metadata page and the content is not changed in any way.

---

---

---

City Research Online:

<http://openaccess.city.ac.uk/>

[publications@city.ac.uk](mailto:publications@city.ac.uk)

---

# **Production and characterisation of graphene oxide reinforced aluminium matrix composites**

A thesis submitted

in partial fulfilment of the requirements for the degree of

**Doctor of Philosophy**

in

**Mechanical Engineering**

**School of Mathematics Computer Science & Engineering**

at

**City, University of London**



by

**BhagyaLakshmi Dasari**

## **DECLARATION**

I hereby declare that the material that I submitted for the assessment on the study leading to the award of a Ph.D. is entirely my own work, have not breached any copyright law and have exercised care to ensure originality of the work. The work has not been taken from the work of others and work that was taken for comparison purposes was cited, acknowledged within the text.

Signed: \_\_\_\_\_

(BhagyaLakshmi Dasari)

# PUBLICATIONS

The presented work in this thesis has been disseminated through the following publications and conferences

## Journals:

- I. **Dasari, B.L.**, Morshed, M., Nouri, J.M., Brabazon, D., and Naher, S., (2018). Mechanical properties of graphene oxide reinforced aluminium matrix composites. *Composites Part B: Engineering*, 145, pp. 136–144.
- II. **Dasari, B.L.**, Nouri, J. M., Brabazon, D., and Naher, S. (2017). Graphene and derivatives – Synthesis techniques, properties and their energy applications. *Energy*, 140, pp. 766–778.
- III. **Dasari, B.L.**, Nouri, J. M., Brabazon, D., and Naher, S., (2017). Parametric study for graphene reinforced aluminium matrix composites production using Box Behnken design. *AIP Conference Proceedings*, 1896, pp. 13006(1)–13006(4).
- IV. **Dasari, B.L.**, Morshed, M., Nouri, J.M., Ul Ahad, I., Brabazon, D., and Naher, S., Optimisation of process parameters to produce graphene oxide reinforced aluminium composites. *Materials & Design*, under review.

## Conferences:

- i. **Dasari, B.L.**, Nouri, J. M., Brabazon, D., and Naher, S., (2018). Prediction of effect of increase in graphene oxide layers on the mechanical properties of aluminium matrix composites. 21<sup>st</sup> International Conference on Advances in Materials & Processing Technologies, Dublin City University, September 4-7, Dublin, Ireland.
- ii. **Dasari, B.L.**, Nouri, J. M., Brabazon, D., and Naher, S., (2018). Effect of process parameters on mechanical properties of graphene oxide reinforced aluminium composites. 5<sup>th</sup> International Conference on Material Science & Smart Materials, University of West of Scotland, August 7-10, Scotland, UK.
- iii. **Dasari, B.L.**, Nouri, J. M., Brabazon, D., and Naher, S., (2018). Production of graphene oxide reinforced aluminium matrix composites.

26<sup>th</sup> International Conference on Composites or Nano Engineering (ICCE-26), July 15-21, Paris, France.

- iv. **Dasari, B.L.**, Nouri, J. M., Brabazon, D., and Naher, S., (2017). Synthesis of graphene reinforced aluminium matrix composites with improved properties. 25<sup>th</sup> Annual International Conference on Composites/Nano Engineering, July 16-22, Rome, Italy.
- v. **Dasari, B.L.**, Nouri, J. M., Brabazon, D., and Naher, S., (2017). Parametric study for graphene reinforced aluminum matrix composites production using box-behnken design, 20<sup>th</sup> International ESAFORM Conference on Material Forming, Dublin City University, April 24-27, Dublin, Ireland.
- vi. **Dasari, B.L.**, Nouri, J. M., Brabazon, D., and Naher, S., (2015). Prediction of properties of graphene reinforced metal matrix composites. 8<sup>th</sup> International Conference on Sustainable Energy & Environmental Protection (SEEP 2015), University of the West of Scotland, August 11-14, Scotland, UK.

*To my loving husband Jai and my son Medhansh*

## **ACKNOWLEDGEMENT**

I would like to express my sincere gratitude to my primary supervisor Dr Sumsun Naher for the continuous support of my Ph.D study and related research, for her patience and motivation. Her guidance helped me in all the time of research and writing of this thesis. I would like to thank my co-supervisor Professor Jamshid M Nouri for his invaluable advice, encouragement and financial support throughout this study. I would like to thank my external supervisor Professor Dermot Brabazon, who provided me an opportunity to join his team as a visiting researcher, who gave access to laboratory and research facilities. Without his precious support it would not be possible to conduct this research.

I am indebted to Dr Muhammad Morshed for his invaluable support during my course work which helped me a lot in analysing and publishing outcomes of my research work. I thank Dr Inam Ul Ahad for his support in exploring the experimental facilities and continue my research work at Dublin City University. I thank Dr Robert Groarke and Dr Komal Bagga for their support and concern which provided the comfort during my visit to DCU. I would like to thank Mr Jim Hooker for his constant support and assistance with the equipment at City, University of London.

A special appreciation goes to my husband Jai Chand Dasari, my mom and dad Padma Chagarlamudi and Appa Rao Chagarlamudi, my mother-in-law and father-in-law Sriranjani Dasari and Vivekananda Dasari, my cousins Ramakrishna Manne and Janardhan Manne, my brother-in-law Roop Chand Dasari who encouraged, inspired and motivated me throughout some difficult times and pushed me to complete and deliver my work on time. I would like to thank my friends Dr Sham Rane and Dr Aishwarya Kumar for their support and constant motivation in difficult times that helped me to focus on my research and progress in career.

Finally, I would like to thank my colleagues, Israt Rumana Kabir, Nusrat Tamanna and Abdullah Qaban for their support in pursuing my research work at City and for making it a joyful experience which I will remember for the rest of my life.

## ABSTRACT

The present work deals with the production of graphene oxide (GO) reinforced aluminium (Al) matrix composites via liquid infiltration and powder metallurgical routes. The experiments were carried out on the optimisation of the process parameters of the composites and these outcomes were considered as input parameters for the prediction of properties using finite element (FE) modelling. The experimental design includes three wt% of GO reinforcement, three compaction pressures and two sintering temperatures. The other parameters investigated were selection of solvent and stirring time. The solvent and stirring time were selected based on visual inspections. Liquid infiltrated composite powders were vacuum filtered, dried and then cold compacted at 500MPa, 540MPa and 580MPa of compaction pressures. The GO/Al samples were sintered in horizontal tube furnace assisted by Ar gas atmosphere. The metallographic study and chemical analysis were performed using a scanning electron microscopy (SEM) integrated with energy dispersive X-ray spectroscopy (EDXS) revealing the existence of GO particles/sheets on Al particles. The percentage of elements at various regions of the GO/Al composites both at powder level and after sintering were investigated. The crystallinity and phase detection of the GO/Al samples were conducted using X-ray diffraction (XRD) system with Cu-K $\alpha$  radiation and 1.54Å wavelength. The presence of GO and number of layers of GO residing on the Al particles were analysed using micro Raman spectroscopy, this also revealed that there was no existence of aluminium carbide (Al<sub>4</sub>C<sub>3</sub>) phase as the carbide formation will deteriorate the properties of the end composites. The hardness properties of the as received Al and produced GO/Al composites were measured by micro-Vickers diamond indentation. The hardness of the GO/Al composite increases by 36% compared to pristine Al when reinforced with 0.2wt% of GO which is better than the hardness of rGO/Al composites reported in literature. Indentation test was used to investigate the effect of addition of GO to the Al on strength, in which it was noted that the addition of GO led to the brittleness in GO/Al composites. The effect of existence of GO on Al particles, variation in volume fraction of GO and existence of GO layers on Al particles on mechanical properties of GO/Al composites were predicted using FE modelling. The findings from the simulation were compared with analytical modelling and experimental results obtained from the current research work. A good agreement between results of FE model, analytical model and experimental investigations were noted.

# LIST OF CONTENTS

Declaration	i
Publications	ii
Acknowledgement	v
Abstract	vi
List of contents	vii
Abbreviations	xi
Nomenclature	xii
List of Figures	xiv
List of Tables	i
CHAPTER 1	1
Introduction	1
1.1 Background	1
1.2 Motivation Aim and objectives of the study	3
1.2.1 Research questions	4
1.3 Thesis outline	5
CHAPTER 2	7
Literature review	7
2.1 Metal matrix composites (MMCs)	7
2.2 Manufacturing techniques of aluminium matrix composites (AMCs)	9
2.3 Graphene	11
2.3.1 Morphology of graphene	12
2.3.2 Properties of graphene	13
2.3.3 Synthesis of graphene	19
2.4 Graphene oxide (GO)	24
2.4.1 Morphology of GO	24
2.4.2 Production of GO	25
2.4.3 Reduction of GO to reduced graphene oxide (rGO)	25
2.5 AMCs reinforced with graphene nano sheets (GNS/Al)	29
2.6 AMCs reinforced with graphene nano particles (GNP/Al)	32

2.7 AMCs reinforced with reduced graphene oxide (rGO/Al)	36
2.8 Summary	37
CHAPTER 3	38
Critical review and gap in literature	38
3.1 Critical reviews	38
3.2 Gaps and questions that are to be filled and answered:	39
3.3 Summary	44
CHAPTER 4	45
Materials and methods	45
4.1 Materials and properties	45
4.2 Powder treatment by liquid infiltration	46
4.3 Fabrication of composites	47
4.4 Characterisation of composites	49
4.4.1 Density measurement	50
4.4.2 Microstructural analysis	51
4.4.3 EDXS analysis	52
4.4.4 XRD analysis	54
4.4.5 Micro Raman analysis	56
4.4.6 Micro Vickers hardness	58
4.4.7 Indentation test	59
4.5 Modelling of GO/Al composites	60
4.5.1 Finite element modelling of GO/Al composites	60
4.5.2 Mesh convergence of FE model	62
4.5.3 Analytical modelling of GO/Al composites	63
4.6 Summary	64
CHAPTER 5	66
Results and discussion	66
5.1 Introduction	66
5.2 Powder treatment	67
5.2.1 Selection of solvent	67
5.2.2 Vacuum filtration	69

5.3 Characterisation of composites	74
5.3.1 Density of GO/Al composites	74
5.3.2 Morphologies of powders and GO/Al samples	79
5.3.3 EDXS analysis of GO/Al powders and sintered samples	82
5.3.4 XRD analysis of GO/Al composites	85
5.3.5 Micro Raman analysis of GO/Al composites	87
5.3.6 Micro Vickers hardness of GO/Al composites	92
5.3.7 Indentation tests of GO/Al composites	94
5.4 Modelling of GO/Al composites	98
5.4.1 Effect of GO addition on stress distribution of GO/Al composites	98
5.4.2 Effect of GO layers on stress distribution	104
5.4.3 Verification of FE model of GO/Al composites with the analytical model of GO/Al composites	113
5.4.4 Validation of FE model of GO/Al composites	114
5.5 Summary	115
CHAPTER 6	116
Conclusion	116
6.1 Production of GO/Al composite powders at optimal process parameters by liquid infiltration	116
6.2 Production of GO/Al pellets at optimal process parameters by powder metallurgy	116
6.3 Characterisation of GO/Al powders and pellets	116
6.4 FE modelling and simulation of GO/Al composites	117
Future work	118
References	119
Appendices	i
A1 Modelling of graphene reinforced Al composites	i
A1.1 Introduction	i
A1.2 Analytical solution	v
A1.3 Results	vii
A1.4 Conclusions	xv
AR1 References	xv
A2 Powder metallurgy	xvii
A2.1 Introduction	xvii

A2.2 Advantages of PM	xvii
A2.3 Limitations of PM	xvii
A2.4 Applications of PM	xvii
A2.5 Powder preparation and blending	xviii
AR2 References	xxiii

## ABBREVIATIONS

AFM	Atomic force microscopy
Al	Aluminium
Al <sub>2</sub> O <sub>3</sub>	Aluminium oxide
Al <sub>4</sub> C <sub>3</sub>	Aluminium carbide
AMC	Aluminium matrix composites
CNT	Carbon nanotubes
CS	Compressive strength
CVD	Chemical vapour deposition
EDXS	Energy dispersive X-ray spectroscopy
FE	Finite element
FLG	Few layer graphene
FT	Fracture toughness
GA	Gas atomisation
GIC	Graphite intercalation compounds
GNP	Graphene nanoparticles
GNS	Graphene nanosheets
GO	Graphene oxide
HOPE	Highly oriented pyrolytic graphite
HV/VH	Vickers hardness
IPA	Isopropyl alcohol/2-propanol
LPE	Liquid phase exfoliation
ME	Mechanical exfoliation
MM	Mechanical milling
MMC	Metal matrix composite
MWCNT	Multi walled carbon nano tubes
PECVD	Plasma enhanced chemical vapor deposition
PM	Powder metallurgy
rGO	Reduced graphene oxide
ROM	Rule of mixtures
RVE	Representative volumetric element
SEM	Scanning electron microscopy
SiC	Silicon carbide
SiC <sub>p</sub>	Silicon carbide particle
SLG	Single layer graphene sheets
SWCNT	Single walled carbon nano tubes
TEM	Transmission electron microscopy
UHV	Ultra-high vacuum
UTS	Ultimate tensile strength
VHN	Vickers hardness number
wt%	Weight percentage
XRD	X-ray diffraction
YS	Yield strength

# NOMENCLATURE

Symbol	Notation	Units
$\rho_A$	Actual density of the sample	g/cm <sup>3</sup>
$\theta$	Bragg's angle	°
$d$	Crystallite size	µm
$y$	Deflection in centre	mm
$\varphi$	Densification	%
$\rho_w$	Density of distilled water	g/cm <sup>3</sup>
$\rho_s$	Density of sintered samples	g/cm <sup>3</sup>
$x$	Diameter of indenter	µm
$\delta d$	Dispersion cohesion parameter	MPa <sup>1/2</sup>
$K_{em}$	Electrical conductivity of matrix	S/m
$\sigma_{eff}$	Effective stress of composite	MPa
$k_f$	Fibre volume fraction of composite	-
$\Delta w$	Full width at half maximum of peak	µm
$\sigma_m$	Flow stress in matrix	MPa
$\sigma_p$	Flow stress in particle	MPa
$\rho_g$	Green density of samples	g/cm <sup>3</sup>
$\delta h$	Hydrogen bonding cohesion parameter	MPa <sup>1/2</sup>
$I_{2D}$	Intensity of 2D-band	a.u
$I_D$	Intensity of D-band	a.u
$I_G$	Intensity of G-band	a.u
$d_{hkl}$	Inter planar distance of consecutive atomic planes	µm
$K_{el11}$	Lamina longitudinal electrical conductivity	S/m
$K_{el22}$	Lamina transverse electrical conductivity	S/m
$d_1$	Length of diagonal 1	µm
$d_2$	Length of diagonal 2	µm
$P$	Load	N
$F$	Load acting on the material	N
$\nu_{12}$	Major Poisson's ratio	-
$k_m$	Matrix volume fraction of composite	-
$I_o$	Maximum intensity	a.u
$\nu_{21}$	Minor Poisson's ratio	-
$\delta_m$	Mixture density	g/cm <sup>3</sup>
$n$	Order of reflection	-
$\beta$	Peak width	µm
$\nu$	Poisson's ratio	-
$\delta p$	Polarity cohesion parameter	MPa <sup>1/2</sup>
$\sigma_r$	Radial stress	MPa
$R$	Radius of circular disk	mm
$\omega_G$	Raman shift	cm <sup>-1</sup>
$w$	Raman wavenumber	cm <sup>-1</sup>
$w_c$	Raman wavenumber at centre	cm <sup>-1</sup>
$K$	Scherr constant	-

$\rho_{Al}$	Density of Al powder	g/cm <sup>3</sup>
$\rho_{GO}$	Density of GO sheets	g/cm <sup>3</sup>
$\sigma_t$	Tangential stress	MPa
$\rho_{th}$	Theoretical density of the samples	g/cm <sup>3</sup>
$t$	Thickness of disk	mm
$V_f$	Volume fraction of fibre	-
$V_m, f_m$	Volume fraction of matrix	-
$f_p$	Volume fraction of particle	-
$\lambda$	Wavelength of x-ray	nm
$W_A$	Weight of sample measured in air	g
$W_w$	Weight of sample measured in water	g
$W_{Al}$	Weight percentage of Al powder	%
$W_{GO}$	Weight percentage of GO	%
$E_f$	Young's modulus of fibre	MPa
$E_m$	Young's modulus of matrix	MPa
$E$	Young's modulus	MPa
$E_p$	Young's modulus of particle	MPa

# LIST OF FIGURES

Figure 1.1: Research questions with the strategies developed in present work.	5
Figure 2.1: Classification of production techniques of metal matrix composites (MMCs).	10
Figure 2.2: Graphene wrapped into fullerenes, nano tubes and graphite [65].	13
Figure 2.3: Schematic representation of in-plane ( $\sigma$ ) bonds and out-of-plane ( $\pi$ ) bonds [69].	13
Figure 2.4: Schematic representation of sequential steps followed to exfoliate graphene layers using the scotch tape method.	20
Figure 2.5: Sequential steps followed during film transfer of graphene films produced via CVD approach [114].	24
Figure 2.6: Oxidation of graphite to GO and reduction to rGO [160].	26
Figure 2.7: (a) Effect of GNS content on UTS and Yield strength of GNS/Al composites and (b) TEM image of 0.25wt% GNS/Al composite showing dislocations and carbide formation [181].	30
Figure 2.8: XRD pattern of pure Al, 1wt% multi-walled nanotubes (MWNT)/Al composites and 0.1wt% of GNS/Al composites [182].	31
Figure 2.9: SEM images showing particle morphologies of 1wt% FLG/Al composites (a) gas atomized and (b) mechanically milled [18].	32
Figure 2.10: SEM images of 0.1wt% GNP/Al composites sintered at 630°C at various sintering times, (a) 120mins and (b) 300mins [183].	34
Figure 2.11: Particle morphologies of ball milled composite powder samples (a)-(b) 1wt% GNP/Al, (c)-(d) 3wt% GNP/Al and (e)-(f) 5 wt% GNP/Al; red arrows represents the existence of GNPs [188].	35

Figure 2.12: Compressive strength and micro hardness of gas atomized, mechanically milled Al, FLrGO and FLG samples after sintering [18].	37
Figure 4.1: Schematic representation of GO/Al powder and composite preparation.	48
Figure 4.2: Loading cycle used in production of GO/Al composites.	49
Figure 4.3: Sintering profile used in production of GO/Al composites.	49
Figure 4.4: Schematic representation of interactions of electron beam with surface of the sample.	51
Figure 4.5: (a) Schematic representation of main components of SEM and (b) photograph of SEM with EDX setup.	53
Figure 4.6: (a) Schematic of Bragg's law, black lines represent plane of atoms and (b) photograph of XRD used in current research.	55
Figure 4.7: (a) Schematic representation of energy levels [202] and (b) photograph of micro Raman spectroscopy setup.	57
Figure 4.8: (a) Principle of Vickers hardness, (b) photograph of micro Vickers hardness tester.	58
Figure 4.9: Photograph of indentation (puncture) test setup.	59
Figure 4.10: FE model of GO/Al composite with application of boundary conditions.	61
Figure 4.11: Mesh convergence plots of (a) FE model with no layer and (b) FE model with 5GO layers.	63
Figure 5.1: Outline of order of results discussed in this chapter.	66
Figure 5.2: Comparison of 1.3wt% of GO dispersion in solvent (a) IPA and (b) acetone.	68
Figure 5.3: Filtered out solution of 1.3 wt% GO/Al (a)IPA as solvent and (b) acetone as solvent.	69
Figure 5.4: Visual inspection of filter papers after vaccum filtration.	69
Figure 5.5: (a) Green density and sintered density against compaction pressure of pure Al samples and (b) percentage of sintered	

density and porosity vs compaction pressure of pure Al samples; n=3.	75
Figure 5.6: Relative sintered density and densification factor of the sintered GO/Al composites.	76
Figure 5.7: Theoretical and measured densities of GO/Al composites sintered at 600°C: (a) compacted at 500MPa, (b) compacted at 540MPa and (c) compacted at 580MPa.	78
Figure 5.8: SEM images of composites showing agglomeration (a) 1wt% of GNP/Al [195] and (b) 0.2wt% of GO/Al in current research.	79
Figure 5.9: Particle morphology of (a) 35µm Al powder (b) 0.05wt% of GO/Al powder (c) 0.1wt% of GO/Al powder and (d) 0.2wt% of GO/Al powder.	80
Figure 5.10: SEM images of surface of GO/Al composites: (a)-(b) 0.05wt%: (a) sintered at 580°C, (b) sintered at 600°C, (c)-(d) 0.1wt% : (c) sintered at 580°C, (d) sintered at 600°C, (e)-(f) 0.2wt%: (e) sintered at 580°C and (f) sintered at 600°C.	81
Figure 5.11: SEM images of 0.2wt% GO/Al composites showing grain size measurements (a) sintered at 580°C and (b) sintered at 600°C.	82
Figure 5.12: EDXS images of dried powders (a) pure Al, (b) 0.05wt% GO/Al, (c) 0.1wt% of GO/Al and (d) 0.2wt% of GO/Al.	83
Figure 5.13: EDXS images of samples sintered at 600°C (a) pure Al, (b) 0.05wt% GO/Al, (c) 0.1wt% of GO/Al and (d) 0.2wt% of GO/Al.	84
Figure 5.14: XRD spectra of monolithic and 0.05wt%, 0.1wt% and 0.2wt% GO/Al composites sintered at 580°C and 600°C.	86
Figure 5.15: Recorded micro Raman for GO/Al composites (a) 0.05wt%, (b) 0.1wt% and (c) 0.2wt%.	90
Figure 5.16: Raman spectra of composites (a)-(c) sintered at 580°C, (d)-(f) sintered at 600°C: (a) 0.05wt% GO/Al, (b) 0.1wt% GO/Al, (c) 0.2wt% GO/Al, (d) 0.05wt% GO/Al, (e) 0.1wt% GO/Al and (f) 0.2wt% GO/Al.	91

Figure 5.17: Vickers hardness of pure Al and GO/Al composite samples (a) sintered at 580°C and (b) sintered at 600°C; n=3, 95% confidence.	93
Figure 5.18: Fracture surfaces of pure Al, 0.05wt%, 0.1wt% and 0.2wt% of GO/Al composites compacted at various pressures and sintered at 580°C.	94
Figure 5.19: Fracture surfaces of pure Al, 0.05wt%, 0.1wt% and 0.2wt% of composites compacted at various pressures and sintered at 600°C.	95
Figure 5.20: Variation of stress developed in the specimens under loading with wt% of GO reinforcement, compaction pressures and sintering temperatures (a) radial stress and (b) tangential stress; n=3, 95% confidence.	96
Figure 5.21: SEM images of fracture morphology on cross sections of crack zones of composites compacted at 580 MPa and sintered at 600°C (a) pure Al, (b) 0.05wt% GO/Al, (c) 0.1wt% GO/Al and (d) 0.2wt% GO/Al.	97
Figure 5.22: Stress profile of FE model containing only Al particles.	99
Figure 5.23: Stress profile of GO/Al composite with 5GO layers (a) stress profile of overall composite and (b) stress profile in respective Al particles.	100
Figure 5.24: Stress profiles of GO/Al composites and their corresponding Al particles with respect to the % of Al particles coated with 5 GO layers.	103
Figure 5.25: Comparison of maximum stress in models with 5GO layers on Al particles with respect to the % of Al particles coated by GO.	104
Figure 5.26: Stress profiles of GO/Al composites with respect to the number of GO layers.	107
Figure 5.27: Comparison of maximum stress in models with respect to the addition of GO layers to Al particles.	108
Figure 5.28: Stress profiles of GO/Al composites with respect to the number of GO layers and % of Al particles coated with GO.	111

Figure 5.29: Comparison of Young's modulus obtained from FE modelling and analytical modelling of GO/Al composites.	113
Figure 5.30: Comparison of Young's modulus of GO/Al composites obtained from experiments obtained from current work and literature with simulation results.	114
Figure A1.1: Schematic representation of composite cells of (a) particulate reinforced composite, and (b) Continuous fiber reinforced composite [3].	i
Figure A1.2: Schematic representation of models used in present study (a) RVE, (b) extruded rod to predict tensile strength.	iv
Figure A1.3: (a) Converged FE model of graphene reinforced aluminium composite, and (b) FE model of extruded rod.	iv
Figure A1.4: Comparison of experimental and simulated values for pure Al.	viii
Figure A1.5: Verification of simulation results with theoretical methods (a) ROM, and (b) Bettie's reciprocal theorem.	ix
Figure A1.6: Comparison of tensile strength of graphene reinforced Al and Cu matrix composites at different vol % of graphene reinforcement.(b)	x
Figure A1.7: Comparison of Young's modulus of different matrix materials with different vol % of graphene reinforcement (0.1%, 0.2%, 0.5%, 1%, 2%, and 5%) (a) longitudinal Young's modulus and (b) transverse Young's modulus.	x
Figure A1.8: Comparison of tensile strength of graphene reinforced Al and Cu matrix composites at different vol % of graphene reinforcement.	xi
Figure A1.9: Comparison of conductance of Al and Cu as matrix material graphene reinforced composites with different vol % of graphene reinforcement (a) 0.1%vol, (b) 0.2%vol, (c) 0.5%vol, (d) 1%vol, (e) 2%vol and (f) 5%vol.	xii
Figure A2.1: Flowchart of powder metallurgical component production [1].	xx

Figure A2.2: Schematic representation of piston-die assembly in press.	xxi
Figure A2.3: Schematic representation of compaction cycle.	xxii
Figure A2.4: Schematic representation of mechanism of sintering.	xxii

## LIST OF TABLES

Table 2.1: Mechanical properties of graphene and its derivatives in comparison with conventional metals.	14
Table 2.2: Electrical properties of graphene and its derivatives in comparison with conventional metals.	17
Table 2.3: Thermal properties of graphene and its derivatives in comparison with conventional metals.	18
Table 2.4: Summary of advantages and disadvantages of graphene synthesis techniques.	28
Table 3.1: Summary of processing parameters and mechanical properties of graphene reinforced AMCs.	40
Table 4.1: Properties of Al at room temperature, source: MSDS, Goodfellow.	45
Table 4.2: Properties of acetone and IPA used in current research, source: MSDS, Fisher scientific.	46
Table 4.3: Properties of GO aqueous dispersion used in current research, source: MSDS, Graphenea.	46
Table 4.4: Amount of raw materials required to produce GO/Al powder at different wt% of GO using acetone and IPA as solvents measured using 5digit balance.	47
Table 4.5: Design of experiment with varying wt% of GO, compaction pressure and sintering temperature: total number of specimens: 54(18×3).	47
Table 4.6: Characterisation techniques used in current research.	50
Table 4. 7: Material properties used in simulation of GO/Al composites.	61
Table 4.8: Properties of materials used in analytical modelling of GO/Al composites.	64
Table A1.1: Matrix materials and properties as applied in the study.	v

# CHAPTER 1

## INTRODUCTION

### 1.1 Background

Metal matrix composites (MMCs) are the range of advanced materials with the combination of a metallic matrix and a non-metallic reinforcement such as ceramic or organic compounds. MMCs demonstrate better mechanical properties and moduli when compared to monolithic metals or alloys [1,2]. The benefits offered by MMCs include high Young's modulus, high strength, retaining at high temperatures, improved wear and fatigue, better impact properties and improved electrical, thermal conductivities. MMCs stand as the ideal materials for engine blocks, pistons, cylinder liners, frames etc., for use in automotive industries and mid-fuselage structures, antenna wave guides etc., in aerospace industries [3,4].

The challenging tasks for composites production includes finding a compatible reinforcement for the available matrices and attaining the uniform distribution of reinforcement. Out of the available metallic matrices aluminium (Al) has been chosen as matrix material for current study as it is inexpensive in comparison to widely used low density metals such as Ti and Mg [3,4]. High corrosion resistance and better formability makes Al a material of choice for automobile applications over other alternatives, including ferrous metals. The general types of reinforcement materials used for Al matrix include silicon carbide (SiC), aluminium oxide ( $Al_2O_3$ ) and graphite. Carbonous nano reinforcements such as CNTs and graphene have been used for aluminium matrix composites (AMCs) and attracted many researchers due to graphene's exceptional mechanical, thermal, electrical and tribological properties and additional advantage of being nano i.e., availability of maximum area for chemical reactions. Out of derivatives of graphene, graphene oxide (GO) has been chosen as reinforcement material for Al matrix in the present study due to its hydrophilic nature and better dispersion in aqueous solutions. The nano particle reinforcement benefits the metallic matrices in improving the tensile strength and elongation. However, the uniform distribution and agglomeration reduces the chances of attaining superior ductility [5,6]. The distribution of

nano particles along the matrix material shows the significant effect on the end properties of composite [7–9], which contributes to the agglomeration of the nano particles around the grain boundaries rather than mixing with grains and will promote crack growth. To address this, many manufacturing techniques such as powder metallurgy [10,11], stir casting [12,13], semi-solid casting [14,15] and semi-solid processing [16,17] are used for the production of AMCs. These techniques have shown to achieve some extent of uniform distribution, but the complete homogeneity is not achieved. This lack in homogeneity has led to the reduction in mechanical properties of the composites. This implies to the necessity of in-depth analysis on material processing stages i.e., mixing parameters of matrix and reinforcement, thermo-physical properties, compatibility of reinforcement with matrix and wettability of particles to improve properties of the end composites.

This study therefore combines the use of novel liquid infiltration synthesis and conventional fabrication routes to obtain composites with better mechanical properties. Powder processing parameters such as solvent selection, wt% of GO reinforcement and stirring time were investigated to understand the interaction of GO reinforcement with the Al matrix. The microscopic and quantitative analysis will be used to investigate and analyse the effect of graphene oxide (GO) addition on microstructural manipulation of base material, aluminium (Al). Although, there are some studies reported on using graphene nanosheets (GNS) [18–21] graphene nano platelets (GNP) [22–26] and reduced graphene oxide (rGO) [18,27–29] as reinforcement materials, the complete potential of graphene addition on Al matrix has not been achieved due to one of the following reasons: inefficient reduction of GO to rGO without effecting the graphene structure, non-homogeneous dispersion of reinforcement on to the matrix and bonding between graphene and Al particles. Some researchers even reported the formation of carbides and contamination of composites as the reasons behind the degradation of properties of end composite. To address this, the present study aims at exploring the potential of GO on manipulating microstructure of Al particles to improve properties of end composite. To avoid the contamination of the produced composites the use of additives or surfactants was avoided during powder preparation for the fabrication of composites. The current study has

made use of wet mixing/liquid infiltration techniques to avoid damage to the graphene structure which is inevitable with mechanical milling processes.

## **1.2 Motivation Aim and objectives of the study**

The excellent properties of graphene caught attention of many researchers globally, using the full benefit of graphene and its derivatives is a matter of concern, especially in composites. There are many challenges in exploring the potential of graphene as a reinforcement for AMCs and their applicability in practical applications. One of the key issues regarding the use of graphene lies in its production on bulk scale as it is very expensive and involves sophisticated characterisations. The use of mechanical milling i.e., ball milling to produce graphene reinforced Al matrix is investigated by many researchers but the increase in properties were not promising as the high energies and long-milling times damages the graphene structure. The damage to the graphene structure will lead to the disorderness and reduction of properties. Moving to the wet mixing techniques from ball milling will enable to achieve better dispersion and hence better properties. The use of liquid exfoliation techniques of graphite in compatible solvent media is a relatively new technique at the commencement of present work but now is becoming a popular technique for graphene production.

Many studies have demonstrated the use of rGO that is obtained by removing the oxide functionalities. This can be achieved either by thermally heating to certain temperatures or by adding appropriate chemicals. The reduction process will disrupt the band structures and will highly effect its properties, for instance, rGO is not as electrically conductive as pure graphene and rGO is more hydrophobic. The thermal reduction of GO reinforced Al powder will lead to the formation of carbides which deteriorates the properties of overall composite. Hence, there is a lack of quick and straightforward techniques to reduce GO and restore properties. None of the studies at the time of writing this thesis have reported the use of GO without reducing it. Regarding the application of graphene, one application of interest is using composites made from GO and Al matrix to be used as pistons, connecting rods and shafts in automobile industries. Most studies carried out used either SiC or Al<sub>2</sub>O<sub>3</sub> as reinforcement on Al matrix. On the other hand, the residual stresses and strain

induced during fabrication must be avoided to make better use of the full potential of reinforcement addition. Hence X-ray diffraction (XRD) and Raman spectroscopy are used to investigate the effect of parameters used in fabrication techniques on the end composites.

After recognizing the potential of graphene oxide itself compared to reduced graphene oxide which was extensively used by researchers, I have made an attempt to use graphene oxide on its own without any reduction steps which was not been explored before. Thus the aim of my research work is to produce graphene oxide reinforced aluminium matrix composites at optimized process parameters.

Objectives:

1. Production of GO/Al powders using liquid infiltration technique in different solvents at different stirring times.
2. Investigation of the effect of powder metallurgical parameters such as compaction pressure, sintering temperature on properties of GO/Al composites.
3. Characterisation of GO/Al powders and GO/Al composites for microstructural, mechanical analysis and comparison with monolithic Al samples.
4. Finite element (FE) modelling and simulation of GO/Al composites to predict the effect of existence of number of layers and volume fraction of GO on Al particles on the stress distribution of the composites.

### **1.2.1 Research questions**

Graphene oxide is one of the economical alternate derivatives of graphene which consists of hydroxyl and carboxylic groups that provides better dispersion in aqueous solutions and many other solvents. The use of GO without any reduction steps as reinforcement for AMCs has not been explored till to date which is one of the major contributions of present research work. Figure 1.1 shows the research questions and strategies developed/adopted in current research work.

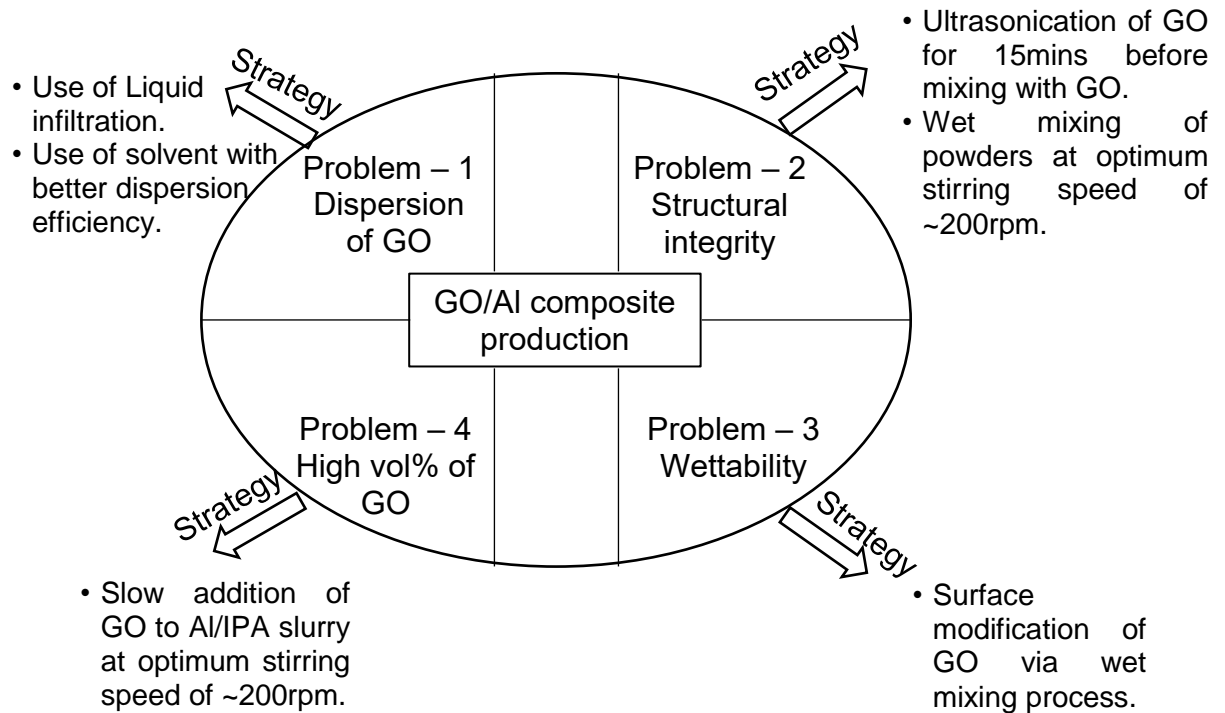


Figure 1.1: Research questions with the strategies developed in present work.

## 1.3 Thesis outline

### ***Chapter 1 Introduction***

In this chapter a brief overview of MMCs as well as the motivation to pursue research in current area and the objectives of current research work are presented.

### ***Chapter 2 Literature review***

This chapter reviews the literature concerning MMCs, graphene in general and graphene reinforced Al matrix composites in particular. A brief introduction to MMC, production techniques of MMCs and a brief introduction of graphene and its derivatives, synthesis techniques, properties are presented targeting mainly the processing techniques related to the production of nano reinforced AMCs.

### ***Chapter 3 Critical summary of literature review***

The summary of AMCs reinforced with various derivatives of graphene together with the processing conditions used and the properties investigated were given in this chapter.

#### ***Chapter 4 Materials and methods***

The materials and characterisation methods used in present research work are presented in this chapter. It comprises of powder preparation, composite fabrication followed by the characterisation of powders and samples. The finite element modelling of composite with parameters used in model setup and boundary conditions are also given in this chapter.

#### ***Chapter 5 Results and discussion***

The Characterisation results of as received Al samples, GO/Al powders, GO/Al composite samples are presented in this chapter. A summary on scanning electron microscopy (SEM), energy dispersive X-ray spectroscopy (EDXS) analysis, X-ray diffraction (XRD), micro Raman spectroscopy, micro Vickers hardness and indentation experimental results and results obtained from composite structural modelling conclude this chapter. The results obtained were discussed with theoretical and literature backup and compared with as received Al samples. The discussion on results obtained from the simulation of composite model are also included in this chapter.

#### ***Chapter 6 Conclusion and future recommendations***

This chapter summarises the results obtained from the current work, concludes thesis with highlights on major findings from this work. Additionally, suggestions for the future work to expand the investigation in critical issues in fabrication of nano reinforced metal matrix composites are mentioned in this chapter.

## CHAPTER 2

### LITERATURE REVIEW

#### 2.1 Metal matrix composites (MMCs)

MMCs combination tailor the best properties out of their constituents such as improved ductility, toughness, strength. MMCs reinforced with ceramic fibers exhibit increase in strength and stiffness compared to the monolithic alloys [30–32]. The matrix material usually transfers and distributes load to reinforcements depending on the bonding interface between matrix and reinforcement [33]. There are several factors that should be considered while selecting the matrix and reinforcement materials for composite systems. These factors include compatibility between matrix and reinforcement, ease of fabrication methods, applicability of the end composite [34]. The selection of matrix material usually depends on ease of manufacturing of the end product with selected fabrication method and most of the matrices are metals and alloys [35]. For an instance, powder is used as matrix material in powder metallurgy [36] and liquid matrix material is used for liquid metal infiltration [37]. Appropriate care should be taken while considering the chemical compatibility and wettability of reinforcement in matrix material while working with liquid infiltration methods. In general, metals such as Al, Ti, Mg, Ni, Cu, Fe and Sn are used as matrix materials out of which light metals such as Al, Mg and Ti has attracted attention recently due to the combination of light weight and high specific strength which makes them promising materials in aeronautical and automobile applications [38]. Out of these light metals, Al is the material of interest to many researchers globally due to its unique combination of high strength, good corrosion resistance and noTable electrical conductivity [39]. The factors that should be considered while selecting the reinforcement are reinforcement type, shape, geometry and chemical compatibility with matrix materials [40].

Nanoparticle reinforcement have proven to be better than the micro sized reinforcements on MMCs even though attaining uniform distribution is a challenging task [41]. The non-homogeneous distribution is due to high chances of agglomeration of nanoparticles and electro-repulsion at high

volume percentages [42,43], which in turn will reduce the mechanical properties. However, the nano reinforcement use will benefit the changes in fracture mode from inter-granular to trans-granular mode. The change in fracture mode leads to increase in tensile properties, enhanced fracture toughness, increased stability at high temperatures and better creep and wear resistance. The most commonly used nanoparticle reinforcements for MMCs are SiC, TiC, Al<sub>2</sub>O<sub>3</sub>, AlN, TiB<sub>2</sub> and WC [44]. Miracle et al. [45] have reported the effect of addition of nano and micro sized SiC reinforcements on Al matrix. It can be noted that the addition of nano reinforcement resulted in enhanced dimensional stability and reduced temperature sensitivity over monolithic Al samples. It was reported that the nano sized reinforcement incorporation in metallic matrices can improve mechanical properties significantly [42,46]. For instance, nano reinforcement improved elastic modulus and yield strength compared to micro reinforcement for the AMCs [47]. This is possible due to increase in barriers to restrict the dislocations but will eventually lead to the reduction in ductility, creep resistance and nano reinforcement will also promote the formation of micro voids [48,49]. The increase in demand for high strength and low weight materials with better electrical and thermal properties have inspired researchers to work with AMCs. Particulate reinforced AMCs are more popular in automotive industries due to their capability to work under high temperatures and pressures [50]. The nano particle reinforcements of SiC and Al<sub>2</sub>O<sub>3</sub> were used with AMCs to improve mechanical properties of base metal [51,52]. Various manufacturing techniques such as stir mixing [53], ball milling [15,54], stir casting and compocasting [55] were used to produce Al<sub>2</sub>O<sub>3</sub> particle reinforced AMCs. It can be noted from reported results in literature that the usage of stir casting methods resulted in severe agglomeration of Al<sub>2</sub>O<sub>3</sub> nanoparticles with contact angles of nearly 100° between Al and Al<sub>2</sub>O<sub>3</sub> particles, whereas poor wetting between Al and nano reinforcement was noted which led to floating of particles on liquid metal surfaces [56]. The ball milling techniques used for fabrication of AMCs reinforced with Al<sub>2</sub>O<sub>3</sub> particles resulted in better dispersion and reduced agglomeration, but the high energies used in ball milling resulted in structural damage of nano reinforcement and induced defects [54]. Even though compocasting methods provided better distribution of reinforcement into the matrix, controlling process parameters

and chemical reactions between matrix and reinforcement proved to be difficult [55]. Hence, there is a need to develop a fabrication technique that provide both homogenous distribution of reinforcement into the matrix and enhance the bonding between reinforcement and matrix.

## **2.2 Manufacturing techniques of aluminium matrix composites (AMCs)**

MMCs can be fabricated through different fabrication routes i.e., solid state processing, liquid state processing and semi-solid processing and the classification is shown in Figure 2.1. The selection of fabrication techniques depends on the phase of matrix and reinforcement materials and applicability of the end composite. For instance, solid-phase processes are used to improve mechanical properties and to reduce the segregation effects. Liquid-phase processes are used to produce parts with difficult shapes with low manufacturing costs, however this process suffers with lack of control on process parameters and chemical reactions between matrix and reinforcement. The semi-solid process offers the advantage of reduced segregation but includes high processing costs of end products. There are different processing techniques reported in literature to produce AMCs that includes powder metallurgy, high energy ball milling, friction stir processing and ultrasonic casting. These processes used to produce AMCs can effect the microstructure of composite, grain growth and porosity levels and hence variation in properties of end product can be observed. This establishes the necessity to control microstructure under various processing conditions.

Powder metallurgical techniques offer control over the homogeneity of mixtures and will aid to produce near net shapes and can avoid segregation and agglomeration of the nano reinforcement particles to the maximum extent if provided with better mixing parameters. Tang et al. [57] have demonstrated the use of ball milling to mix Al matrix and silicon carbide particle ( $\text{SiC}_p$ ) reinforcement and it can be noted that the tensile strength of  $\text{SiC}_p/\text{Al}$  material improved than the monolithic Al samples and better dispersion of  $\text{SiC}_p$  reinforcement in Al matrix was noted. Kang et al. [58] have used mechanical alloying process to produce  $\text{SiC}_p$  reinforced Al composites using different volume percentage of  $\text{SiC}_p$ . It was observed that the tensile yield strength of

composite was increased until the application of critical load and then decreased, which was due to the agglomeration of SiC<sub>p</sub> at grain boundaries.

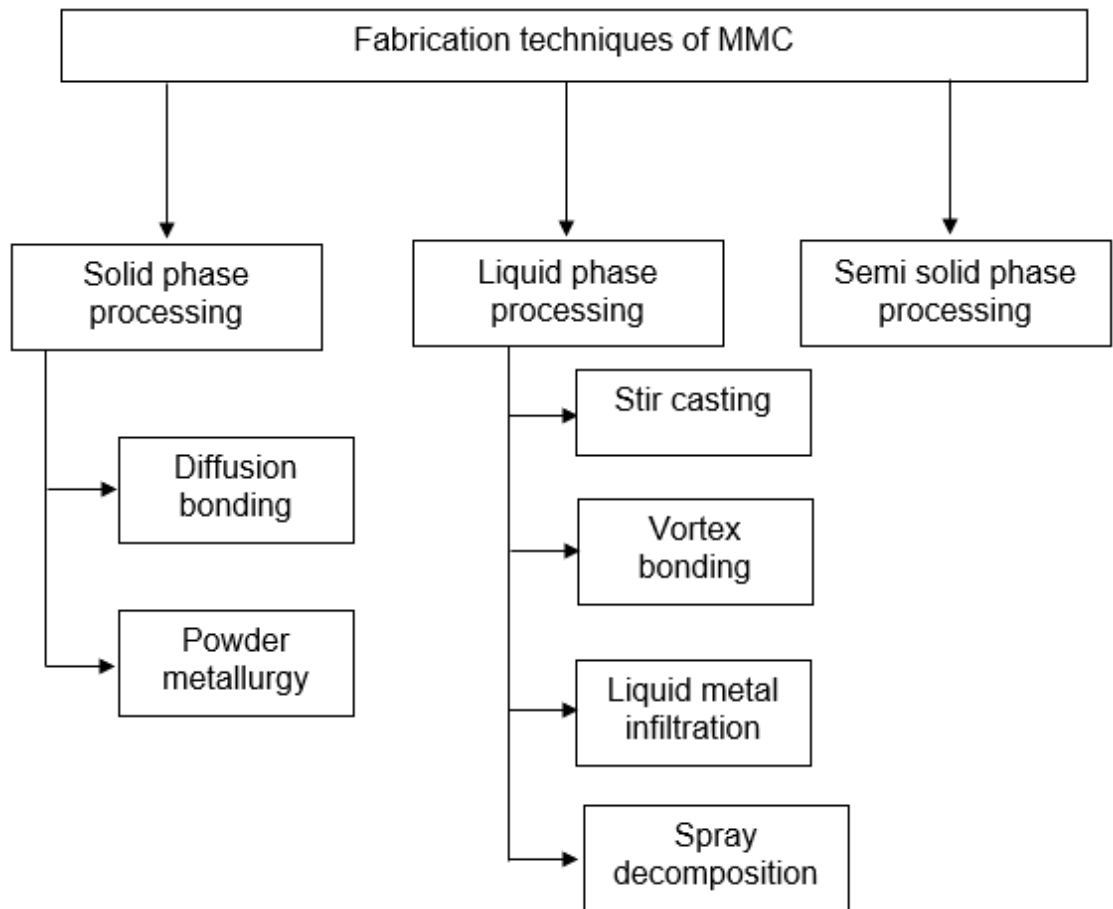


Figure 2.1: Classification of production techniques of metal matrix composites (MMCs).

Liquid-phase fabrication techniques involve stirring of particles into melts, which provides perfect bonding between the matrix and reinforcement. However, the liquid-based processing of SiC<sub>p</sub>/Al composites study conducted by researchers have reported that high percentage of brittleness in composites due to difference in thermal expansion coefficients between SiC<sub>p</sub> and Al and poor wettability [59]. Mandal et al. [60] have reported the formation of undesired reactions between the SiC<sub>p</sub> and Al in SiC<sub>p</sub>/Al composites and heat treatment process resulted in formation of aluminium carbide (Al<sub>4</sub>C<sub>3</sub>). The production of SiC<sub>p</sub> reinforced A356 Al alloy using ultrasonication assisted casting process was reported by Yang et al. [61], noted an effective distribution of SiC<sub>p</sub> into the matrix through cavitation in the liquid metals and hence

improving yield strength by 50%. However, this process is not suitable for nanoparticle reinforcements due to high chances of clustering of particles at high volume percentage of nano reinforcement.

Semi-solid processing techniques have caught the attention of many researchers as it provides better dispersions for nano reinforcements in MMCs, especially in AMCs [62]. Curle et al. [63] have reported the production of SiC<sub>p</sub> micro sized reinforced Al composites through semi-solid processing, it was reported that the wear resistance of composite was increased by the order of 72%. Jiang et al. [64] have reported the effect of nano sized SiC<sub>p</sub> reinforcement on Al matrix in SiC<sub>p</sub>/Al composites produced by using rheocasting process. The tensile properties of the produced composites were enhanced with increase in stirring times. However, the tensile properties started diminishing above 1vol% of SiC<sub>p</sub> reinforcement, this was attributed to the agglomeration.

The manufacturing of MMCs especially AMCs face critical challenges of achieving uniform distribution of nanoparticles into the matrix and agglomeration of nanoparticles which is attributed to high surface to volume ratios. These two hurdles deteriorate mechanical properties especially ductility and fracture toughness of end composite. The main parameters that effects the agglomeration are: stirring time, temperature of stirring, type of reinforcement and amount of reinforcement. Liquid phase fabrication offers advantage of better matrix and reinforcement bonding in comparison to powder metallurgy. However, this process suffers from lack of wettability and uniform distribution unlike powder metallurgy. It is therefore essential to obtain more insight on microstructural changes due to nano reinforcement addition to produce high performance AMCs for different applications. Hence, the interest of current research is to combine liquid-based powder preparation and powder metallurgical fabrication of composites.

## **2.3 Graphene**

Professor Andre Giem and Professor Kostya Novoselov at the University of Manchester successfully isolated the 2D graphene sheets [65], which disapproved the assumptions that 2D materials couldn't exist without 3D base

which is an integral part of large 3D structures. It can also be noted that the invented 2D materials did not violate the Peierls rule [66], which states that the thermal fluctuations in 2D crystals would destroy the crystalline order in a long range [67].

### **2.3.1 Morphology of graphene**

Graphene is a monolayer of carbon atoms arranged in 2D honey comb structure [68]. It can be considered as a basic allotrope of carbon to extract/form other allotropes, shown in Figure 2.2 [65]. For instance, graphene sheet can be wrapped around to form 0D fullerene (it doesn't have any particular dimensions in which it displays translational symmetry unlike a sheet or tube) or rolled to form 1D carbon nanotubes (CNTs) or can be stacked with number of layers to form 3D graphite. The  $sp^2$  hybridised C-C bond length of graphene is in the order of 0.142nm, when the graphene layers are stacked together, the interplanar spacing will be 0.335nm [68]. The unit cell of single layer graphene sheets (SLGs) consists of two atoms in it and consequently there will be four atoms in bilayer cell. In graphene, a carbon atom have 3 $\sigma$  bonds and 1 $\pi$  bond, the in-plane  $\sigma$  bonds are extremely strong and partially filled  $P_z$  orbital,  $\pi$  bond are responsible for electrical conductivity and the graphene layers interactions. The schematic representation of the  $\sigma$  and  $\pi$  bonds in graphene is shown in Figure 2.3 [69]. However, the transmission electron microscopy (TEM) analysis of SLG suspensions done by Meyer et al. [68] have revealed that the SLG sheets are not completely flat and exhibit intrinsic static microscopic roughening which is called ripple. The ripples on suspended SLGs significantly effect electrical properties [70], it can be noted that the larger the ripples (73nm) are, the lower electrical conductivity will be [71]. Apart from these ripples, graphene can have defects like vacancies, adsorbed impurities, cracks, adatoms (atoms lying on the crystal surface) etc [72].

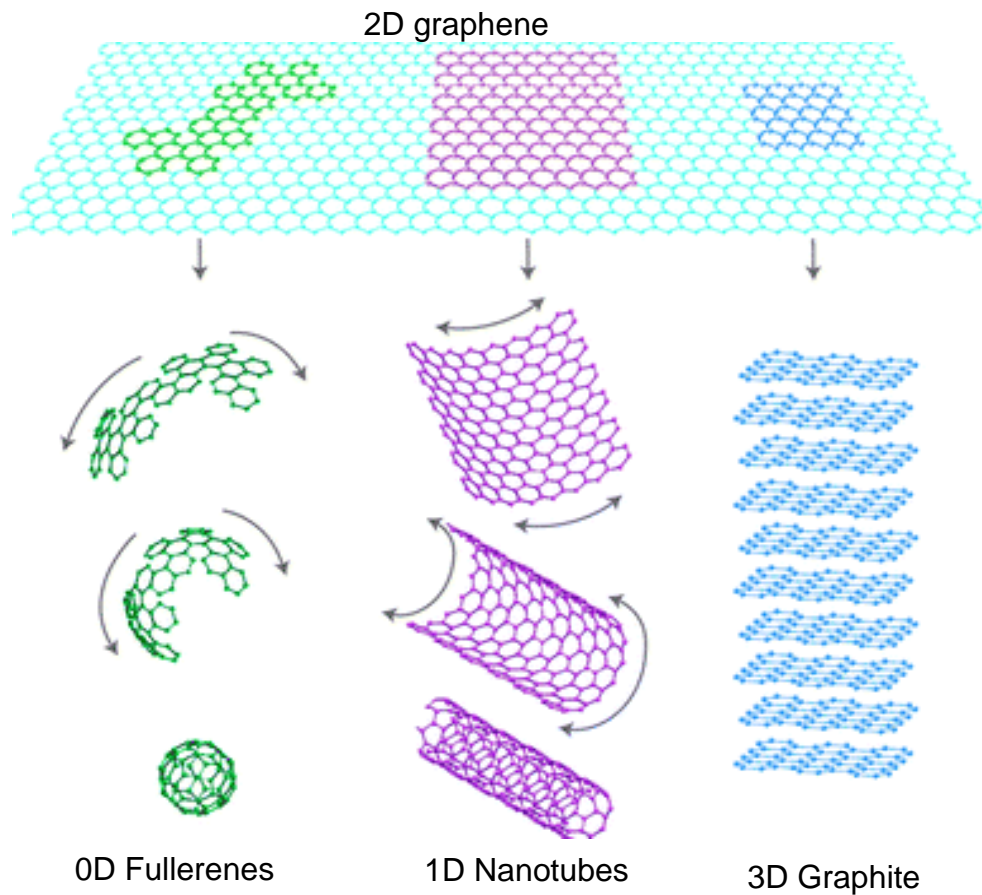


Figure 2.2: Graphene wrapped into fullerenes, nano tubes and graphite [65].

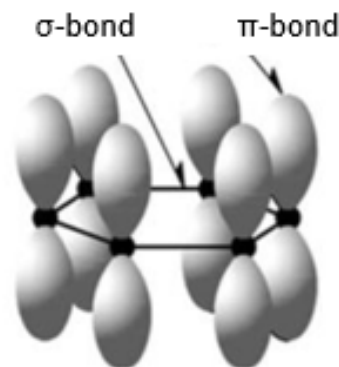


Figure 2.3: Schematic representation of in-plane ( $\sigma$ ) bonds and out-of-plane ( $\pi$ ) bonds [69].

### 2.3.2 Properties of graphene

#### **Mechanical properties**

In any practical applications, an external application of stress and unwanted strain will effect the performance and durability of the product. It was anticipated that the graphene can outperform the CNTs with high strength and

stiffness. Lee et al. [73] have used atomic force microscopy (AFM) to measure elastic properties of monolayer graphene and reported Young's modulus of  $1\pm 0.1$ TPa and intrinsic strength of  $130\pm 10$ GPa. Tsoukleri et al. [74] have used Raman spectroscopy to measure the strain by applying compression and tension loads on SLG and reported a strain of 1.3% and 0.7% in tension and compression respectively. Lee et al. [75] have reported the use of AFM to measure Young's modulus and strength of graphene, reported Young's modulus of 1.02TPa, 1.04TPa and 0.98TPa and fracture strength of 130GPa, 126GPa and 101GPa respectively for mono layer, bi-layer and tri-layer graphene respectively. Raman spectroscopy can be used to measure the compressive and tensile strains in graphene sheets by measuring the change in G and 2D peaks with applied stress. Ni et al. [76] have mentioned that it is possible to tune the band gap by introducing a controlled strain, as the strain may change electric band structure. Cristina et al. [77] have reported that the successful production of chemically modified graphene by reducing graphene oxide with hydrogen plasma, Young's modulus of 0.25TPa was noted from the results. Table 2.1 gives the overview of mechanical properties of graphene and its derivatives, it can be noted from the Table that increase in number of graphene nano sheet layers leads to the reduction in properties.

Table 2.1: Mechanical properties of graphene and its derivatives in comparison with conventional metals.

Material	Young's modulus (MPa)	Tensile strength (MPa)	Fracture toughness ( $\text{MPa}\sqrt{m}$ )	Reference
Graphene (mono layer)	$10^6$	$1.3\times 10^5$	4-5	[75,78]
Reduced graphene oxide (rGO)	$2.5\times 10^5$	$0.9\times 10^3$	2.8-3	[77]
Graphene nano sheets (GNS-bi-layer/tri-layer/multi layers)	$0.98\times 10^6$ - $0.76\times 10^6$	$1.26\times 10^5$ - $1.01\times 10^5$	3.8-3.2	[75]
Aluminum	$6.83\times 10^4$ - $7.0\times 10^4$	130-195	27.5-30	[79]
Stainless steel (Grade 304)	$19\times 10^4$ - $20.3\times 10^4$	510-620	119-228	[80]
Copper	$110\times 10^4$ - $128\times 10^4$	210-390	40-100	[81]
Titanium	$116\times 10^4$	220	84-107	[82]

### ***Electrical properties***

Pristine graphene or monolayer graphene is an efficient zero-gap semiconductor known to mankind. The charge carriers in graphene behave as Dirac fermions (massless relativistic particles) and these behave abnormally compared to electrons when subjected to magnetic field [83], this was even observed at room temperatures. The low defect density of graphene's crystal lattice leads to high quality of single layer graphene sheets which is the main reason behind the high electrical conductivity of monolayer graphene sheets. The electrons in graphene behave as particles of light that do not scatter, which makes graphene a good conductor of electricity. Interfacial phonons [84], substrate ripples [68] and surface charge traps [85] are the factors that affect the conductivity of graphene sheets. Bolotin et al. [86] have demonstrated the minimum scattering using monolayer graphene layer in a suspended condition and demonstrated the effect of impurities on the surface of graphene sheets. A bipolar electrical field effect is another important characteristic of monolayer graphene sheets, this means by applying a gate voltage the charge carriers can be tuned between electrons and holes [65]. The major hurdle for graphene in practical applications is its zero-energy gap, for eg: field effect transistor, which needs on/off switch. Recent research in graphene have reported the modification of graphene band structure by constraining graphene in nanoribbons [87–89] and graphene in quantum dots [90] and by biasing bi-layer graphene [91,92]. Evaldsson et al. [93] have reported the variation of the width of ribbons and disorders in the edges of both zigzag and armchair nanoribbons, this observation was supported by both experimental results and theoretical explanations.

Due to the advantage of scalability to electronics, epitaxial graphene has gained a lot of interest in recent years. There was a mixed opinion among researchers about the bandgap opening in epitaxial graphene, zero band gap on graphene layers was reported by Pen et al. [94] whereas 0.26eV was reported by Kim et al. [89]. An innovative method of growing epitaxial graphene on SiC substrate was developed by Deheer et al. [95]. It was reported that the mobility of graphene grown on Si-terminated face is less than that of the graphene grown on carbon-terminated face. This is due to the difference in structures and this can also be gated. They have also reported the reduction in

energy gap with an increase in thickness and it can be zero if the number of layers exceeds 4-5. This matches well with observations reported by Peng et al. [78], in which energy gap was 0.26eV for mono layer graphene 0.14eV for the triple layer.

Reina et al. [91] have used CVD to synthesise graphene layers on Ni substrate and reported a huge variation in field effect mobility of 100-2000cm<sup>2</sup>/Vs due to ineffective modulated resulted from the non-homogenous thickness of graphene films. Kim et al. [96] have synthesised graphene layers through CVD technique on Ni and transferred it to SiO<sub>2</sub> substrate and the charge mobility was measured as 3700cm<sup>2</sup>/Vs which confirm the existence of mono layer graphene. Even though Ni is the most used metallic substrate to grow graphene [74,92,97,98] of high quality, this suffers a drawback of solubility of carbon-nickel and deposition of multi layers at grain boundaries. Copper was used as an alternative to Ni to overcome the difficulty of high solubility. It was reported that the graphene layer is grown on copper foil through CVD shown a mobility of 4050cm<sup>2</sup>/Vs [92] and a mobility of ~3000cm<sup>2</sup>/Vs [97] by depositing graphene film on a large wafer of the copper substrate. The existence of difficulties in the synthesis of mono layer graphene sheets leads to the research related to the production of bi-layer and FLG. Novoselov et al. [99] reported that bi-layer graphene is almost gapless and remains metallic at neutrality points and charge particles are similar to that of the massless Dirac fermions but possess a finite mass and are called as massive Dirac fermions. Castro et al. [100] have reported a possibility of using bi-layer graphene as a tunable energy band gap semiconductor for energy applications through tuning the band gap by applying a magnetic field and it can be tuned up to 0.2eV.

Numerous efforts have been made so far to reduce GO effectively in order remove oxygenated functional groups which incorporate the high electrical resistance 4MΩ/square. It can also be noted that the thermal and chemical reduction can partially restore the electrical conductivity but introduces the structural defects that degrade the electrical properties when compared to pristine graphene. Gomez et al. [101] have measured the mobility and conductivity of rGO as 2-200cm<sup>2</sup>/Vs and 0.05-2S/cm respectively. Li et al. [102] have reported the production of GNS and 72S/m of electrical conductivity at room temperature was noted from the observations, however the conductivity

of the GNS obtained was not promising compared to monolayer graphene. The recent results published by researchers from Graphenea Spain, have reported that the electrical conductivity of rGO reached to a value of 666.7S/m for a film of 20nm thickness [98]. Table 2.2 gives the overview of electrical properties of graphene and its derivatives from the most recent studies. It can be noted from the Table that the electrical conductivity of the rGO can be partially restored after the reduction process, which is only to 1% of the conductivity of pristine graphene, this was due to the disruption to the band structure of graphene.

Table 2.2: Electrical properties of graphene and its derivatives in comparison with conventional metals.

Material	Electrical conductivity (S/m)	Electron charge mobility (cm <sup>2</sup> /Vs)	Energy gap (eV)	Reference
Graphene (mono layer)	10 <sup>8</sup>	15,000-200,000	0.26	[100]
Reduced graphene oxide (rGO)	666.7	17-2000	Tunable gap of 0.35-0.78	[98,101]
Graphene nano sheets (GNS-bi-layer/tri-layer/multi layers)	72	5-290	0.42	[102,103]
Aluminum	3.74x10 <sup>7</sup>	5600-7000	0.31-0.32	[79]
Stainless steel (Grade 304)	1.30x10 <sup>6</sup> -1.52x10 <sup>6</sup>	4000-6000	0.32	[80]
Copper	6.0x10 <sup>7</sup>	5900-7400	0.30	[81]
Titanium	6.2-6.8x10 <sup>5</sup>	2000-2700	0.33-0.35	[82]

### ***Thermal properties***

Graphene finds most of its applications in the field of electronics as it is the best conductor of electricity known so far, thermal management is one of the major issues that needs to be addressed while working with the electrical devices. During the operation of the electronic devices considerable amount of heat can be generated and dissipated. It is well known that the allotropes of carbon, i.e. graphite, diamond and CNTs possess high thermal conductivity due to the strong C-C covalent bonding. Until the arrival of graphene, single walled CNTs (SWCNT) and multi-walled CNTs (MWCNT) were well known for having the

highest conductivities of 3500W/mK and 3000W/mK respectively [104–107]. Blandin et al. [108] have reported that the thermal conductivity of monolayer graphene sheet as 5000W/mK using confocal micro-Raman spectroscopy. Ghosh et al. [109] have reported the use of confocal Raman spectroscopy to measure the conductivity of suspended graphene flakes for thermal management applications and thermal conductivity of 4100-4800W/mK at room temperature was noted. Seol et al. [110] have measured the thermal conductivity of single layer graphene sheet grown on SiO<sub>2</sub> support and reported conductivity of 600W/mK. There was a speculation among the researchers that the thermal conductivity of graphene was over estimated and lee et al. [111] have reported the conductivity as 1200-2700W/mK and bi layer graphene as 600-500W/mK [112]. It can be noted that the electrical conductivity of graphene is affected by defect edge scattering and isotropic doping. The thermal properties of graphene and its derivatives are summarised in Table 2.3. It can be noted from the Table that the thermal properties of the graphene decreases with increase in graphene layers and thermal conductivity of the rGO is less than the multilayer graphene.

Table 2.3: Thermal properties of graphene and its derivatives in comparison with conventional metals.

Material	Thermal conductivity (W/mK)	References
Graphene	1200-2700	[111]
Reduced graphene oxide (rGO)	30-250	[111]
Graphene nano sheets (GNS- bi-layer/tri-layer/multi layers)	600-500	[112]
Aluminium	237	[79]
Stainless steel (Grade 304)	14-17	[80]
Copper	147-370	[81]
Titanium	17-21.9	[82]

### ***Other properties***

Nair et al. [113] have reported that the SLG sheets absorbs nearly 2.3% of the incident light with <0.1% of reflectance. The combination of optical, mechanical

and electrical properties makes graphene ideal material for flexible electronics [114]. Graphene also possess theoretical surface area of  $2600\text{m}^2/\text{g}$  and experimentally measured surface area of  $270\text{-}1550\text{m}^2/\text{g}$  [115], which benefits in improving matrix-graphene interactions in graphene based composites production.

### **2.3.3 Synthesis of graphene**

There are two different approaches to produce graphene. One approach is top-down in which graphite will break down to graphene with application of external forces and another approach is bottom-up which includes building graphene from molecular level.

#### ***Mechanical exfoliation (ME) of graphene***

Mechanical exfoliation was the initial technique used to synthesise graphene, this method was first developed in lab by Professor Giem and Professor Novoselov [116]. The piece of bulk graphite is repeatedly peeled using scotch™ tape by overcoming the vanderwalls forces between the layers and hence reduction of thickness of graphene layers, schematic is shown in Figure 2.4. Even though this process facilitates the production of bulk amount of GO monolayer, Raman spectroscopy have shown that the existence of structural defects [117]. These effects can negatively affect the electrical conductivity due to the disruption of electronic structure. Jayasena et al. [118] have reported cleaving of graphite using oscillator-aided ultra-sharp single crystal edge to produce FLG, and the flakes obtained are of  $>100\mu\text{m}$  lateral dimension and few tens of nm thickness. Chen et al. [119] have reported the use of three roll mills to produce SLG and FLG by exfoliating graphene using poly vinyl chloride (PVC), in which PVC acted as an adhesive during the peeling process. However, the temperatures upto  $500^\circ\text{C}$  were required to remove the residual PVC and dioctyl phthalate that were used during the synthesis, this complicates the whole process.

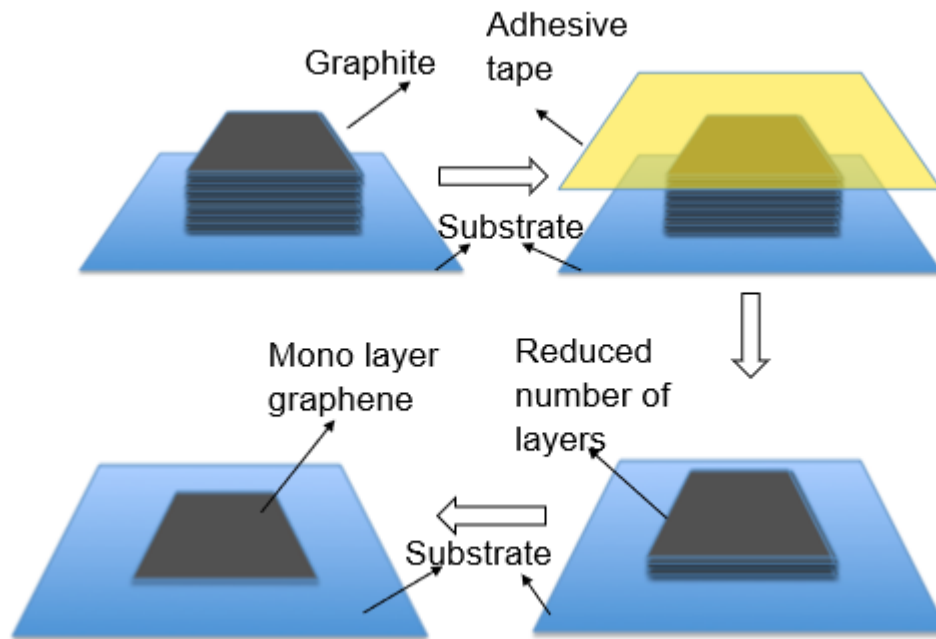


Figure 2.4: Schematic representation of sequential steps followed to exfoliate graphene layers using the scotch tape method.

### ***Liquid phase exfoliation (LPE) graphene***

The exfoliation process in LPE technique can be done either by using solvents or surfactant/stabilizer in aqueous media. The process involves following steps, dispersion, exfoliation and purification. The efficiency of degree of exfoliation can be estimated by analysing the number of graphene flake, i.e., analysing the results from FTIR, Raman spectroscopy and AFM, out of them Raman spectroscopy is the most commonly used technique. LPE methods are performed at room temperatures and does not involve any strong oxidants; pristine graphene with edge defects can be obtained [120–122].

Liquid immersion will result in successful exfoliation, as this will aid to overcome the Van der waal attraction by reducing interfacial tension between graphene and solvent, hence better graphene's dispersion [123,124]. Generally used solvents for graphene are 1-methyl 2-pyrrolidinome (NMP), ortho-dicholoro benzene and N-dimethylformamide (DMF) [125], the selection is done mainly based on surface tensions and contact angle measurements. Blake et al. [126] have reported the production of SLG and FLG in DMF at around 3hrs of sonication followed by centrifugation at around 1300rpm to obtain sTable dispersions. The sonication time highly effects the dispersion

and quantity of graphene, for instance 0.01mg/ml of graphene was obtained at around 30mins sonication followed by centrifugation at 500rpm for 90mins [127], whereas 1.2mg/ml of graphene was obtained at 460hrs of sonication [128] in NMP. Khan et al. [129] have used the vacuum filtered graphene films and dispersed them in fresh NMP and sonicated for 460hrs, obtained graphene concentrations of ~63mg/ml with average flake length of 1 $\mu$ m and are of 3-4layers thick. It can also be noted from this research work that the decrease in centrifugation speed will result in increase in thickness [130]. It can also be noted from Khan's group work that the sonication is a non-destructive process and doesn't introduce any defects in graphene sheets [128–130]. However, Skaltsas et al. [131] and Bracamonte et al. [132] have reported the existence of basal plane (surface) defects as a result of sonication that will effect the graphene's applicability. This calls for the importance of investigating induced defects in graphene and graphene-based composites during sonication. Bourlinos et al. [133] reported the use of per fluorinated aromatic solvents like penrafluorobenzonitrile, pentaflouropyridine and hexaflurobenzene to LPE graphene from graphite, out of which pentaflurobenzonitrile proved to be effective, i.e. producing graphene of 0.1mg/ml at sonication time of 1hr.

Use of surfactants like polymers can be effective in exfoliating graphite in aqueous solvents. The use of surfactant will minimise the aggregation of graphene sheets through electrostatic repulsion. Lotya et al. [134] reported the exfoliation of graphite in sodium decyl benzenesulfonate (SDBS), ~0.05mg/ml of dispersion was obtained at sonication time of 30mins and centrifugation at 500rpm for 90mins. The use of sodium collate surfactant in aqueous media for graphite exfoliation was demonstrated by Hersam et al. [135], graphene concentrations of nearly 0.09mg/ml were obtained and the obtained suspensions have thickness of <5 layers. The polymer surfactants like IGEPAL CO-890, Tween 20, Tween 80 and Brij 700 etc., are also used for exfoliation [136]. The use of polyvinylpyrrolidone (PVP) as surfactant to exfoliate graphite into graphene in organic solvents such as NMP have yielded graphene concentrations of 0.4-0.74mg/ml at sonication time of 1hr followed by centrifugation at 5000rpm for 4hrs [137]. Adamson et al. [138] have reported

the production of high graphene concentrations of 50mg/ml using co-solvent system of 1:1 mixture of hexafluoro benzene and benzene. The graphene obtained from these methods can be easily transformed into powders by using cooling by evaporation.

### ***Electro chemical exfoliation***

The electrochemical methods include utilizing electric current to facilitate the structural expansion of graphite in liquid electrolytes [139]. This method involves production of graphite intercalation compounds (GIC) through intercalation of anion or cations from electrolyte by applying potential to electrodes and then exfoliation of GIC's into graphene. In comparison, GIC exfoliation through cation intercalate shows lower degree of chemical focalisation which facilitates to preserve pristine nature of graphene [140]. Parvez et al. [141] have reported anodic exfoliation of graphite to form graphene in organic solvents i.e., in sodium sulphate, graphene sheets of low density (C/O of 17.2) and approximately 1-3 layers thickness were obtained. The anodic exfoliation mostly results in partially oxidised or chemically functionalised graphene, which is not suitable for some practical applications. Cooper et al. [142] have reported the cathodic exfoliation of highly oriented pyrolytic graphite (HOPE) in tetra alkylammonium salts to form FLG of approximately 2-5 layers, no functionalization and negligible oxide groups were noted.

### ***Chemical vapour deposition (CVD)***

This is one of the most investigated bottom-up technique to produce SLGs and FLGs on large scale. This method involves decomposition of carbon feed stock by applying heat and then rearrangement of atoms to form  $sp^2$  carbons, this process will take place in presence of catalyst [143]. Chemical vapour deposition (CVD) is one of the most promising techniques to produce monolayers of graphene sheets on a large scale. Somani et al. [144] have successfully produced FLGs through CVD, by using camphor as the precursor on Ni. This has opened a new path to researchers to address controlling the number of layers, and to control the thickness on various metal substrates [92,97,145–148]. Bae et al. [114] have reported the synthesis of 0.76m wide graphene films through CVD. The process includes adhesion and etching

followed by transfer of layers to the substrate. The schematic representation of the sequential steps followed during the process is shown in Figure 2.5 [114]. It is also noted that the produced graphene films have shown half-integer Quantum Hall effect which indicates the high-quality graphene monolayers. It can be noted that the graphene layers synthesised by this method possess a potential to replace commercially available transparent electrodes. The possibility of substitutional doping by the introduction of other gases, e.g.  $\text{NH}_3$  during growth, is one interesting feature of the CVD approach [146]. Qu et al. [149] have demonstrated the application of nitrogen doped graphene for the reduction of oxygen in fuel cells and it can be noted from the results that graphene electrodes displayed catalytic current of  $\sim 3$  times higher than that of the Pt/C electrode. It can also be noted that N-graphene electrode facilitates long-term stability and Poisson's effect over the Pt/C electrode during oxygen reduction in alkaline electrolytic solutions. The potential application of graphene in lithium-ion batteries has also been reported, as this has a notable reverse discharge potential ( $\sim 2$  times of pristine graphene) due to surface defects induced by nitrogen doping [150]. Graphene can also be synthesized at low temperatures than the thermal CVD process of  $1000^\circ\text{C}$ , by a technique known as plasma enhanced chemical vapor deposition (PECVD). This technique was first developed in 2004 using a gas mixture of 5-100%  $\text{CH}_4$  in  $\text{H}_2$  at a power of 900W, at substrate temperature of  $680^\circ\text{C}$  to produce mono and few-layer graphene sheets [151,152]. The major advantage of the PECVD technique is a lower deposition time of  $\sim 5$ mins and a lower growth temperature compared to the conventional CVD process. Researchers have reported a method of producing graphene using ultra high vacuum (UHV) annealing of SiC which proved to be beneficial in the semiconductor industry due to the advantage of obtaining the products on the surface of SiC [69,95,153]. The mechanism of UHV annealing of SiC involves heating the SiC substrate under UHV, to sublime the silicon atoms from the substrate, this leads to the re-arrangement of graphene layers with surface carbon atoms. The annealing time strongly influences the thickness of the obtained graphene layers. Tedesco et al. [154] and Emstev et al. [155] have reported the production of few-layer graphene (FLG) sheets with improved thickness and homogeneity at higher temperatures,  $\sim 400^\circ\text{C}$  above the UHV temperature.

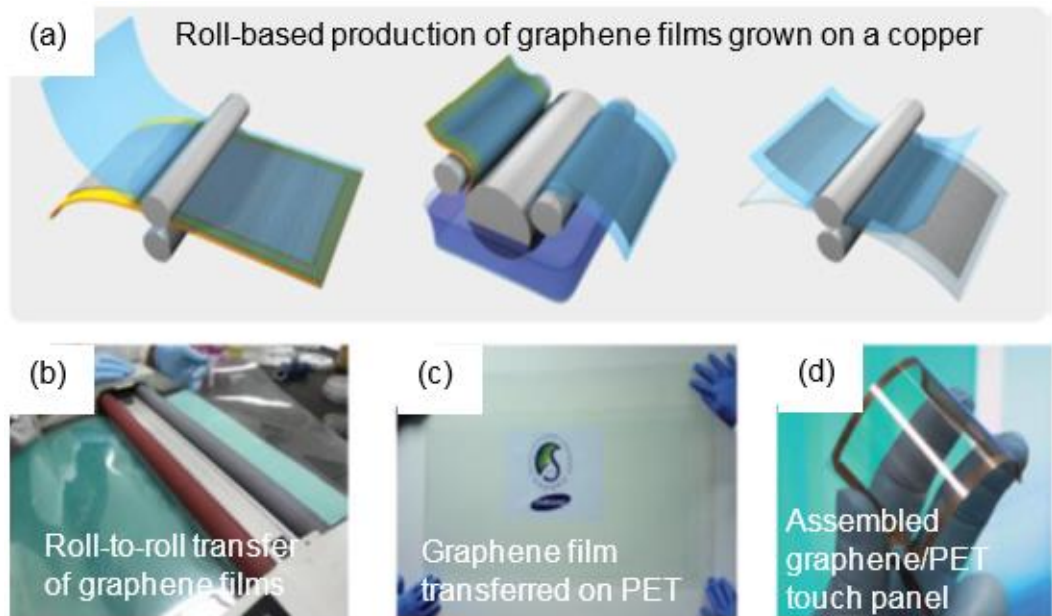


Figure 2.5: Sequential steps followed during film transfer of graphene films produced via CVD approach [114].

Even though the results obtained have in terms of homogeneity are promising, the challenging aspects of using this method for industrial applications is the control over the thickness of graphene layers and the epitaxial growth patterns of different SiC polar face. This method also lacks in addressing the existence of interface layer in between graphene, substrate and its effect on properties of the product. A similar technique can be applied to grow graphene layers on metallic substrates. Porga et al. [156] and Sutler et al. [157] have reported the synthesis of epitaxial graphene sheets on ruthenium (Ru) crystals under UHV. A strong bonding of the first layer of graphene sheets with Ru substrate was reported. Whereas the second layer did not interact with the substrate and demonstrated a similar electronic structure as that of the freestanding graphene (monolayer graphene).

## 2.4 Graphene oxide (GO)

### 2.4.1 Morphology of GO

Graphene oxide is one of the most popular derivatives of graphene which is easy to synthesise and is hydrophilic nature unlike pristine graphene which is hydrophobic. The determination of GO structure is difficult as it is a non-stoichiometric compound. The GO structure proposed by Dreyer et al. [158] consists of epoxy and hydroxyl groups on  $sp^3$  hybridized carbon in the basal

plane and carboxyl groups on  $sp^2$  hybridized carbon. This leads to the hydrophilic nature of GO and can be easily exfoliated in aqueous solutions. GO is a monolayer material produced from exfoliation of graphite and have similar chemical properties as that of graphite oxide. It can also be noted that the existence of hydroxyl and epoxy functional groups disrupts the electronic structure and GO behaves as an insulating material with irreversible defects.

#### **2.4.2 Production of GO**

The chemical conversion of graphene into GO is a promising economical alternative [101,159,160]. One of the popular methods of producing GO is using Hummers method [161], this method involved oxidizing graphite using oxidants like  $H_2SO_4$ ,  $HNO_3$  and  $HMnO_4$ . The GO films produced are thicker than the pristine graphene sheets of 0.34nm thickness due to the displacement of  $sp^3$  hybridized atoms. The produced GO is negatively charged, which facilitates the stability of GO in water and certain organic solvents without use of surfactants [162].

#### **2.4.3 Reduction of GO to reduced graphene oxide (rGO)**

The chemical reduction of GO sheets can be performed in the presence of different reducing agents, including hydrazine [101,117,163–165], sodium borohydride [166–168], hydroquinone [169] and ascorbic acid [170]. Out of all the reducing agents hydrazine hydride was referred as the best reducing agent to produce very thin graphene sheets and it does not react with water. During the reduction process, the oxygen atoms can be removed, which results in less hydrophilic nature of GO sheets [117,171]. The molecular structures of GO during oxidation and reduction of GO using hydrazine are shown in Figure 2.6 [160]. It can also be noted that the rGO can tend to agglomerate due to the hydrophobic nature until and unless stabilized by the selected surfactants.  $NaB_4$  is another reducing agent that effectively reduces the GO [166] and it is also reported that  $NaB_4$  is more effective than hydrazine but the problem with  $NaB_4$  lies in its slow hydrolyzation by water. McAllister et al. [172] have reported the production of rGO using  $NaB_4$  and the comparison of rGO obtained by two different reducing agents hydrazine and  $NaB_4$  was also reported. It can be noted from their results that rGO obtained by using  $NaB_4$  has low sheet resistance of  $59k\Omega/square$  compared to that of the rGO produced using

hydrazine of 780kΩ/square. High C:O ratio of 13.4:1 was recorded for rGO produced using NaB<sub>4</sub>, which was high compared to that of the rGO produced using hydrazine which was in the order of 6.2:1. Out of all the chemical reduction processes, reduction by hydrogen proved to be effective with C:O ratio of 10.8-14.9:1.

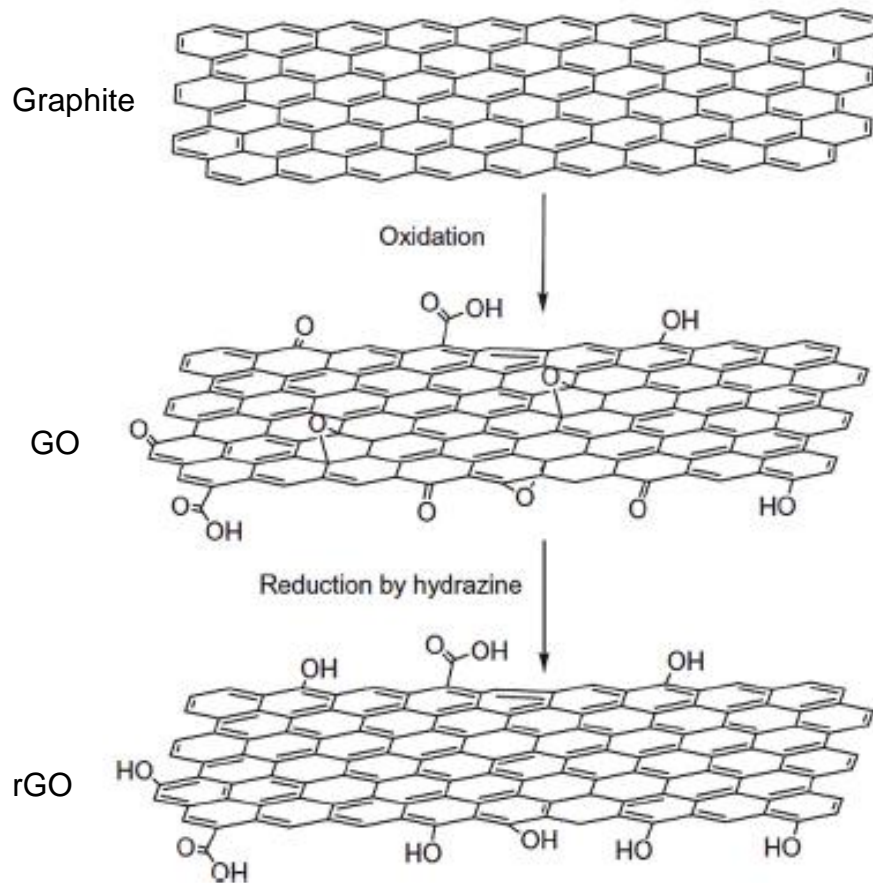


Figure 2.6: Oxidation of graphite to GO and reduction to rGO [160].

Thermal reduction is another way of reducing GO that involves the removal of oxide functional groups by heat treatment. Allister et al. [173] have reported the removal of oxide functional groups with CO and CO<sub>2</sub> as by-products by heating GO to 1050°C in the presence of inert atmosphere. During thermal reduction process, the rapid heating results in decomposition of oxide functional groups attached to the carbon planes and decompose into gases creating a huge pressure between the stacked layers (~40MPa of pressure will be generated at 300°C and only 2.5MPa of pressure is required to separate two stacked platelets). It was reported from the AFM study that the thermal reduction can result in ~80% of single layer rGO, whereas 30% of mass can be lost due to

the removal of oxide functionalities which leaves vacancies and structural defects that may affect the mechanical and electrical properties of the produced rGO and the production of rGO at low temperatures is proposed by Dubin et al. [174]. This involves production of rGO dispersion at 200°C in organic solvents like N-methyl-2-pyrrolidinone (NMP).

It is important to control the exfoliation behaviour of GO and rGO which helps in widening their potential applications and this can be achieved using surface functionalization of GO. There are two mechanisms in surface functionalization they are: covalent functionalization and non-covalent functionalization. If the oxygen functional groups on GO surfaces that includes carboxylic acid groups at the edge of the epoxy/hydroxyl groups on the basal plane are used to change the surface functionality of GO then it is called covalent functionalization. The carboxylic acid groups should be activated to use them on GO to stabilize other molecules and the activation can be done either by using thionyl chloride [175], 1-ethyl-3-carbodiimide [176] and N-dicyclohexyl carbodiimide [176]. The weak  $\pi$ - $\pi$  interactions between the GO and target molecules can be used to functionalize GO in non-covalent functionalization. The conjugated polymers and aromatic compounds can be used to stabilise the rGO resulted from reduction reaction, can be used in the production of composite materials. The conjugated and aromatic polymers used are sulfonated polyaniline [177], conjugated poly electrolyte [178], porphyrin [179] and cellulose derivatives [180]. The summary of advantages and disadvantages of various synthesis techniques used to produce mono and multi-layer graphene is given in Table 2.4.

Table 2.4: Summary of advantages and disadvantages of graphene synthesis techniques.

Technique	Advantages	Disadvantages
Exfoliation	<ul style="list-style-type: none"> <li>• This is a relatively simple and low budget technique of producing graphene sheets.</li> <li>• This process can produce pristine graphene.</li> </ul>	<ul style="list-style-type: none"> <li>• Graphene sheets produced by this process will be of several sizes, irregular shapes and orientations, this will limit the applicability.</li> <li>• This process has less relevance to the commercial high-end applications.</li> </ul>
Chemical vapour deposition (CVD)	<ul style="list-style-type: none"> <li>• This process facilitates the large-scale production of graphene to the size of substrate.</li> <li>• Mono layer and bi-layer graphene sheets can be obtained.</li> <li>• Less costly process as the cost per unit area of graphene produced will be limited to the size of the substrate.</li> </ul>	<ul style="list-style-type: none"> <li>• The transfer process often effects the integrity and performance of produced graphene.</li> <li>• Transfer process enhances the formation of wrinkles, impurities and structural defects.</li> <li>• Selection of substrate effects the process cost.</li> </ul>
Organic synthesis	<ul style="list-style-type: none"> <li>• Product obtained by this method can be substituted with aliphatic chains to modify the solubility.</li> </ul>	<ul style="list-style-type: none"> <li>• Size of the sheets produced from this process is limited due to the reduction of solubility.</li> <li>• Increase in unwanted side reactions will lead to difficulties in dispersion preservation.</li> <li>• The cost incurred in characterising the products of chemical reactions is high.</li> </ul>
Chemical derivation of graphene	<ul style="list-style-type: none"> <li>• Nearly 80% of single layer rGO sheets can be obtained by this process.</li> <li>• This is the most affordable technique to produce graphene.</li> </ul>	<ul style="list-style-type: none"> <li>• The formation of functional groups during the oxidation process leads to the irreversible effects to the band structures and reduces the electrical conductivity.</li> </ul>

## **2.5 AMCs reinforced with graphene nano sheets (GNS/Al)**

Utilizing GNS as reinforcement for Al matrix is the effective alternative to improve the properties of base material, Al. J Liu et al. [29] have reported the production of GNS/Al composites using powder metallurgical technique at various weight percentage (wt%) of GNS addition. It can be noted from their results that the stirring time during the powder preparation of GNS in Al matrix highly effected the properties of the composite. The hardness increased with increase in wt% of GNS reinforcement, for instance the highest increase of 43% in hardness over monolithic Al was noted at 0.15wt% GNS/Al compared to 0.07wt% and 1wt%. Gang li et al. [181] have successfully fabricated GNS/Al composites using high energy ball milling followed by hot pressing. The effect of wt% of GNS addition on microstructural and tensile propertied of Al matrix were investigated, the ultimate tensile strength (UTS) of GNS/Al composites reduced with increase in wt% of GNS addition, shown in Figure 2.7(a) due to the formation of aluminium carbide ( $Al_4C_3$ ) at interfaces and dislocations are also found near interfaces, shown in Figure 2.7(b). Shin et al. [20] have also reported the formation of  $Al_4C_3$  at the interfaces which restricted the stress transfer in GNS/Al composites. It can also be noted from the results that with increase in testing temperature, the dislocation moment was reduced and led to the severe softening of matrix, and hence reduced the yield strength of the composite.

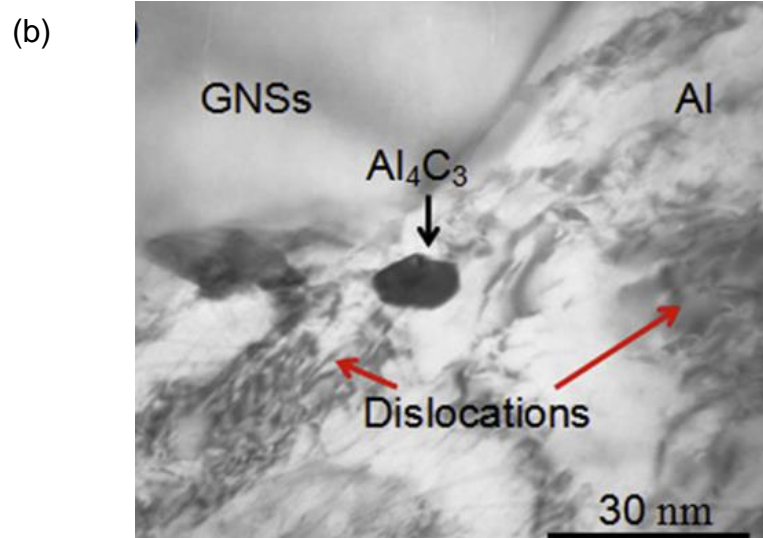
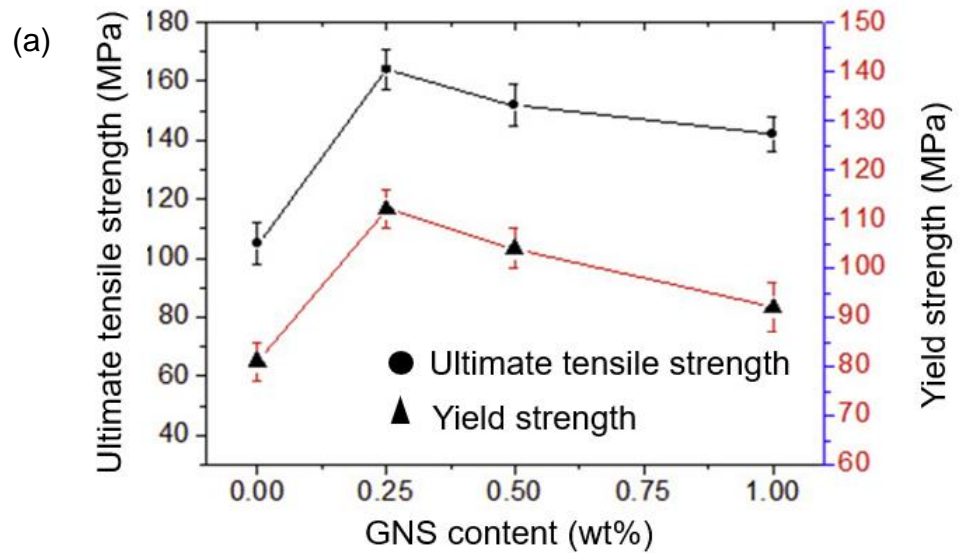


Figure 2.7: (a) Effect of GNS content on UTS and Yield strength of GNS/Al composites and (b) TEM image of 0.25wt% GNS/Al composite showing dislocations and carbide formation [181].

Bratolucci et al. [182] noted that the hardness and UTS of the 0.1%GNS/Al composites that were extruded at 50T, 12.5mm/sec were reduced compared to pristine Al samples which was due to the formation of  $Al_4C_3$  at the working temperature of 550°C, carbide formation was evident in XRD analysis of samples, shown in Figure 2.8.

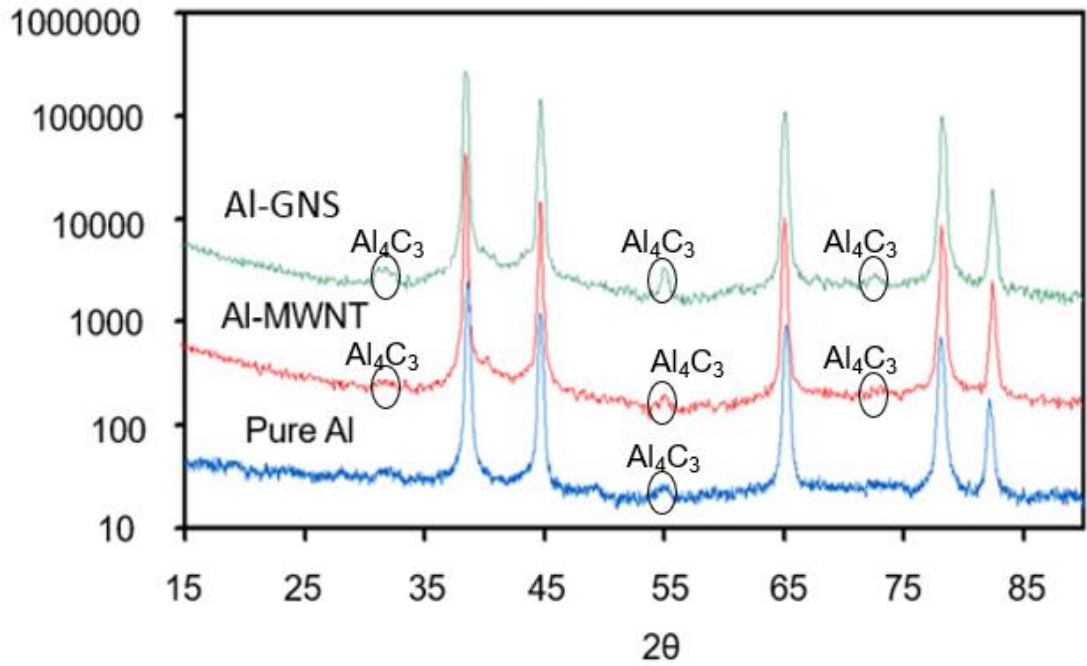


Figure 2.8: XRD pattern of pure Al, 1wt% multi-walled nanotubes (MWNT)/Al composites and 0.1wt% of GNS/Al composites [182].

To provide better bonding in between GNS reinforcement, Al matrix and to obtain better density 1.5wt% of Sn was added to GNS/Al mixture [18], both hardness and compressive strength (CS) of the composite were increased by 17.5% and 5.16% respectively, and no Al<sub>4</sub>C<sub>3</sub> was observed. The particle morphology was shown in Figure 2.9. This paper also reported the effect of gas atomization and mechanical milling processes on the GNS/Al composite. For instance, gas atomization proved to be effective for strength enhancement and mechanical milling proved to be effective to increase hardness of GNS/Al composite. GNS have the unique benefit of reducing the agglomeration of metal oxide, more investigation is needed to explore the effect of GNS addition to the metal matrices and efficient ways to avoid the formation of Al<sub>4</sub>C<sub>3</sub>. In this aspect, the use of powder metallurgical routes proved to be effective for the uniform distribution [183].

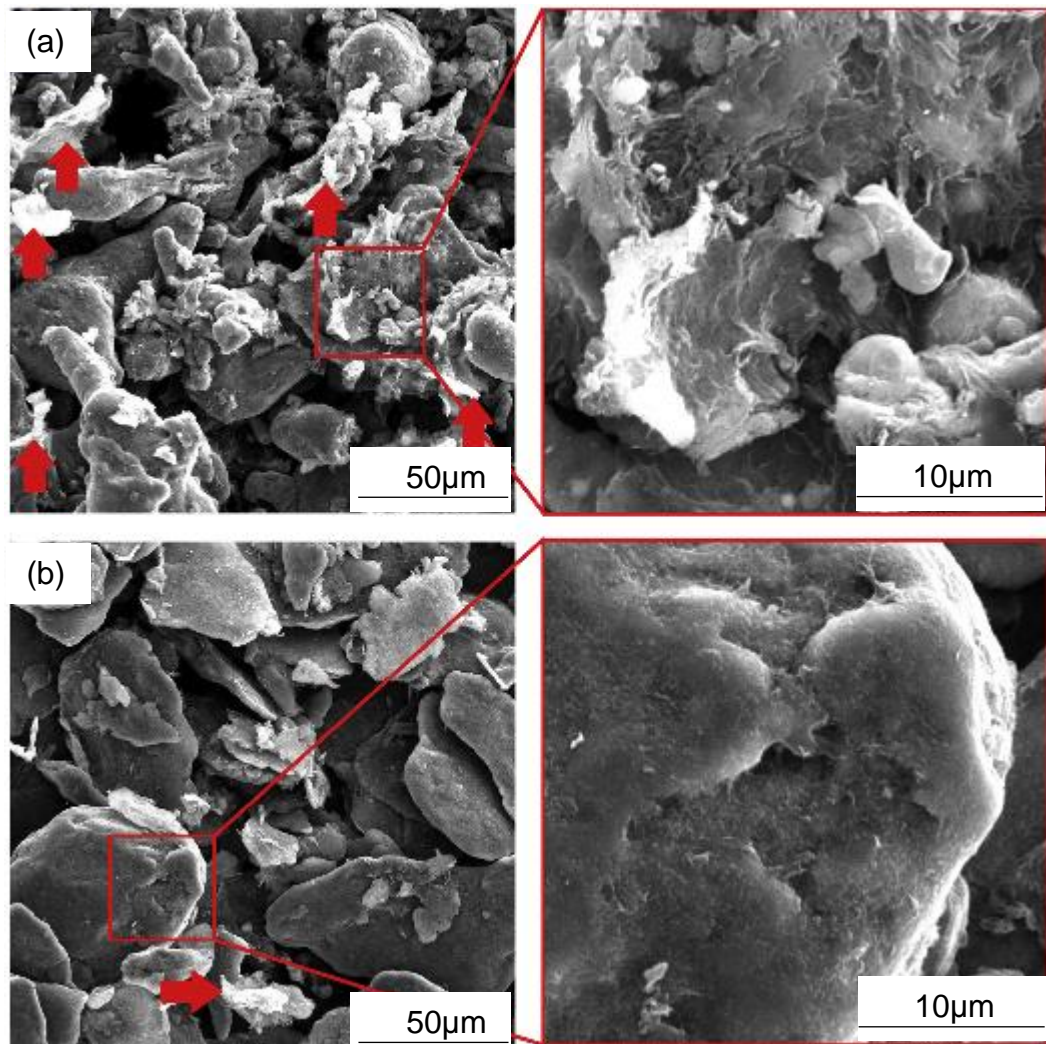


Figure 2.9: SEM images showing particle morphologies of 1wt% FLG/Al composites (a) gas atomized and (b) mechanically milled [18].

## 2.6 AMCs reinforced with graphene nano particles (GNP/Al)

The density difference between the nano particle and the matrix is the main reason behind the agglomeration during liquid holding or casting. Nanoparticle reinforcement is employed on the Al matrices to enhance the capacity to withstand high temperatures and pressures [50]. However, non-homogeneous dispersion and poor interface bonding are the major concerns while using the conventional methods to produce GNP/Al composites [2,184]. Perez et al. [22] have fabricated 1wt% of GNP/Al composites, cold compacted at 950MPa followed by sintering at 500°C for 5hrs of ball milled powders, in which 138% of increase in hardness compared to monolithic Al is observed. The effect of process parameters such as milling time and sintering time on the properties

of GNP/Al were also recorded, the increase in milling time increases the hardness of the composites. Whereas, reduction in hardness values by 13% were noted for the 1wt% of GNP/Al composites produced by cold compaction at 200MPa followed by hot compaction at 525°C and 500MPa [185], reduction in properties was mainly due to the non-homogenous dispersion of GNPs in Al matrix that led to the agglomeration. Lathief et al. [23] have fabricated 2wt% GNP/Al composites using wet mixed powder in acetone, followed by cold compaction and sintering. The Vickers hardness and compressive strength were increased by 67% and 21% respectively. Another work published by the same research group reported an increase in 34% in hardness and 22% in CS of GNP/Al composites [24] by reducing wt% of GNP from 5wt% to 3wt%, which implies to that under the similar working conditions, tendency of agglomeration varies with variation in wt% of GNPs content and plays a key role in altering the mechanical properties of the GNP/Al composites. Rashad et al. [186] have reported the production of 0.3wt% of GNP/Al composites through powder metallurgy in which the GNP/Al was mixed in acetone for 1hr. The powders were then cold compacted at 170MPa and hot extruded at 470°C followed by sintering at 600°C for 6hrs. The produced composite samples shown an increase of 11.8% in hardness, 11.1% in UTS and decrease of 7.8% in CS. The increase in properties was due to the efficient load transfer between the soft matrix and reinforcement, Orowan looping. The reduction in CS was due to the buckling nature of reinforcement (when the load was applied, the graphene flakes buckles, bent at angle of 45° as the GNPs were parallel to the extension direction). Whereas Guvbuz et al. [187] have reported that the hardness of the GNP/Al composite reduced with increase in wt% of GNP reinforcement from 0.1wt% (↑9.67%) to 0.5wt% (↓ 21.41% HV). This was due to the restriction of settlement of particles and non-uniform distribution of GNPs in Al matrix that weakens the contact area between the particles and hence increases the porosity and reduces hardness, the SEM images of GNP/Al composites were shown in Figure 2.10. It can be noted from the Figure that the increase in sintering time has increased the grain size and hence altered the properties of the GNP/Al composite.

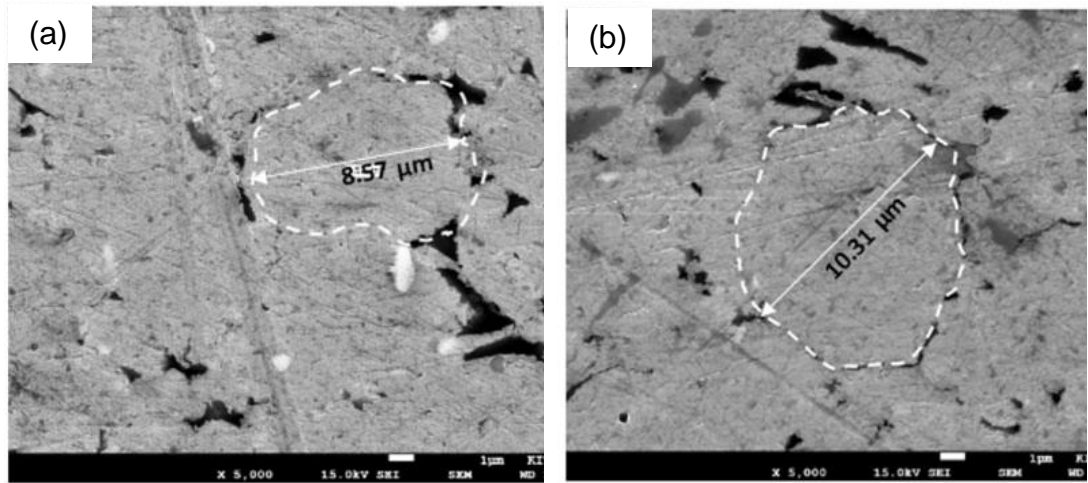


Figure 2.10: SEM images of 0.1wt% GNP/Al composites sintered at 630°C at various sintering times, (a) 120mins and (b) 300mins [183].

Khan et al. [188] have fabricated 5wt% GNP/Al composite through semi-powder metallurgy in which ball milled GNP/Al powders were cold compacted at 125MPa followed by sintering at 600°C for 6hrs. A huge increase in CS of 433% and only 35% increase in hardness were recorded, increase in CS is due to alignment of GNPs perpendicular to the direction of applied load, hence reduction in buckling and increase in hardness was due to the uniform dispersion of GNPs, shown in Figure 2.11. Li et al. [26] have made an attempt to improve the distribution of GNP in Al matrix and hence improve mechanical properties of the GNP/Al composites by using ball milling and cold drawing. The reported results for 0.4wt% GNP/Al composites have shown an increase of 9.5% in Young's modulus and 51.1% in UTS whereas 2wt% GNP/Al composites have shown 22.6% increase in Young's modulus and 1.45% decrease in UTS, the increase in properties of 0.4wt% is attributed to the strong interfacial bonding whereas, the UTS of 2wt% of GNP was reduced due to the increased agglomeration tendency. Yang et al. [189] have reported the fabrication of GNP/Al composites by using pressure infiltration technique in which extrusion enhanced grain refinement, the yield strength of 0.54wt% of GNP/Al composite was increased from 116% to 228% after extrusion whereas tensile strength was increased from 45% to 93% after extrusion, this was due to the strengthening effect of GNPs after extrusion.

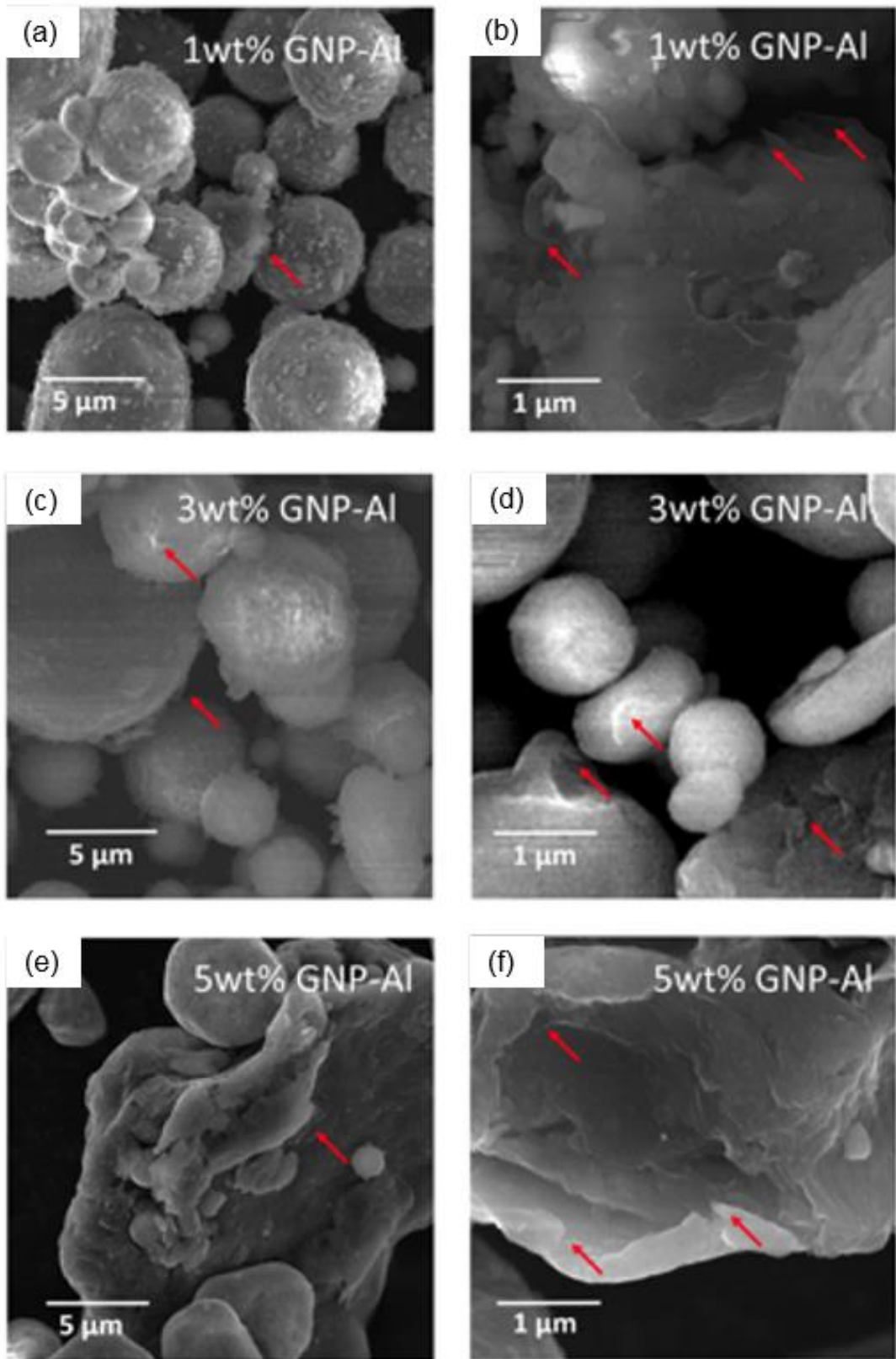


Figure 2.11: Particle morphologies of ball milled composite powder samples (a)-(b) 1wt% GNP/Al, (c)-(d) 3wt% GNP/Al and (e)-(f) 5 wt% GNP/Al; red arrows represents the existence of GNPs [188].

## **2.7 AMCs reinforced with reduced graphene oxide (rGO/Al)**

Reduction of GO to rGO has caught the attention of many researchers in scientific community due to the provision of using easily producible GO and reducing it to retain the properties as pristine graphene. Z Li et al. [27] have successfully fabricated 0.3wt% rGO/Al composites through hot pressing at 600MPa and 530°C, noted an increase of 18% and 17% in Young's modulus and hardness respectively. The increase in properties was noted due to the preliminary reduction of GO to restore graphene properties and the ionic bonds formed due to the electrostatic absorption of GO on Al surface which led to the interfacial bonding of rGO and Al. For the same wt% of GNP/Al composites (0.3wt%) and with same solvent (ethanol) as Li et al. [27], Wang et al. [28] have recorded nearly 62% of increase in UTS, this was due to the use of advanced fabrication technique i.e., hot extrusion of composite at 440°C followed by sintering at 580°C for 2hrs. However, the increase noted was only 20% of graphene's potential this was due to the incomplete reduction of GO to rGO that led to the weak interfacial bonding between rGO nano sheets and Al and lack of optimisation of process parameters. Similar effect was observed by Jing et al. [190] while fabricating rGO/Al composites by using powder metallurgical route, only 32% of increase in hardness was recorded. Asgharzadeh et al. [18] have made an attempt to investigate the effect of stirring mechanisms i.e., gas atomisation (GA) and mechanical milling (MM) to obtain well dispersed FLrGO/Al and FLG/Al powders for the production of composites. The comparison of hardness and compressive strength of the FLrGO/Al and FLG/Al composites with respect to the mixing processes was shown in Figure 2.12. It can be noted that the MM process of mixing powders proved to be effective for FLG/Al composites for improved properties whereas, GA process of mixing powders was effective for rGO/Al composites.

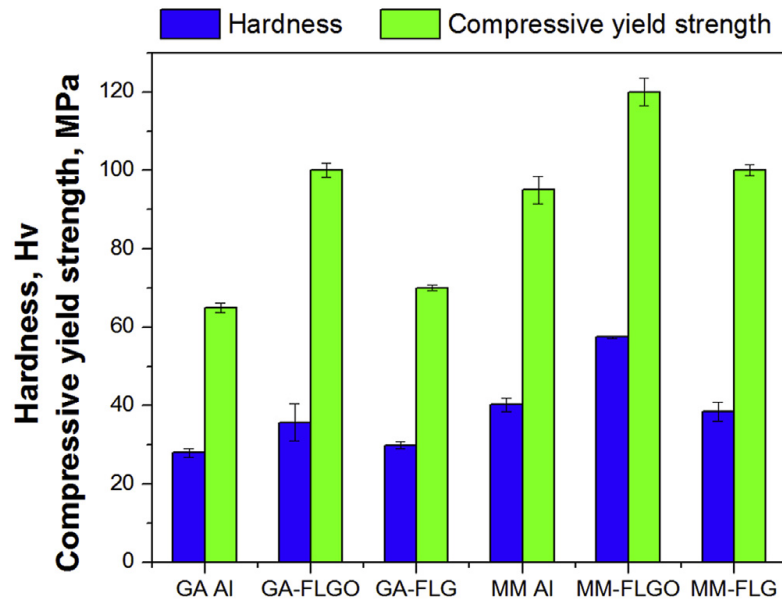


Figure 2.12: Compressive strength and micro hardness of gas atomized, mechanically milled Al, FLrGO and FLG samples after sintering [18].

## 2.8 Summary

The review of morphology, mechanical, electrical and thermal properties of graphene and its derivatives is presented in this chapter. The processing techniques and properties of AMCs reinforced with graphene and its derivatives are also given, which shows the potential of graphene as a reinforcement filler to increase strength, hardness, electrical and thermal conductivities of AMCs.

## CHAPTER 3

### CRITICAL REVIEW AND GAP IN LITERATURE

The summary of processing parameters and techniques used to produce graphene derivatives reinforced AMCs and their properties with respect to the variation in process parameters is shown in Table 3.1. Having discussed the available research work in this chapter, the summary of critical reviews is provided below together with the gaps and questions that are to be filled and answered.

#### 3.1 Critical reviews

- A variety of techniques used to produce graphene and its derivatives are reported, out of which CVD is the most preferable technique for the mass production of large and high-quality monolayer graphene, while for the fabrication of GO/rGO in large quantities, the chemical conversion of graphene from graphite is more suitable.
- Conventional techniques such as powder metallurgy assisted by ball milling, hot rolling and friction stir processing are used to produce graphene reinforced AMCs showing promising improvement in properties. However, at some processing parameters (those are detailed in Table 2.5), the compressive strength, hardness, UTS and yield strength of the AMCs reinforced by graphene and its derivatives are reduced. This is mainly attributed to the formation of aluminium carbide ( $Al_4C_3$ ) and inefficient reduction of GO.
- The use of surfactants, binders and purity of the raw materials has contributed to the deterioration in properties of the graphene reinforced AMCs.
- Two major characterisation techniques namely XRD and micro Raman are used to characterise the graphene reinforced AMCs. XRD is used to analyse the phase crystallinity, identification of phases and existence of  $Al_4C_3$ . Micro Raman is used to analyse the occurrence of defects, investigate the existence of graphene and number of layers of graphene.

- Negligible amount of research work is reported on the modelling and simulation of graphene reinforced AMCs and predicting the effect of existence of number of graphene layers and percentage of reinforcement distribution on Al particles on mechanical properties of the AMCs.
- The model developed and presented in current study is relatively new and not yet has been analysed by other researchers and the effect of orientation of the graphene layers on Al particles and their cumulative effect on mechanical properties of the AMCs is still unknown.

### **3.2 Gaps and questions that are to be filled and answered:**

- Why GO without either chemical/thermal reduction steps isn't used as reinforcement for AMCs?
- How good is liquid infiltration assisted powder metallurgical technique to produce graphene reinforced AMCs compared to ball milling assisted powder metallurgical technique?
- How important is the optimisation of process parameters such as selection of solvent, stirring time and stirring speed on the distribution of graphene in Al matrix?
- How to control/avoid the formation of aluminium carbide at the sintering temperatures of 550°C-600°C?
- How does the performance of composite i.e., strength and hardness vary with the variation in wt% of graphene reinforcement? (The importance of examination/investigation of agglomeration with variation in wt% of graphene addition).
- How does the existence of number of graphene layers and orientation of graphene layers effects the performance of graphene reinforced AMCs?
- How to incorporate the layers of graphene on to the Al particles and percentage of distribution graphene reinforced Al particles in the composite in modelling and simulation of graphene reinforced AMCs.

Table 3.1: Summary of processing parameters and mechanical properties of graphene reinforced AMCs.

Base material	Derivative of graphene	Wt% of reinforcement (%)	Mixing type/ Solvent	Cold compaction/ Extrusion/ Hot pressing	Sintering	Mechanical properties
Al [27]	rGO (Reduced graphene oxide)	0.3	Wet/Ethanol for 1hr	Hot pressing at 530°C and 600MPa		↑18% (90.1GPa) E ↑17% (1.59GPa) Hardness
Al [28]			Wet/Ethanol	Hot extrusion at 440°C	580°C for 2hrs in N atmosphere	↑62% (249MPa) UTS
Al [29]			Wet/Acetone for 3hrs	Cold compaction 560MPa	600°C for 4hrs in Ar atmosphere	↑32% (34.5) HV
Al-1.5wt% Sn [18]	FLrGO (Few-layer reduced graphene oxide)	1	Wet/Ethanol, Ethanol water for 1hr	Cold compaction 500MPa	600°C for 1hr in N atmosphere	↑65% (46) HV ↑53.84% (100MPa) CS
	Ball milling at 350rpm for 4hrs in Ar atmosphere		↑43% (57) HV ↑26% (120MPa) CS			
	GNS/FLG (Graphene nanosheets/ few-layer graphene)		Wet/Ethanol, Ethanol water for 1hr	Cold compaction 500MPa	600°C for 1hr in N atmosphere	↑7.14% (30) HV ↑21.54% (79MPa) CS
	Ball milling at 350rpm for 4hrs in Ar atmosphere		↑17.5% (47) HV ↑5.16% (100MPa) CS			

Base material		Wt% of reinforcement (%)	Mixing type/ Solvent	Cold compaction/ Extrusion/ Hot pressing	Sintering	Mechanical properties
Al <sub>2</sub> O <sub>3</sub> [19]		2	Wet/Water	SPS 1300°C, 50MPa for 3mins		↑53% (5.21MPa) FT
Al [29]		0.15	Wet/Acetone for 3hrs	Cold compaction 560MPa	600°C for 4hrs in Ar atmosphere	↑43% (37.6) HV
Al [181]		0.25	Ball milling at 250rpm for 24hrs in Ar atmosphere	Hot pressing at 610°C for 4hrs and 30MPa		↑56.19% (164MPa) UTS ↑38.27% (112MPa) YS
Al [20]		0.7	Ball milling at 200rpm for 1hr	Hot rolled at 500°C		↑71.8% (440MPa) UTS
Al [182]		0.1	Blending using an acoustic mixer for 5min, milled under an Ar atmosphere for 1hr	Hot pressing at 375°C for 20mins, Extrusion 50Tons, 4:1 ratio and 12.5mm/s		↓18% (265MPa) UTS ↓12.5% (84) HV ↓34% (198MPa) YS
Al-Si alloy [191]		1	Pre-mixed alloy powders for 30mins at 180rpm followed by ball milling of GNS/alloy powders for 20hrs at 250rpm in Ar atmosphere	Cold pressing at 350MPa, degasifying at 400°C for 2hrs followed by vacuum hot pressing under 50MPa at 500°C		↑115% (80.2) HV

Base material	Derivative of graphene	Wt% of reinforcement (%)	Mixing type/ Solvent	Cold compaction/ Extrusion/ Hot pressing	Sintering	Mechanical properties
Al [22]	GNP (Graphene nano particles)	1	Ball milling for 5hrs in Ar atmosphere	Cold compaction 950MPa	500°C for 5hrs	↑138% (93) HV
Al [185]			Ball milling at 500rpm for 6hrs	Cold compaction 200MPa followed by hot compaction 525°C and 500MPa		↓13% (97) HV
Al [23]		3	Wet/Acetone	Cold compaction 520MPa for 5mins	600°C for 6hrs	↑67% (75) HV ↑21% (170MPa) CS
Al [24]		5	Wet/Acetone in dispenser at speed of 2000rpm for 30min	Cold compaction 500MPa for 5mins	600°C for 6hrs	↑34% (67) HV ↑22% (180MPa) CS
Al [186]		0.3	Wet/Acetone for 1hr in mechanical agitator	Cold compaction 170MPa and hot extrusion 470°C	600°C for 6hrs	↑11.8% (85) HV ↑11.1% (280MPa) UTS ↓7.8% (457MPa) CS
Al [187]		0.1-0.5	Wet/Ethanol for 1hr and left ground for 12hrs	Cold compaction 600MPa	630°C for 5hrs	↑9.67% (56.95) HV- ↓21.41% (40.81) HV
Al [188]		5	Ball milling at 350rpm for 2hrs	Cold compaction 125MPa	600°C for 6hrs	↑35% (28) HV ↑433% (82MPa) CS

Base material		Wt% of reinforcement (%)	Mixing type/ Solvent	Cold compaction/ Extrusion/ Hot pressing	Sintering	Mechanical properties
Al [26]		0.4	Ball milling at 200rpm for 5hrs and 0.5% stearic acid as control agent	Cold compaction at 200MPa, ingots preheated at 450°C at 10°C/min for 1hr then extruded at 1mm/min, extrusion ratio of 25:1. The specimens are then heat treated at 300°C for 10min and cold drawing at 100mm/min		↑9.5% (76.7±4.7GPa) E ↑51.1% (219±10.4MPa) UTS
		2				↑22.6% (85.5±5.6GPa) E ↓1.45% (137±12.6MPa) UTS
Al [189]		0.54	Ball milling at 100rpm for 1hr	Preheated pressure infiltrated dies at 730°C, 15MPa of pressure is applied during infiltration for 5mins. Hot extruded at 450°C followed by annealing at 400°C for 2hrs		↑228% (200MPa) YS ↑93% (270MPa) UTS
Al [192]		0.5	Ethanol for 60mins and GNP/Al/Ethanol for 60mins at 100rpm in agitator	Cold compacted in a uniaxial steel die at 500 MPa followed by furnace sintering at 620°C in N <sub>2</sub> atmosphere for 2hrs.		↑31% (47) HV ↓98.25% (0.14×10 <sup>-5</sup> mm <sup>3</sup> /N-m) Wear rate
AlMg5 [193]	GO (Graphene oxide)	1	Ball milling at 360rpm for 20hrs in Ar atmosphere	Heating mold at 500°C for 1.5hrs and compacted at 570MPa		↑114% (556MPa) UTS

E- Young's modulus, UTS- Ultimate tensile strength, HV- Vickers hardness, CS- Compressive strength, FT- Fracture toughness and YS- Yield strength

### **3.3 Summary**

Various derivatives of graphene such as rGO, FLrGO, GNS, GPL, FLG and GNP are used as reinforcement for AMCs, out of these GNS, rGO and GNP are the most widely used reinforcements and no research work is reported on GO without reduction as reinforcement for pure Al matrix composites the best of author's knowledge. The gaps and questions mentioned in this chapter have been addressed and partially answered in results obtained from the experimental work (in chapter 4) and in the results and discussion (in chapter 5).

## CHAPTER 4

### MATERIALS AND METHODS

This chapter describes the materials used in current research work together with their corresponding properties. Powder treatment for the synthesis of composites is given in detail. The experimental conditions used for the characterisations are described briefly in this chapter. Model setup of composite model done in ANSYS is mentioned together with the boundary conditions used.

#### 4.1 Materials and properties

The materials used to produce GO reinforced Al matrix composites include Al powder, IPA, acetone and GO aqueous dispersion. Al powder with typical particle size of 35 $\mu$ m, 99% pure bought from Good Fellow was used as matrix and the properties are given in Table 4.1. The solvents Isopropyl alcohol (2-propanol (IPA)) and acetone of 99.8% and 99.6% purity respectively bought from fisher scientific were used as solvents to disperse matrix and reinforcement, properties are shown in Table 4.2. The reinforcement material i.e., GO aqueous dispersion of 4mg/ml concentration is purchased from Graphenea, Spain and the corresponding properties were given in Table 4.3. Whatman filter papers of 11 $\mu$ m pore size were used to filter the GO/Al powders through vacuum filtration.

Table 4.1: Properties of Al at room temperature, source: MSDS, Goodfellow.

Density (g/cm <sup>3</sup> )	2.70
Melting point (°C)	660
Thermal conductivity (W/mK)	237
Electrical conductivity (S/m)	3.74x10 <sup>7</sup>
Hardness (HV)	35-48
Tensile strength (MPa)	130-195
Young's modulus (MPa)	70 x10 <sup>4</sup>
Poisson's ratio	0.345

Table 4.2: Properties of acetone and IPA used in current research, source: MSDS, Fisher scientific.

Property	Acetone	IPA
Chemical formula	C <sub>3</sub> H <sub>6</sub> O	C <sub>3</sub> H <sub>8</sub> O
Purity (%)	99.6	99.8
Viscosity (mPa.s)	0.32	2.27
Boiling point (°C)	56.0	82.6

Table 4.3: Properties of GO aqueous dispersion used in current research, source: MSDS, Graphenea.

Density (g/cm <sup>3</sup> )	1.8
Young's modulus (GPa)	380 - 470
Tensile strength (GPa)	3 - 33

## 4.2 Powder treatment by liquid infiltration

As received Al powders were dispersed in solvents acetone and IPA separately using hot plater magnetic stirrer at room temperature for 15mins. Three wt% of GO reinforcements i.e., 0.05%, 0.1% and 0.2% were used in current research work, the mixture calculations are given in Table 4.4 by assuming that the powder weight of each sample would be 0.5g. The measured GO dispersion based on calculations is ultra-sonicated for 15mins to disperse GO particles (as they have high tendency to agglomerate and settle down). The ultra-sonicated GO is then added slowly drop by drop to the Al/IPA and Al/acetone slurries separately and stirred until the uniform dispersions are obtained. The stirring times vary depending on the wt% of GO used. Once the desired dispersion is obtained, the dispersion is then vacuum filtered to obtain GO/Al composite powder. The design of experiment at various processing conditions that were used in the current research work is given in Table 4.5.

Table 4.4: Amount of raw materials required to produce GO/Al powder at different wt% of GO using acetone and IPA as solvents measured using 5digit balance.

wt% of GO	Al(g)	IPA/acetone (L)	GO (ml)
0.05	20.23988	5.4	2.53125
0.1	20.22975	5.4	5.0625
0.2	20.2095	5.4	10.125

Table 4.5: Design of experiment with varying wt% of GO, compaction pressure and sintering temperature: total number of specimens: 54(18x3).

Sample No	Parameters		
	wt% of GO	Compaction pressure (MPa)	Sintering temperature (°C)
1	0.05	500	580
2	0.1		
3	0.2		
4	0.05	540	
5	0.1		
6	0.2		
7	0.05	580	
8	0.1		
9	0.2		
10	0.05	500	600
11	0.1		
12	0.2		
13	0.05	540	
14	0.1		
15	0.2		
16	0.05	580	
17	0.1		
18	0.2		

### 4.3 Fabrication of composites

As received Al powders and GO/Al powders were cold compacted at three different pressures of 500MPa, 540MPa and 580MPa by using Specac 40T press. The die surfaces were coated with rhombic boron nitride powder to

facilitate easy removal of green samples. The powder required for each compact sample (pellet) has scaled to 0.5g and poured in evacuable pellet dies of 20mm diameter. The schematic representation of the process is shown in Figure 4.1. The thickness of the green sample obtained was 0.5mm.

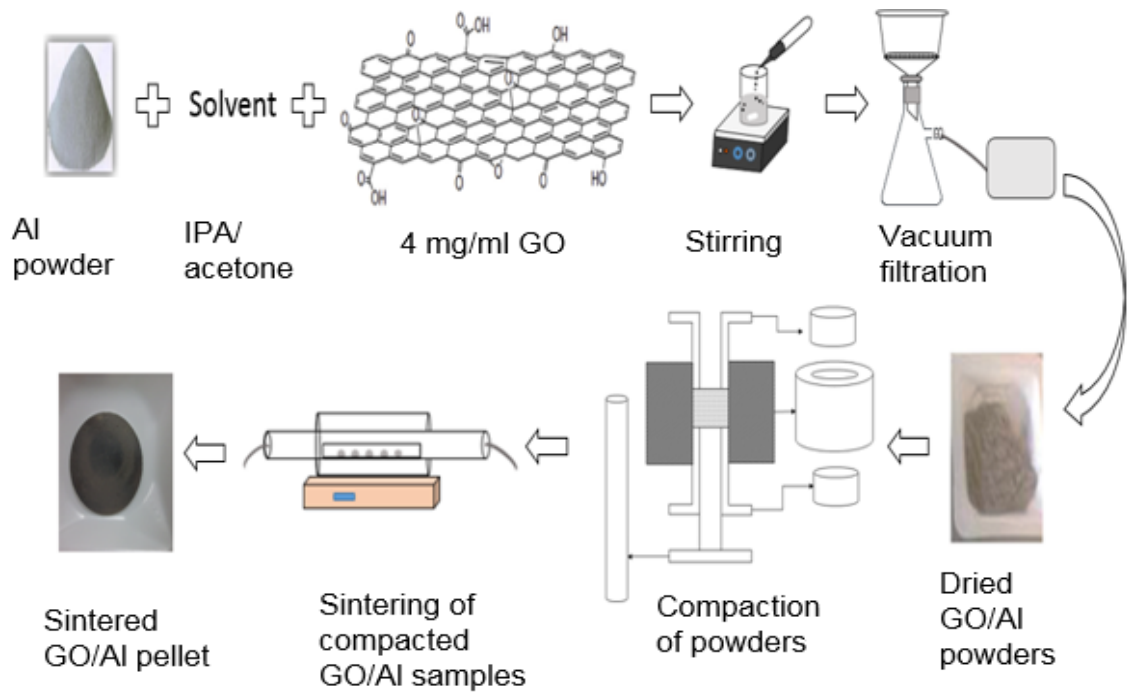


Figure 4.1: Schematic representation of GO/Al powder and composite preparation.

To obtain the green samples with maximum strength, the load is increased gradually to the desired value using the customised settings in the press. Once the desired load value is reached, load is maintained for 15mins followed by releasing the load at slow release rate. The loading cycle is shown in Figure 4.2.

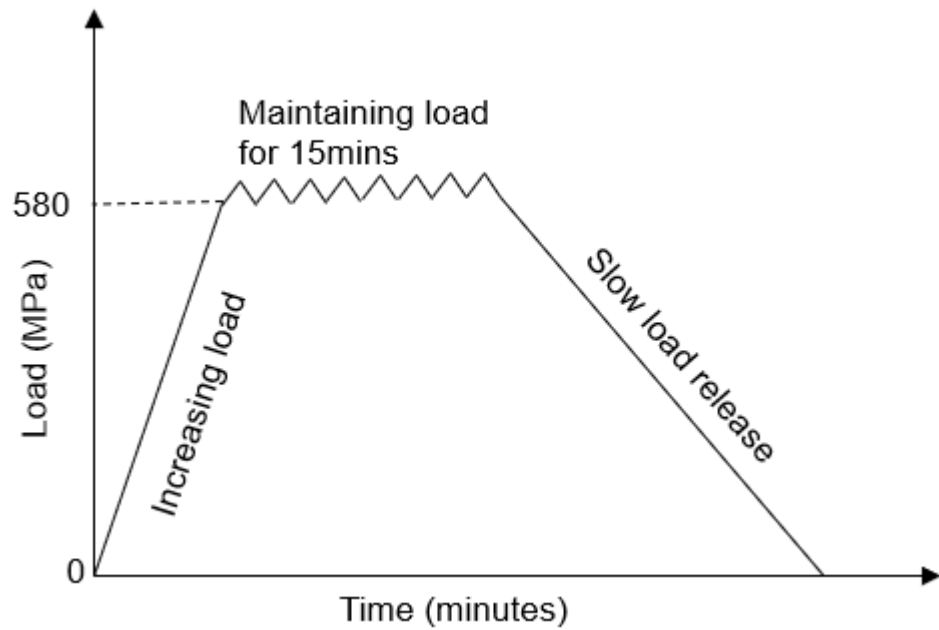


Figure 4.2: Loading cycle used in production of GO/Al composites.

To obtain metallurgical bonding, the green samples were then sintered to temperatures of 580°C and 600°C in horizontal tube furnace in argon gas atmosphere, the heating cycle is shown in Figure 4.3.

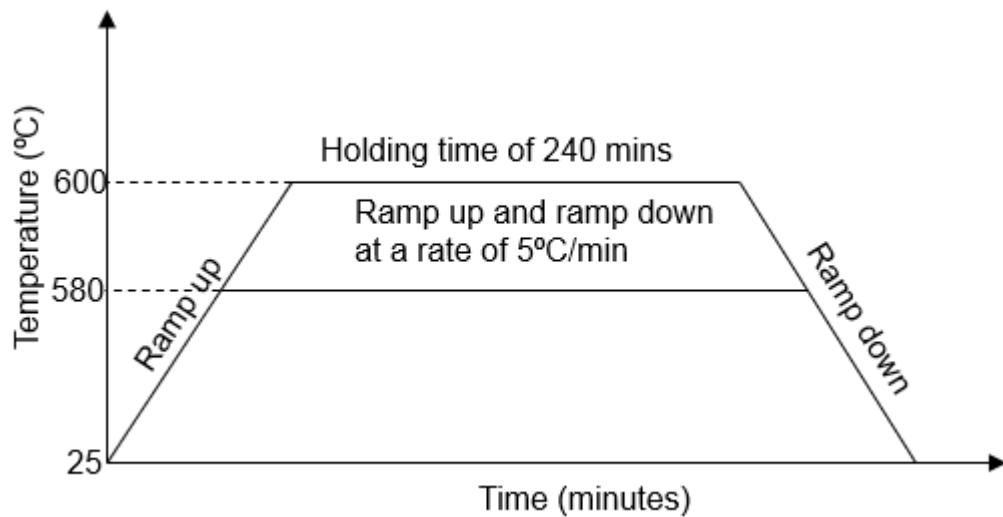


Figure 4.3: Sintering profile used in production of GO/Al composites.

#### 4.4 Characterisation of composites

GO/Al composites fabricated by powder metallurgy associated with liquid infiltration process were used for different types of testing and analysis. Table 4.6 shows the techniques used for characterisation and their expected

outcomes. The characterisation techniques comprise of morphological study (SEM and EDXS analysis), XRD analysis, micro Raman analysis, density measurement, micro hardness and indentation tests. The cross section of the fracture surfaces after Indentation tests were studied using SEM.

Table 4.6: Characterisation techniques used in current research.

CHARECTERISATION TECHNIQUES					
Metallographic/structural/chemical			Physical		
<b>Microstructural analysis</b> <ul style="list-style-type: none"> <li>• Distribution of GO and Al.</li> <li>• Grain size analysis.</li> </ul> <b>Chemical composition analysis</b> <ul style="list-style-type: none"> <li>• % of elemental composition.</li> </ul>	<b>XRD analysis</b> <ul style="list-style-type: none"> <li>• Identification of phases.</li> <li>• Crystallinity of materials.</li> </ul>	<b>Micro Raman analysis</b> <ul style="list-style-type: none"> <li>• Investigation of number of GO layers.</li> <li>• Defects in GO.</li> </ul>	<b>Density measurement</b> <ul style="list-style-type: none"> <li>• Measuring green density.</li> <li>• Measuring sintered density.</li> <li>• Calculation of densification parameter.</li> </ul>	<b>Micro Vickers hardness</b> <ul style="list-style-type: none"> <li>• Measuring hardness of samples.</li> </ul>	<b>Indentation test</b> <ul style="list-style-type: none"> <li>• Radial stress measurement.</li> <li>• Tangential stress measurement.</li> </ul>

#### 4.4.1 Density measurement

Archimedes' principle was used to calculate the green and sintered densities of the Al pellets and GO/Al composite pellets. The theoretical mixture densities were calculated using rule of mixtures given in equation (4.1), using theoretical densities of aluminium and GO as 2.699 g/cm<sup>3</sup> and 2.0 g/cm<sup>3</sup> respectively.

$$\delta_m = \frac{100}{\frac{w_{Al}}{\rho_{Al}} + \frac{w_{GO}}{\rho_{GO}}} \quad \text{----- (4.1)}$$

where  $\delta_m$  is the mixture density,  $w_{Al}$  is the weight percentage of Al powder,  $\rho_{Al}$  is the density of Al powder,  $w_{GO}$  is the weight percentage of GO and  $\rho_{GO}$  is the density of GO sheets.

The green and sintered densities of the samples were calculated by using Archimedes' principle, based on ASTM B962 standards and the equation is given by

$$\frac{\rho_A}{\rho_w} = \frac{w_A}{w_A - w_w} \times 100\% \quad \text{----- (4.2)}$$

where  $\rho_A$  is the actual density of the sample,  $\rho_w$  is the density of distilled water,  $w_A$  is the weight of sample measured in air and  $w_w$  is the weight of sample measures in distilled water.

The percentage densification of the GO/Al samples during sintering was calculated by using the following equation.

$$\varphi = \frac{\rho_s - \rho_g}{\rho_{th} - \rho_g} \times 100 \quad \text{----- (4.3)}$$

where  $\varphi$  is the densification parameter of samples,  $\rho_s$  is the density of sintered samples,  $\rho_g$  is the green density of samples and  $\rho_{th}$  is the theoretical density of the samples.

#### 4.4.2 Microstructural analysis

Scanning electron microscope (SEM) is one of the advanced equipment to investigate microstructure and elemental composition of material. SEM is used when the wavelength becomes limiting factor while using the optical microscope. SEM uses electron beam instead of photons or light particles, as electrons have much shorter wavelengths and will give better resolution (optical microscope has resolution of  $\sim 2000\text{\AA}$  whereas SEM has  $>100,000\times$ ) when the electron beam is incident on the sample, the interactions will result in emission of secondary electrons, Auger electrons, backscattered electrons, x-rays, schematic is shown in Figure 4.4, for a typical analysis the operating voltage is in between 5-25kV.

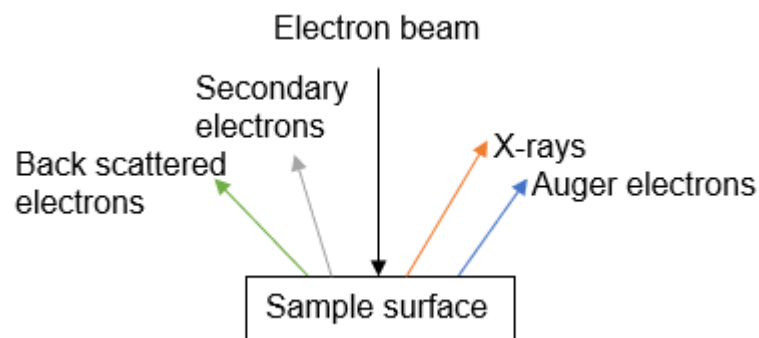


Figure 4.4: Schematic representation of interactions of electron beam with surface of the sample.

The Interactions between the electron beam and sample surface can be either elastic or inelastic. The elastically scattered electrons are known as backscattering electrons which are used to study the compositions of material under investigation. The amount of backscattering depends on the mass and

atomic number of the element being examined whereas in the inelastic scattering, the electron beam will knock out the electron from the outer shell of the atoms of the material under investigation, the ejected electrons from atoms are known as secondary electrons. The secondary electrons usually have low energies (<50eV) and play a key role in visualization of sample topology. A high quality image of the sample will be generated with increase in number of emitted secondary electrons. However, when the electron is removed from the outer shell, a vacancy will be generated (hole), the next excited electron will try to fill in the vacancy by losing some energy which will be transferred to the next available electron, which is ejected from atom; this second electron ejected is Auger electron spectroscopy.

The microstructural observations were performed on monolithic Al powders, GO/Al powders, monolithic Al and GO/Al sintered pellets using Carl-Zeiss EVO-L515 SEM. The particle morphologies of the GO/Al powders were studied by observing the colour changes on the particle, for an instance grey colour represents Al powder and black colour represents carbon content [29]. The GO/Al composite pellets were characterised using SEM, to identify the porosity levels, the resolution and voltage level were adjusted to obtain better contrast. Together with this the existence of interfaces at grain boundaries was investigated by observing SEM image. Grain sizes were measured using the image analyser interface available i.e., Image J software that works based on ferrites diameter (distance between two parallel lines that touches the edges of the grain). This was done by setting the scale on micrograph, thresholding and subtraction.

#### **4.4.3 EDXS analysis**

The excess energy of electron integrated to fill the vacancy created in the inner shell can exit X-ray instead of Auger electron in some materials. These X-rays are collected by the EDX spectrometer and will generate elemental analysis, using the X-ray peak intensities and positions. The schematic representation of the SEM system with EDX setup is shown in Figure 4.5(a). The samples are mounted on stage provided at the bottom the top column consists of a Tungsten filament from which electron beam will be emitted, the electrons emitted are accelerated further with the help of anodes. Series of magnetic

lens are used to focus the electron beam; condenser lens will adjust the spot size and objective lens adjusts the focus. In current work, Carl-Zesis EVO LS-15 with two column vacuum chambers and EDX setup is used for morphology and elemental composition investigation of the samples, photograph of the SEM system is shown in Figure 4.5(b).

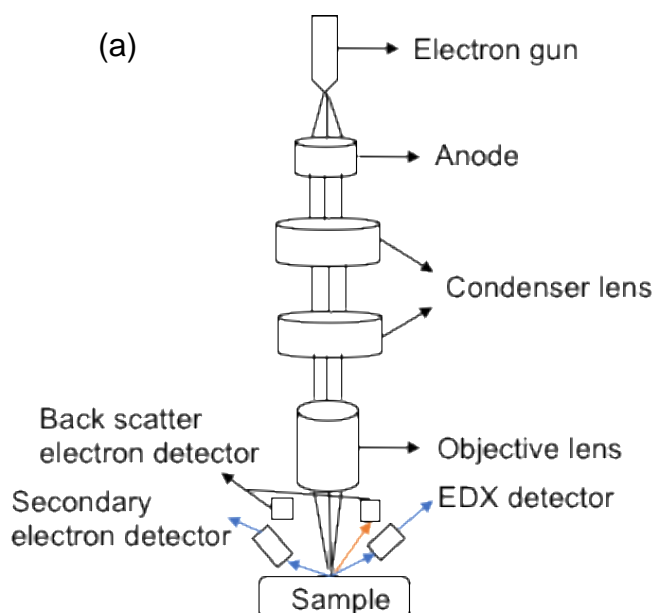


Figure 4.5: (a) Schematic representation of main components of SEM and (b) photograph of SEM with EDX setup.

The chemical compositions of the GO/Al powders and GO/Al sintered pellets were measured as the detector attached to the SEM collects the composition

data while the microstructure is being investigated. To ensure the efficient data collection, the EDXS detector was set at ~14mm of focusing distance. A sophisticated software associated with the machine identifies the elements on the sample with respect to intensities.

#### **4.4.4 XRD analysis**

X-ray diffractometry is one of the non-destructive tests to investigate the crystalline structures, phase analysis and grain size measurement. When a beam of x-rays incident on the sample, the electrons will be scattered in different directions. The wavelength of X-rays and diffraction patterns are obtained through the periodic arrangement of distance of separation of scattering centres analogous to the wavelengths. The scattering of waves can be either elastic or inelastic. The inelastic waves formed from electrons doesn't interfere with each other as there is no phase relationship and hence no crystallographic information. Thus, the 3D lattice of crystalline material consists of atomic planes (repeated atomic planes) arranged in regular manner. The condition for the interferences of rays reflected by the atomic planes is given by Bragg's law, it is given below

$$n\lambda = 2d_{hkl}\sin\theta \quad \text{----- (4.4)}$$

Where,  $n$  is the order of reflection,  $\lambda$  is the wavelength of x-ray used for investigation,  $\theta$  is the Bragg's angle,  $d_{hkl}$  is the inter planar distance of consecutive atomic planes.

The schematic representation of Bragg's diffraction is shown in Figure 4.6(a). The XRD methods can also be used to investigate the crystallite sizes, this can be done for the crystallites in the range of 3-100nm as the peak will be too broad for sizes below 3nm and for the sizes >100nm peak brooding will be too small. The crystallite sizes are determined using Scherr's equation, it is given by,

$$d = \frac{K\lambda}{\beta\cos\theta} \quad \text{----- (4.5)}$$

Where,  $d$  is the crystallite size,  $\lambda$  is the x-ray wavelength used for investigation,  $\theta$  is the Bragg's angle  $\beta$  is the peak width and  $K$  is the Scherr constant.

K value varies depending on crystal shape, it is 0.8-1.39 for the spherical particles it is 1. In the current work, Bruker AXS D8 advance diffractometer is used to investigate the presence of lattice planes using copper  $K_{\alpha}$  radiation of wavelength  $1.542\text{\AA}$ , photograph of the XRD system used in current work is shown in Figure 4.6(b).

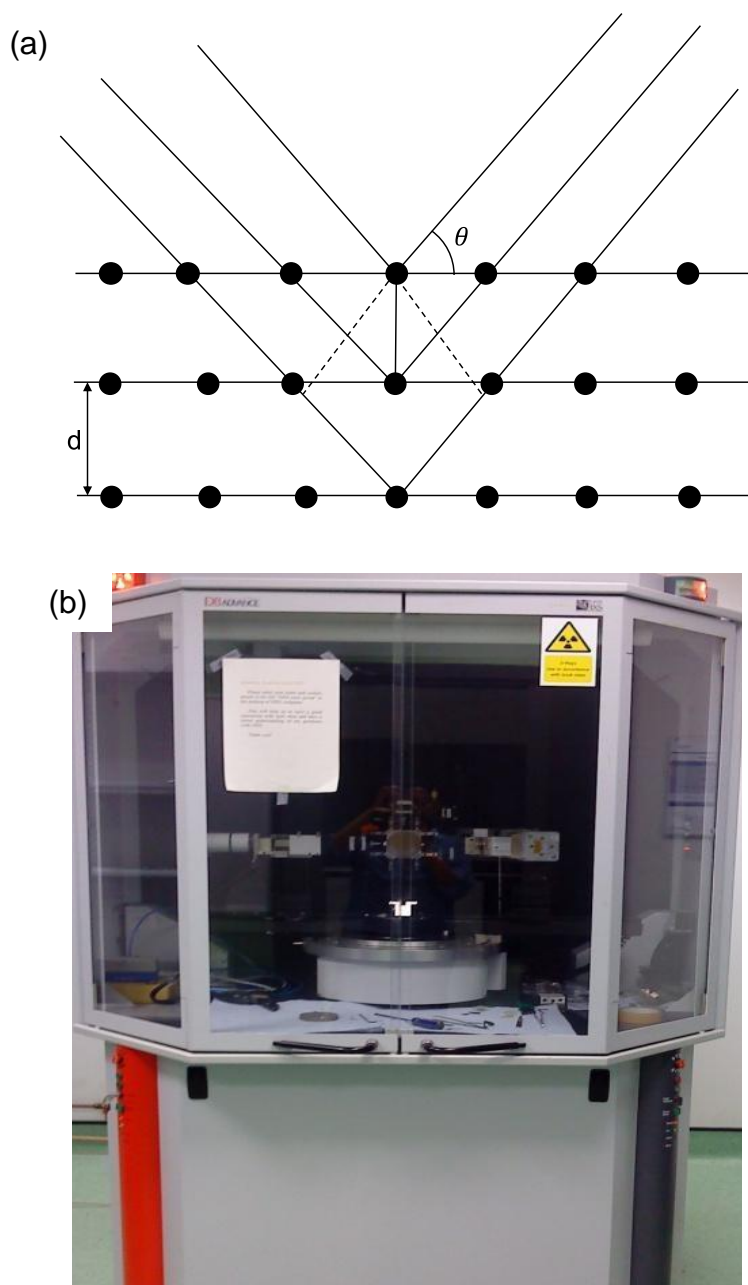


Figure 4.6: (a) Schematic of Bragg's law, black lines represent plane of atoms and (b) photograph of XRD used in current research.

The XRD patterns of the sample were recorded using Bruker D8 XRD system, XRD commander software was used to identify the phases using Bragg's law.

The stage position was adjusted to ensure the signal captivity in between the source and detector. A Z-scan was used to position the sample for optimal output. A Z-scan was performed from 0.99 to 1.99, chi-scan from -3 to 3 and phi-scan from -180° to 180° were performed to fix the position of sample for further investigations. Once the position is fixed at 20°, scan from 20° to 90° at scan rate of 5secs/step and increment of 0.1 at each step was performed. The 2θ data was plotted against intensity to investigate the presence of phases.

#### **4.4.5 Micro Raman analysis**

Raman spectroscopy is one of the advanced characterisation techniques used for graphene-based materials. It is a vibrational microscopy in which the molecular vibrations give rise to the energy differences and the intensity of the peaks depend on presence of number of molecules at vibrational states. Wherever light incidents on the material surface, some of the light maybe absorbed, transmitted, reflected or scattered, most of the scattered waves have the same energy (same frequency) as that if the incident beam, are called Rayleigh scatter waves (elastic scattering). Minority of the scattered waves have energies different than the incident beam, this process is called as Raman scattering (inelastic scattering). The Raman scatterings generates the information existence of chemical bonds in the molecules, the schematic representation of energy levels is shown in Figure 4.7(a) [194] and the photograph of Raman spectroscopic setup is shown in Figure 4.7(b). The interaction of photons (incident beam) with molecules exists it to a virtual state and upon relaxation the photon emitted to certain vibration state, having either Rayleigh scattering, stokes Raman scattering or anti-stokes Raman scattering. The vibrational information obtained from Raman analysis is specific to the chemical bonds and symmetry of molecules; hence, this is a powerful tool for investigation of molecular bonds of a material. The data is typically plotted as the intensity of scattered light against wavenumber difference between scattered light and incident light in  $\text{cm}^{-1}$  (i.e., difference in between incident photon energy and scattered photon energy ( $1 \text{ meV} = 8.065547\text{cm}^{-1}$ ) [195] the peak spectra positions of spectra were fitted using Lorentzian curve, given as

$$I = \frac{I_o}{1 + 4\left(\frac{w - w_c}{\Delta w}\right)^2} \quad \text{----- (4.6)}$$

Where,  $w$  is Raman wavenumber ( $\text{cm}^{-1}$ ),  $w_c$  at the centre,  $I_o$  is maximum intensity,  $\Delta w$  full width at half maximum of peak.

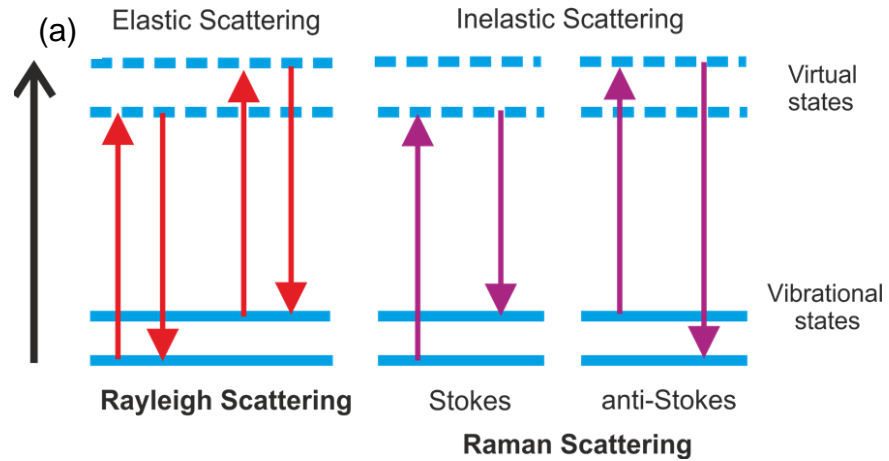


Figure 4.7: (a) Schematic representation of energy levels [202] and (b) photograph of micro Raman spectroscopy setup.

The Raman bands associated with graphene are D-band at  $\sim 1350 \text{ cm}^{-1}$ , G-band at  $\sim 1580 \text{ cm}^{-1}$  and 2D band at  $\sim 2700 \text{ cm}^{-1}$ , in general 2D bands and G-bands are prominent. The sample was placed on stage in Job in yvon horiba lab RAM 800 spectrometer equipped with 488 nm argon laser. The laser beam was focused on surface of sample at 50X working distance objective lens, the spot size of laser fixed at around  $2 \mu\text{m}$ . The scattered light was filtered with notch filters to filter out ray light scattering, and Raman lines were separated.

The intensity of the collected light was given as a function of its wavelength ( $\text{cm}^{-1}$ ) and the peak positions obtained were fitted with Lorentzian curve.

#### 4.4.6 Micro Vickers hardness

Vickers hardness (VH) test is one of the characterisation techniques used to investigate the micro hardness of the material, i.e., the resistance to the indentation while working with micro particles. The hardness value is obtained by measuring the indentation depth or the indentation area. Then schematic representation of Vickers hardness setup and photograph of Vickers hardness equipment are shown in the Figure 4.8(a) and (b) respectively. The hardness of the material is given by,

$$VHN = \frac{2F \sin\left(\frac{136^\circ}{2}\right)}{d^2} \quad \text{----- (4.7)}$$

Where  $F$  is the load acting on the material under investigation and  $d$  is the average of the two diagonals  $d_1$ ,  $d_2$  (shown in Figure 4.8(a)).

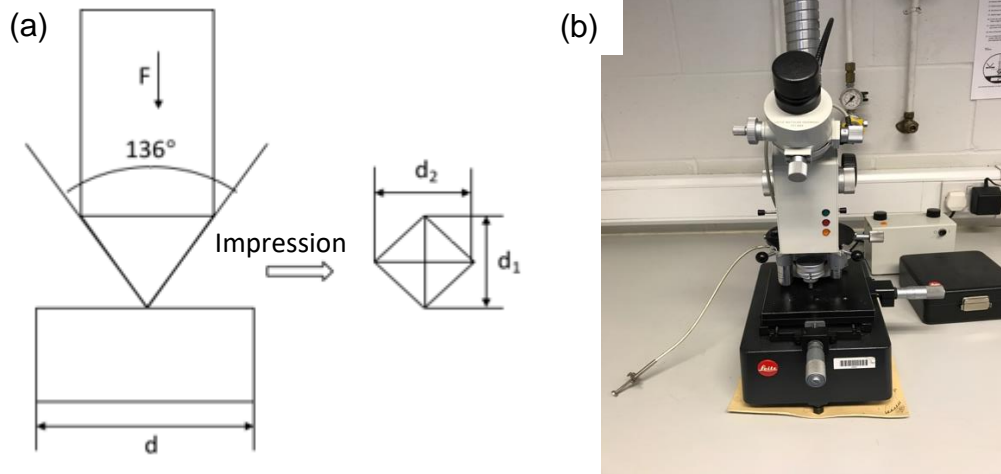


Figure 4.8: (a) Principle of Vickers hardness, (b) photograph of micro Vickers hardness tester.

The micro hardness properties of GO/Al composite were measured using Leitz mini load tester at 981mN force using a diamond indenter. The measurements were recorded at four random locations within the cross section of the sample being investigated. The tests were performed according to ASTM E384-99 standards, based on which there should be at least three indents gap between

each indent. The load was applied on to the sample for 20secs and slowly removed.

#### 4.4.7 Indentation test

The tangential and axial stress developed within a material under application of load, are measured using indentation to pin testing. The specimen will be placed on base, load is applied at a fixed loading velocity and the deflection at the centre is noted. Then schematic representation of indentation tester is shown in Figure 4.9.

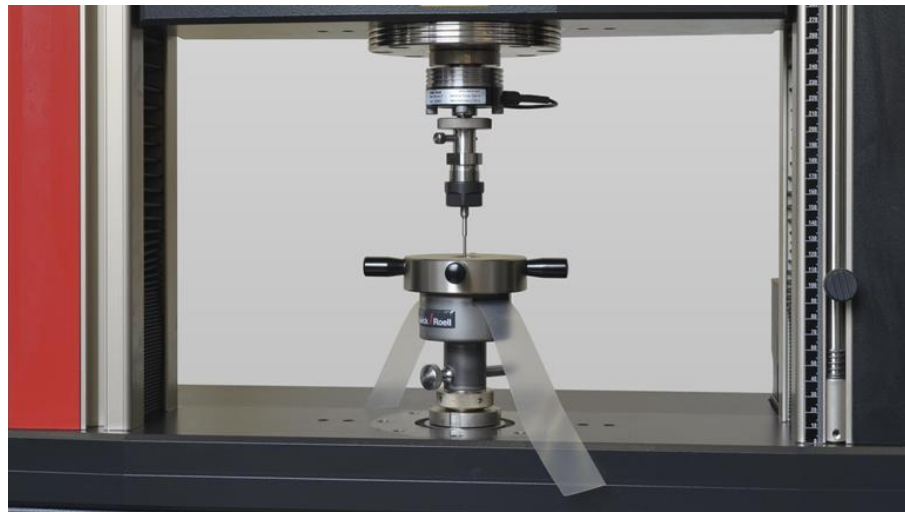


Figure 4.9: Photograph of indentation (puncture) test setup.

The compression test i.e., indentation tests were performed on GO/Al composite samples using Zwick Roell testing machine, Z005, TI-FR005TNA50. The samples were placed on stage and the load was applied on the samples using a pin indenter at a loading velocity of 1mm/min and load of 5kN. Depending on the recorded force during testing the deflection at the centre of sample, radial and tangential stress were calculated by using the equations (4.8)-(4.10) [196,197]. The fracture surfaces were characterised using SEM to observe the mixing quantity and porosity levels.

$$y = \frac{3PR^2}{4\pi Et^3} (3 + \nu)(1 - \nu) \quad \text{----- (4.8)}$$

$$\sigma_r = \frac{3P}{2\pi t^2} (1 + \nu) \log \frac{R}{x} \quad \text{----- (4.9)}$$

$$\sigma_t = \frac{3P}{2\pi t^2} \left( (1 + \nu) \log \frac{R}{x} + (1 - \nu) \right) \quad \text{----- (4.10)}$$

Where,  $y$  is the deflection in centre,  $P$  is the load,  $R$  is the radius of circular disk,  $t$  is thickness of disk,  $E$  is Young's modulus,  $\nu$  is Poisson's ratio,  $\sigma_r$  is radial stress,  $\sigma_t$  is tangential stress,  $x$  is the diameter of indenter.

## **4.5 Modelling of GO/Al composites**

### **4.5.1 Finite element modelling of GO/Al composites**

Finite element modelling and analysis was performed to investigate the effect of GO reinforcement on the Al particles in GO/Al composites. The main objectives of the FE simulation is to predict the effect of three parameters i.e., GO existence in Al matrix, GO layers and percentage of Al particles coated with GO on the stress distribution of GO/Al composites. Static structural analysis was used in current modelling work to predict the stress distribution in GO/Al composites. The number of GO layers were obtained from the micro Raman investigation done experimentally on GO/Al composites and used to develop model in-line with the experimental observations. Due to the complexity of GO/Al composite modelling, at first the Al particles, GO reinforcement layers and joints connecting particles were designed in Hyper Mesh™. The model was then imported to ANSYS 16.0 for the addition of material properties, meshing, boundary conditions and parametric analysis was carried out. Al particles of 35µm size and each GO layer of 0.134nm were modelled in a cube of 140×140×140 dimensions. For the analysis SOLID 185 element was considered and the corresponding translational (U) and rotational (ROT) boundary conditions, constraint equations (CE) and force (F) were applied on the model. The contacts/connections between particles were simulated using rigid elements, these contact elements were highlighted in pink colour in Figure 4.10. The contact elements provide bonding strength to the particles and the load tolerance limit for the contact elements is given as 100%. All degrees of freedom i.e., for both translational and rotational in X, Y and Z-directions are constrained at 0 at the bottom of the GO/Al composite and a compressive static load of 2.5N is applied in Y-direction at the top of the GO/Al composite. The properties of the materials used in simulation were

given in Table 4.7 and the FE model of GO/Al composite with the application of boundary conditions is shown in Figure 4.10.

### Assumptions

In current study, the following assumptions were considered to model GO/Al composites.

- The GO reinforcement was uniformly distributed on to the Al particles.
- The matrix and reinforcement are isotropic materials.
- No interfacial compounds formed in between GO and Al particles.
- The load applied to the GO/Al composite is within the elastic limit.

Table 4. 7: Material properties used in simulation of GO/Al composites.

Material	Young's modulus (MPa)	Poisson's ratio (N/A)
Al	$7 \times 10^4$	0.34
GO	$33 \times 10^4$	0.14

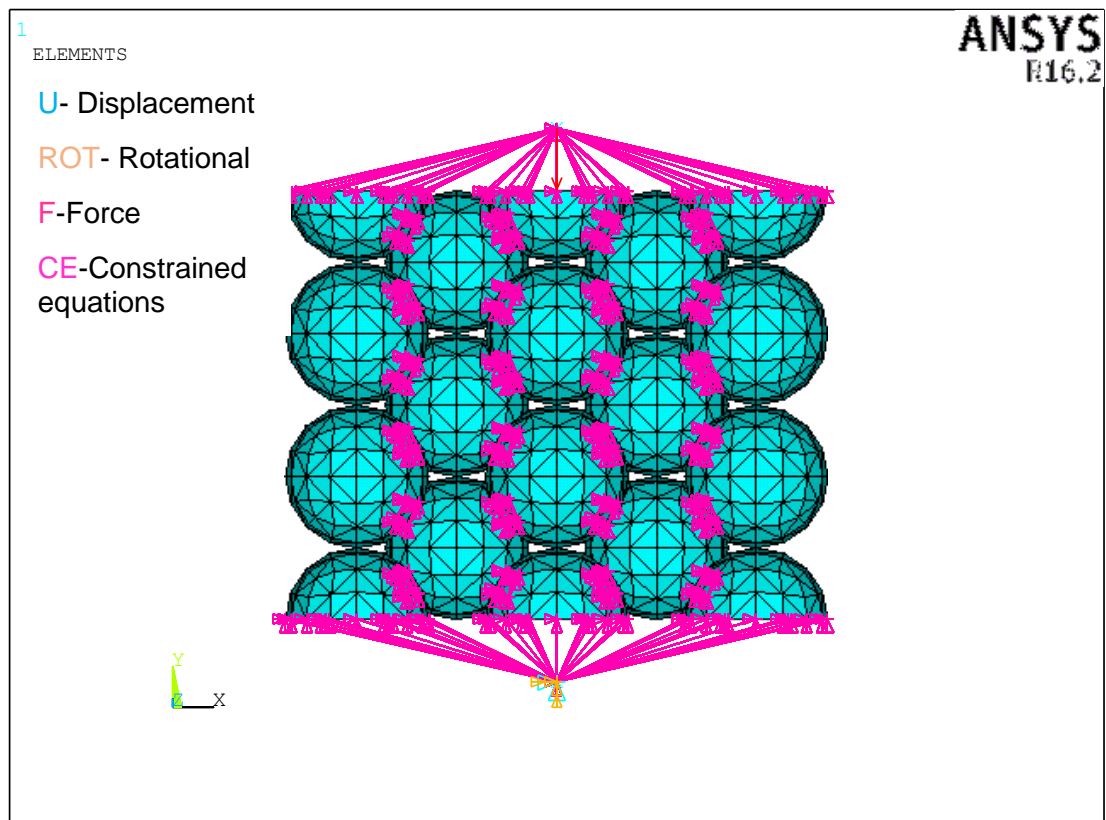


Figure 4.10: FE model of GO/Al composite with application of boundary conditions.

#### **4.5.2 Mesh convergence of FE model**

The FE model used in current research work was tested for convergence at different element sizes starting from  $0.8\mu\text{m}$  to  $0.1\mu\text{m}$  (increasing number of elements). The complexity of the model vs response was recorded, in current research complexity is the element size (number of elements) and response of interest was the corresponding stress. Varying the element size in the FE model varies the stress generated in the composite shown in Figure 4.11. Four convergence runs were performed on FE models with and without GO layers reinforced on Al particles. Figure 4.11(a) shows the convergence plot of FE model without GO layers on Al particles, it can be noted from the plot that at  $0.2\mu\text{m}$  of element size the model was converged i.e., the difference in stress values obtained at  $0.2\mu\text{m}$  element size and  $0.1\mu\text{m}$  element size is around 1% which is within the acceptability limit of 5%. The convergence plot of FE model with Al particles reinforced with 5GO layers is shown in Figure 4.11(b), in which the difference in stress values obtained at  $0.2\mu\text{m}$  element size and  $0.1\mu\text{m}$  element size is around 0.7% which is within the acceptability limit of 5%. It can be noted that the FE model with and without GO layers is converged at  $0.2\mu\text{m}$  of element size.

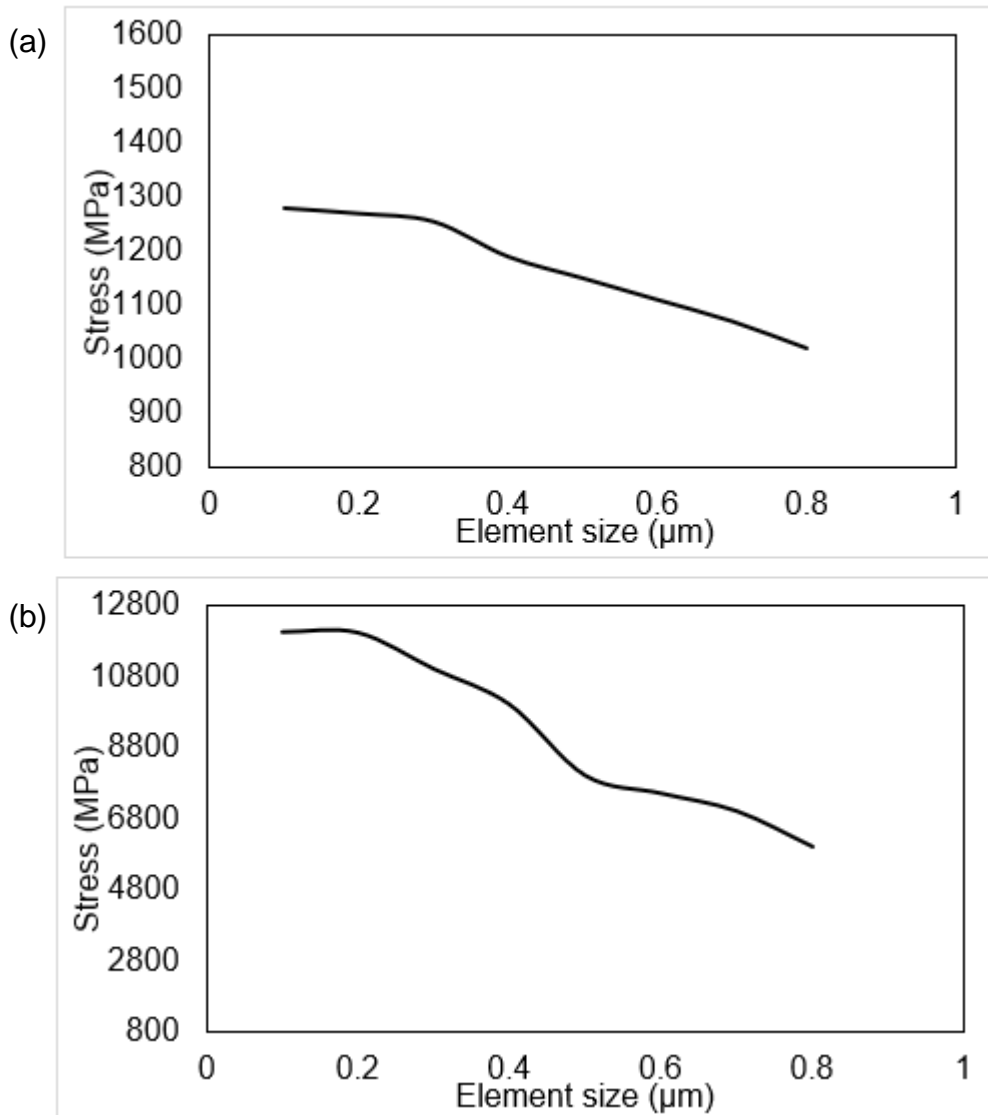


Figure 4.11: Mesh convergence plots of (a) FE model with no layer and (b) FE model with 5GO layers.

#### 4.5.3 Analytical modelling of GO/Al composites

Rule of mixtures (ROM) is one of the effective, simple and intuitive method of determining the effective properties of the composites in terms of its constituents i.e., matrix and reinforcement. Mainly two theories are available in literature to predict the effective mechanical properties of the composite, one is Voigt model that uses equal strain assumption and other is Reuss model that uses equal stress assumption [47]. ROM not only used for finding the effective properties of composites with uniformly distributed second phase particles but also for the nanocrystalline materials. The effective stress and Young's modulus of the composites can be obtained from the equations (4.11)-

(4.13) [198]. In current research work Young's modulus was considered for the analytical modelling due to the lack of literature available for the flow stress measurements of GO.

$$\sigma_{eff} = f_p \sigma_p + f_m \sigma_m \quad \text{----- (4.11)}$$

$$\sigma_{eff} = \left( \frac{f_p}{\sigma_p} + \frac{f_m}{\sigma_m} \right)^{-1} \quad \text{----- (4.12)}$$

$$E_c = f E_p + (1 - f) E_m \quad \text{----- (4.13)}$$

where,  $\sigma_{eff}$  is the effective stress of composite,  $f_p$  is the volume fraction of particle,  $\sigma_p$  is the flow stress of particle reinforcement,  $f_m$  is the volume fraction of matrix,  $\sigma_m$  is the flow stress of matrix,  $E_c$  is the Young's modulus of composite,  $E_p$  is the Young's modulus of particle reinforcement,  $E_m$  is the Young's modulus of the matrix and  $f$  is the volume fraction and is calculated by the equation (4.14).

$$f = \frac{f_p}{(f_p + f_m)} \quad \text{----- (4.14)}$$

Analytical modelling of the GO/Al composites is done at various volume fractions of GO reinforcement of 0.05, 0.15, 0.2 and 0.5. The properties used to calculate the Young's modulus of the composite are given in Table 4.8. the values obtained from the analytical model will be compared with results obtained from FE modelling of GO/Al composites.

Table 4.8: Properties of materials used in analytical modelling of GO/Al composites.

Young's modulus of GO reinforcement (MPa)	$33 \times 10^4$
Young's modulus of Al matrix (MPa)	$7 \times 10^4$
Volume fraction of GO reinforcement (%)	0.05, 0.15, 0.25, 0.50
Volume fraction of Al matrix (%)	0.95, 0.85, 0.75, 0.50

## 4.6 Summary

The current chapter presented the materials used to produce GO/Al composites together with their properties. This chapter also mentioned the elaborated experimental procedure used to fabricate composites and the

experimental conditions used for testing. The FE model generation and boundary conditions employed with a goal of comparing the model against experimental observations obtained in present research work were given in detail.

# CHAPTER 5

## RESULTS AND DISCUSSION

### 5.1 Introduction

In this chapter an overview of results obtained in the current research initiated from the selection of solvent, vacuum filtration of powders is reported. The results concerned with density of samples, particle morphologies, crystalline phase analysis using diffraction patterns, micro Raman analysis, micro hardness and indentation analysis on monolithic Al samples and GO/Al composites are also reported. The order of results presented in this chapter is outlined in Figure 5.1. The results of GO/Al composites obtained were discussed in comparison with monolithic Al.

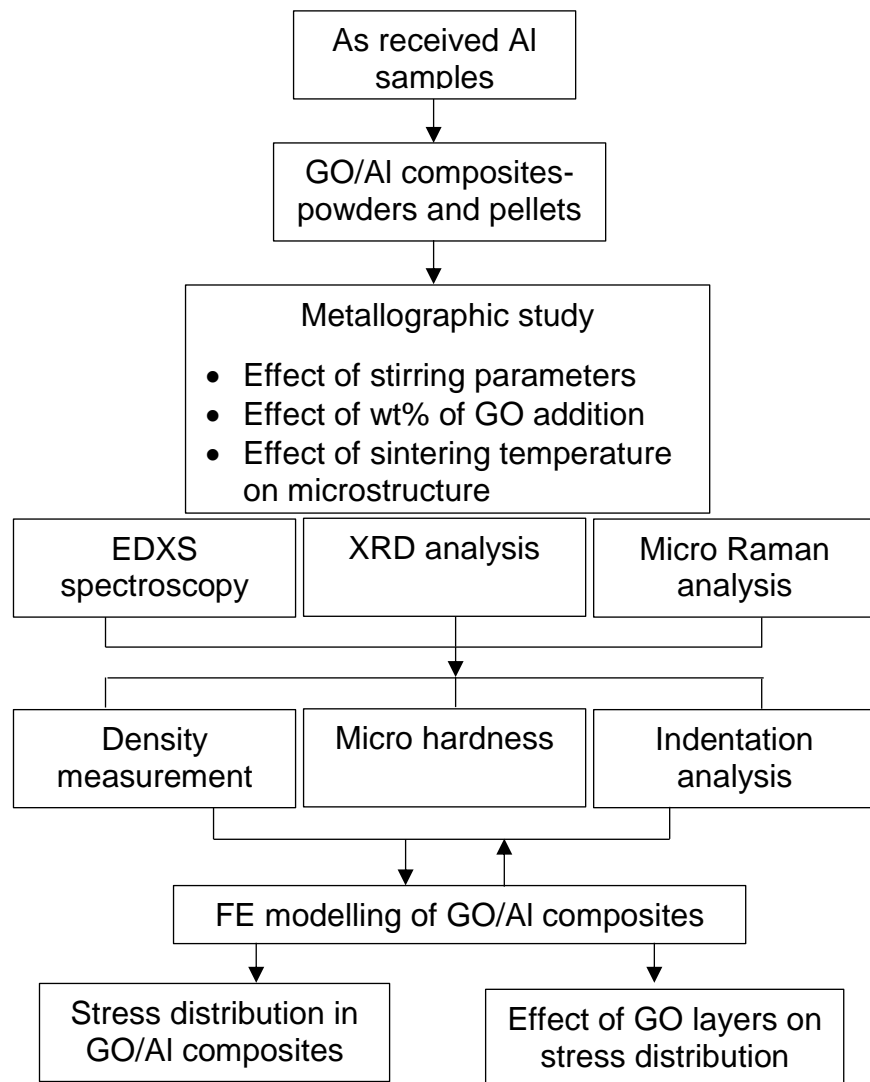


Figure 5.1: Outline of order of results discussed in this chapter.

## 5.2 Powder treatment

For an efficient fabrication of the GO/Al composite the powder was treated with different solvents at various stirring times to obtain an optimum powder.

### 5.2.1 Selection of solvent

The selection of appropriate solvent to disperse GO efficiently is one of the key aspects in GO/Al composite production. since the mechanical properties of the final resulting composites depends highly on the dispersion of the GO, as the dispersion determines the thickness of GO and distribution of GO in Al matrix. In the current research, two solvents namely, IPA and acetone have been used to produce GO/Al composites. Figure 5.2 shows the photographs of beakers with 1.3wt% GO/Al dispersed in acetone and in IPA respectively after 8hrs of stirring. It can be observed that once the stirring was stopped the Al particles were still dispersed in IPA whereas in acetone the particles were accumulated as a black slurry at the bottom in acetone. Figure 5.3 (a), (b) shows the leftover solution after filtering out the GO/Al/IPA and GO/Al/acetone solutions, in which filtered out solution in which IPA was used as solvent was clear where as solution in which acetone was used as solvent is in dark brown colour. This implies to that the GO wasn't dispersed effectively in acetone compared to IPA, IPA was choosed as the solvent for the GO/Al composite produced in current research work. The wet mixing/liquid infiltration process resulted in better dispersion of GO around the Al particles in GO/Al powders. This was possible by the selection of appropriate solvent for the dispersion of GO in Al matrix. As mentioned by Parket al. [199] that the dispersibility of carbon fillers in organic solvents depend on solubility parameters such as dispersion cohesion parameter ( $\delta_d$ ), polarity cohesion parameter ( $\delta_p$ ) and hydrogen bonding cohesion parameter ( $\delta_h$ ). Hence, the higher the  $\delta_d + \delta_h$  value is the better the graphene dispersion will be. The higher values of  $\delta_d + \delta_h$  of IPA (11.97) than acetone (9.77) led to the better dispersion of GO in Al which was evident from Figure 5.2(a)-(b). It was noted that the GO particles in IPA were stable after 30mins of standby while GO in acetone agglomerate and settle down at the bottom of the beaker. This was also reflected on morphologies of the particles. The stirring parameters used for powder treatment of GO/Al composites were optimised in such a way that the stirring

speed won't exceed the threshold, induce defects in GO particles/sheets that might effect end properties of the composite [200,201]. At the lower stirring speeds and times, the particles will cluster in localised region and particles will be non-homogeneously distributed at lower stirring speeds. Even though, the inter-particle distances increased by increase in stirring speed, the clustering will be prominent at less stirring time [202]. In current research no clustering of particles were observed at the optimised stirring times, speeds at each wt% of GO reinforcement, this was inturn reflected on the microstructure of the composites.

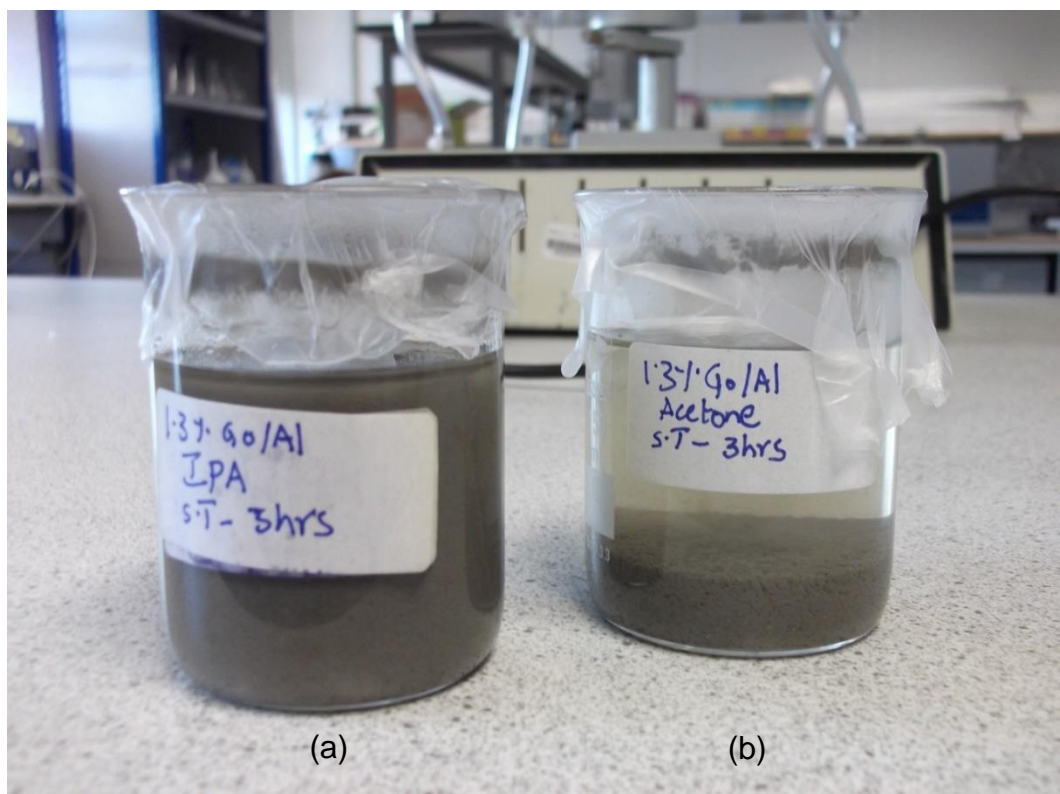


Figure 5.2: Comparison of 1.3wt% of GO dispersion in solvent (a) IPA and (b) acetone.

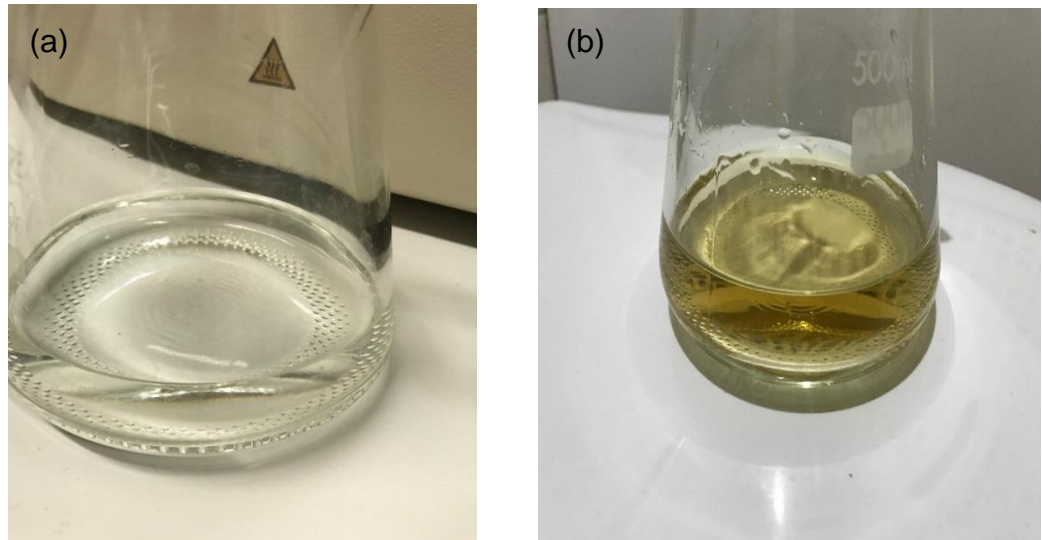


Figure 5.3: Filtered out solution of 1.3 wt% GO/Al (a)IPA as solvent and (b) acetone as solvent.

### 5.2.2 Vacuum filtration

The GO/Al/IPA dispersions were vacuum filtered in fume hood and the efficiency of stirring parameters was investigated by using visual inspection of the filter papers, shown in Figure 5.4. There was no evidence of dark brown colour on the filter papers which implies to that GO particles were residing on the Al particles and were not filtered out. Similar results were observed even with the increase in wt% of GO reinforcement i.e., from 0.05wt% to 0.1wt% and 0.2wt%.

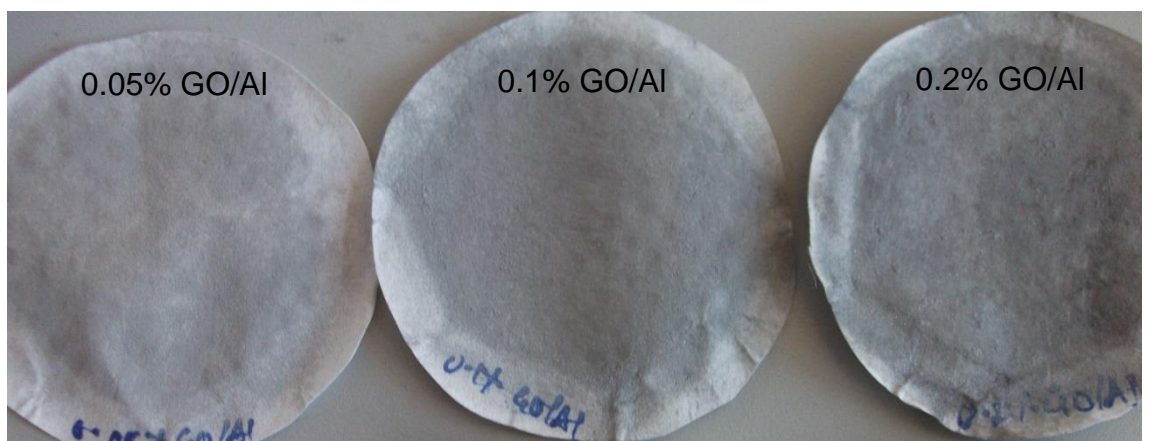


Figure 5.4: Visual inspection of filter papers after vacuum filtration.

The initial results of visual inspection were consolidated in Table 4.1, in which wt% of GO reinforcement, solvent, stirring time, powder drying conditions and sintering temperature of the samples, were given as process parameters. At

the initial stages of experiments, GO of wt% of 0.7% and 1.3% were under investigation to produce GO/Al composites but it was hard to attain the uniform dispersions due to the high percentage of agglomerations. To avoid agglomeration of GO particles, less wt% of GO i.e., 0.05%, 0.1% and 0.2% were used for further investigation of GO/Al samples. The GO/Al powders production at the fixed processing conditions using visual inspections were highlighted in bold and the corresponding reasons for the failure and consideration of processing conditions were also given in Table 4.1. All the samples were sintered in horizontal tube furnace in Ar atmosphere for 4hrs of holding time and each processing condition of the samples was analysed through visual inspection. The comments about whether the sample passed or failed were noted via observing the sample condition after sintering i.e., while taking out the samples from sintering dishes some samples fall apart as powders and some samples were so delicate that they broke while handling.

Table 5.1: Summary of results of visual inspection at processing conditions for different wt% of GO reinforcement, solvent, stirring time, powder drying and sintering temperature.

wt% of GO	Solvent	Stirring time (hr)	Powder drying	Sintering temperature (°C)	Pass/Fail	Comments	
0	IPA	1	N	500	F	Moisture was observed in powder, need to improve filtration method and drying powders	
			Y		F	Sintering temperature was not enough as the samples were so delicate	
				580	<b>P</b>	<b>Samples became hard and stirring time was enough</b>	
0.7		2	N	500	F	Moisture was observed in powder, need to improve filtration method and drying powders	
				500	F	Sintering temperature was not enough as the samples were so delicate	
		4	Y	580	F	F	Stirring time was not enough, dark coloured filtered out solutions were recorded
					F	F	Stirring time was not enough, dark coloured filtered out solutions were recorded
					F	F	Stirring time was not enough, dark coloured filtered out solutions were recorded
				<b>P</b>	<b>P</b>	<b>Samples became hard and stirring time was enough</b>	
1.3	4	N	500	F	Moisture was observed in powder, need to improve filtration method and drying powders		
		Y		F	Sintering temperature was not enough as the samples were so delicate		

		10		580	F	Stirring time was not enough, dark coloured filtered out solutions were recorded
					F	Stirring time was not enough, dark coloured filtered out solutions were recorded
					<b>P</b>	<b>Samples became hard and stirring time was enough</b>
0.05		1		500	F	Sintering temperature was not enough as the samples were so delicate
				580	<b>P</b>	<b>Samples became hard and stirring time was enough</b>
0.1		2		500	F	Sintering temperature was not enough as the samples were so delicate
				580	F	Stirring time was not enough, dark coloured filtered out solutions were recorded
0.2		3		500	F	Sintering temperature was not enough as the samples were so delicate
				580	F	Stirring time was not enough, dark coloured filtered out solutions were recorded
					<b>P</b>	<b>Samples became hard and stirring time was enough</b>
0		5		580	<b>P</b>	<b>Samples became hard and stirring time was enough</b>
					2	<b>P</b>
0.7	Acetone	2	N	500	F	Moisture was observed in powder, need to improve filtration method and drying powders
			Y		F	Sintering temperature was not enough as the samples were so delicate
		4		Y	580	F
			F		Stirring time was not enough, dark coloured filtered out solutions were recorded	

		6		F	Stirring time was not enough, dark coloured filtered out solutions were recorded
		8		<b>P</b>	<b>Samples became hard and stirring time was enough</b>
				<b>P</b>	<b>Samples became hard and stirring time was enough</b>
1.3		4		F	Stirring time was not enough, dark coloured filtered out solutions were recorded
		6		F	Stirring time was not enough, dark coloured filtered out solutions were recorded
		10		<b>P</b>	<b>Samples became hard and stirring time was enough</b>
0.05		1	500	F	Sintering temperature was not enough as the samples were so delicate
			580	F	Stirring time was not enough, dark coloured filtered out solutions were recorded
0.1		2	500	F	Sintering temperature was not enough as the samples were so delicate
			580	F	Stirring time was not enough, dark coloured filtered out solutions were recorded
		5		<b>P</b>	<b>Samples became hard and stirring time was enough</b>
0.2		3	500	F	Sintering temperature was not enough as the samples were so delicate
			580	F	Stirring time was not enough, dark coloured filtered out solutions were recorded
		6		<b>P</b>	<b>Samples became hard and stirring time was enough</b>

## **5.3 Characterisation of composites**

### **5.3.1 Density of GO/Al composites**

The densities of the bulk composites before and after sintering were measured using Archimedes principle. Figure 5.5(a) shows the summary of green and sintered densities of pure Al samples with respect to compaction pressures. It can be noted that the green density of the samples increases with increase in compaction pressure. Figure 5.5(b) shows the percentage of density and porosity as the functions of compaction pressures, the porosity of the GO/Al composites reduced with increase in compaction pressure. The percentage of densification of GO/Al samples and relative density of the samples with respect to the percentage of GO reinforcement are in shown in Figure 5.6. It can be noted that all the samples were densified during sintering. The addition of GO shows minor effect on densification of the GO/Al samples for instance the density of the samples increases with increase in wt% of reinforcement up to 0.2wt% of GO, the density of 0.2wt% GO/Al samples was less compared to 0.05wt% GO/Al but more than monolithic Al. This implies that the wet mixing of 0.2wt% and GO dispersion in Al is not efficient enough and leads to agglomeration and resulting in porosity.

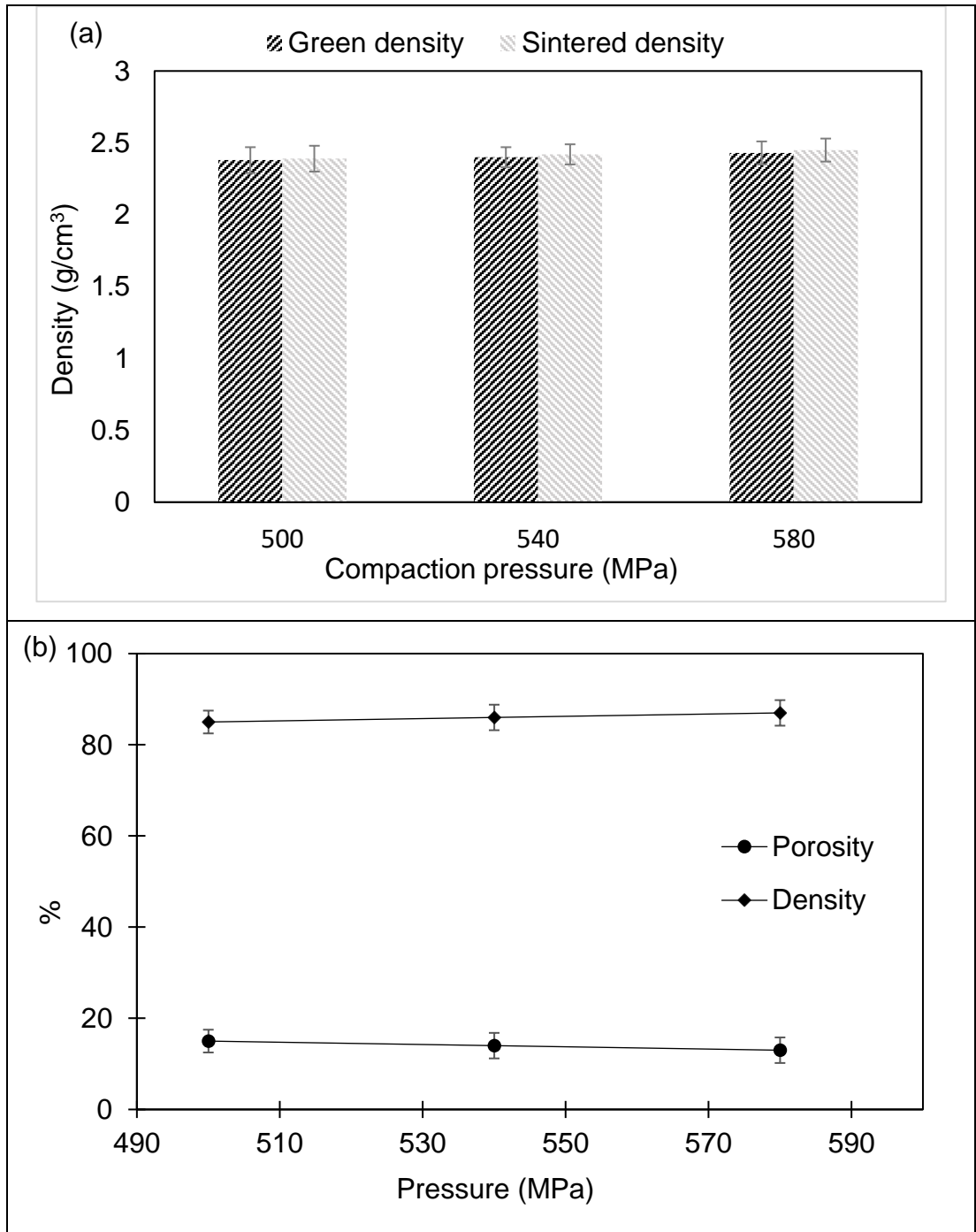


Figure 5.5: (a) Green density and sintered density against compaction pressure of pure Al samples and (b) percentage of sintered density and porosity vs compaction pressure of pure Al samples; n=3.

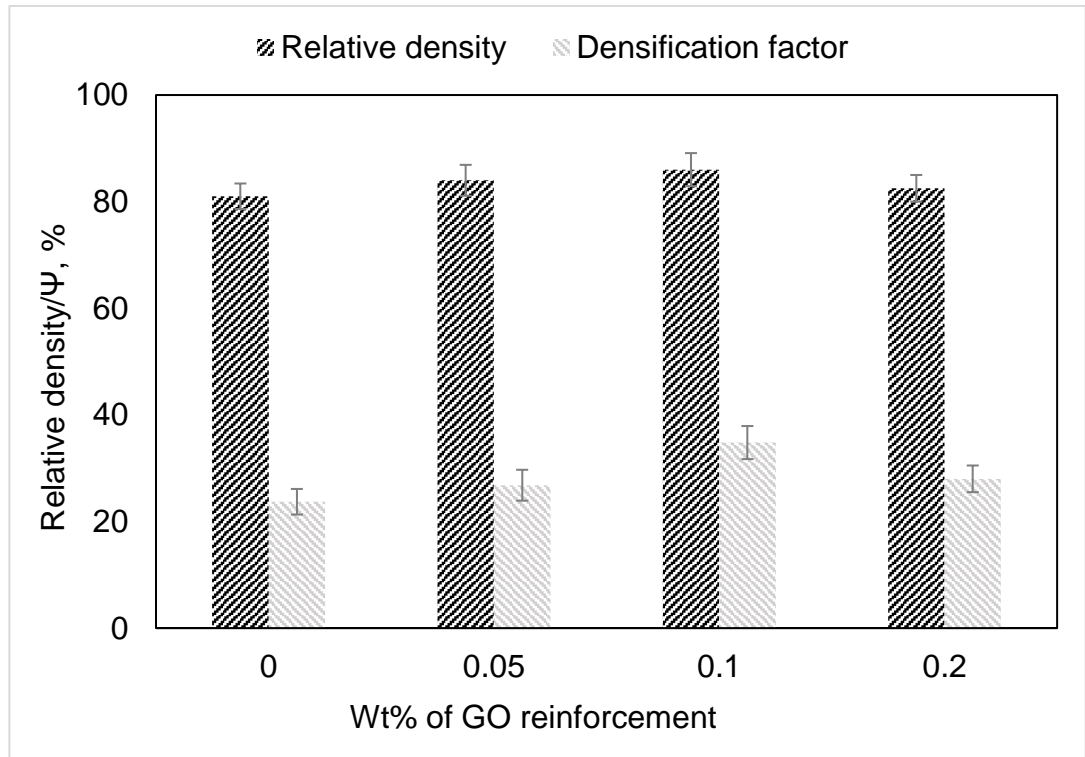
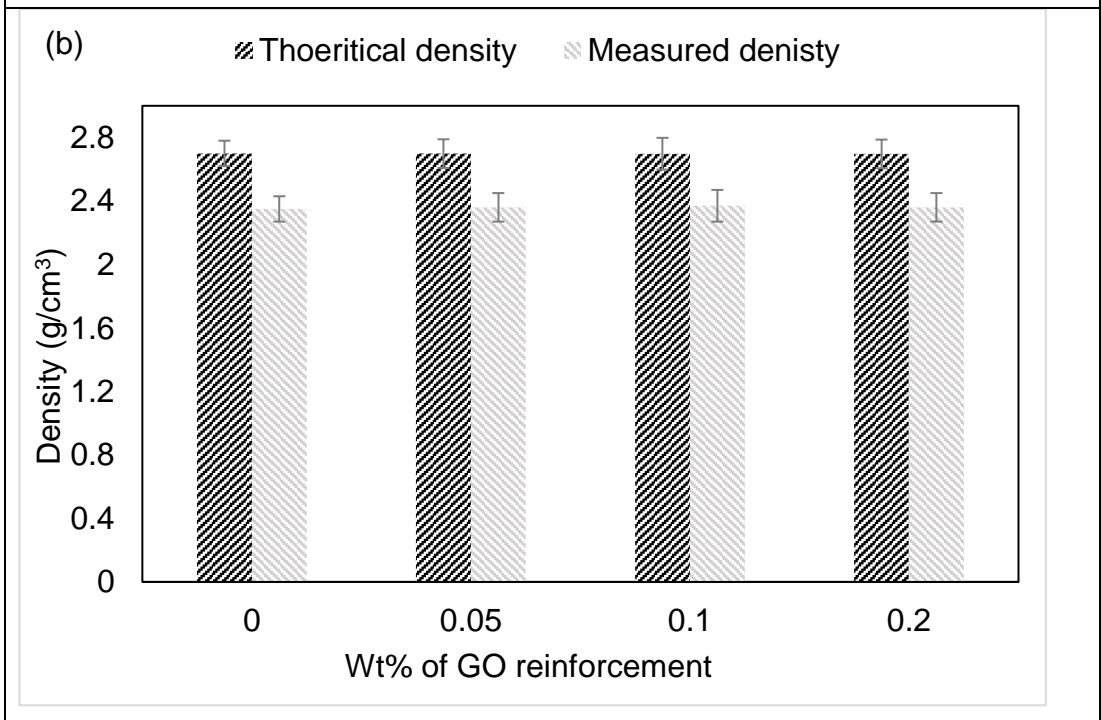
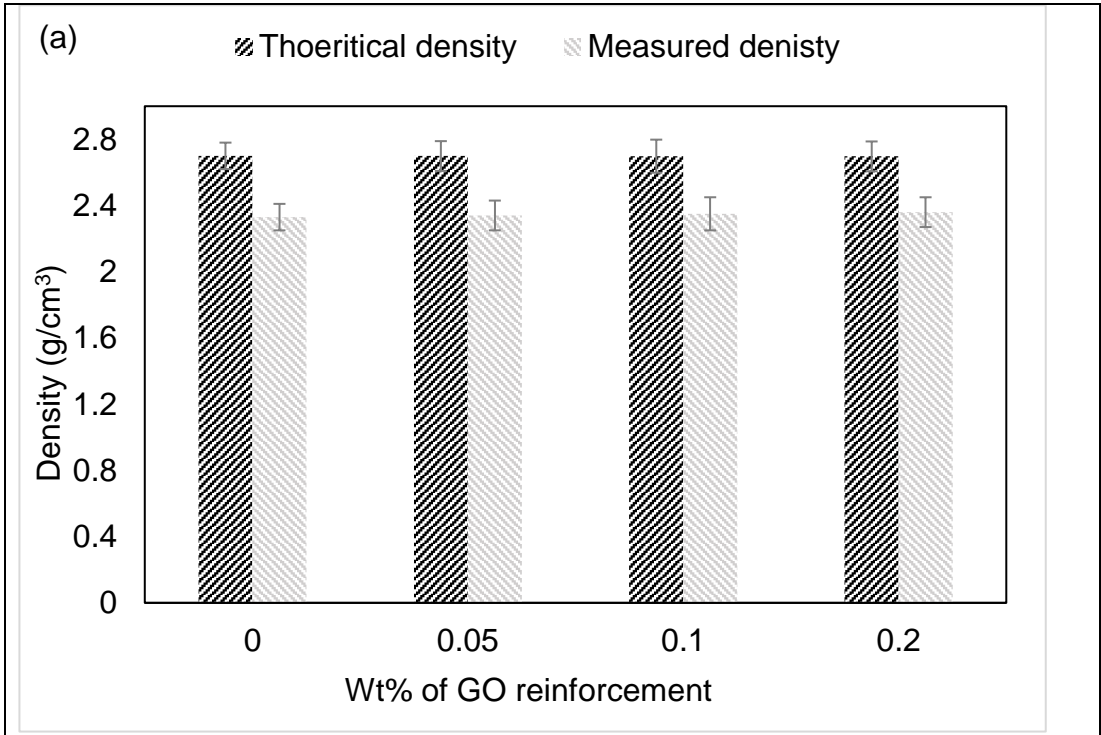


Figure 5.6: Relative sintered density and densification factor of the sintered GO/Al composites.

The theoretical and measured densities of the sintered samples with respect to the compaction pressures, wt% reinforcements are shown in the Figure 5.7(a)-(c). Three samples were tested for each process parameters to obtain repeatable and reliable results and the results were plotted at 95% confidence intervals.



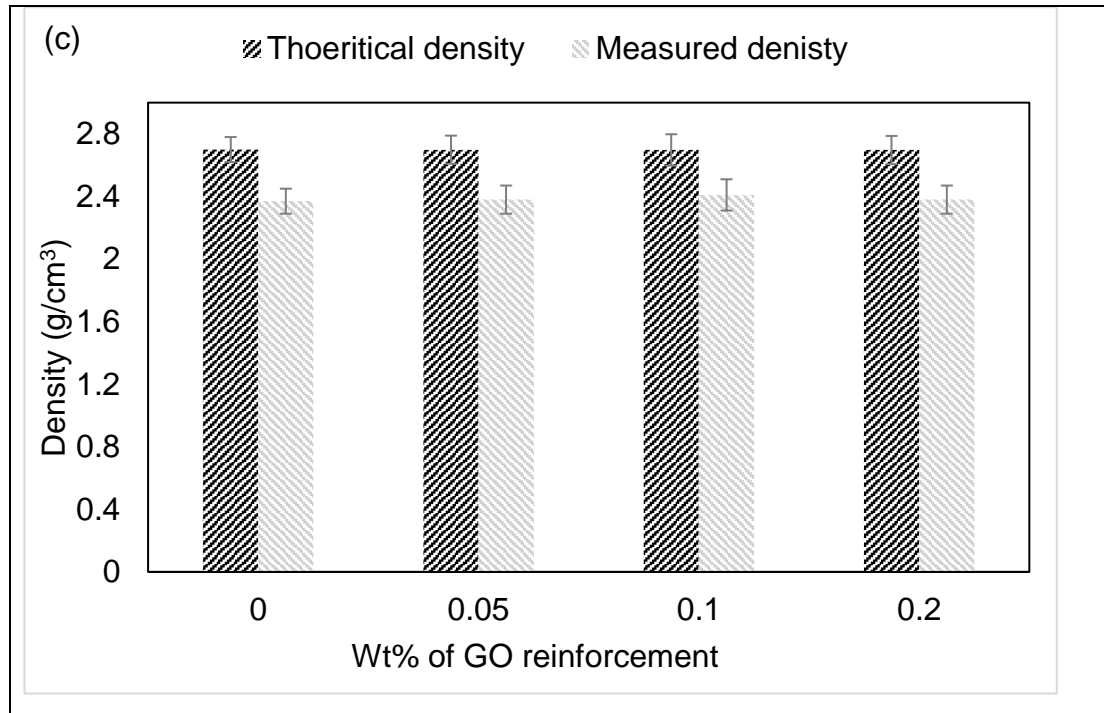


Figure 5.7: Theoretical and measured densities of GO/Al composites sintered at 600°C: (a) compacted at 500MPa, (b) compacted at 540MPa and (c) compacted at 580MPa.

The nano particles are more prone to form agglomeration (hence non-homogeneous distribution) in matrix due to their high surface to volume ratio which provides high surface energy and hence leading to more agglomeration. The uncontrolled agglomeration of nano particle reinforcement might occur in between particles due to existence of Van der waal forces. It was mentioned by Sudarshan et al. [203] that the mechanical stirring can only provide small shear force high enough to break large clusters, but it is not effective for breaking up the small clusters especially at nano level. Saboori et al. [204] have reported an increase in agglomeration with increase in wt% of graphene reinforcement in Al matrix. In current research similar results were recorded where porosity was observed because of agglomeration, the microstructure of composites in current research work were compared with the composites in literature and shown in Figure 5.8(a)-(b). In current research, with the increase in wt% of GO reinforcement the spacing in between the grain boundaries of composites effected the sinterability of the composites. The agglomerated regions observed on the composites acted as barriers for the diffusion of grain

boundaries during sintering process and hence effected the sintered density of the composite.

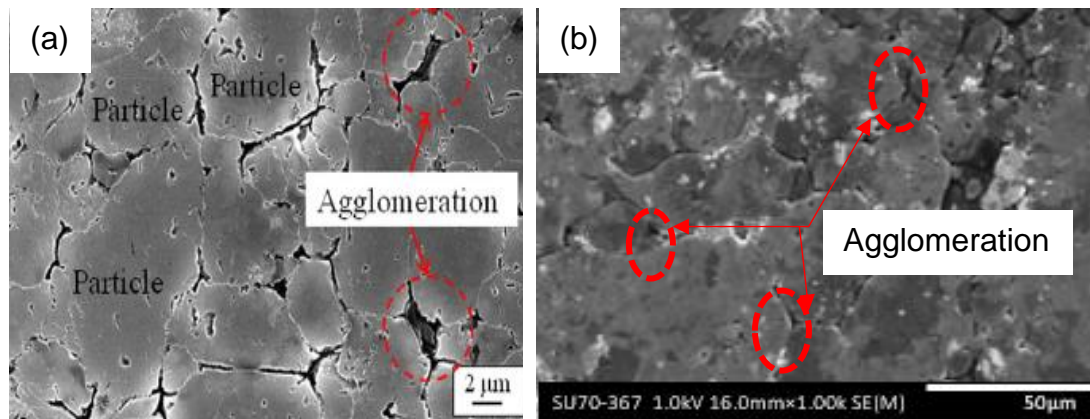


Figure 5.8: SEM images of composites showing agglomeration (a) 1wt% of GNP/Al [195] and (b) 0.2wt% of GO/Al in current research.

### 5.3.2 Morphologies of powders and GO/Al samples

Figure 5.9(a)-(d) shows the morphology of Al, 0.05wt% GO/Al, 0.01wt% GO/Al and 0.2wt% GO/Al powders after wet mixing process, GO sheets were observed on Al particles in GO/Al composite. However, the absorption of GO sheets on Al particles was rarely detected (shown in expanded view of highlighted boxes of Figure 5.9(b)-(d)) and were mostly placed with Al particles, an appropriate interface between GO and Al particles was not created. This was noted in accordance with Figure 5.1 in which GO was well dispersed in solution during wet mixing process. The effect of sintering temperatures on the grain growth and microstructures of GO/Al composites were demonstrated in Figure 5.10(a)-(f). The grain size of the 0.05wt% GO/Al composites sintered at 580°C and 600°C are shown in Figure 5.10(a) and (b), it was observed that the grain size increased with increase in temperature and grain sizes were estimated approximately as 33.8 and 34.6μm respectively. Although the grain size was less at 580°C, it has porous microstructure due to either insufficient sintering temperature or excess holding time. The monolithic Al samples have shown good metallurgical bonding in between particles. There was a good chemical bonding in between the GO and Al particles, further investigation on absorption of GO on to the Al matrix was done using EDXS analysis, given in section 5.3.3.

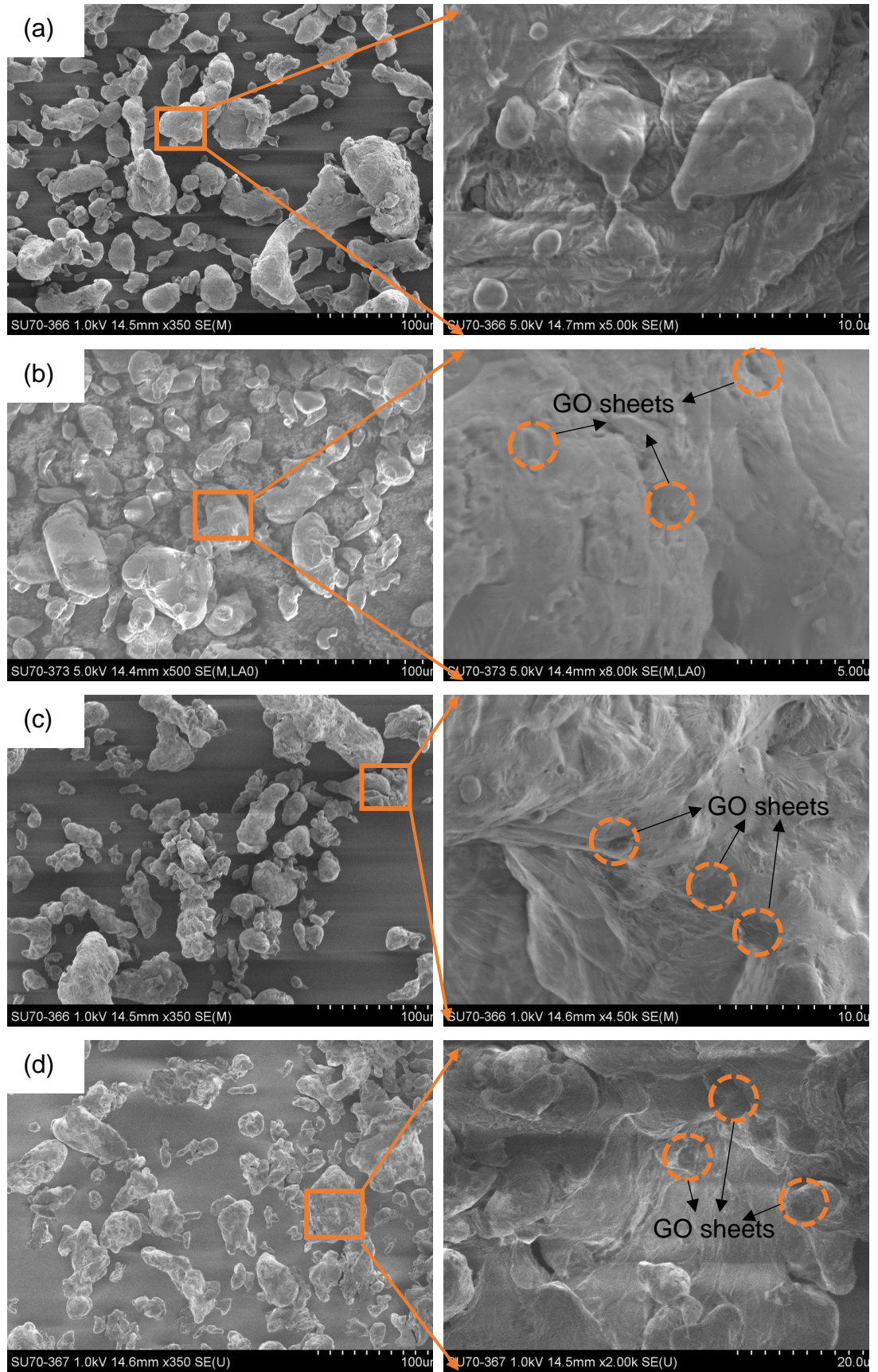


Figure 5.9: Particle morphology of (a) 35µm Al powder (b) 0.05wt% of GO/Al powder (c) 0.1wt% of GO/Al powder and (d) 0.2wt% of GO/Al powder.

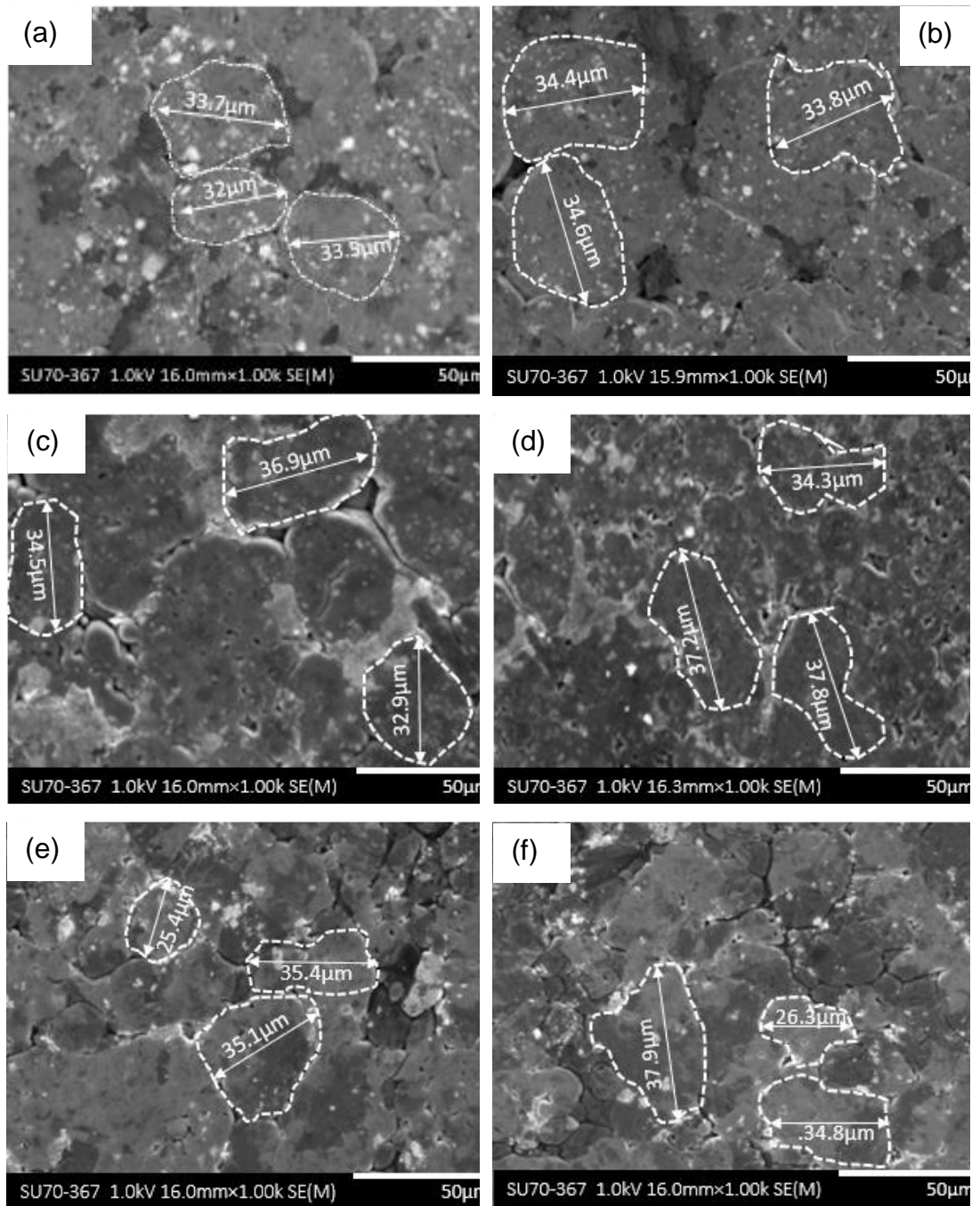


Figure 5.10: SEM images of surface of GO/Al composites: (a)-(b) 0.05wt%: (a) sintered at 580°C, (b) sintered at 600°C, (c)-(d) 0.1wt% : (c) sintered at 580°C, (d) sintered at 600°C, (e)-(f) 0.2wt%: (e) sintered at 580°C and (f) sintered at 600°C.

The microstructure of the GO/Al composites were effected by the sintering temperatures, i.e., at 580°C and 600°C. Higher sintering temperatures provides ease of diffusion of atoms and hence increasing the sinterability of the end composite [205]. However, the increase in wt% of GO reinforcement resulted in reduction of density of the Al composite as melting point of GO

particles is ~3600°C [206], has a very low tendency to melt at the temperatures used in current research and led to the weak network of GO and Al. The sintering process have also induced dimensional changes of particles due to shrinkage process. The resultant grain sizes GO/Al composites with increase in sintering temperature were shown in Figure 5.11(a)-(b) which fits well with the theory [205]. The increase in sinterability will inturn effect the mechanical properties of end composite.

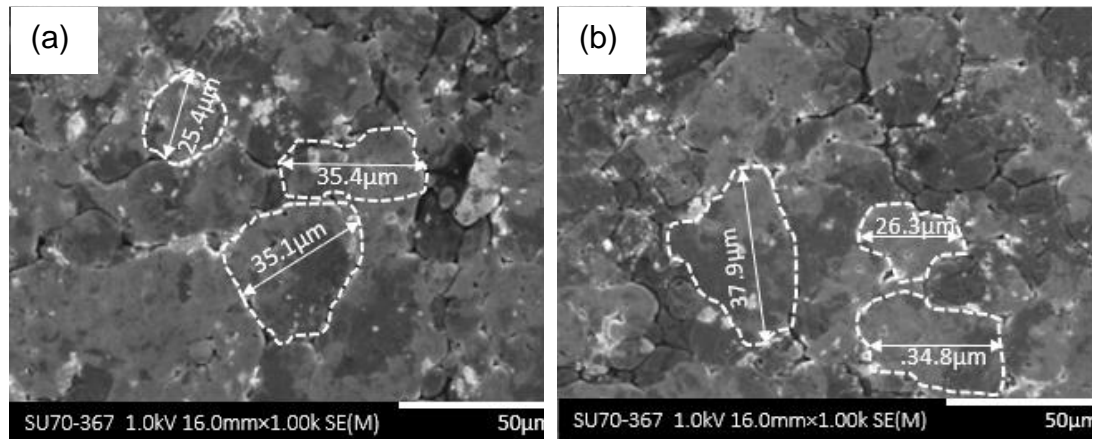


Figure 5.11: SEM images of 0.2wt% GO/Al composites showing grain size measurements (a) sintered at 580°C and (b) sintered at 600°C.

### 5.3.3 EDXS analysis of GO/Al powders and sintered samples

The EDXS analysis of GO/Al composite powders were shown in Figure 5.12(a)-(d) in which traces of oxygen were found in Al powder and some amount of oxygen together with carbon was noted in all GO/Al powders irrespective of the wt% of GO. The analysis was performed at three random locations and almost similar concentrations of elements were observed which implies to the better dispersion of GO on the Al particles. However, no other elements than the elements in the used materials i.e., carbon, Al and oxygen were found which implies to the contamination free powders. The EDXS images of GO/Al sintered composites were shown in Figure 5.13(a)-(d), it was noted that the elements that were observed at powder state still exists even after the sintering which implies to the efficient sintering process that proved to be successful as there was not contamination recorded. Further analysis of the crystalline phases of the GO/Al composites was done by using XRD, given in detail in section 5.3.4.

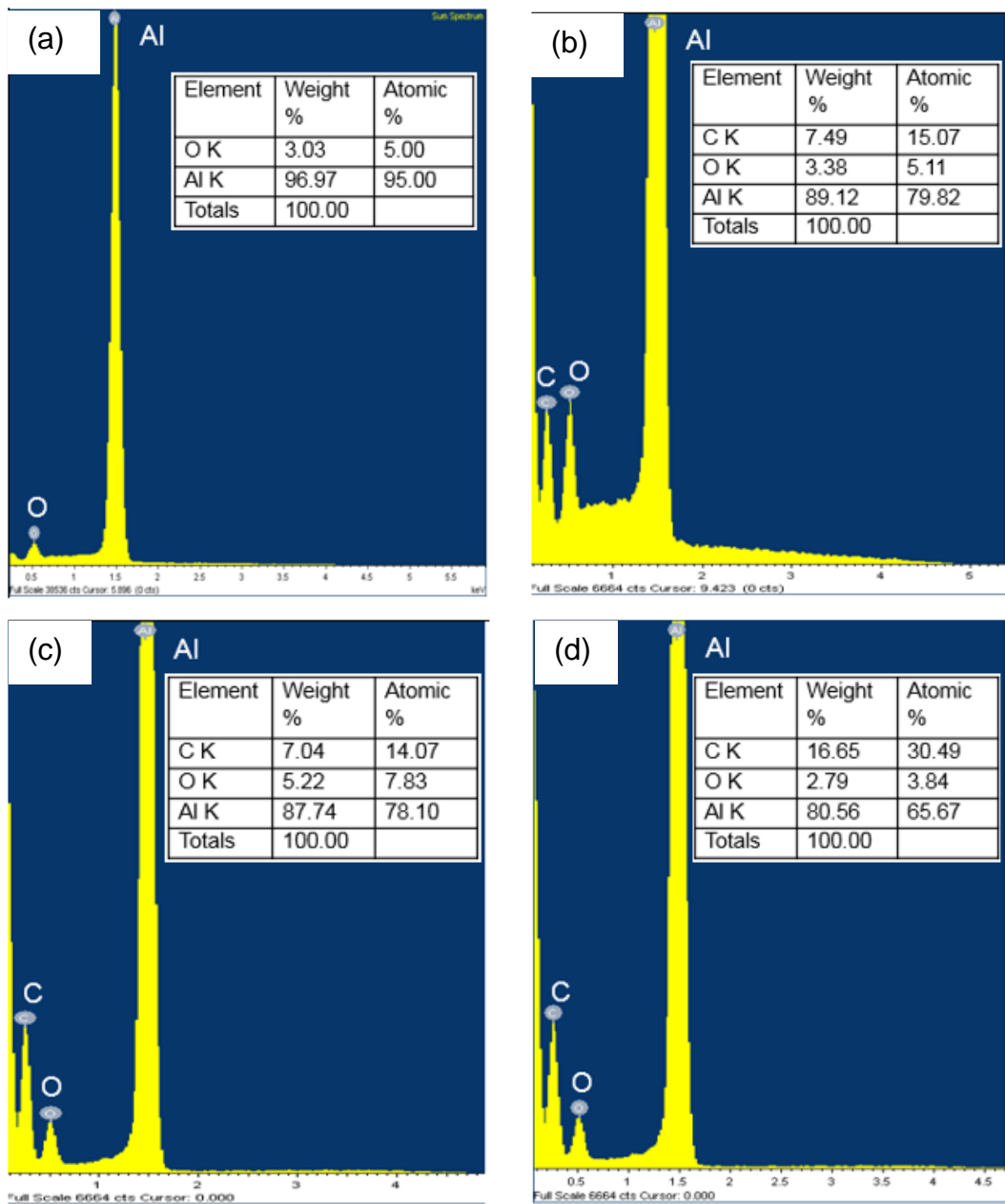


Figure 5.12: EDXS images of dried powders (a) pure Al, (b) 0.05wt% GO/Al, (c) 0.1wt% of GO/Al and (d) 0.2wt% of GO/Al.

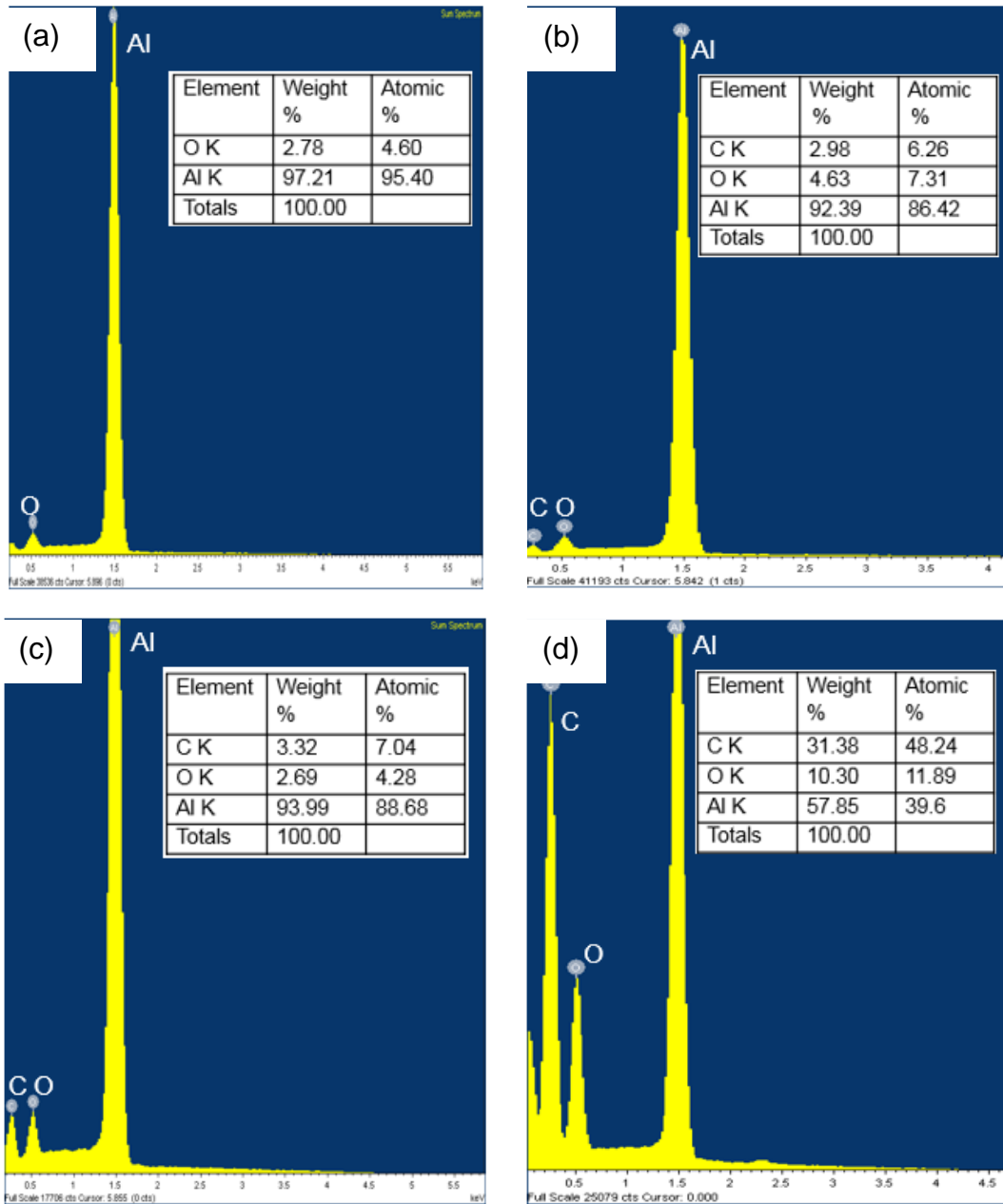


Figure 5.13: EDXS images of samples sintered at 600°C (a) pure Al, (b) 0.05wt% GO/Al, (c) 0.1wt% of GO/Al and (d) 0.2wt% of GO/Al.

The EDXS analysis have shown the carbon content for GO/Al composites compared to the monolithic Al samples both at powder state and after sintering. However, EDXS shows the high carbon content as the equipment is sensitive to lower mass elements. The EDXS analysis were performed by scanning the sample at random points for each sample. From the EDXS results (Figure 5.13(a)-(d)) it can be observed that the carbon content increases with increase in wt% of GO where as the oxygen content varied from composite to composite due to the level of oxidation occurred at each processing stage. The

parameters used in mixing of powders such as stirring speed, stirring time has effect on distribution of the elements which was reflected in EDXS spectra. By heating the samples to 600°C which is nearly 88% of the melting temperature of Al at which it has more propensity to react with carbon and contamination but the samples in current work have yielded the same elements as the elements recorded at powder state. From the conducted analysis the existence of elements like C, O and Al, the range of their compositions at both powder state and sintered state were discussed. It is worthwhile to note that the presence of elements highly depends on the purity of base materials, mixing conditions and provision of sintering atmospheres. The adverse effect of this contamination, formation of alien compounds and their effect on end products were reported in previous works [182].

#### **5.3.4 XRD analysis of GO/Al composites**

The structural changes and crystalline phases of GO/Al composites were evaluated and shown in Figure 5.14. The phases were evaluated based on Bragg's law and  $2\theta$  values. GO/Al composites sintered at 580°C and 600°C resulted in same phases, i.e., Al (111) at 38.6°, Al (222) at 82.7°, and have displayed the presence of Al<sub>2</sub>O<sub>3</sub>. The calculation of crystallite sizes from XRD data on this occasion was not possible due to the limitation of peak broadening. The process of diffusing carbon into Al grains haven't resulted in significant amount of residual stresses in GO/Al composites as there was no evidence of angular shift of GO/Al composites compared to monolithic Al samples. In comparison, the peaks of both monolithic Al and GO/Al samples sintered at 580°C were at Bragg angle of  $\sim 0.1^\circ$  more than the peaks observed for monolithic Al and GO/Al samples sintered at 600°C, this implies to that the residual stress of the samples were revealed with increase in sintering temperature. However, the information regarding graphene was not obtained from the XRD analysis as it was reported in literature that both graphite and rGO display peaks at 24° [207] and thus micro Raman analysis of GO/Al samples was performed and reported in section 5.3.5.

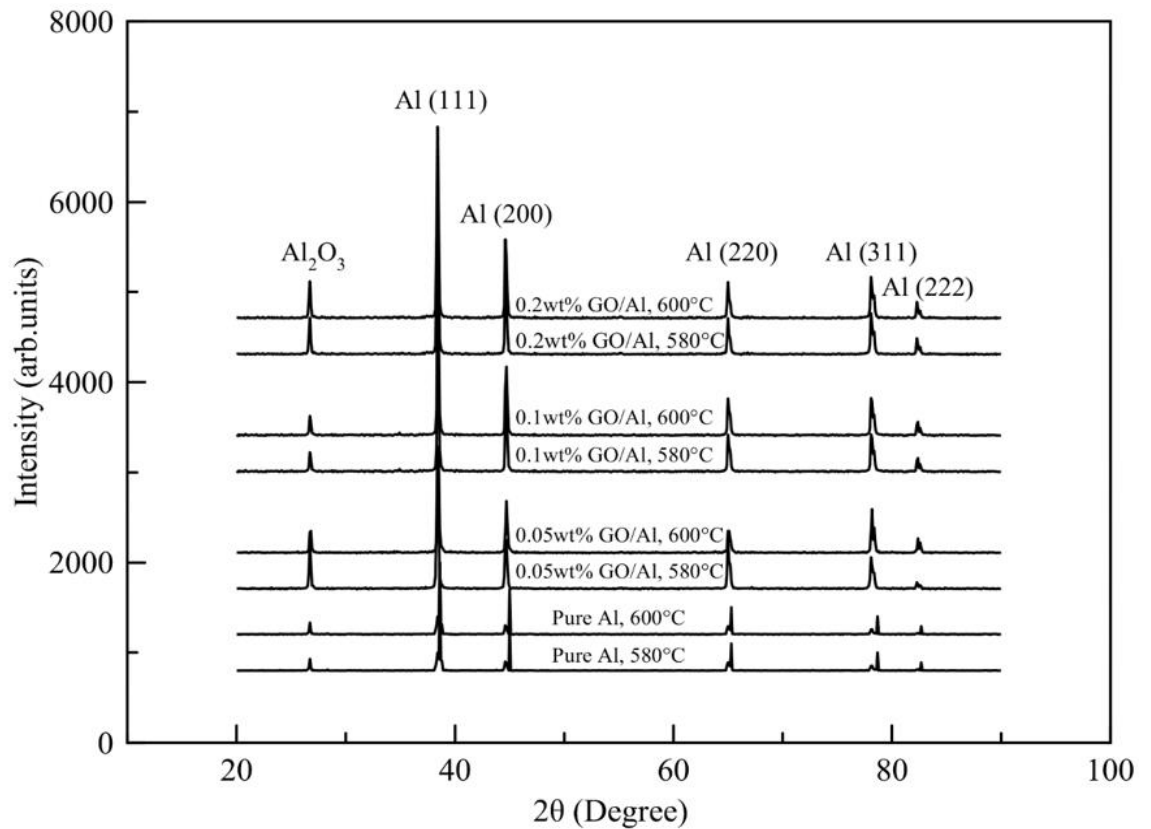


Figure 5.14: XRD spectra of monolithic and 0.05wt%, 0.1wt% and 0.2wt% GO/Al composites sintered at 580°C and 600°C.

The peak deflection analysis of the GO/Al samples were conducted between 20° and 90° Bragg's angle and was enough to investigate the crystalline phases and peak broadening of composites. The addition of graphene content Al matrix resulted in a peak shift to a higher angle [19]. The sharp and strong peaks obtained in current research reflects to the well-crystalline nature of Al, the peak intensities reduction was a result of reduction in phase crystallinity. The process parameters such as sintering temperature and content of GO which has attributed the formation of intense Al<sub>2</sub>O<sub>3</sub> peaks. The typical peaks of Al, Al<sub>2</sub>O<sub>3</sub> were seen in all the samples including monolithic Al and GO/Al samples, while any peak corresponding to the graphene particles were not detected expect minor intense peak in 0.2wt% GO/Al composite [208]. The similar peaks were reported in GNP reinforced Al composites processed by powder metallurgical route associated with ball milled powder [188] and these peaks were also reported with ceramic matrix composites [209,210]. One possible reason for lack of detection might be sensitivity of equipment (detection limit) which couldn't detect the presence of graphene particles in

composites containing 0.05wt% and 0.1wt% GO and this was also observed by Bastwros et al. [211] and Rashad et al. [205]. It was also noted that peaks corresponding to the  $Al_4C_3$  were not observed in GO/Al composites produced in current research [212]. The reason might be either lack of reaction between Al and GO or the quantity of  $Al_4C_3$ . The formation of micro sized grains have attributed to the intensities of peaks observed in GO/Al composites. Minor broadening effect was observed on some composites due to increase in grain boundaries and sub-grain formations. The increase would reduce mechanical and corrosion resistance of Al matrix material reinforced with nano reinforcements [189].

Sintering temperature from 580°C to 600°C have resulted in reduction of diffraction angle (diffraction shift) which was due to the removal of linear defects and related internal stresses and resulted in removal of porous regions. The high temperatures of annealing i.e., at 600°C can cause formation of oxide layers on metal surface, i.e., formation of  $Al_2O_3$ , inert gas atmosphere was used to avoid this. However,  $Al_2O_3$  was observed in all GO/Al composite samples which was due to the oxidation of Al particles at powder state, this was evident from Figure 5.12(a). The findings from XRD analysis were in well agreement with the evaluation of phases reported in literature [20,182,188]. In this way, the novel composites with better properties can be developed by liquid infiltration methods and powder metallurgy without the formation of  $Al_4C_3$  [22].

### **5.3.5 Micro Raman analysis of GO/Al composites**

Raman spectroscopy was employed in current research to investigate the evolution of structure of graphene i.e., defects, layer formation during processing of composites. The Raman spectroscopy of the bulk GO/Al composites sintered at 600°C are shown in Figure 5.15(a)-(c) and the corresponding Raman data is given in Table 5.2(a)-(c). Three major peaks of D-band, G-band and 2D-band were recorded after sintering. The ratio of intensities  $I_D/I_G$  that were obtained from spectroscopic data were used to investigate the disorderliness and defect densities of graphene. Figure 5.15(a) shows the Raman spectra of 0.05wt% GO/Al composite at three random locations it can be noted from the spectra that the G-band was recorded at

approximately  $1604\text{cm}^{-1}$ . The ratio of intensities varies from location to location which implies to the need for improvement in dispersion of GO in composite and similar trends were observed from 0.1wt% GO/Al shown in Figure 5.15(b) and 0.2wt% GO/Al shown in Figure 5.15(c). From the spectral data, the ratio of  $I_D/I_G$  decreases from 0.05wt% to 0.1wt% but increased from 0.1wt% to 0.2wt% due to increase in physical force applied on particles with increase in stirring time, this has contributed to the increase in defects and disorderness in graphene. It was proposed in the literature that the number of graphene layers increase with increase in intensities ratio of  $I_G/I_{2D}$ . In present research work, the  $I_G/I_{2D}$  ratio increases from 0.69(GO) to 0.89(0.2wt% GO/Al) due to the increased agglomeration. The G-band peak positions were evaluated to investigate stresses experienced by GO/Al composites.

In the present research, the wavenumber of GO/Al is more than the as received GO due to increase in residual compressive stress with reduction in interatomic distances in graphene. The Raman spectra of GO/Al composites with various wt% of GO reinforcement, sintered at  $580^\circ\text{C}$  and  $600^\circ\text{C}$  is shown in Figure 5.16, the peaks were altered with variation in sintering temperature. It can be noted that the defects and disorderness of the GO/Al composites reduced with increase in sintering temperature.

The Raman spectra are highly related to quality of samples, all the  $\text{sp}^2$  hybridised samples investigated under Raman will exhibit strong peaks in the range of  $2500\text{-}2800\text{cm}^{-1}$ . The G-band combined with this strong peak is the signature of  $\text{sp}^2$  graphitic materials and was recognised as 2D (G) band. D-peak in the spectra was usually caused by disordered structure of graphene and led to the resonance in Raman spectra. The first order G-band and D-band were raised due to vibrations from  $\text{sp}^2$  carbons [213]. Since, the G-band peaks of higher frequencies were recorded in all the GO/Al composites in current research, GO was not reduced to rGO during sintering process [214]. As mentioned earlier, the D-band intensity was an indication of degree of disorderness, this can be theoretically reduced by successful reduction of GO. In current research work, the D-band intensity increased due to increase in structural defects and lack of reduction. The higher intensities of D-band and G-band ( $I_D/I_G$ ) indicates the increase in number of defects and disorderness in GO sheets caused by processing techniques used in current study i.e., wet

mixing. These defects were raised due to the disruptions of functional groups of GO surfaces and the binding sites after processing of composites which led to disordering in carbon lattice [215]. It is well known that the 2D-band position was highly dependent on graphene layers, tensile and compressive strains [216]. From the  $I_G/I_{2D}$  ratios and the wavelengths recorded in current research that the GO reinforcement in Al matrix resulted in formation of many number of layers because of agglomeration of GO particles. However, the peak recorded at  $1899\text{cm}^{-1}$  in the Raman spectra referred to the stretching vibration of C=C bond [217]. The increase in number of GO layers attributed to reduction in mechanical strength due to dislocation of layers upon application of load.

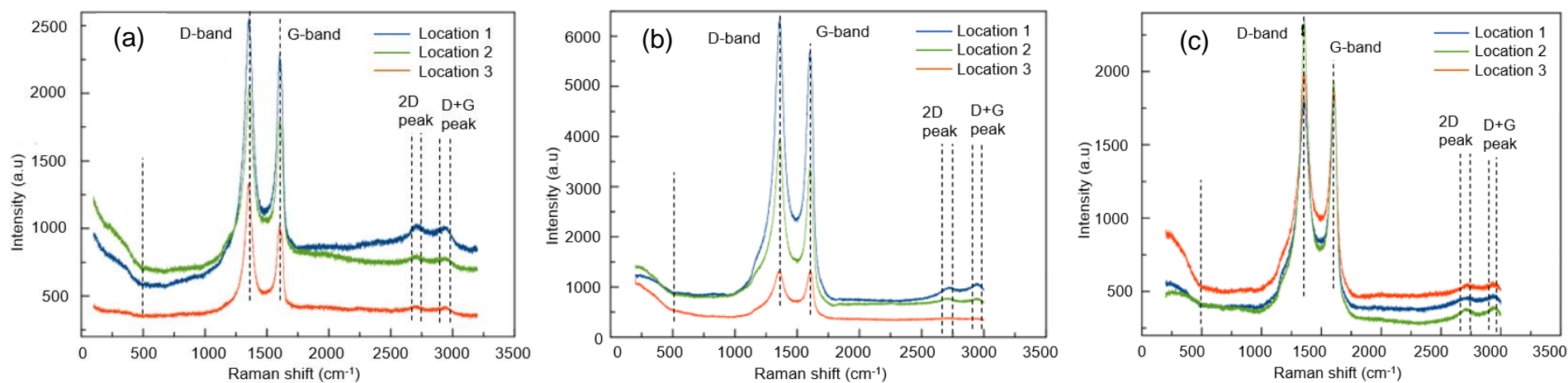


Figure 5.15: Recorded micro Raman for GO/Al composites (a) 0.05wt%, (b) 0.1wt% and (c) 0.2wt%.

Table 5.2: Raman data of the GO/Al composite at random locations (a) 0.05wt%, (b) 0.1wt% and (c) 0.2wt%.

Material	$I_D/I_G$	$I_G/I_{2D}$	$\omega_G$ (cm <sup>-1</sup> )
Pristine GO	1.07	0.69	1507.7
Location 1	1.147	0.72	1606.07
Location 2	1.311	0.7	1598.92
Location 3	1.137	0.69	1600.23

(a)

Material	$I_D/I_G$	$I_G/I_{2D}$	$\omega_G$ (cm <sup>-1</sup> )
Pristine GO	1.07	0.69	1507.7
Location 1	1.105	0.78	1604.23
Location 2	1.004	0.74	1604.49
Location 3	1.184	0.76	1608.72

(b)

Material	$I_D/I_G$	$I_G/I_{2D}$	$\omega_G$ (cm <sup>-1</sup> )
Pristine GO	1.07	0.69	1507.7
Location 1	1.006	0.82	1606.87
Location 2	1.087	0.89	1606.08
Location 3	1.211	0.869	1605.02

(c)

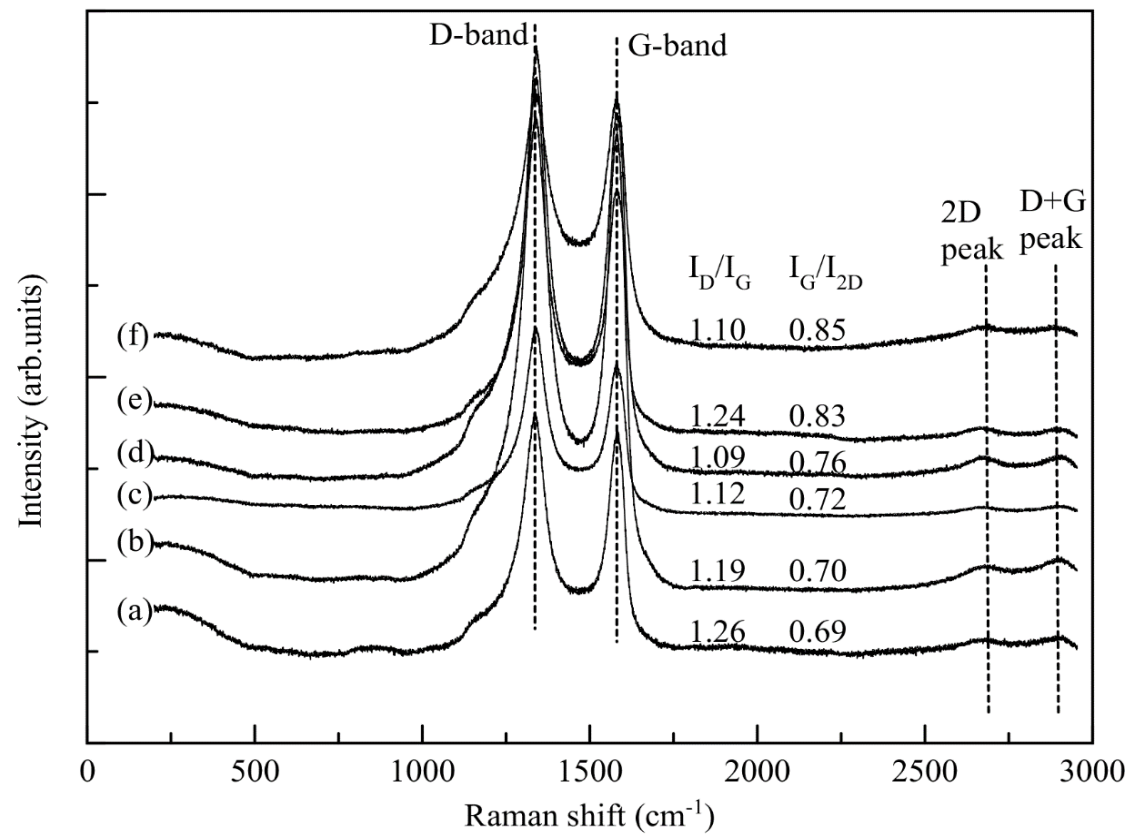


Figure 5.16: Raman spectra of composites (a)-(c) sintered at 580°C, (d)-(f) sintered at 600°C: (a) 0.05wt% GO/Al, (b) 0.1wt% GO/Al, (c) 0.2wt% GO/Al, (d) 0.05wt% GO/Al, (e) 0.1wt% GO/Al and (f) 0.2wt% GO/Al.

### **5.3.6 Micro Vickers hardness of GO/Al composites**

The micro Vickers hardness (VHN) of GO/Al composites at various wt% of reinforcement, sintered at 580°C and 600°C was shown in Figure 5.17(a)-(b). It was observed that the hardness of GO/Al composites increases with increase in sintering temperature. This was observed due to the existence of more refined grain structures and better chemical bonding between GO and Al particles which facilitated the enhancement in hardness. The hardness of the composites increases with increase in wt% of the reinforcement which is in line with the results from literature and in-conjunction with rule of mixtures (ROM) for composite. It can be noted that the hardness of composites increases with increase in processing conditions of sintering temperature and wt% of GO. Approximately 35% of increment over the pure Al was noted for 0.2wt% of GO/Al composite sintered at 600°C.

The SEM images showing microstructure of the GO reinforced Al composite samples suggested that the wetting in between GO, and Al particles was not perfect enough. Hence, the solid-state sintering mechanism was less effective and did not display 100% densification. It was worthwhile to note that in spite of less densification, GO/Al composites displayed superior hardness properties. This can be attributed to the development of effective interface and better bonding between GO and Al particles. The improvement in hardness of GO/Al composites provide high restraining force to deform during the indentation process [181] and furthermore densification of material during sintering contributed to the better properties. It was also noted from the results that the densification of GO/Al composites reduced with increase in wt% of GO where as the Vickers hardness was increasing, which was due to the dominant effect of reinforcement on resistance to indentation which proved to be better than results obtained by Gürüz et al. [187] where hardness reduced with increase in graphene addition.

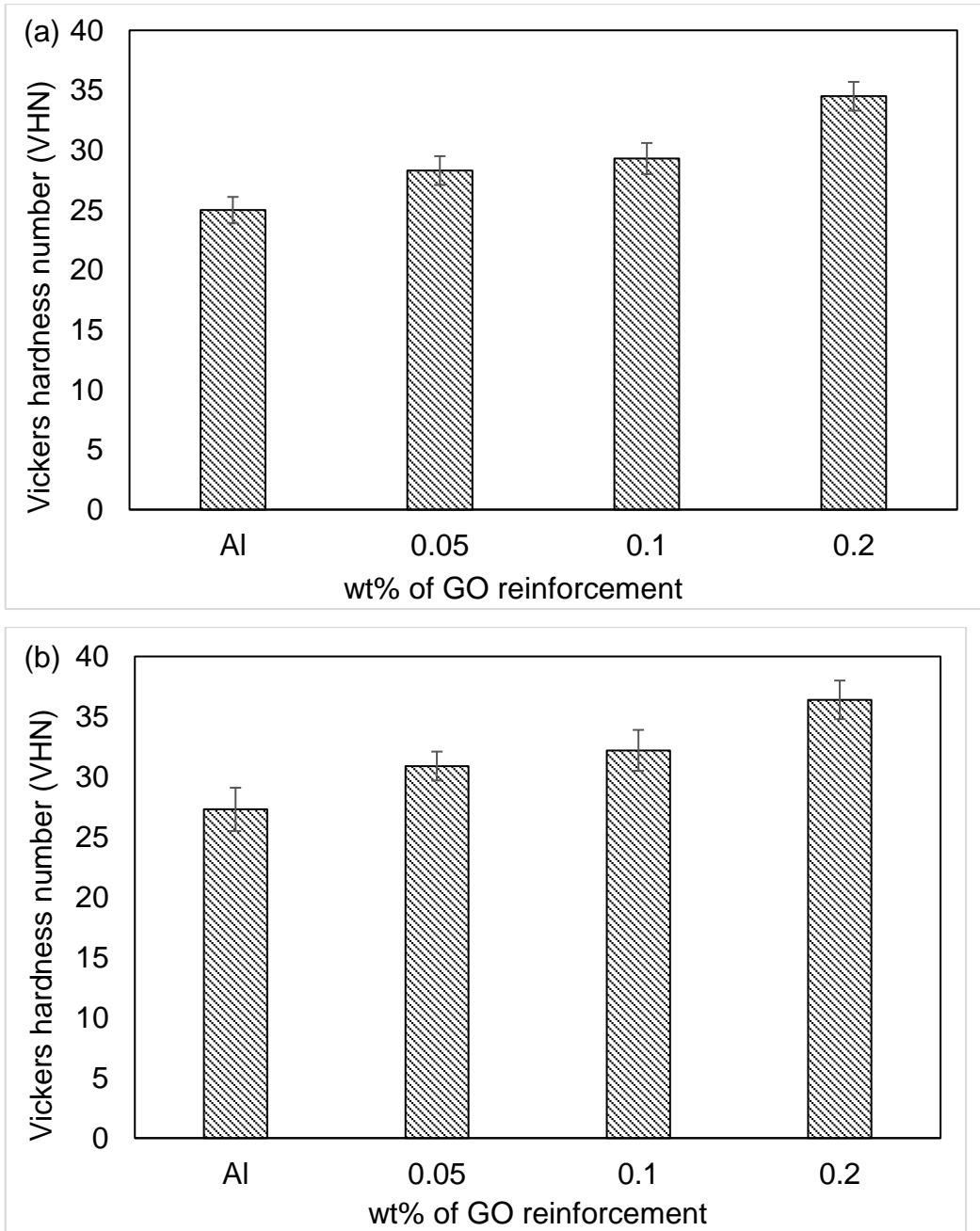


Figure 5.17: Vickers hardness of pure Al and GO/Al composite samples (a) sintered at 580°C and (b) sintered at 600°C; n=3, 95% confidence.

### 5.3.7 Indentation tests of GO/Al composites

The indentation compression load of 5kN was applied centrally on the specimens of pure Al, 0.05wt%, 0.1wt% and 0.2wt% of GO reinforced composites compacted at various pressures and sintered at various temperatures. The fracture surfaces of GO/Al composites sintered at 580°C were shown in Figure 5.18. It can be noted from visual inspection that the pure Al samples at all compaction pressures used in current research resulted in ductile failure. The GO reinforcement on Al lead to the brittle failure of composite materials. The fracture surfaces of the composites compacted at 500MPa, 540MPa and 580MPa and sintered at 600°C at various wt% of GO reinforcement were shown in Figure 5.19.

Material	P <sub>c</sub> - 500MPa	P <sub>c</sub> - 540MPa	P <sub>c</sub> - 580MPa	Type of failure
Pure Al				Ductile
0.05wt% GO/Al				Ductile-shear
0.1wt% GO/Al				Brittle
0.2wt% GO/Al				Brittle

Figure 5.18: Fracture surfaces of pure Al, 0.05wt%, 0.1wt% and 0.2wt% of GO/Al composites compacted at various pressures and sintered at 580°C.

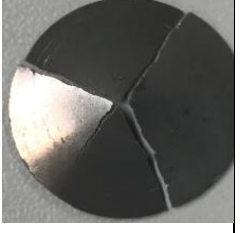
Material	$P_c$ - 500MPa	$P_c$ - 540MPa	$P_c$ - 580MPa	Type of failure
Pure Al				Ductile
0.05wt% GO/Al				Ductile-shear
0.1wt% GO/Al				Brittle
0.2wt% GO/Al				Brittle

Figure 5.19: Fracture surfaces of pure Al, 0.05wt%, 0.1wt% and 0.2wt% of composites compacted at various pressures and sintered at 600°C.

It was observed that the increase in sintering temperature doesn't effect the failure pattern whereas the increase in wt% of GO reinforcement led to more brittleness. From Figures 5.18 and 5.19, it can be observed that the fracture surfaces of pure Al specimen were in semi-spherical shape that indicates necking. This fracture can be identified as ductile-shear fracture. The specimens have experienced breaking without any plastic deformation or necking, due to porosity. The stress developed in the material in both radial and tangential directions was calculated using equations 4.8-4.10, shown in Figure 5.20(a)-(b). From the graphs, it can be noted that the tangential stresses were higher than radial stress.

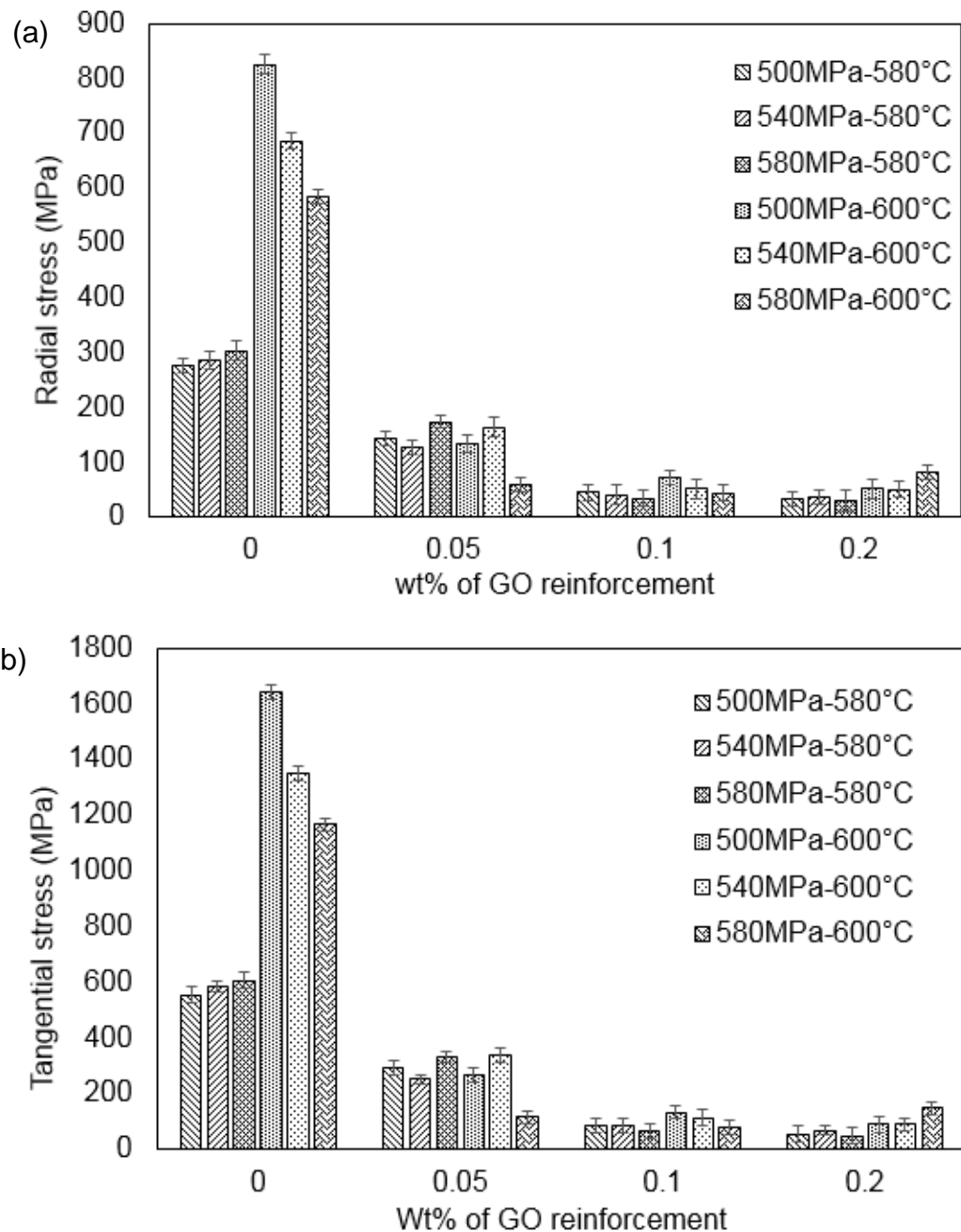


Figure 5.20: Variation of stress developed in the specimens under loading with wt% of GO reinforcement, compaction pressures and sintering temperatures (a) radial stress and (b) tangential stress; n=3, 95% confidence.

The increase in sintering temperature have shown a significant effect on stress in Al specimens and doesn't show much variation of stress for GO/Al composites. It was noted that at 580°C of sintering temperature with increase in compaction pressure, the tangential stress and radial stress increased upto 0.05wt% GO/Al and started decreasing whereas at 600°C sintering

temperature with increase in compaction pressure, the tangential and radial stress decrease with increase in wt% of GO reinforcement. The 0.2wt% GO/Al composites showed lowest strength due to agglomeration and formation of graphene layers.

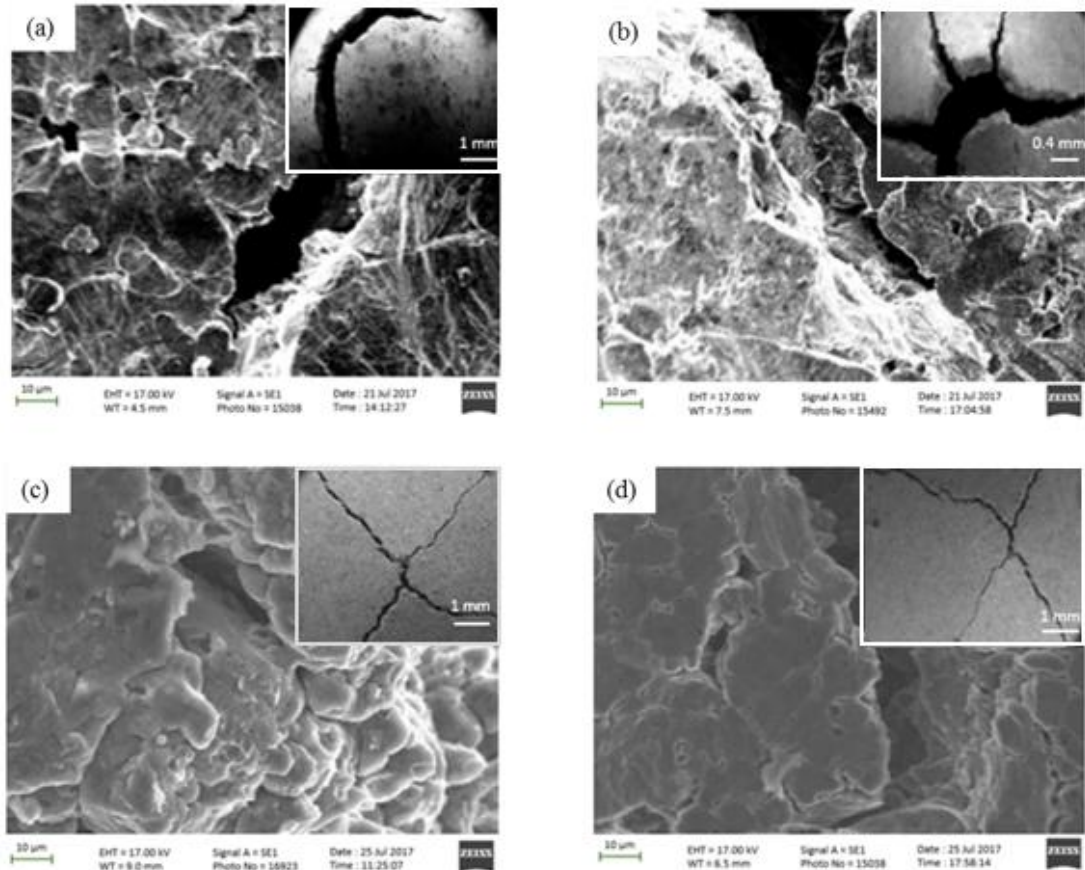


Figure 5.21: SEM images of fracture morphology on cross sections of crack zones of composites compacted at 580 MPa and sintered at 600°C (a) pure Al, (b) 0.05wt% GO/Al, (c) 0.1wt% GO/Al and (d) 0.2wt% GO/Al.

The fracture morphology of composite pellets was studied using SEM, shown in Figure 5.21(a)-(d). Semi-spherical areas were observed for Al specimens, shown in Figure 5.21(a), it can be noted that the sample have undergone ductile failure with necking and no strain hardening. Whereas the un-melted particles in 0.05wt% GO/Al composites prompted nucleation of porosity and led to propagation of crack, shown in Figure 5.21(b), similar pattern was observed in all GO/Al composites irrespective of processing conditions. More porous sites were observed with increase in wt% of GO reinforcement and led to the cracks as these structures have more stress concentration and hence brittle behaviour, shown in Figure 5.21(c) and 5.21(d).The strength of the

composite can be attributed to the three aspects: grain refinement, stress transfer and dislocation strengthening. As the solid-state sintering was employed in current research the effect of grain refinement on current composites was negligible. Hence dislocation strengthening and stress transfer plays key role in strength of composites produced in current research. The stress transfer between the Al and GO particles depends on quality of interfacial bonding and there was no evidence of  $Al_4C_3$  phase. The interfacial bonding between the GO and Al particles have provided an efficient stress transfer in between them whereas the mismatch of thermal expansion coefficients between Al and GO led to the dislocations and the hard GO obstruct the movement of dislocations, led to increase in dislocation density and hence facilitating dislocation strengthening. However, the strengthening mechanisms observed in current study were dominated by the formation of number of GO layers which led to the delamination of layers due to weak network in between layers and hence reducing the strength of the GO/Al composites.

## **5.4 Modelling of GO/Al composites**

### ***5.4.1 Effect of GO addition on stress distribution of GO/Al composites***

The stress profiles of GO reinforced Al composites were simulated with the model as described in section 4.5 with input parameters as mentioned in Table 4.7. From Figure 5.22 it can be noted that the stress is distributed along the Al particles without obstruction, this is due existence of rigid elements between the Al particles that acted as perfect bond in between the particles. Figure 5.23(a) shows the stress profile of GO/Al composites with 5GO layers covering/reinforcing each Al particle from which it can be noted that the maximum stress developed in Al particles reinforced with GO layers is more compared to the maximum stress developed in the model with only Al particles. Since the GO reinforcement on Al particles has a load bearing capacity of 100% which means it can bear the maximum load protecting the Al particles from loading which follows Rule of mixtures (ROM) which states that the strength of the material increases with addition of reinforcement phase to the matrix phase (base material). Figure 5.23(b) shows the stress developed in Al particles in GO/Al particles which is less than the overall stress developed in

GO/Al composite. This is due to the load bearing capacity of the GO reinforcement covering the Al particles. The maximum stress values with and without GO reinforcement are consolidated in Table 5.3.

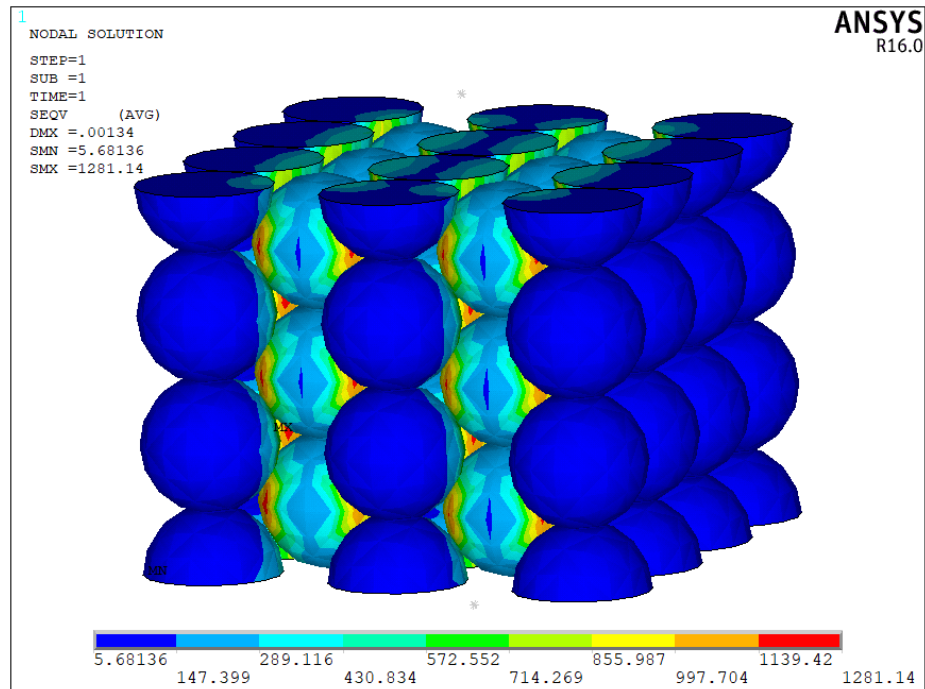
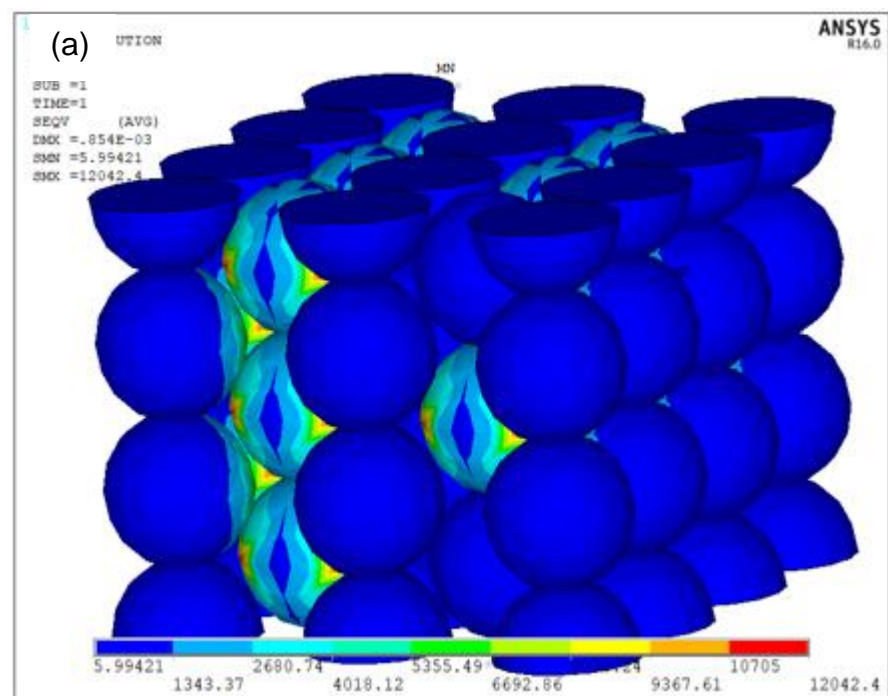


Figure 5.22: Stress profile of FE model containing only Al particles.



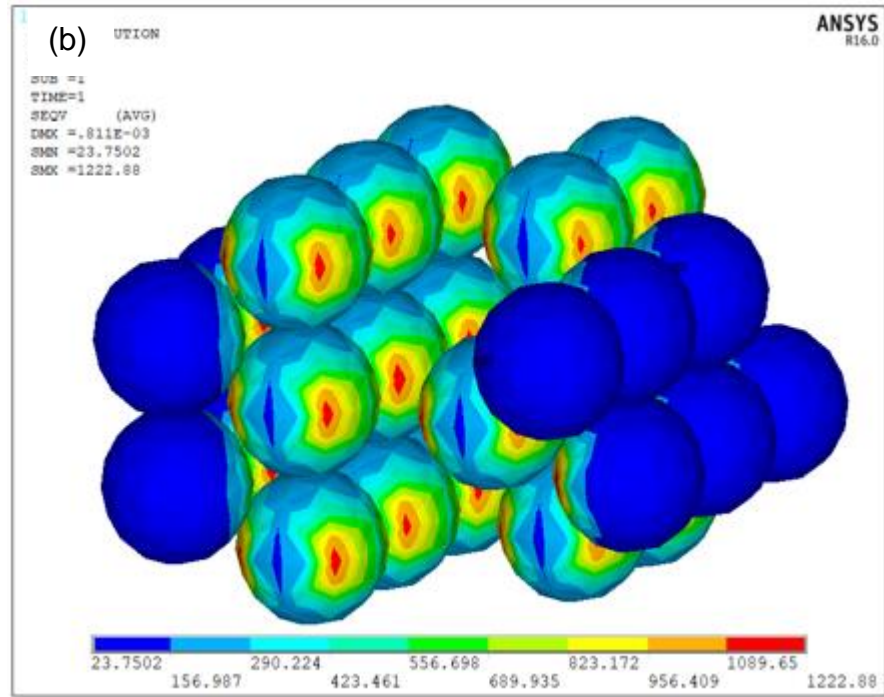


Figure 5.23: Stress profile of GO/Al composite with 5GO layers (a) stress profile of overall composite and (b) stress profile in respective Al particles.

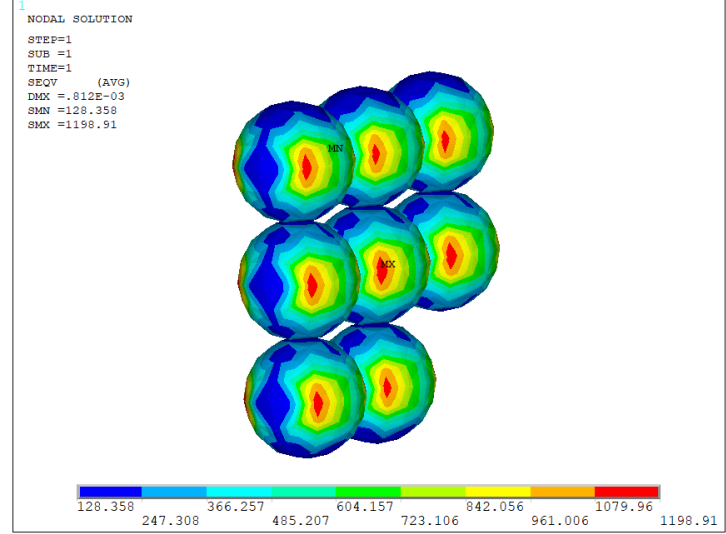
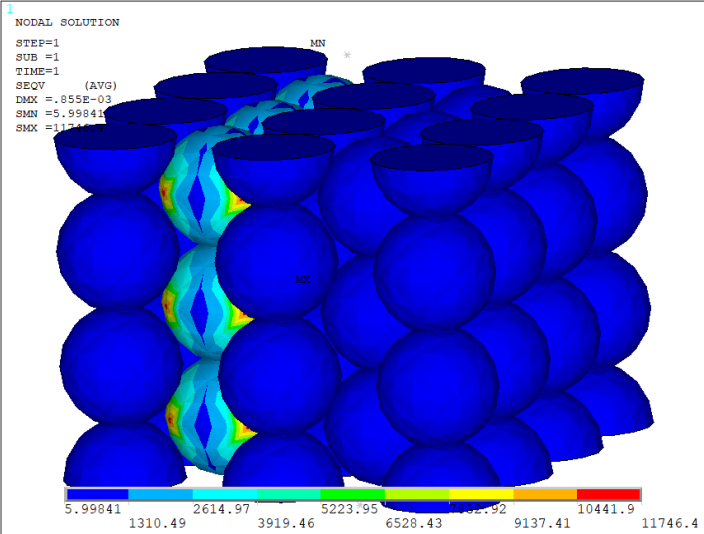
Table 5.3: Comparison of maximum stress in FE models with and without GO layers on Al particles.

FE model details		Stress (MPa)
Al sphere	No layer	1281.14
Al sphere	5 Layers	1222.88
GO coating		12042.40

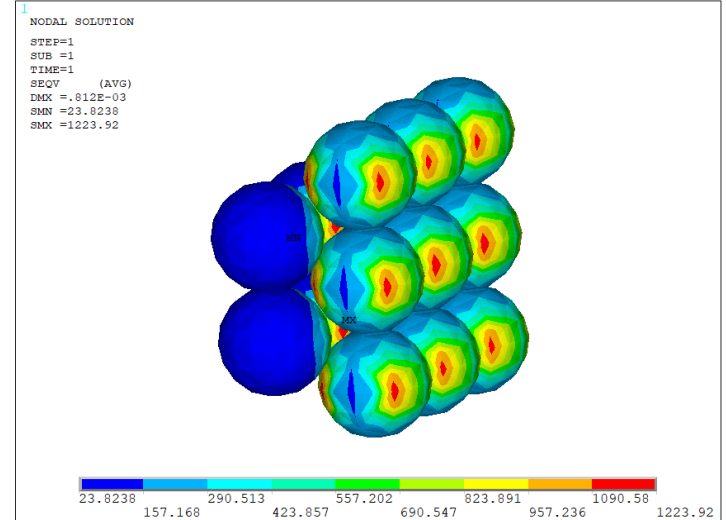
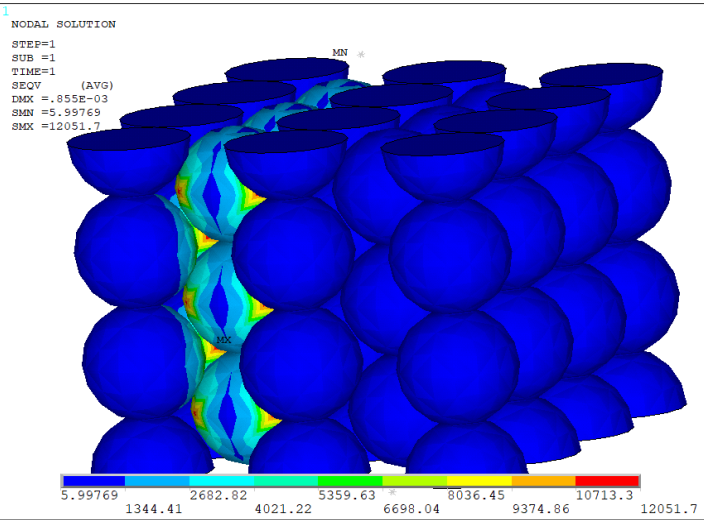
The effect of distribution of GO on to the Al particles was also investigated by varying % of Al particles coated with GO, in current simulations four scenarios of percentage of GO distribution were presented i.e., 5%, 15%, 25% and 50% of the Al particles in the GO/Al composite were coated with GO. The corresponding stress profiles were shown in Figure 5.24 and the comparison of maximum stress values was shown in Figure 5.25. It can be noted that the strength of the composite varied with distribution of GO, negligible variation in stress values noted in between 5% and 15% of GO distribution whereas the stress values varied notably from 15% to 25% (3% variation).

% of Al particles coated with GO	Stress in GO/Al composite	Respective stress in Al particles
5%	<pre> 1 NODAL SOLUTION STEP=1 SUB =1 TIME=1 SEQV (AVG) DMX =.855E-03 SMN =6.00131 SMX =11748.8           </pre>	<pre> 1 NODAL SOLUTION STEP=1 SUB =1 TIME=1 SEQV (AVG) DMX =.812E-03 SMN =128.405 SMX =1199.15           </pre>

15%



25%



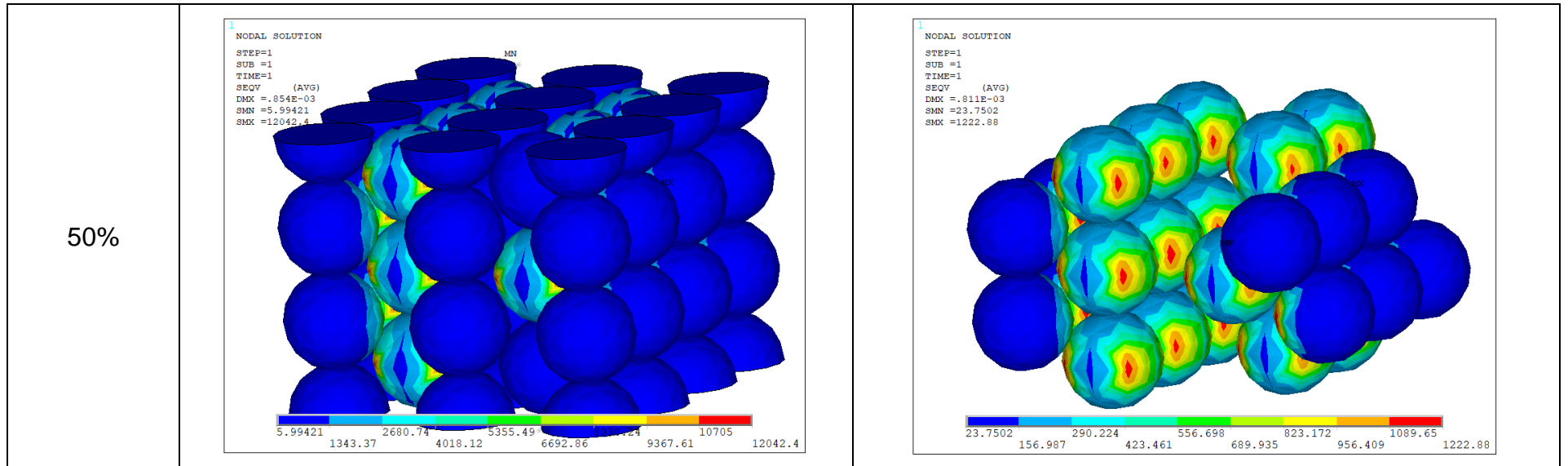


Figure 5.24: Stress profiles of GO/Al composites and their corresponding Al particles with respect to the % of Al particles coated with 5 GO layers.

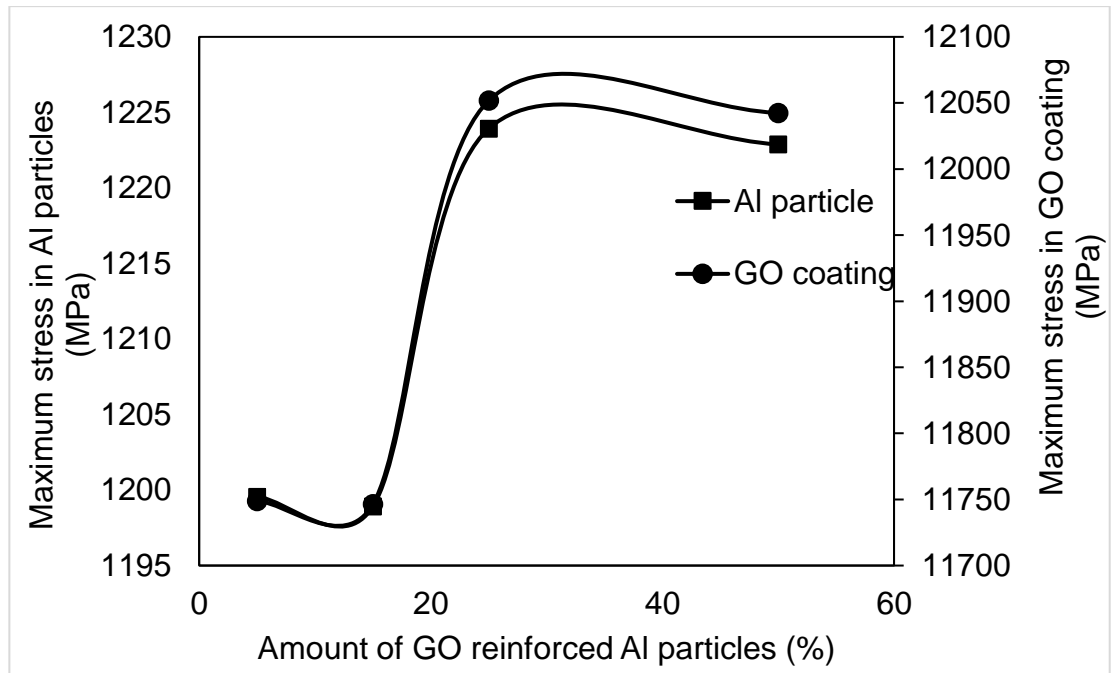
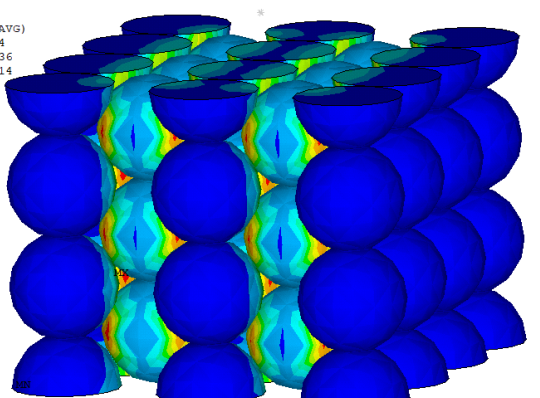
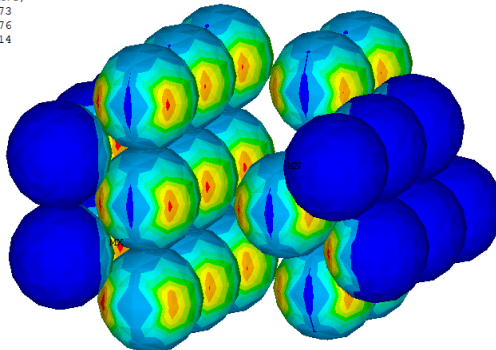


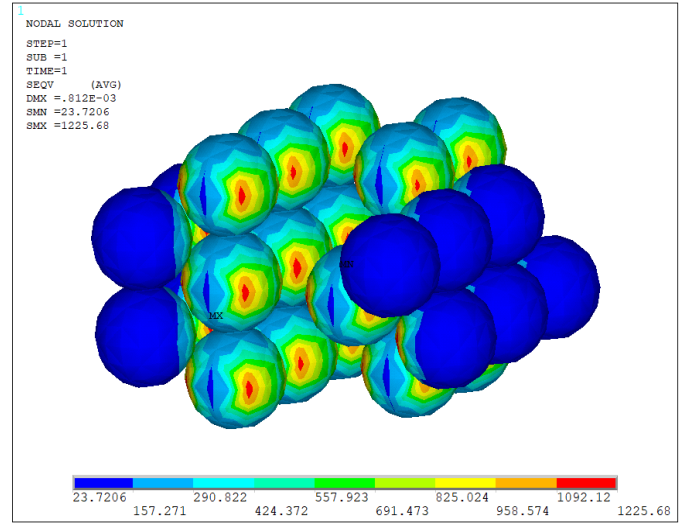
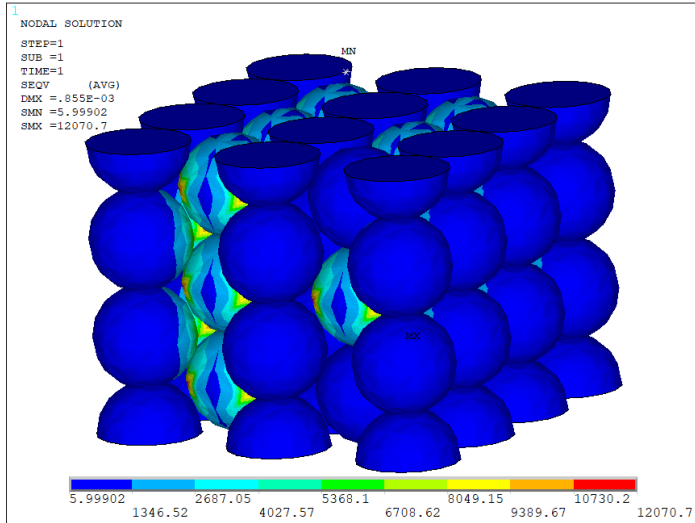
Figure 5.25: Comparison of maximum stress in models with 5GO layers on Al particles with respect to the % of Al particles coated by GO.

#### 5.4.2 Effect of GO layers on stress distribution

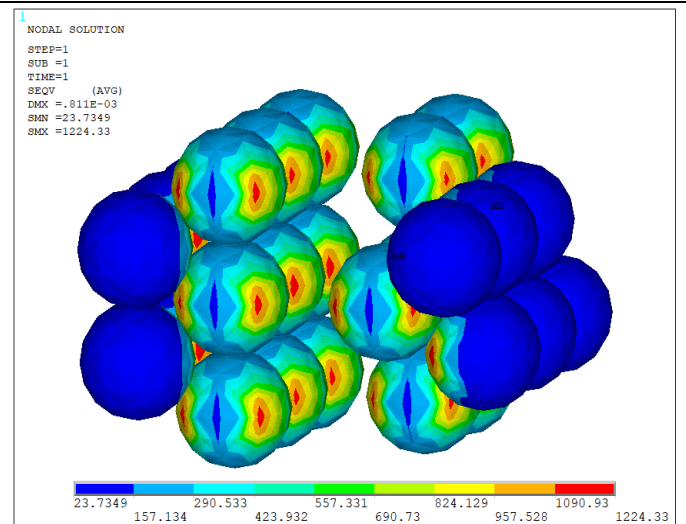
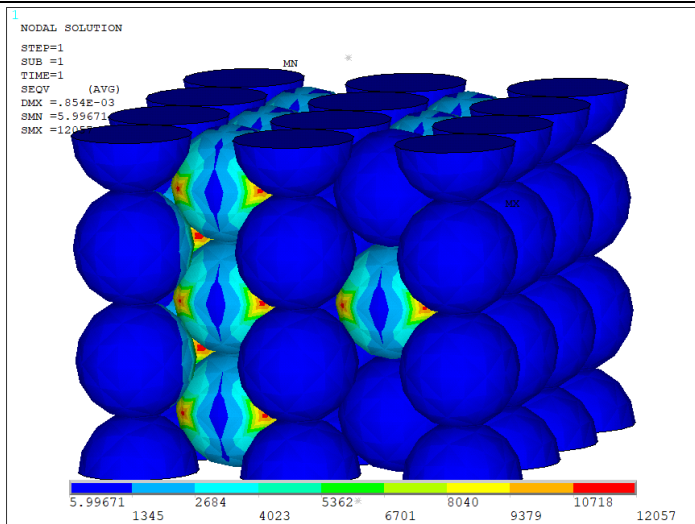
The effect of addition of GO reinforcement to the Al particles is indirectly analysed experimentally through micro Raman analysis that provides the information regarding the existence of number of layers of GO on the Al particles. This information was used as one of the processing condition for the simulation of GO/Al composites. Figure 5.26 shows the stress profiles of GO/Al composites with respect to the existence of number of GO layers and stress profiles in corresponding Al particles. It can be noted from the profiles that the GO addition to the Al particles improved the strength of the composite compared to pristine Al. It can also be noted that, the increase in number of layers haven't effected the stress distribution pattern however changes in the stress values were noted. The maximum stress values obtained for each processing condition with respect to the stress in GO coating and Al particle were consolidated in Figure 5.27. It can be noted that with increase in number of GO layers the stress experience by the Al particles reduced whereas the stress experience by the GO coating increased. When the GO layers increased more than 2 layers the stress experienced by GO layers started to decrease which might be due to the delamination effect.

FE model details	Stress in GO/Al composite	Stress in Al particles
No layer of GO	<p>NODAL SOLUTION  STEP=1  SUB =1  TIME=1  SEQV (AVG)  DMX =.00134  SMN =5.68136  SMX =1281.14</p>  <p>ANSYS R16.0</p>	<p>NODAL SOLUTION  STEP=1  SUB =1  TIME=1  SEQV (AVG)  DMX =.001273  SMN =23.6676  SMX =1281.14</p>  <p>ANSYS R16.0</p>

Single layer



Three layers



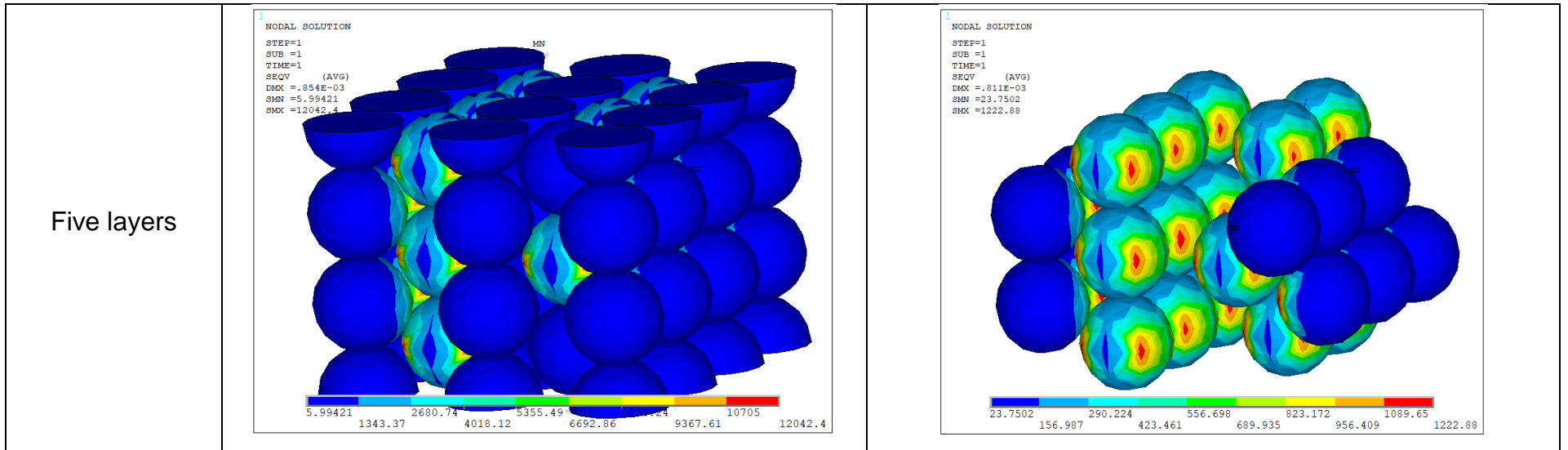


Figure 5.26: Stress profiles of GO/Al composites with respect to the number of GO layers.

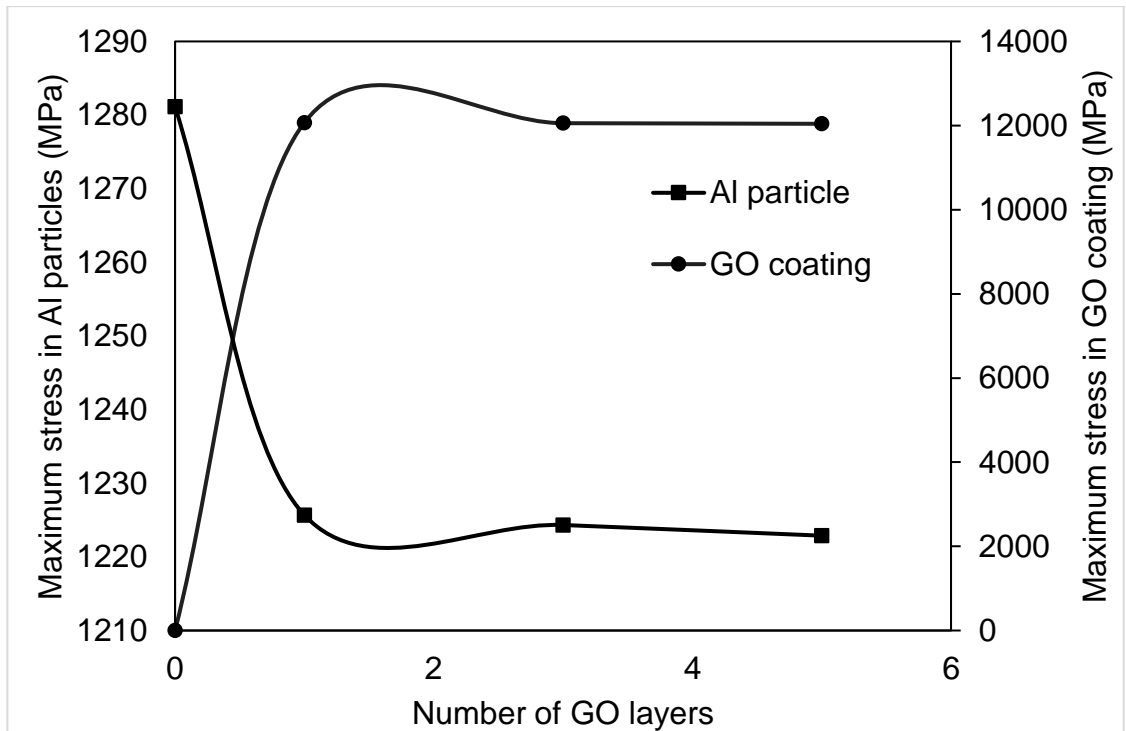
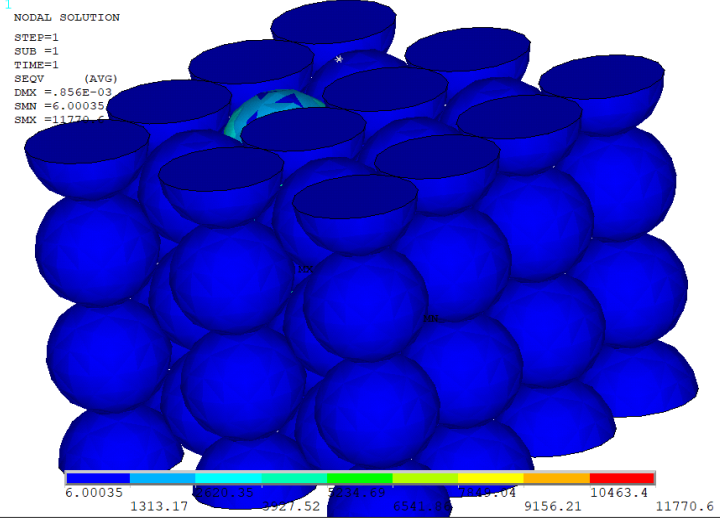
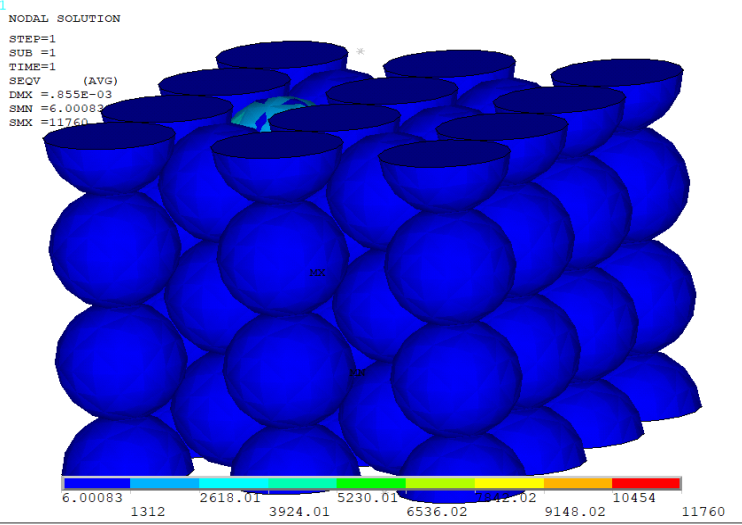
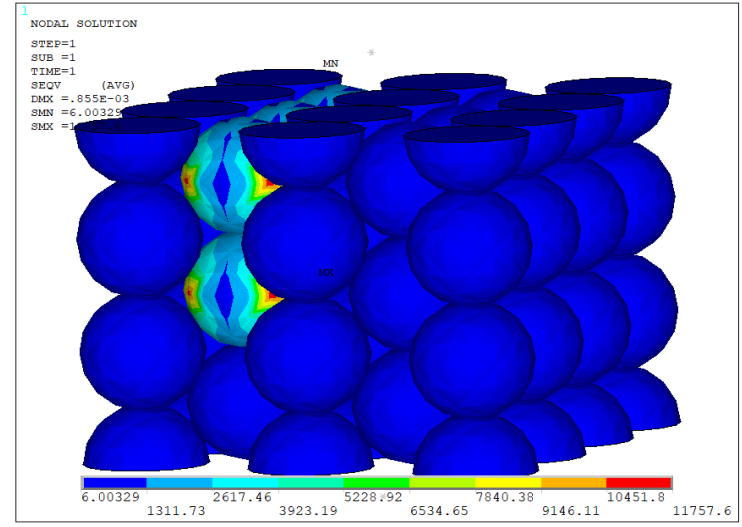
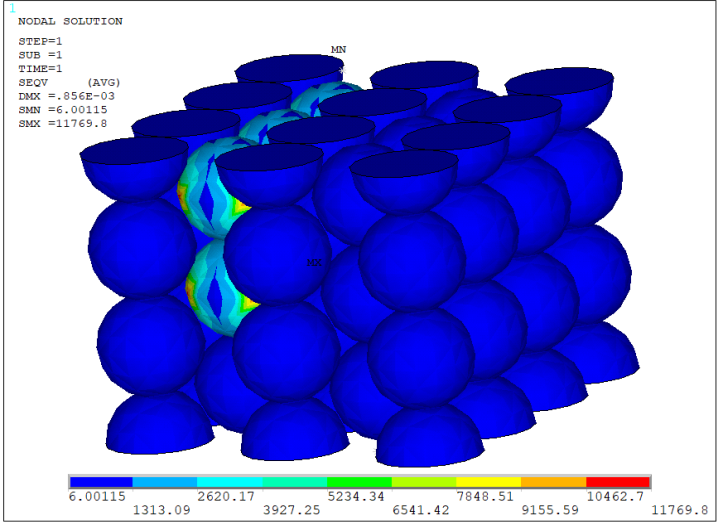


Figure 5.27: Comparison of maximum stress in models with respect to the addition of GO layers to Al particles.

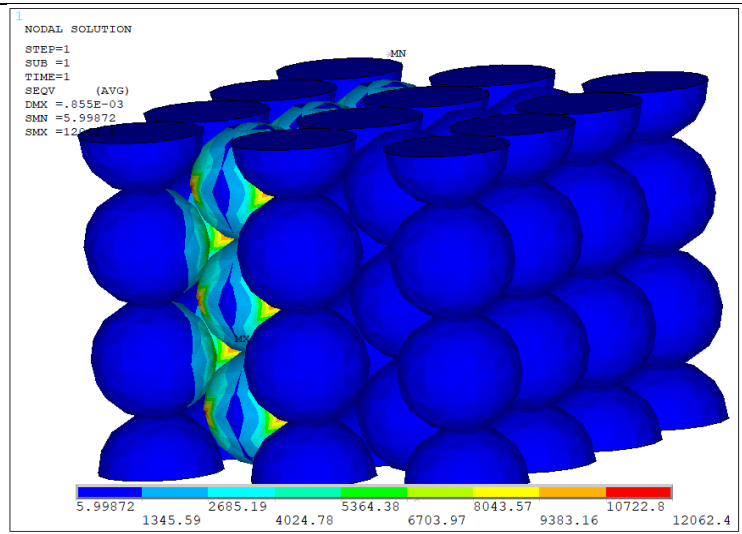
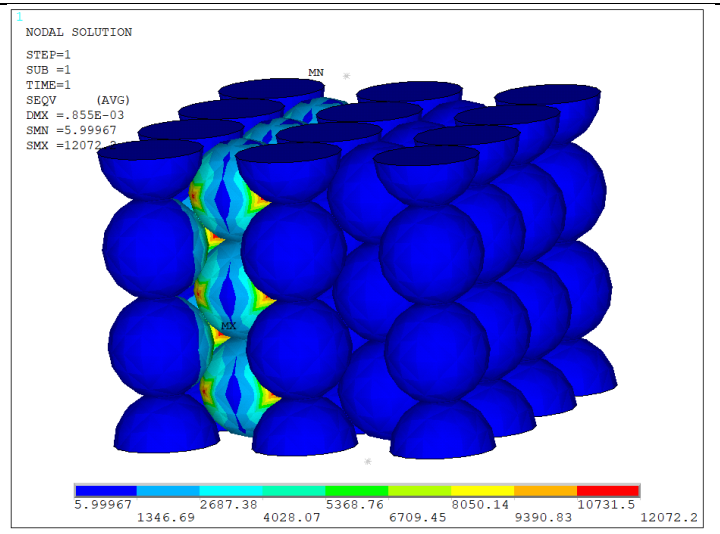
The stress profiles of GO/Al composites with respect to the distribution of GO coating on to the Al particles and existence of number of GO layers is shown in Figure 5.28. The comparison of maximum stress values with respect to the GO distribution and GO layers is tabulated in Table 5.4. It can be noted that the stress profile of the GO/Al composite varied with variation in GO distribution whereas the profiles weren't effected by the increase in GO layers.

% of Al particles filled with GO	Single layer	Three layers
5%	 <pre data-bbox="459 534 582 662"> 1 NODAL SOLUTION STEP=1 SUB =1 TIME=1 SEQV (AVG) DMX =.856E-03 SMN =6.00035 SMX =11770.6 </pre>	 <pre data-bbox="1288 534 1411 662"> 1 NODAL SOLUTION STEP=1 SUB =1 TIME=1 SEQV (AVG) DMX =.855E-03 SMN =6.00083 SMX =11760 </pre>

15%



25%



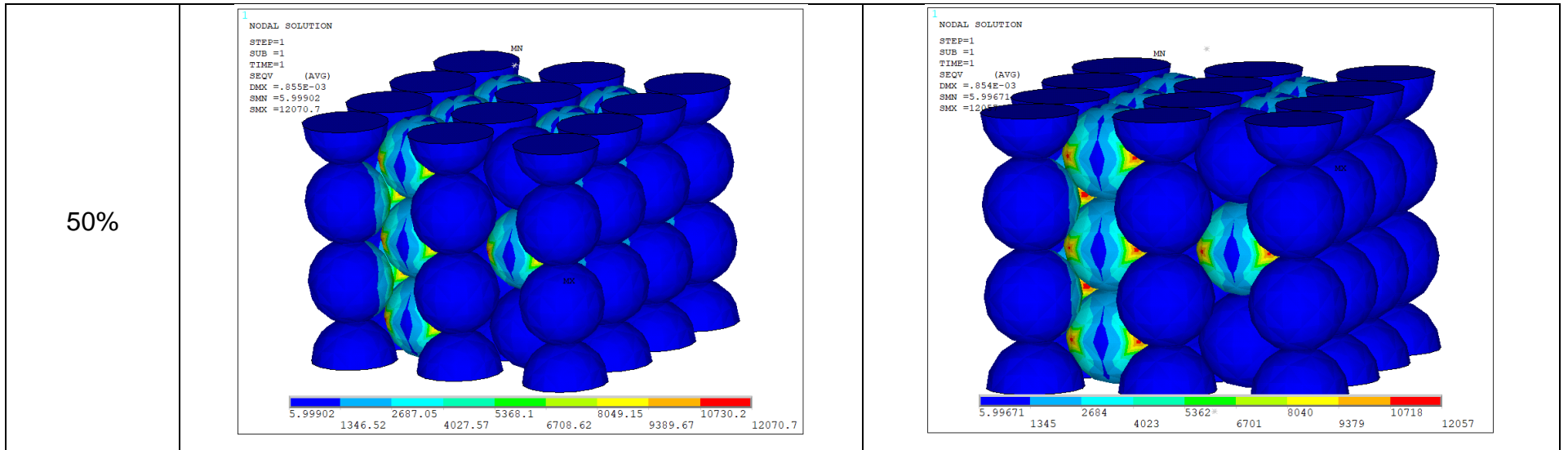


Figure 5.28: Stress profiles of GO/Al composites with respect to the number of GO layers and % of Al particles coated with GO.

Table 5.4: Comparison of maximum stress in models with respect to the addition of GO layers to Al particles and % of Al particles coated with GO.

Coating Condition		Stress (MPa)			
		5%	15%	25%	50%
No layer		1281.14	1281.14	1281.14	1281.14
Al sphere	Single Layer	1201.33	1201.25	1225.93	1225.68
	Three Layers	1200.28	1200.03	1224.96	1224.33
	Five Layers	1199.55	1198.91	1223.92	1222.88
GO coating	Single Layer	11770.60	11769.80	12072.20	12070.70
	Three Layers	11760.00	11757.60	12062.40	12057.00
	Five Layers	11748.80	11746.40	12051.70	12042.40

The simulations of stress distribution in the GO/Al composite can allow for the prediction of stress experienced by the composite at desired locations. The existing rule of mixtures (ROM) that is used to calculate the overall strength of the composite with respect to the volume percentage of graphene reinforcement doesn't account for the contribution/effect of variation of number of layers of graphene or the orientation of the graphene sheets on the overall strength of the composite. The elastic modulus and the tensile strength of the graphene nanocomposites increases with increase in volume percentage of reinforcement [218]. The mechanical properties also increases with increase in number of layers if better bonding between the layers is provided [219]. It was also proved that the disorientation of graphene sheets effects the overall properties of graphene reinforced Al matrix composites [219]. The number of GO layers in GO/Al composites in current research work were correlated to the strength of the composites. The maximum stress of 12070MPa is experienced by the single GO layer reinforced Al matrix composite which is 9 times higher than the stress experienced by pristine Al i.e., 1281MPa. Hence, there exists a strong relationship between variation of strength and GO layers. The simulation findings can therefore be used to predict the strength of composites measured experimentally. The proposed model was found to be

useful and important for the provision of maps for the mechanical property profiles for the production and application of GO/Al composites.

#### **5.4.3 Verification of FE model of GO/Al composites with the analytical model of GO/Al composites**

The Young's modulus obtained from FE model of GO/Al composite with single layer of GO coated on Al particles at different volume fractions (percentage of Al particles coated with GO particles) was compared with the Young's modulus of GO/Al composites obtained from analytical modelling. The comparison was shown in Figure 5.29, it can be noted from the graph that the results obtained from FE model developed in the current work has shown a good agreement with results obtained from the analytical model of GO/Al composites. However, a difference of ~1-1.8% in Young's modulus was noted in between the FE model and analytical model which was due to the distribution of particles i.e., in FE modelling the distribution/location of GO/Al particles in the composite plays a key role in the stress distribution.

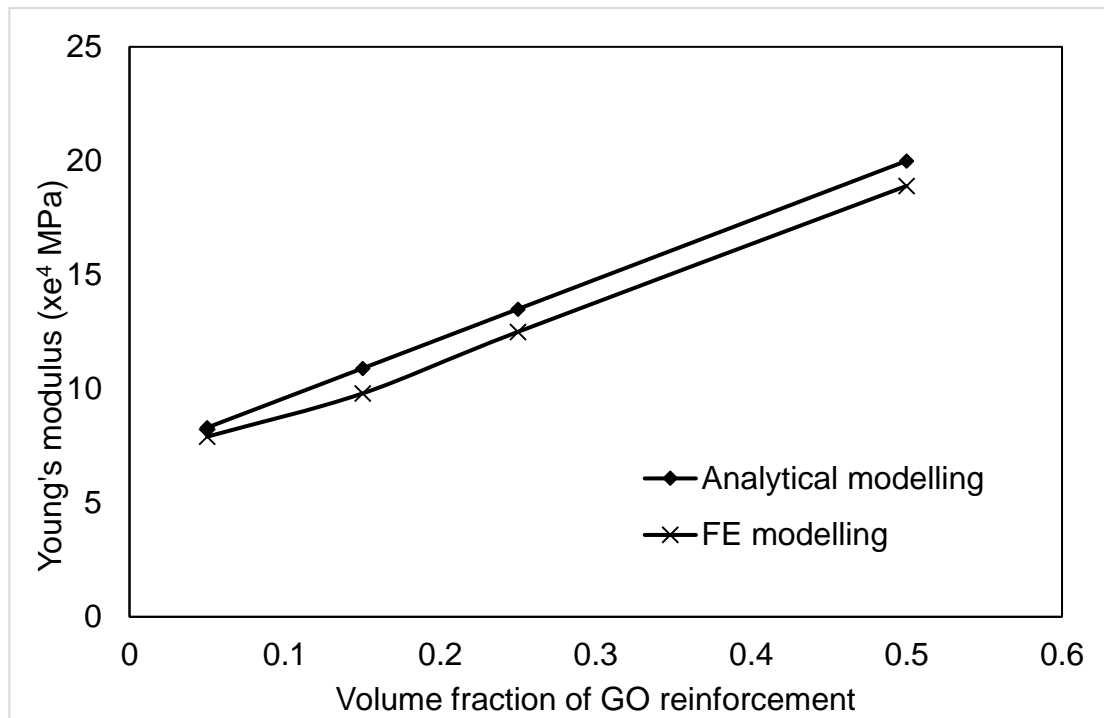


Figure 5.29: Comparison of Young's modulus obtained from FE modelling and analytical modelling of GO/Al composites.

#### 5.4.4 Validation of FE model of GO/Al composites

The FE model of GO/Al composite developed in the current research work is validated against the experimental results obtained from the GO/Al composites produced in current study and experimental results from literature, shown in Figure 5.30. It can be noted that from the results that, the Young's modulus obtained from simulations of GO/Al composites are ~3 times higher than the Young's modulus obtained from experimental characterisation. This was due to the agglomeration of GO and variation in grain sizes that were resulted during the production of GO/Al composites that has reduced the strength of the bonds and hence reduction in properties. It can also be noted that the produced GO/Al composites in current research work has many layers of GO which has resulted in reduced strength of composites due to the delamination of GO layers.

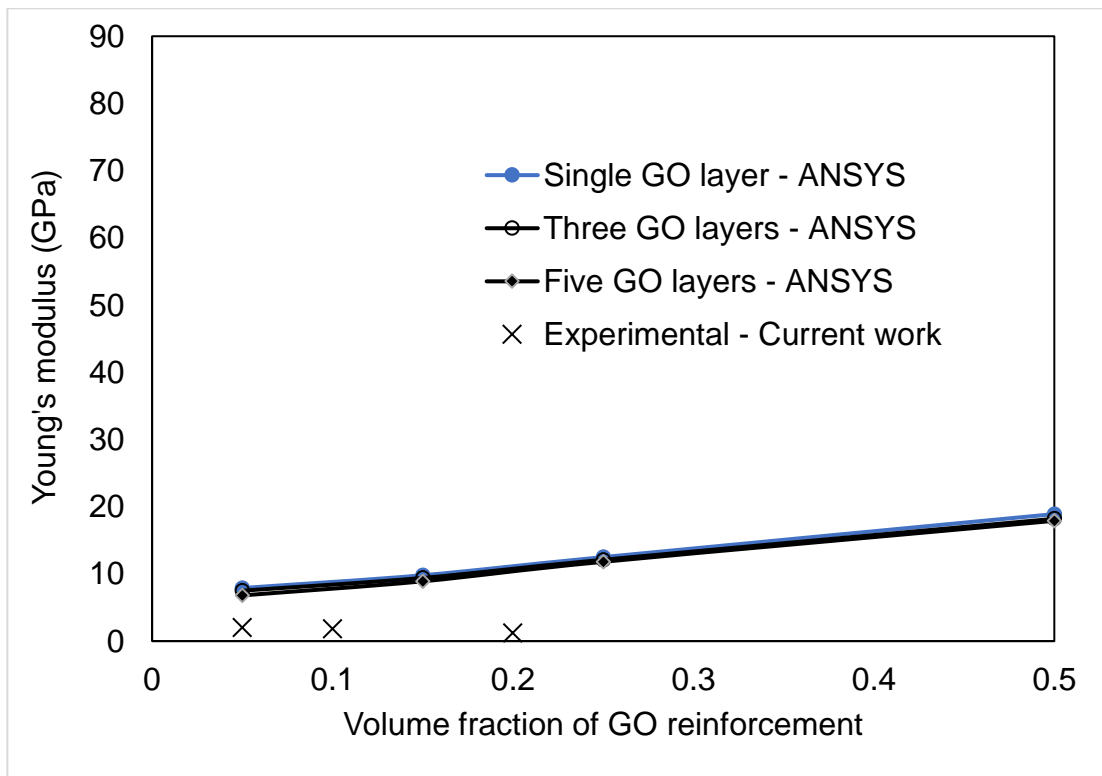


Figure 5.30: Comparison of Young's modulus of GO/Al composites obtained from experiments obtained from current work and literature with simulation results.

## **5.5 Summary**

The current chapter presented the results obtained from the characterisation of GO/Al powders and GO/Al sintered samples at various processing conditions. The stress profiles of GO/Al composites modelled in FE at various input parameters were also reported. The results obtained from FE model are compared with the results obtained from analytical model of GO/Al composite and validated against the experimental results.

## CHAPTER 6

### CONCLUSION

The production of GO/Al metal matrix composites was explored in this thesis. The liquid infiltration and powder metallurgical route have been examined with various process parameters, including solvent type, wt% of GO reinforcement, stirring time, compaction pressure and sintering temperature. The findings presented in this thesis from the current research work can be concluded as following:

#### ***6.1 Production of GO/Al composite powders at optimal process parameters by liquid infiltration***

- GO particles were uniformly dispersed amongst the surfaces of Al powder particles during wet mixing process in IPA solution.
- A minimum stirring time of 1hr for 0.05wt% GO/Al, 3hrs for 0.1wt% GO/Al and 5hrs for 0.2wt% GO/Al is required to obtain the better dispersions of GO aqueous solution in Al slurry.

#### ***6.2 Production of GO/Al pellets at optimal process parameters by powder metallurgy***

- Increase in compaction pressure increased the degree of green density of the GO/Al composites irrespective of the wt% of GO.
- Solid state sintering mechanism gave rise to the notable degree of densification of GO/Al composites from 0.05wt% to 0.1wt% of GO, but the densification reduced with increase in wt% of GO to 0.2wt% due to agglomeration of GO segregated at grain boundaries.
- Increase in gran size was noted with increase in sintering temperatures irrespective of the wt% of the GO addition.

#### ***6.3 Characterisation of GO/Al powders and pellets***

- From the metallographic study, a significant effect of GO addition, stirring time and sintering temperature on particle distribution and grain sizes was determined.

- Change in elemental composition of GO/Al composites with the addition of GO was detected. The effect of level of oxidation on elemental compositions were also discussed. The high composition of carbon and various amounts of oxygen were observed with variation in wt% of GO.
- A significant reduction of phase crystallinity was observed with variation in process parameters. Typical peaks of  $\text{Al}_2\text{O}_3$ , Al were recorded and GO peak was recorded only for 0.2wt% GO/Al composite due to high wt% of GO compared to other composites. Previous works have reported the formation of  $\text{Al}_4\text{C}_3$  at the process parameters used in current study. However, there was no evidence of  $\text{Al}_4\text{C}_3$  in all GO/Al composites produced in current study.
- From the Raman spectra, with the increase in wt% of GO reinforcement the number of graphene layers increased and the non-homogeneity of GO/Al composites also increased with increase in wt% of GO. This has attributed to the change in end properties of the composites.
- The hardness of the GO/Al composites were superior to the monolithic Al due to the appropriate interface formation in between GO and Al composites.
- The strength of GO/Al composites were dominated by the effect of formation of layers in which delamination played key role in deterioration of properties.

#### ***6.4 FE modelling and simulation of GO/Al composites***

- In this work, an FE model was developed to predict the stress distribution among the GO/Al composite particles. The stress distribution achieved was attributed to the microstructure obtained in current experimental work.
- The simulations of GO/Al composites can predict the effect of GO layers on the strength of GO/Al composite.
- By evaluating the effect of layers, the stress distribution can be visualised, these findings are important for scaling the modelling of particulate reinforced composites.

- A good agreement of simulation results with the analytical modelling results were noted and the model was successfully validated against the experimental results.

### **Future work**

- The work reported in this thesis can be further extended to produced graphene reinforced Al matrix composites through spark plasma sintering (SPS) to improve the densification parameters and hence improving the strength.
- Strengthening mechanisms such as Hall-Petch strengthening and Orowan looping must be studied in more detail to facilitate strengthening of the GO/Al composites for potential applications.
- Many studies focused on Al matrix composites especially reinforced with reduced graphene oxide (rGO) and graphene nanosheets (GNS) have not been properly characterised to understand the effect of graphene layer formation and orientation of layers on properties of the composite. Hence, the current work can be extended to investigate the effect of orientation of GO layers on the end properties of GO/Al composites.
- The present computational model developed could be applied to the graphene reinforced metal matrix composites by changing model parameters such as material properties, layers of graphene and vol% of graphene reinforcement and to validate the obtained results experimentally.

## REFERENCES

1. Kai, X. Z.; Li, Z. Q.; Fan, G. L.; Guo, Q.; Xiong, D. B.; Zhang, W. L.; Su, Y. S.; Lu, W. J.; Moon, W. J.; Zhang, D. Materials Science & Engineering A Enhanced strength and ductility in particulate-reinforced aluminum matrix composites fabricated by flake powder metallurgy. **2013**, *587*, 46–53, doi:10.1016/j.msea.2013.08.042.
2. Xiong, B.; Xu, Z.; Yan, Q.; Cai, C.; Zheng, Y.; Lu, B. Fabrication of SiC nanoparticulates reinforced Al matrix composites by combining pressureless infiltration with ball-milling and cold-pressing technology. **2010**, *497*, 4–7, doi:10.1016/j.jallcom.2010.02.184.
3. C.Flemings, A. M. J. . C. and Solidification processing of metal matrix composites. *Mater. Des.* **1989**, *10*, 69–76.
4. Hoover, D. E. H. and W. R. Advances in castable Al-SiC composites. In *Science and engineering of light metals*; 1991; pp. 447–452.
5. Esawi, A. M. K.; Morsi, K.; Sayed, A.; Gawad, A. A.; Borah, P. Fabrication and properties of dispersed carbon nanotube – aluminum composites. **2009**, *508*, 167–173, doi:10.1016/j.msea.2009.01.002.
6. Morsi, K.; Esawi, A. M. K.; Borah, P.; Lanka, S.; Sayed, A.; Taher, M. Properties of single and dual matrix aluminum – carbon nanotube composites processed via spark plasma extrusion ( SPE ). *Mater. Sci. Eng. A* **2010**, *527*, 5686–5690, doi:10.1016/j.msea.2010.05.081.
7. Bakshi, S. R.; Lahiri, D.; Agarwal, A. Carbon nanotube reinforced metal matrix composites – a review. **2010**, *55*, 41–64, doi:10.1179/095066009X12572530170543.
8. Schmidt, C. W.; Knieke, C.; Maier, V.; Ho, W. Accelerated grain refinement during accumulative roll bonding by nanoparticle reinforcement. **2011**, *c*, 245–248, doi:10.1016/j.scriptamat.2010.10.013.
9. Akbari, M. K.; Mirzaee, O.; Baharvandi, H. R. Fabrication and study on mechanical properties and fracture behavior of nanometric Al<sub>2</sub>O<sub>3</sub> particle-reinforced A356 composites focusing on the parameters of vortex method. *Mater. Des.* **2013**, *46*, 199–205, doi:10.1016/j.matdes.2012.10.008.
10. Tahamtan, S.; Halvae, A.; Emany, M.; Jiang, Z. Y.; Boostani, A. F. Exploiting superior tensile properties of a novel network-structure AlA206 matrix composite by hybridizing micron-sized Al<sub>3</sub>Ti with Al<sub>2</sub>O<sub>3</sub> nano particulates. **2014**.
11. Rajmohan, T.; Palanikumar, K.; Arumugam, S. Composites : Part B Synthesis and characterization of sintered hybrid aluminium matrix composites reinforced with nanocopper oxide particles and microsilicon carbide particles. *Compos. PART B* **2014**, *59*, 43–49, doi:10.1016/j.compositesb.2013.10.060.
12. Seo, Y. H. and K. Effects of hot extrusion through a curved die on the mechanical properties of SiCp/Al composites fabricated by melt-stirring.

*Compos. Sci. Technol.* **1999**, *59*, 643–654.

13. Karbalaei Akbari, M.; Baharvandi, H. R.; Shirvanimoghaddam, K. Tensile and fracture behavior of nano/micro TiB<sub>2</sub>particle reinforced casting A356 aluminum alloy composites. *Mater. Des.* **2015**, *66*, 150–161, doi:10.1016/j.matdes.2014.10.048.
14. Dao, V.; Zhao, S.; Lin, W.; Zhang, C. Effect of process parameters on microstructure and mechanical properties in AlSi9Mg connecting-rod fabricated by semi-solid squeeze casting. *Mater. Sci. Eng. A* **2012**, *558*, 95–102, doi:10.1016/j.msea.2012.07.084.
15. Tahamtan, S.; Halvae, A.; Emamy, M.; Zabihi, M. S. Fabrication of Al / A206 – Al<sub>2</sub>O<sub>3</sub> nano / micro composite by combining ball milling and stir casting technology. *Mater. Des.* **2013**, *49*, 347–359, doi:10.1016/j.matdes.2013.01.032.
16. Bastwros, M.; Kim, G. Y.; Zhu, C.; Zhang, K.; Wang, S.; Tang, X.; Wang, X. Effect of ball milling on graphene reinforced Al6061 composite fabricated by semi-solid sintering. *Compos. Part B Eng.* **2014**, *60*, 111–118, doi:10.1016/j.compositesb.2013.12.043.
17. Wu, Y.; Kim, G. Carbon nanotube reinforced aluminum composite fabricated by semi-solid powder processing. *J. Mater. Process. Tech.* **2011**, *211*, 1341–1347, doi:10.1016/j.jmatprotec.2011.03.007.
18. Asgharzadeh, H.; Sedigh, M. Synthesis and mechanical properties of Al matrix composites reinforced with few-layer graphene and graphene oxide. *J. Alloys Compd.* **2017**, *728*, 47–62, doi:10.1016/j.jallcom.2017.08.268.
19. Wang, K.; Wang, Y.; Fan, Z.; Yan, J.; Wei, T. Preparation of graphene nanosheet/alumina composites by spark plasma sintering. *Mater. Res. Bull.* **2011**, *46*, 315–318, doi:10.1016/j.materresbull.2010.11.005.
20. Shin, S. E.; Choi, H. J.; Shin, J. H.; Bae, D. H. Strengthening behavior of few-layered graphene/aluminum composites. *Carbon N. Y.* **2015**, *82*, 143–151, doi:10.1016/j.carbon.2014.10.044.
21. Bartolucci, S. F.; Paras, J.; Rafiee, M. A.; Rafiee, J.; Lee, S.; Kapoor, D.; Koratkar, N. Graphene-aluminum nanocomposites. *Mater. Sci. Eng. A* **2011**, *528*, 7933–7937, doi:10.1016/j.msea.2011.07.043.
22. Pérez-Bustamante, R.; Bolaños-Morales, D.; Bonilla-Martínez, J.; Estrada-Guel, I.; Martínez-Sánchez, R. Microstructural and hardness behavior of graphene-nanoplatelets/aluminum composites synthesized by mechanical alloying. *J. Alloys Compd.* **2015**, *615*, S578–S582, doi:10.1016/j.jallcom.2014.01.225.
23. Latief, F. H.; Sherif, E. S. M.; Almajid, A. A.; Junaedi, H. Fabrication of exfoliated graphite nanoplatelets-reinforced aluminum composites and evaluating their mechanical properties and corrosion behavior. *J. Anal. Appl. Pyrolysis* **2011**, *92*, 485–492, doi:10.1016/j.jaap.2011.09.003.
24. Latief, F. H.; Sherif, E. S. M. Effects of sintering temperature and

graphite addition on the mechanical properties of aluminum. *J. Ind. Eng. Chem.* **2012**, *18*, 2129–2134, doi:10.1016/j.jiec.2012.06.007.

25. Koc, E. The effect of sintering time , temperature , and graphene addition on the hardness and microstructure of aluminum composites. **2018**, doi:10.1177/0021998317740200.
26. Li, J.; Zhang, X.; Geng, L. Improving graphene distribution and mechanical properties of GNP/Al composites by cold drawing. *Mater. Des.* **2018**, doi:10.1016/j.matdes.2018.02.024.
27. Li, Z.; Fan, G.; Tan, Z.; Guo, Q.; Xiong, D.; Su, Y.; Li, Z.; Zhang, D. Uniform dispersion of graphene oxide in aluminum powder by direct electrostatic adsorption for fabrication of graphene/aluminum composites. *Nanotechnology* **2014**, *25*, 325601, doi:10.1088/0957-4484/25/32/325601.
28. Wang, J.; Li, Z.; Fan, G.; Pan, H.; Chen, Z.; Zhang, D. Reinforcement with graphene nanosheets in aluminum matrix composites. *Scr. Mater.* **2012**, *66*, 594–597, doi:10.1016/j.scriptamat.2012.01.012.
29. Liu, J.; Khan, U.; Coleman, J.; Fernandez, B.; Rodriguez, P.; Naher, S.; Brabazon, D. Graphene oxide and graphene nanosheet reinforced aluminium matrix composites: Powder synthesis and prepared composite characteristics. *Mater. Des.* **2016**, *94*, 87–94, doi:10.1016/j.matdes.2016.01.031.
30. Daoud, A. Microstructure and tensile properties of 2014 Al alloy reinforced with continuous carbon fibers manufactured by gas pressure infiltration. **2014**, *391*, 114–120, doi:10.1016/j.msea.2004.08.075.
31. Tjong, S. C.; Lau, K. C. Abrasion resistance of stainless-steel composites reinforced with hard TiB<sub>2</sub> particles. **2000**, *60*, 1–6.
32. Tjong, S. C.; Mai, Y. W. Processing-structure-property aspects of particulate- and whisker-reinforced titanium matrix composites. *Compos. Sci. Technol.* **2008**, *68*, 583–601, doi:10.1016/j.compscitech.2007.07.016.
33. Huda, D.; Baradie, M. A. E.; H, M. S. J. Metal-matrix composites : Materials aspects . Part II. **1993**, *37*, 529–541.
34. Huda, D., H. M. and E. B. MMC's: materials, manufacturing and mechanical properties. *Key Eng. maetrails, Met. matrix Compos. Manuf. Asp. Part II.* **1995**, *104–107*, 37–64.
35. Samuel, A S and Samuel, F. . Foundary aspects of particulate reinforced aluminium MMC's: factors controlling composite quality. *Key Eng. Mater.* **1995**, *104–107*, 65–98.
36. Bhagat, R. B. Emering P/M metal matrix composites. *Adv. powder Metall. particulate Mater.* **1992**, *9*, 139–146.
37. Lim CS and Clegg AJ The production and evaluation of metal matrix composite casting produced by a pressure-assisted investment casting process. *J. Mater. Process. Technol.* **1997**, *67*, 13–18.

38. Dasari, B. L.; Morshed, M.; Nouri, J. M.; Brabazon, D.; Naher, S. Mechanical properties of graphene oxide reinforced aluminium matrix composites. *Compos. Part B Eng.* **2018**, *145*, 136–144, doi:10.1016/j.compositesb.2018.03.022.
39. Properties and selection: Nonferrous alloy and special purpose materials. ASM handbook. **1996**.
40. Rohatgi, P. . Future directions in solidification of metal matrix composites. *Key Eng. Mater.* **1995**, *104–107*, 293–312.
41. Sie, B.; Tjong, C. Novel Nanoparticle-Reinforced Metal Matrix Composites with Enhanced Mechanical Properties. **2007**, 639–652, doi:10.1002/adem.200700106.
42. Sahin, Y.; Acilar, M. Production and properties of SiCp-reinforced aluminium alloy composites. *Compos. Part A Appl. Sci. Manuf.* **2003**, *34*, 709–718, doi:10.1016/S1359-835X(03)00142-8.
43. An introduction to metal matrix composites. *Cambridge: Cambridge University press.* **1993**.
44. Henrique, P.; Camargo, C.; Satyanarayana, K. G.; Wypych, F. Nanocomposites: Synthesis , Structure , Properties and New Application Opportunities. **2009**, *12*, 1–39.
45. Miracle, D. B. Metal matrix composites – From science to technological significance. *Compos. Sci. Technol.* **2005**, *65*, 2526–2540, doi:10.1016/j.compscitech.2005.05.027.
46. Raming, T. P.; Zyl, W. E. Van; Carton, E. P.; Verweij, H. Sintering , sinterforging and explosive compaction to densify the dual phase nanocomposite system Y<sub>2</sub>O<sub>3</sub> -doped ZrO<sub>2</sub> and RuO<sub>2</sub>. **2004**, *30*, 629–634, doi:10.1016/j.ceramint.2003.09.006.
47. Clyne T, W. P. *An introduction to metal matrix composites: Cambridge University Press;* 1995;
48. Arzt, E.; Dehm, G.; Gumbsch, P.; Kraft, O.; Weiss, D. Interface controlled plasticity in metals : dispersion hardening and thin ® lm deformation. **2001**, *46*, 283–307.
49. Dao, M. Toward a quantitative understanding of mechanical behavior of nanocrystalline metals. **2007**, *55*, 4041–4065, doi:10.1016/j.actamat.2007.01.038.
50. Dorri Moghadam, A.; Omrani, E.; Menezes, P. L.; Rohatgi, P. K. Mechanical and tribological properties of self-lubricating metal matrix nanocomposites reinforced by carbon nanotubes (CNTs) and graphene - A review. *Compos. Part B Eng.* **2015**, *77*, 402–420, doi:10.1016/j.compositesb.2015.03.014.
51. Leparoux, M. Nano-silicon carbide reinforced aluminium produced by high-energy milling and hot consolidation. **2011**, *528*, 6606–6615, doi:10.1016/j.msea.2011.05.037.

52. Tan, M. J.; Zhang, X. Powder metal matrix composites: selection and processing. **1998**, *244*, 80–85.
53. Tahamtan, S.; Emamy, M.; Halvaei, A. Effects of reinforcing particle size and interface bonding strength on tensile properties and fracture behavior of Al-A206 / alumina micro / nanocomposites. **2014**, doi:10.1177/0021998313509860.
54. Mazahery, A.; Abdizadeh, H.; Baharvandi, H. R. Development of high performance A356/nano-Al<sub>2</sub>O<sub>3</sub> composites. *Mater. Sci. Eng. A* **2009**, *518*, 61–64, doi:10.1016/j.msea.2009.04.014.
55. El-Mahallawi, I.; Abdelkader, H.; Yousef, L.; Amer, A.; Mayer, J.; Schwedt, A. Influence of Al<sub>2</sub>O<sub>3</sub> nano-dispersions on microstructure features and mechanical properties of cast and T6 heat-treated Al Si hypoeutectic Alloys. *Mater. Sci. Eng. A* **2012**, *556*, 76–87, doi:10.1016/j.msea.2012.06.061.
56. Naidich, J. The wettability of solids by liquid metals. *Prog. Surf. Membr. Sci.* **1981**, *14*, 353–484.
57. Tang, F.; Hagiwara, M.; Schoenung, J. M. Microstructure and tensile properties of bulk nanostructured Al-5083 / SiC p composites prepared by cryomilling. **2005**, *407*, 306–314, doi:10.1016/j.msea.2005.07.056.
58. Kang, Y.; Chan, S. L. Tensile properties of nanometric Al<sub>2</sub>O<sub>3</sub> particulate-reinforced aluminum matrix composites. **2004**, *85*, 438–443, doi:10.1016/j.matchemphys.2004.02.002.
59. El-eskandarany, M. S. Mechanical solid state mixing for synthesizing of SiC. **1998**, *279*, 263–271.
60. Mandal, D.; Viswanathan, S. Effect of heat treatment on microstructure and interface of SiC particle reinforced 2124 Al matrix composite. *Mater. Charact.* **2013**, *85*, 73–81, doi:10.1016/j.matchar.2013.08.014.
61. Yang, Y.; Lan, J.; Li, X. Study on bulk aluminum matrix nano-composite fabricated by ultrasonic dispersion of nano-sized SiC particles in molten aluminum alloy. **2004**, *380*, 378–383, doi:10.1016/j.msea.2004.03.073.
62. Weiss D, B. M. Using Semi-Solid Extrusion for the Production of Aluminum-Nanocomposite Master Alloys. *Solid State Phenom.* **2015**, *217*, 426–430.
63. Curle, U. A.; Ivanchev, L. Wear of semi-solid rheocast SiC p / Al metal matrix composites. *Trans. Nonferrous Met. Soc. China* **2010**, *20*, 852–856, doi:10.1016/S1003-6326(10)60594-8.
64. Jiang J, W. Y. Microstructure and mechanical properties of the rheoformed cylindrical part of 7075 aluminum matrix composite reinforced with nano-sized SiC particles. *Mater. Des.* **2015**, *79*, 32–41.
65. Geim, A. K.; Novoselov, K. S. The rise of graphene. *Nat. Mater.* **2007**, *6*, 183–191, doi:10.1038/nmat1849.
66. Fasolino, A.; Katsnelson, M. I. Intrinsic ripples in graphene. **2007**, *6*,

doi:10.1038/nmat2011.

67. Peierls, R. Remarks on transition temperatures. *Sel. Sci. Pap. sir Rudolf Peierls* **1997**, 137–138.
68. Meyer, J. C.; Geim, A. K.; Katsnelson, M. I.; Novoselov, K. S.; Booth, T. J.; Roth, S. The structure of suspended graphene sheets. **2007**, *446*, doi:10.1038/nature05545.
69. Hass, J. The growth and morphology of epitaxial multilayer graphene. *J. Phys. Condens. matter* **2008**, *20*, 323202.
70. Deshpande, A.; Bao, W.; Miao, F.; Lau, C. N.; Leroy, B. J. Spatially resolved spectroscopy of monolayer graphene on SiO<sub>2</sub>. **2009**, 1–6, doi:10.1103/PhysRevB.79.205411.
71. Xu, K.; Cao, P.; Heath, J. R. Scanning Tunneling Microscopy Characterization of the Electrical Properties of Wrinkles in Exfoliated Graphene Monolayers. **2009**.
72. Zhu, Y.; Murali, S.; Cai, W.; Li, X.; Suk, J. W.; Potts, J. R.; Ruoff, R. S. Graphene and graphene oxide: Synthesis, properties, and applications. *Adv. Mater.* **2010**, *22*, 3906–3924, doi:10.1002/adma.201001068.
73. Lee, C.; Wei, X.; Kysar, J. W.; Hone, J.; Lee, C.; Wei, X.; Kysar, J. W.; Hone, J. Measurement of the Elastic Properties and Intrinsic Strength of Monolayer Graphene. *Science*. **2016**, *321*, 385–388.
74. Tsoukleri, G.; Parthenios, J.; Papagelis, K.; Jalil, R.; Andrea, C.; Geim, A. K.; Novoselov, K. S.; Galiotis, C. Subjecting a graphene monolayer to tension and compression. *Small*. **2009**, 2397-2402.
75. Lee, C. Wei, X. Elastic and frictional properties of graphene. *Phys status solidi B Basic solid state phys* **2009**, *246*, 2562.
76. Zhen Hua Ni, Ting Yu, Yun Hao Lu, Ying Ying Wang, Yuan Ping Feng, Z. X. S. Uniaxial strain on graphene: Raman spectroscopy study and bandgap opening. *ACS Nano* **2008**, *2*, 2301.
77. Gómez-Navarro, C.; Burghard, M.; Kern, K. Elastic properties of chemically derived single graphene sheets. *Nano Lett.* **2008**, *8*, 2045–9, doi:10.1021/nl801384y.
78. Zhang, P.; Ma, L.; Fan, F.; Zeng, Z.; Peng, C.; Loya, P. E.; Liu, Z.; Gong, Y.; Zhang, J.; Zhang, X.; Ajayan, P. M.; Zhu, T.; Lou, J. Fracture toughness of graphene. *Nat. Commun.* **2014**, *5*, 1–7, doi:10.1038/ncomms4782.
79. Aluminium - Advantages and Properties of Aluminium. *AZO Materials*. **2018**.
80. Stainless Steel - Grade 304 ( UNS S30400) The Different Properties and Applications. *AZO Materials*. **2018**.
81. Copper, The Different Properties and Applications. *AZO Materials*. **2018**.
82. Titanium ( Ti ), The Different Properties and Applications. *AZO Materials*.

**2018.**

83. K. S. Novoselov, D. Jiang, F. Schedin, T. J. Booth, V. V. Khotkevich, S. V. Morozov, and A. K. G. Two-dimensional atomic crystals. *Proc. Natl. Acad. Sci. USA* **2005**, *102*, 10451–10453.
84. Chen, J. H.; Jang, C.; Xiao, S.; Ishigami, M.; Fuhrer, M. S. Intrinsic and Extrinsic Performance Limits of Graphene Devices on SiO<sub>2</sub>.
85. Hwang, E. H.; Adam, S.; Sarma, S. Das Carrier transport in 2D graphene layers. *Phys Rev Lett* **2007**, *98*, 186806.
86. Bolotin, K. I.; Sikes, K. J.; Jiang, Z.; Klima, M.; Fudenberg, G.; Hone, J.; Kim, P.; Stormer, H. L. Ultrahigh electron mobility in suspended graphene. **2008**, 1–5.
87. Son, Y.; Cohen, M. L.; Louie, S. G. Energy Gaps in Graphene Nanoribbons. **2008**, *32*, 1–4.
88. Han, M. Energy band-gap engineering of graphene nanoribbons. *Phys Rev Lett* **2007**, *98*, 206805.
89. Kim, S.; Choi, H. Origin of anomalous electronic structures of epitaxial graphene on silicon carbide. *Phys Rev Lett* **2008**, *100*, 176802.
90. Bulaev, D. V.; Loss, D.; Burkard, G. Spin qubits in graphene quantum dots. **2007**, *3*.
91. Reina A, Jia X, Ho J, Nezich D, Son H, Bulovic V, et al. Large area, few-layer graphene films on arbitrary substrates by chemical vapor deposition. *Nano Lett* **2008**, *9*, 30.
92. Kim, K. S.; Zhao, Y.; Jang, H.; Lee, S. Y.; Kim, J. M.; Kim, K. S.; Ahn, J. H.; Kim, P.; Choi, J. Y.; Hong, B. H. Large-scale pattern growth of graphene films for stretchable transparent electrodes. *Nature* **2009**, *457*, 706–710, doi:10.1038/nature07719.
93. Evaldsson, M.; Zozoulenko, I. V.; Xu, H.; Heinzl, T. Edge disorder induced Anderson localization and conduction gap in graphene nanoribbons. **2008**, 1–4.
94. Peng X, A. R. Symmetry breaking induced bandgap in epitaxial graphene layers on SiC. *Nano Lett* **2008**, *8*, 4464.
95. de Heer, W. A.; Berger, C.; Wu, X.; First, P. N.; Conrad, E. H.; Li, X.; Li, T.; Sprinkle, M.; Hass, J.; Sadowski, M. L.; Potemski, M.; Martinez, G. Epitaxial graphene. **2007**, doi:10.1016/j.ssc.2007.04.023.
96. Kim KS, Zhao Y, Jang H, Lee SY, Kim JM, K. K. Large-scale pattern growth of graphene films for stretchable transparent electrodes. *Nature* **2009**, *457*, 706.
97. Cao, H.; Yu, Q.; Colby, R.; Pandey, D.; Park, C. S.; Lian, J.; Childres, I.; Drachev, V.; Stach, E. A.; Hussain, M.; Li, H.; Pei, S. S.; Chen, Y. P. Large-scale Graphitic Thin Films Synthesized on Ni and Transferred to Insulators : Structural and Electronic Properties. 1–20.

98. Shuai W, Priscilla KA, Ziqian W, Tang Ai L, John TL, K. P. High mobility, printable, and solution-processed graphene electronics. *Nano Lett* **2010**, *10*, 92–98.
99. Novoselov KS, McCann E, Morozov SV, Fal'ko VI, Katsnelson MI, Zeitler U Unconventional quantum Hall effect and Berry's phase of  $2\pi$  in bilayer graphene. *Nat Phys* **2006**, *2*, 177.
100. Castro EV, Novoselov KS, Morozov SV, Peres NMR, dos Santos JMBL, N. J. Biased bilayer graphene: semiconductor with a gap tunable by the electric field effect. *Phys Rev Lett* **2007**, *99*, 216802.
101. Gomez-Navarro, C.; Weitz, R. T.; Bittner, A. M.; Scolari, M.; Mews, A.; Burghard, M.; Kern, K. Electronic Transport Properties of Individual Chemically Reduced Graphene Oxide Sheets. *Nano Lett.* **2007**, *7*, 3499–3503, doi:10.1021/nl901209z.
102. Wallace, G. G.; Kaner, R. B.; Muller, M.; Gilje, S.; Li, D.; Li, D. Processable aqueous dispersions of graphene nanosheets Publication. *Nat. Nanotechnol.* **2008**, *3*, 101–105, doi:10.1038/nnano.2007.451.
103. Nilsson, J.; Neto, A. H. C.; Peres, N. M. R. Electronic properties of bilayer and multilayer graphene. **2007**, 1–36.
104. Pop, E.; Mann, D.; Wang, Q.; Goodson, K.; Dai, H. Thermal Conductance of an Individual Single-Wall Carbon Nanotube above Room Temperature. **2006**, *6*.
105. Kim, P.; Shi, L.; Majumdar, A.; Mceuen, P. L. Thermal Transport Measurements of Individual Multiwalled Nanotubes. 2–5.
106. Wang, Y.; Shi, Z.; Huang, Y.; Ma, Y.; Wang, C.; Chen, M.; Chen, Y. Supercapacitor Devices Based on Graphene Materials. *J. Phys. Chem. C* **2009**, *113*, 13103–13107, doi:10.1021/jp902214f.
107. Khrapach, I.; Withers, F.; Bointon, T. H.; Polyushkin, D. K.; Barnes, W. L.; Russo, S.; Craciun, M. F. Novel highly conductive and transparent graphene-based conductors. *Adv. Mater.* **2012**, *24*, 2844–2849, doi:10.1002/adma.201200489.
108. Balandin, A. A.; Ghosh, S.; Bao, W.; Calizo, I.; Teweldebrhan, D.; Miao, F.; Lau, C. N. Superior Thermal Conductivity of Single-Layer Graphene. *Nano Lett.* **2008**, *8*, 902–907.
109. Ghosh, S.; Calizo, I.; Teweldebrhan, D.; Pokatilov, E. P.; Nika, D. L.; Balandin, A. A. Extremely high thermal conductivity of graphene: Prospects for thermal management applications in nanoelectronic circuits. **2008**, 2008–2010, doi:10.1063/1.2907977.
110. Seol JH, Jo I, Moore AL, Lindsay L, Aitken ZH, P. M. Two-dimensional phonon transport in supported graphene. *Science.* **2010**, *328*, 213.
111. Lee J, Yoon D, Kim Lee SW, C. H. Thermal conductivity of suspended pristine graphene measured by Raman spectroscopy. *Phys Rev B* **2011**, *83*, 8.

112. Pettes MT, Jo I, Yao Z, S. L. Influence of polymeric residue on the thermal conductivity of suspended bilayer graphene. *Nano Lett* **2011**, *11*, 1195–2000.
113. Nair, R. R.; Blake, P.; Grigorenko, A. N.; Novoselov, K. S.; Booth, T. J.; Stauber, T.; Peres, N. M. R.; Geim, A. K. Fine structure constant defines visual transparency of graphene. *Science (80-. )*. **2008**, *320*, 1308, doi:10.1126/science.1156965.
114. Bae, S.; Kim, H.; Lee, Y.; Xu, X.; Park, J. S.; Zheng, Y.; Balakrishnan, J.; Lei, T.; Ri Kim, H.; Song, Y. II; Kim, Y. J.; Kim, K. S.; Özyilmaz, B.; Ahn, J. H.; Hong, B. H.; Iijima, S. Roll-to-roll production of 30-inch graphene films for transparent electrodes. *Nat. Nanotechnol.* **2010**, *5*, 574–578, doi:10.1038/nnano.2010.132.
115. Rao, C. N. R.; Sood, A. K.; Subrahmanyam, K. S.; Govindaraj, A. Graphene: The new two-dimensional nanomaterial. *Angew. Chemie - Int. Ed.* **2009**, *48*, 7752–7777, doi:10.1002/anie.200901678.
116. Novoselov, K. S.; Geim, A. K.; Morozov, S. V.; Jiang, D.; Zhang, Y.; Dubonos, S. V.; Grigorieva, I. V.; Firsov, A. A. Electric field effect in atomically thin carbon films. *Science (80-. )*. **2004**, *306*, 666–669, doi:10.1126/science.1102896.
117. Stankovich, S.; Dikin, D. a.; Piner, R. D.; Kohlhaas, K. a.; Kleinhammes, A.; Jia, Y.; Wu, Y.; Nguyen, S. T.; Ruoff, R. S. Synthesis of graphene-based nanosheets via chemical reduction of exfoliated graphite oxide. *Carbon N. Y.* **2007**, *45*, 1558–1565, doi:10.1016/j.carbon.2007.02.034.
118. Jayasena, B.; Subbiah, S. A novel mechanical cleavage method for synthesizing few-layer graphenes. *Nanoscale Res. Lett.* **2011**, *6*, 1–7, doi:10.1186/1556-276X-6-95.
119. Chen, J. Duan, M and Chen, G. Continuous mechanical exfoliation of graphene sheets via three-roll mill. *J. Mater. Chem.* **2012**, *22*, 19625–29628.
120. Ciesielski, A.; Samorì, P. Graphene via sonication assisted liquid-phase exfoliation. *Chem. Soc. Rev.* **2014**, *43*, 381–398, doi:10.1039/c3cs60217f.
121. Smith, R. J.; King, P. J.; Wirtz, C.; Duesberg, G. S.; Coleman, J. N. Lateral size selection of surfactant-stabilised graphene flakes using size exclusion chromatography. *Chem. Phys. Lett.* **2012**, *531*, 169–172, doi:10.1016/j.cplett.2012.02.027.
122. Du, W.; Jiang, X.; Zhu, L. From graphite to graphene: Direct liquid-phase exfoliation of graphite to produce single- and few-layered pristine graphene. *J. Mater. Chem. A* **2013**, *1*, 10592–10606, doi:10.1039/c3ta12212c.
123. Bonaccorso, F.; Lombardo, A.; Hasan, T.; Sun, Z.; Colombo, L.; Ferrari, A. C. Production and processing of graphene and 2d crystals. *Mater. Today* **2012**, *15*, 564–589, doi:10.1016/S1369-7021(13)70014-2.

124. Israelachvili, J. N. Intermolecular and Surface, the Forces Between Atoms and Molecules: Principles and Concepts. *Interactions* **2010**, 3152–3158, doi:10.1002/elps.201000212.
125. Dasari, B. L.; Nouri, J. M.; Brabazon, D.; Naher, S. Graphene and derivatives – Synthesis techniques, properties and their energy applications. *Energy* **2017**, *140*, 766–778, doi:10.1016/j.energy.2017.08.048.
126. Blake, P.; Brimicombe, P. D.; Nair, R. R.; Booth, T. J.; Jiang, D.; Schedin, F.; Ponomarenko, L. A.; Morozov, S. V.; Gleeson, H. F.; Hill, E. W.; Geim, A. K.; Novoselov, K. S. Graphene-based liquid crystal device. *Nano Lett.* **2008**, *8*, 1704–1708, doi:10.1021/nl080649i.
127. Hernandez, Y.; Nicolosi, V.; Lotya, M.; Blighe, F.; Sun, Z.; De, S.; McGovern, I. T.; Holland, B.; Byrne, M.; Gunko, Y.; Boland, J.; Niraj, P.; Duesberg, G.; Krishnamurti, S.; Goodhue, R.; Hutchison, J.; Scardaci, V.; Ferrari, a. C.; Coleman, J. N. High yield production of graphene by liquid phase exfoliation of graphite. *Nat. Nanotechnol.* **2008**, *3*, 563–8, doi:10.1038/nnano.2008.215.
128. Khan, U.; O'Neill, A.; Lotya, M.; De, S.; Coleman, J. N. High-concentration solvent exfoliation of graphene. *Small* **2010**, *6*, 864–871, doi:10.1002/smll.200902066.
129. Khan, U.; Porwal, H.; Neill, A. O.; May, P.; Coleman, J. N. Solvent-exfoliated graphene at extremely high concentration Solvent-Exfoliated Graphene at Extremely High Concentration. **2011**, 9077–9082, doi:10.1021/la201797h.
130. Khan, U.; O'Neill, A.; Porwal, H.; May, P.; Nawaz, K.; Coleman, J. N. Size selection of dispersed, exfoliated graphene flakes by controlled centrifugation. *Carbon N. Y.* **2012**, *50*, 470–475, doi:10.1016/j.carbon.2011.09.001.
131. Skaltsas, T.; Ke, X.; Bittencourt, C.; Tagmatarchis, N. Ultrasonication induces oxygenated species and defects onto exfoliated graphene. *J. Phys. Chem. C* **2013**, *117*, 23272–23278, doi:10.1021/jp4057048.
132. Bracamonte, M. V.; Lacconi, G. I.; Urreta, S. E.; Foa Torres, L. E. F. On the nature of defects in liquid-phase exfoliated graphene. *J. Phys. Chem. C* **2014**, *118*, 15455–15459, doi:10.1021/jp501930a.
133. Bourlinos, A. B.; Georgakilas, V.; Zboril, R.; Sterioti, T. A.; Stubos, A. K. Liquid-Phase Exfoliation of Graphite Towards Solubilized Graphenes. *Small* **2009**, *5*, 1841–1845, doi:10.1002/smll.200900242.
134. Lotya, M.; Hernandez, Y.; King, P. J.; Smith, R. J.; Nicolosi, V.; Karlsson, L. S.; Blighe, M.; De, S.; Wang, Z.; MCGovern, I. T.; Duesberg, G. S.; Coleman, J. N.; Blighe, F. M. Liquid Phase Production of Graphene by Exfoliation of Graphite in Surfactant / Water Solutions Liquid Phase Production of Graphene by Exfoliation of Graphite in Surfactant / Water Solutions. **2009**, 3611–3620, doi:10.1021/ja807449u.
135. Green , A.A and Hersham, M. . Solution phase production of graphene

with controlled thickness via density differential. *Nano Lett* **2009**, *9*, 4031–4036.

136. Guardia, L.; Fernández-Merino, M. J.; Paredes, J. I.; Solís-Fernández, P.; Villar-Rodil, S.; Martínez-Alonso, A.; Tascón, J. M. D. High-throughput production of pristine graphene in an aqueous dispersion assisted by non-ionic surfactants. *Carbon N. Y.* **2011**, *49*, 1653–1662, doi:10.1016/j.carbon.2010.12.049.
137. Wajid, A. S.; Das, S.; Irin, F.; Ahmed, H. S. T.; Shelburne, J. L.; Parviz, D.; Fullerton, R. J.; Jankowski, A. F.; Hedden, R. C.; Green, M. J. Polymer-stabilized graphene dispersions at high concentrations in organic solvents for composite production. *Carbon N. Y.* **2012**, *50*, 526–534, doi:10.1016/j.carbon.2011.09.008.
138. Adamson, D. H. Stabilization of Graphene Sheets by a Structured Benzene/ Hexafluorobenzene Mixed Solvent. *J. Am. Chem. Soc.* **2012**, *134*, 5018–5021.
139. Low, C. T. J.; Walsh, F. C.; Chakrabarti, M. H.; Hashim, M. A.; Hussain, M. A. Electrochemical approaches to the production of graphene flakes and their potential applications. *Carbon N. Y.* **2013**, *54*, 1–11, doi:10.1016/j.carbon.2012.11.030.
140. Abdelkader, A. M.; Cooper, A. J.; Dryfe, R. A. W.; Kinloch, I. A. How to get between the sheets: A review of recent works on the electrochemical exfoliation of graphene materials from bulk graphite. *Nanoscale* **2015**, *7*, 6944–6956, doi:10.1039/c4nr06942k.
141. Parvez, K.; Wu, Z.; Li, R.; Liu, X.; Graf, R. Exfoliation of Graphite into Graphene in Aqueous Solutions. *J. Am. Chem. Soc.* **2014**, *136*, 6083–6091, doi:10.1021/ja5017156.
142. Cooper, A. J.; Wilson, N. R.; Kinloch, I. A.; Dryfe, R. A. W. Single stage electrochemical exfoliation method for the production of few-layer graphene via intercalation of tetraalkylammonium cations. *Carbon N. Y.* **2014**, *66*, 340–350, doi:10.1016/j.carbon.2013.09.009.
143. Rummeli, M. H.; Rocha, C. G.; Ortmann, F.; Ibrahim, I.; Sevincli, H.; Börrnert, F.; Kunstmann, J.; Bachmatiuk, A.; Pötschke, M.; Shiraishi, M.; Meyyappan, M.; Büchner, B.; Roche, S.; Cuniberti, G. Graphene: Piecing it together. *Adv. Mater.* **2011**, *23*, 4471–4490, doi:10.1002/adma.201101855.
144. Somani, P. R.; Somani, S. P.; Umeno, M. Planer nano-graphenes from camphor by CVD. *Chem. Phys. Lett.* **2006**, *430*, 56–59, doi:10.1016/j.cplett.2006.06.081.
145. Bhaviripudi, S.; Jia, X.; Dresselhaus, M. S.; Kong, J. Role of kinetic factors in chemical vapor deposition synthesis of uniform large area graphene using copper catalyst. *Nano Lett.* **2010**, *10*, 4128–4133, doi:10.1021/nl102355e.
146. Chae, S. J.; Güneş, F.; Kim, K. K.; Kim, E. S.; Han, G. H.; Kim, S. M.; Shin, H.; Yoon, S. M.; Choi, J. Y.; Park, M. H.; Yang, C. W.; Pribat, D.;

- Lee, Y. H. Synthesis of large-area graphene layers on poly-nickel substrate by chemical vapor deposition: Wrinkle formation. *Adv. Mater.* **2009**, *21*, 2328–2333, doi:10.1002/adma.200803016.
147. Lee, S.; Lee, K.; Zhong, Z. Wafer scale homogeneous bilayer graphene films by chemical vapor deposition. *Nano Lett.* **2010**, *10*, 4702–7, doi:10.1021/nl1029978.
  148. Wang, X.; Li, J.; Zhong, Q.; Zhong, Y.; Zhao, M. Wafer-scale synthesis and transfer of monolayer graphene. *Proc. IEEE Conf. Nanotechnol.* **2013**, *10*, 652–655, doi:10.1109/NANO.2013.6720807.
  149. Qu, L. T.; Liu, Y.; Baek, J. B.; Dai, L. M. Nitrogen-Doped Graphene as Efficient Metal-Free Electrocatalyst for Oxygen Reduction in Fuel Cells. *ACS Nano* **2010**, *4*, 1321–1326, doi:10.1021/nn901850u.
  150. Leela, A.; Reddy, M.; Srivastava, A.; Gowda, S. R.; Gullapalli, H.; Dubey, M.; Ajayan, P. M. Synthesis Of Nitrogen-Doped Graphene. *ACS Nano* **2010**, *4*, 6337–6342, doi:10.1021/nn101926g.
  151. Wang, J. J.; Zhu, M.; Outlaw, R. A.; Zhao, X. Free-standing subnanometer graphite sheets. *Appl. Phys. Lett.* **2004**, *85*, 1265–1267.
  152. Wang, J.; Zhu, M.; Outlaw, R. A.; Zhao, X.; Manos, D. M.; Holloway, B. C. Synthesis of carbon nanosheets by inductively coupled radio-frequency plasma enhanced chemical vapor deposition. *Carbon N. Y.* **2004**, *42*, 2867–2872, doi:10.1016/j.carbon.2004.06.035.
  153. Varchon, F.; Feng, R.; Hass, J.; Li, X.; Nguyen, B. N.; Naud, C.; Mallet, P.; Veillen, J. Y.; Berger, C.; Conrad, E. H.; Magaud, L. Electronic structure of epitaxial graphene layers on SiC: effect of the substrate. **2007**, doi:10.1103/PhysRevLett.99.126805.
  154. Tedesco, J. L.; Jernigan, G. G.; Culbertson, J. C.; Hite, J. K.; Yang, Y.; Daniels, K. M.; Myers-Ward, R. L.; Eddy, C. R.; Robinson, J. A.; Trumbull, K. A.; Wetherington, M. T.; Campbell, P. M.; Gaskill, D. K. Morphology characterization of argon-mediated epitaxial graphene on C-face SiC. *Appl. Phys. Lett.* **2010**, *96*, 1–12, doi:10.1063/1.3442903.
  155. Emtsev, K. V.; Bostwick, A.; Horn, K.; Jobst, J.; Kellogg, G. L.; Ley, L.; McChesney, J. L.; Ohta, T.; Reshanov, S. A.; Röhrl, J.; Rotenberg, E.; Schmid, A. K.; Waldmann, D.; Weber, H. B.; Seyller, T. Towards wafer-size graphene layers by atmospheric pressure graphitization of silicon carbide. *Nat. Mater.* **2009**, *8*, 203–207, doi:10.1038/nmat2382.
  156. Vázquez De Parga, A. L.; Calleja, F.; Borca, B.; Passeggi, M. C. G.; Hinarejos, J. J.; Guinea, F.; Miranda, R. Periodically rippled graphene: Growth and spatially resolved electronic structure. *Phys. Rev. Lett.* **2008**, *100*, 1–5, doi:10.1103/PhysRevLett.100.056807.
  157. Sutter, P. W.; Flege, J. I.; Sutter, E. A. Epitaxial graphene on ruthenium. *Nat. Mater.* **2008**, *7*, 406–411, doi:10.1038/nmat2166.
  158. Dreyer, D. . The chemistry of graphene oxide. *Chem. Soc. Rev.* **2010**, *39*, 228–240.

159. Schniepp, H. C.; Li, J. L.; McAllister, M. J.; Sai, H.; Herrera-Alonson, M.; Adamson, D. H.; Prud'homme, R. K.; Car, R.; Seville, D. A.; Aksay, I. A. Functionalized single graphene sheets derived from splitting graphite oxide. *J. Phys. Chem. B* **2006**, *110*, 8535–8539, doi:10.1021/jp060936f.
160. Singh, V.; Joung, D.; Zhai, L.; Das, S.; Khondaker, S. I.; Seal, S. Graphene based materials: Past, present and future. *Prog. Mater. Sci.* **2011**, *56*, 1178–1271, doi:10.1016/j.pmatsci.2011.03.003.
161. Hummers, W. . Preparation of graphitic oxide. *J. Chem. Soc.* **1958**, *80*, 1339–1339.
162. Parades, J. I.; Villar-Rodil, S.; Martínez-Alonso, A.; Tascón, J. M. D. Graphene oxide dispersions in organic solvents. *Langmuir* **2008**, *24*, 10560–10564, doi:10.1021/la801744a.
163. Becerril HA, Man J, Liu Z, Stoltenberg RM, Bao Z, C. Y. Evaluation of Solution-Processed Reduced Graphene Oxide Films as Transparent Conductors. *ACS Nano* **2008**, *2*, 463–470.
164. Eda, G.; Fanchini, G.; Chhowalla, M. Large-area ultrathin films of reduced graphene oxide as a transparent and flexible electronic material. *Nat. Nanotechnol.* **2008**, *3*, 270–274, doi:10.1038/nnano.2008.83.
165. Lee, C. G.; Park, S.; Ruoff, R. S.; Dodabalapur, A. Integration of reduced graphene oxide into organic field-effect transistors as conducting electrodes and as a metal modification layer. *Appl. Phys. Lett.* **2009**, *95*, 3–5, doi:10.1063/1.3176216.
166. Bourlinos, A. B.; Gournis, D.; Petridis, D.; Szabo, T.; Szeri, A.; Dekany, I. Graphite oxide: Chemical reduction to graphite and surface modification with primary aliphatic amines and amino acids. *Langmuir* **2003**, *19*, 6050–6055, doi:10.1021/la026525h.
167. Shin, H. J.; Kim, K. K.; Benayad, A.; Yoon, S. M.; Park, H. K.; Jung, I. S.; Jin, M. H.; Jeong, H. K.; Kim, J. M.; Choi, J. Y.; Lee, Y. H. Efficient reduction of graphite oxide by sodium borohydride and its effect on electrical conductance. *Adv. Funct. Mater.* **2009**, *19*, 1987–1992, doi:10.1002/adfm.200900167.
168. Si, Y.; Samulski, E. T. Synthesis of water soluble graphene. *Nano Lett.* **2008**, *8*, 1679–82, doi:10.1021/nl080604h.
169. Guoxiu Wang, Juan Yang, Jinsoo Park, Xinglong Gou, Bei Wang, H. L. and J. Y. Facile Synthesis and Characterization of Graphene Nanosheets. *J. Phys. Chem. C* **2008**, *112*, 8192–8195.
170. Dua, V.; Surwade, S. P.; Ammu, S.; Agnihotra, S. R.; Jain, S.; Roberts, K. E.; Park, S.; Ruoff, R. S.; Manohar, S. K. All-organic vapor sensor using inkjet-printed reduced graphene oxide. *Angew. Chemie - Int. Ed.* **2010**, *49*, 2154–2157, doi:10.1002/anie.200905089.
171. Stankovich, S.; Piner, R. D.; Chen, X.; Wu, N.; Nguyen, S. T.; Ruoff, R.

- S. Stable aqueous dispersions of graphitic nanoplatelets via the reduction of exfoliated graphite oxide in the presence of poly(sodium 4-styrenesulfonate). *J. Mater. Chem.* **2006**, *16*, 155–158, doi:10.1039/b512799h.
172. McAllister, M. J.; Abdala, A. A. Single Sheet Functionalized Graphene by Oxidation and Thermal Expansion of Graphite. *Chem. Mater.* **2007**, *19*, 4396–4404.
  173. Schniepp, H. C.; Li, J. L.; McAllister, M. J.; Sai, H.; Herrera-Alonson, M.; Adamson, D. H.; Prud'homme, R. K.; Car, R.; Seville, D. A.; Aksay, I. A. Functionalized single graphene sheets derived from splitting graphite oxide. *J. Phys. Chem. B* **2006**, *110*, 8535–8539, doi:10.1021/jp060936f.
  174. Dubin S, Gilje S, Wang K, Tung VC, Cha K, H. A. A one-step, solvothermal reduction method for producing reduced graphene oxide dispersions in organic solvents. *ACS Nano* **2010**, *4*, 3845–3852.
  175. Xu, Y.; Liu, Z.; Zhang, X.; Wang, Y.; Tian, J.; Huang, Y.; Ma, Y.; Zhang, X.; Chen, Y. A graphene hybrid material covalently functionalized with porphyrin: Synthesis and optical limiting property. *Adv. Mater.* **2009**, *21*, 1275–1279, doi:10.1002/adma.200801617.
  176. Zhuang Liu, Joshua T. Robinson, Xiaoming Sun, and H. D. PEGylated Nano-Graphene Oxide for Delivery of Water Insoluble Cancer Drugs. *J. Am. Chem. Soc.* **2008**, *130*, 10876–10877.
  177. Bai, H.; Xu, Y.; Zhao, L.; Li, C.; Shi, G. Non-covalent functionalization of graphene sheets by sulfonated polyaniline. *Chem. Commun.* **2009**, 1667–1669, doi:10.1039/b821805f.
  178. Qi, X.; Pu, K. Y.; Zhou, X.; Li, H.; Liu, B.; Boey, F.; Huang, W.; Zhang, H. Conjugated-polyelectrolyte-functionalized reduced graphene oxide with excellent solubility and stability in polar solvents. *Small* **2010**, *6*, 663–669, doi:10.1002/smll.200902221.
  179. Geng J, J. H.-T. Porphyrin Functionalized Graphene Sheets in Aqueous Suspensions: From the Preparation of Graphene Sheets to Highly Conductive Graphene Films. *J. Phys. Chem. C* **2010**, *114*, 8227–8234.
  180. Yang Q, Pan X, Huang F, L. K. Fabrication of High-Concentration and Stable Aqueous Suspensions of Graphene Nanosheets by Noncovalent Functionalization with Lignin and Cellulose Derivatives. *J. Phys. Chem. C* **2010**, *114*, 3811–3816.
  181. Li, G.; Xiong, B. Effects of graphene content on microstructures and tensile property of graphene-nanosheets / aluminum composites. *J. Alloys Compd.* **2017**, *697*, 31–36, doi:10.1016/j.jallcom.2016.12.147.
  182. Bartolucci, S. F.; Paras, J.; Rafiee, M. a.; Rafiee, J.; Lee, S.; Kapoor, D.; Koratkar, N. Graphene–aluminum nanocomposites. *Mater. Sci. Eng. A* **2011**, *528*, 7933–7937, doi:10.1016/j.msea.2011.07.043.
  183. Suryanarayana, C.; Ivanov, E.; Boldyrev, V. V. The science and technology of mechanical alloying. *Mater. Sci. Eng. A* **2001**, *304*–306,

151–158, doi:10.1016/S0921-5093(00)01465-9.

184. Zhang, Q. Q.; Wu, G. Q.; Huang, Z.; Tao, Y. Effects of particle/matrix interfaces on the mechanical properties for SiCpor YAl<sub>2</sub>preinforced Mg-Li composites. *J. Alloys Compd.* **2014**, *588*, 1–6, doi:10.1016/j.jallcom.2013.11.004.
185. Tabandeh-Khorshid, M.; Omrani, E.; Menezes, P. L.; Rohatgi, P. K. Tribological performance of self-lubricating aluminum matrix nanocomposites: Role of graphene nanoplatelets. *Eng. Sci. Technol. an Int. J.* **2016**, *19*, 463–469, doi:10.1016/j.jestch.2015.09.005.
186. Rashad, M.; Pan, F.; Tang, A.; Asif, M. Effect of Graphene Nanoplatelets addition on mechanical properties of pure aluminum using a semi-powder method. *Prog. Nat. Sci. Mater. Int.* **2014**, *24*, 101–108, doi:10.1016/j.pnsc.2014.03.012.
187. Gürbüz, M.; Can Şenel, M.; Koç, E. The effect of sintering time, temperature, and graphene addition on the hardness and microstructure of aluminum composites. *J. Compos. Mater.* **2017**, 002199831774020, doi:10.1177/0021998317740200.
188. Khan, M.; Amjad, M.; Khan, A.; Ud-Din, R.; Ahmad, I.; Subhani, T. Microstructural evolution, mechanical profile, and fracture morphology of aluminum matrix composites containing graphene nanoplatelets. *J. Mater. Res.* **2017**, *32*, 2055–2066, doi:10.1557/jmr.2017.111.
189. Yang, W.; Zhao, Q.; Xin, L.; Qiao, J.; Zou, J.; Shao, P.; Yu, Z.; Zhang, Q.; Wu, G. Microstructure and mechanical properties of graphene nanoplates reinforced pure Al matrix composites prepared by pressure infiltration method. *J. Alloys Compd.* **2018**, *732*, 748–758, doi:10.1016/j.jallcom.2017.10.283.
190. Jinghang Liu, Bea Fernandez, Pablo Rodriguez, Sumsun Naher, Brabazon, D. Powder processing methodology for production of graphene oxide reinforced aluminium matrix composites. *Adv. Mater. Process. Technol.* **2016**, *2(4)*, 437–450.
191. Zhang, J.; Chen, Z.; Zhao, J.; Jiang, Z. Microstructure and mechanical properties of aluminium-graphene composite powders produced by mechanical milling. **2018**.
192. Baig, Z.; Mamat, O.; Mustapha, M.; Mumtaz, A.; Ali, S.; Sarfraz, M. Surfactant-decorated graphite nanoplatelets (GNPs) reinforced aluminum nanocomposites: sintering effects on hardness and wear. *Int. J. Miner. Metall. Mater.* **2018**, *25*, 704–715, doi:10.1007/s12613-018-1618-3.
193. Kwon, H.; Mondal, J.; AloGab, K.; Sammelseig, V.; Takamichi, M.; Kawaski, A.; Leparoux, M. Graphene oxide-reinforced aluminum alloy matrix composite materials fabricated by powder metallurgy. *J. Alloys Compd.* **2017**, *698*, 807–813, doi:10.1016/j.jallcom.2016.12.179.
194. Ewen Smith, G. D. *Modern Raman Spectroscopy: A Practical Approach*; **2013**.

195. Ferrari, A.; Basko, D. Raman spectroscopy as a versatile tool for studying the properties of graphene. *Nat. Nanotechnol.* **2013**, *8*, 235–46, doi:10.1038/nnano.2013.46.
196. Timoshenko, S.; Woinosky-Krieger, S. *Theory of Plates and Shells Classic.* **1959**, 580.
197. Hearn, E. J. *Mechanics of Materials 2: The mechanics of elastic and plastic deformation of solids and structural materials*; 1997;
198. Kim, H. S.; Hong, S. I.; Kim, S. J. On the rule of mixtures for predicting the mechanical properties of composites with homogeneously distributed soft and hard particles. *J. Mater. Process. Technol.* **2001**, *112*, 109–113, doi:10.1016/S0924-0136(01)00565-9.
199. Park, S.; An, J.; Jung, I.; Piner, R. D.; An, S. J.; Li, X.; Velamakanni, A.; Ruoff, R. S. Colloidal suspensions of highly reduced graphene oxide in a wide variety of organic solvents. *Nano Lett.* **2009**, *9*, 1593–1597, doi:10.1021/nl803798y.
200. Haar, S.; El Gemayel, M.; Shin, Y.; Melinte, G.; Squillaci, M. A.; Ersen, O.; Casiraghi, C.; Ciesielski, A.; Samorì, P. Enhancing the Liquid-Phase Exfoliation of Graphene in Organic Solvents upon Addition of n-Octylbenzene. *Sci. Rep.* **2015**, *5*, 1–9, doi:10.1038/srep16684.
201. Jing, N.; Xue, Q.; Ling, C.; Shan, M.; Zhang, T.; Zhou, X.; Jiao, Z. Effect of defects on Young's modulus of graphene sheets: A molecular dynamics simulation. *RSC Adv.* **2012**, *2*, 9124–9129, doi:10.1039/c2ra21228e.
202. Prabu, S. B.; Karunamoorthy, L.; Kathiresan, S.; Mohan, B. Influence of stirring speed and stirring time on distribution of particles in cast metal matrix composite. *J. Mater. Process. Technol.* **2006**, *171*, 268–273, doi:10.1016/j.jmatprotec.2005.06.071.
203. Sudarshan; Surappa, M. K. Synthesis of fly ash particle reinforced A356 Al composites and their characterization. *Mater. Sci. Eng. A* **2008**, *480*, 117–124, doi:10.1016/j.wear.2007.11.009.
204. Saboori, A.; Pavese, M.; Badini, C.; Fino, P. Microstructure and thermal conductivity of al-graphene composites fabricated by powder metallurgy and hot rolling techniques. *Acta Metall. Sin. (English Lett.)* **2017**, *30*, 675–687, doi:10.1007/s40195-017-0579-2.
205. Rashad, M.; Pan, F.; Tang, A.; Lu, Y.; Asif, M.; Hussain, S.; She, J.; Gou, J.; Mao, J. Effect of graphene nanoplatelets (GNPs) addition on strength and ductility of magnesium-titanium alloys. *J. Magnes. Alloy.* **2013**, *1*, 242–248, doi:10.1016/j.jma.2013.09.004.
206. Graphenea Product Datasheet Graphenea Reduced Graphene Oxide (rGO).  
[https://cdn.shopify.com/s/files/1/0191/2296/files/Graphenea\\_rGO\\_Data sheet\\_2016-03-15.pdf?2554876021307449506](https://cdn.shopify.com/s/files/1/0191/2296/files/Graphenea_rGO_Data_sheet_2016-03-15.pdf?2554876021307449506) 22.
207. Thema, F. T.; Moloto, M. . Synthesis and characterization of graphene

thin films by chemical reduction of exfoliated and intercalated graphite oxide. *J. Chem.* **2012**, *2013*, 1–6.

208. Tian, W.; Li, S.; Wang, B.; Chen, X.; Liu, J.; Yu, M. Graphene-reinforced aluminum matrix composites prepared by spark plasma sintering. *Int. J. Miner. Metall. Mater.* **2016**, *23*, 723–729, doi:10.1007/s12613-016-1286-0.
209. Ahmad, I.; Islam, M.; Subhani, T.; Zhu, Y. Characterization of GNP-Containing Al<sub>2</sub>O<sub>3</sub>Nanocomposites Fabricated via High Frequency-Induction Heat Sintering Route. *J. Mater. Eng. Perform.* **2015**, *24*, 4236–4243, doi:10.1007/s11665-015-1738-0.
210. Ahmad, I.; Islam, M.; Abdo, H. S.; Subhani, T.; Khalil, K. A.; Almajid, A. A.; Yazdani, B.; Zhu, Y. Toughening mechanisms and mechanical properties of graphene nanosheet-reinforced alumina. *Mater. Des.* **2015**, *88*, 1234–1243, doi:10.1016/j.matdes.2015.09.125.
211. Bastwros, M.; Kim, G. Y.; Zhu, C.; Zhang, K.; Wang, S.; Tang, X.; Wang, X. Effect of ball milling on graphene reinforced Al6061 composite fabricated by semi-solid sintering. *Compos. Part B Eng.* **2014**, *60*, 111–118, doi:10.1016/j.compositesb.2013.12.043.
212. Zhang, H.; Xu, C.; Xiao, W.; Ameyama, K.; Ma, C. Enhanced mechanical properties of Al5083 alloy with graphene nanoplates prepared by ball milling and hot extrusion. *Mater. Sci. Eng. A* **2016**, *658*, 8–15, doi:10.1016/j.msea.2016.01.076.
213. Eda, G.; Chhowalla, M. Chemically derived graphene oxide: Towards large-area thin-film electronics and optoelectronics. *Adv. Mater.* **2010**, *22*, 2392–2415, doi:10.1002/adma.200903689.
214. Shih, C.-J. Understanding the pH-Dependent Behavior of Graphene Oxide Aqueous Solutions: A Comparative Experimental and Molecular Dynamics Simulation Study. *Langmuir* **2012**, *28*, 235–241.
215. Chen, W.; Yan, L.; Bangal, P. R. Preparation of graphene by the rapid and mild thermal reduction of graphene oxide induced by microwaves. *Carbon N. Y.* **2010**, *48*, 1146–1152, doi:10.1016/j.carbon.2009.11.037.
216. Singh, V.; Joung, D.; Zhai, L.; Das, S.; Khondaker, S. I.; Seal, S. Graphene based materials: Past, present and future. *Prog. Mater. Sci.* **2011**, *56*, 1178–1271, doi:10.1016/j.pmatsci.2011.03.003.
217. Macmillan *Introduction to organic spectroscopy*; **1987**.
218. Su, Y.; Li, Z.; Yu, Y.; Zhao, L.; Li, Z.; Guo, Q.; Xiong, D.; Zhang, D. Composite structural modeling and tensile mechanical behavior of graphene reinforced metal matrix composites. *Sci. China Mater.* **2018**, *61*, 112–124, doi:10.1007/s40843-017-9142-2.
219. Gao, C.; Zhan, B.; Chen, L.; Li, X. A micromechanical model of graphene-reinforced metal matrix nanocomposites with consideration of graphene orientations. *Compos. Sci. Technol.* **2017**, *152*, 120–128, doi:10.1016/j.compscitech.2017.09.010.

# APPENDICES

## A1 Modelling of graphene reinforced Al composites

### A1.1 Introduction

The model proposed in this chapter was the initial model developed while working with the graphene reinforced Al composites. This model was based on considering a representative volumetric element (RVE) representing the composite. Chang et al. [1] developed theoretical predictive models of the electrical resistivity of metal matrix composites with different reinforcements (continuous fibers, whiskers and particulate) and they verified their results with the experimental data. Both model and experimental values followed the same trend of enhancing mechanical properties with increasing reinforcement levels. The composite cells considered for their study are shown in Figure A1.1. Figure A1.1 (a) and (b) show the particulate reinforced composite and continuous fiber reinforced cells respectively. Fibers were aligned in the longitudinal direction. There is no evidence of similar types of models having been applied for conductivity analysis for graphene nanosheets. Georgios et al. [2] have reported the application of RVE to predict the effective properties of graphene-based composite in which epoxy was used as a base material and various vol% of graphene i.e., from 0.02 to 0.1 was used as a reinforcement, a linear enhancement of stiffness was observed even at the lower vol% of graphene reinforcement.

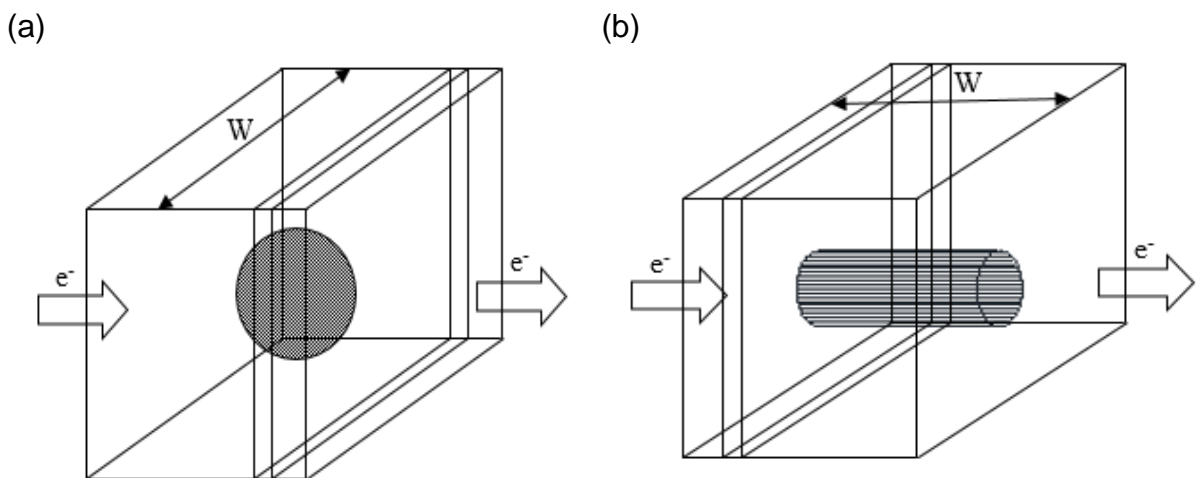


Figure A1.1: Schematic representation of composite cells of (a) particulate reinforced composite, and (b) Continuous fiber reinforced composite [3].

The possible effects of reinforcing a material can be understood by conducting difficult and time consuming experimental work which involves a lot of cost. Simulation validated by previous experimental work provides an alternate route to understand the selection and optimisation of reinforcement in a particle reinforced metal matrix composite. Therefore, an attempt was made to predict the effectiveness of graphene reinforcement on the properties of Young's modulus, Poisson's ratio and conductivity of the composite materials using the finite element method. Modelling work was performed with aluminium as the matrix metal for this study.

The modelling of a composite material can be accomplished using two different techniques. One is continuum modelling which assumes continuous material structure and the second is molecular which considers the molecular behaviour to obtain the overall global response. To achieve the present modelling objective, a micromechanical analogy associated with FE method was applied for graphene reinforced metal matrix composite. The properties such as Young's modulus, Poisson's ratio and tensile strength of composites with different volume fraction of graphene reinforcement (0.1, 0.2, 0.5, 1, and 2%) were examined. The FE model was constructed with different element sizes during meshing in order to test for an ensure mesh convergence. The tensile strength of graphene reinforced aluminium composite at different volume fractions of reinforcement was predicted using the FE based ANSYS mechanical APDL and the results were compared with experimental results done in the current work and also from the literature. Simulation results were also verified with other theoretical methods like ROM and Bettie's reciprocal theorem. After verification, the analysis was extended to examine different metal matrix materials using graphene as the reinforcement to predict the longitudinal and transverse properties of the composite. The analysis is focussed to predict the electrical properties of the composite i.e., effective electrical conductivity of the composite with different cross-sectional areas. Conductance was predicted taking account of the various levels of volume fractions of reinforcement. To achieve this, the same model that considered for the mechanical property analysis is used to predict the effective properties of composite such as resistivity, conductivity.

### A1.1.1 Model set-up

The present problem is solved in 2 steps, the first step includes the modelling of Representative Volumetric Element (RVE) to predict effective properties of composite material, and second step includes modelling of tensile testing specimen to predict tensile strength of the materials. The model was developed based on a micromechanical approach used a rectangular shaped RVE was considered. The mechanical response of graphene for small sizes is strongly size dependent [4]. Graphene was idealised as a plate geometry with a thickness of 0.34nm. Figure A1.2 (a) shows the schematic representation of RVE considered for the analysis, where  $L_m$ ,  $W_m$ ,  $t_m$  represents the length, width and thickness of matrix respectively and  $L_r$ ,  $W_r$ ,  $t_r$  represents the gauge length, width and thickness of reinforcement respectively. The dimensions of the RVE is the same as the dimensions of the matrix and are fixed at 10mm x10mm x 1mm. The length and width of the graphene sheet are calculated based on volume percentage of reinforcement and dimensions of matrix using equation A1.1.

$$V_r = \frac{(w_r \times L_r \times t_r)}{((w_r \times L_r \times t_r) + (w_m \times L_m \times t_m))} \quad \text{----- (A1.1)}$$

Figure A1.2 (b) represents the schematic representation of extruded rod with gauge length of  $L_g$  (25mm) and diameter of  $d$  (5mm), the model is based on control displacement loading with strain rate of  $1e^{-3}/\text{sec}$ . the model is then divided into finite number of nodes for accurate results, with 100 steps and 10000 sub steps.

Due to the symmetry in the geometry, the boundary conditions and loading was applied on a one quarter portion of the RVE to increase computation speed. The element used for the present analysis was SOLID 185 of ANSYS, based on 3D elasticity theory. This was divided into various numbers of nodes, depending on resolution, with three degrees of freedom at each node. A screen shot of the meshed RVE modelled is shown in Figure A1.3 (a), shows a typical finite element mesh of the model for a composite with 2% volume fraction of

graphene as reinforcement within aluminium as matrix. Figure A1.3 (b) shows the converged FE model of extruded rod.

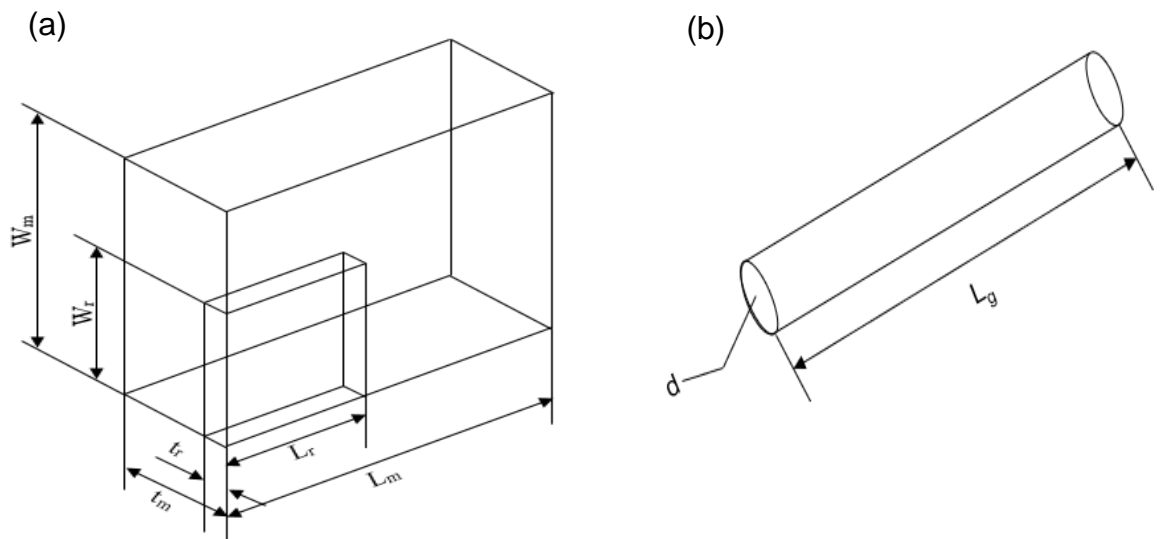


Figure A1.2: Schematic representation of models used in present study (a) RVE, (b) extruded rod to predict tensile strength.

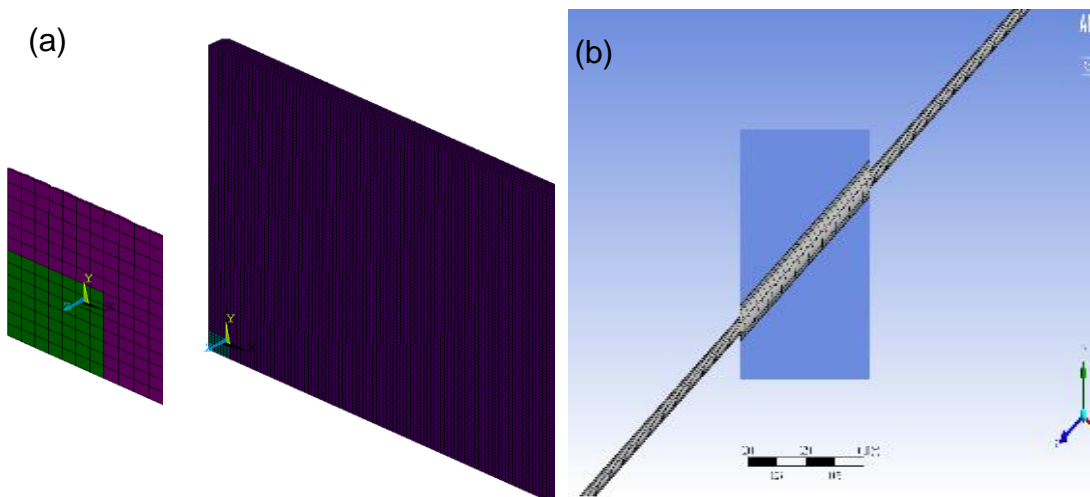


Figure A1.3: (a) Converged FE model of graphene reinforced aluminium composite, and (b) FE model of extruded rod.

### A1.1.2 Materials

The properties of graphene used for the present analysis were a Young's modulus of 1TPa, a Poisson's ratio of 0.186, and a conductivity of  $1 \times 10^8 \text{S/m}$  at  $20^\circ\text{C}$ . All models developed in this study has a constant thickness of 0.34nm for graphene. The list of materials and their properties that were examined as matrix materials is given based on decreasing conductivity in Table A1.1. The

properties of GO and rGO were set as Young's moduli and thicknesses of 444.8GPa, 0.7nm [6] and  $0.25 \pm 0.15$ TPa, 1nm [7].

Table A1.1: Matrix materials and properties as applied in the study.

Matrix (Metal)	Young's modulus (GPa)	Poisson's ratio	Conductivity (S/m) at 20°C ( $\times 10^6$ )
Cu	110	0.34	59.5
Al	70	0.35	35.5
Ti	116	0.32	2.38
Mg	45	0.29	2.07
Ni	200	0.31	14.7
Fe	211	0.29	10.0

#### *A.1.1.3 Boundary conditions*

The following assumptions were made for the model set-up.

- The composite considered for the analysis is free of voids
- Matrix is homogeneously reinforced with the reinforcement
- The load applied on the composite is within the elastic limit
- The composite cell represents the whole composite
- The reinforcement and the matrix are perfectly bonded
- There is no interfacial layer in between the matrix and reinforcement
- The flow of current is by free electron migration

Due to the symmetry of the problem, the following symmetric boundary conditions were also applied, at  $X=0$   $U_x=0$ ; at  $Y=0$ ,  $U_y=0$ ; at  $Z=0$   $U_z=0$  and on the positive faces (X, Y & Z) of RVE, multipoint constraints were imposed. A uniform tensile load of 1MPa was applied on the positive Z-plane and for the electrical analysis a current of 100A was applied while resistivity and conductivity were calculated.

#### **A1.2 Analytical solution**

The mechanical properties of the graphene reinforced metal matrix composites were predicted and then verified using the following two theoretical methods.

### A1.2.1 Rule of mixture (ROM)

Rule of mixtures was used to calculate the effective properties of the fiber reinforced composite. In general the value obtained from ROM gives the overall property values in direction parallel to the fibers. The formulae used to calculate longitudinal Young's modulus was,

$$E_c = fE_f + (1 - f)E_m \quad \text{----- (A1.2)}$$

where,

$$f = \frac{V_f}{(V_f + V_m)} \text{ is the volume fraction}$$

The general equations to solve Young's modulus are given as

Young's modulus in fibre direction,

$$E_1 = \sigma_1 / \varepsilon_1 \quad \text{----- (A1.3)}$$

Young's modulus in transverse direction,

$$E_2 = \sigma_2 / \varepsilon_2 \quad \text{----- (A1.4)}$$

where,

$V_f$  is Volume fraction of fibre;

$V_m$  is Volume fraction of matrix;

$E_f$  is Young's modulus in fibre direction; and

$E_m$  is Young's modulus in matrix direction.

Equations to calculate the electrical conductivity of the composite (neglecting voids) are given below as [8], longitudinal electrical conductivity,

$$Ke_{111} = K_f Ke_{f11} + K_m Ke_m \quad \text{----- (A1.5)}$$

and transverse electrical conductivity,

$$Ke_{122} = (1 - \sqrt{K_v}) + \left( \frac{\sqrt{K_f} Ke_m}{1 - \sqrt{K_f} \left(1 - \frac{Ke_m}{Ke_{f22}}\right)} \right) \quad \text{----- (A1.6)}$$

where,

$Ke_m$  is Electrical conductivity of matrix;

$k_m$  is Matrix volume fraction of composite;

$k_f$  is Fibre volume fraction of composite;  
 $K_{el11}$  is Lamina longitudinal electrical conductivity;  
 $K_{el22}$  is Lamina transverse electrical conductivity

### ***A1.2.2 Bettie's Reciprocal Theorem***

Bettie's reciprocal theorem states that whenever an object is subjected to tensile loading, the ratio of longitudinal Young's modulus to major Poisson's ratio will be equal to the ratio of transverse Young's modulus to minor Poisson's ratio [9] i.e.,

$$E_1/v_{12} = E_2/v_{21} \quad \text{----- (A1.7)}$$

where,

$v_{12}$  is Major Poisson's ratio; the ratio of normal strain in transverse direction to the normal strain in longitudinal direction when load is applied in longitudinal direction; and

$v_{21}$  is Minor Poisson's ratio; the ratio of normal strain in longitudinal direction to the normal strain in transverse direction when load is applied in transverse direction.

### ***A1.3 Results***

The models were developed and tested to ensure solution convergence. The models were then verified with theoretical method and validated using experimental data reported in previous work [10]. Figure A1.4 shows the stress/strain comparison between the experimental and prediction results for pure aluminium. From the stress-strain graph, it is clear that there is a very good agreement between the experimental and simulated results which shows that the boundary conditions and the modelling approach were accurate and provides confidence in predicted results presented in this report. Figure A1.5 shows the comparison of electrical conductivity of GO/Al at different volume percentage of GO reinforcement. There is nearly 6% of variation in between the experimental and ANSYS results and the variation increased with increase in volume percentage of GO. This is due to the formation of  $Al_2O_3$  which increases the resistivity of the composite on the other hand there is no evidence of  $Al_4C_3$ .

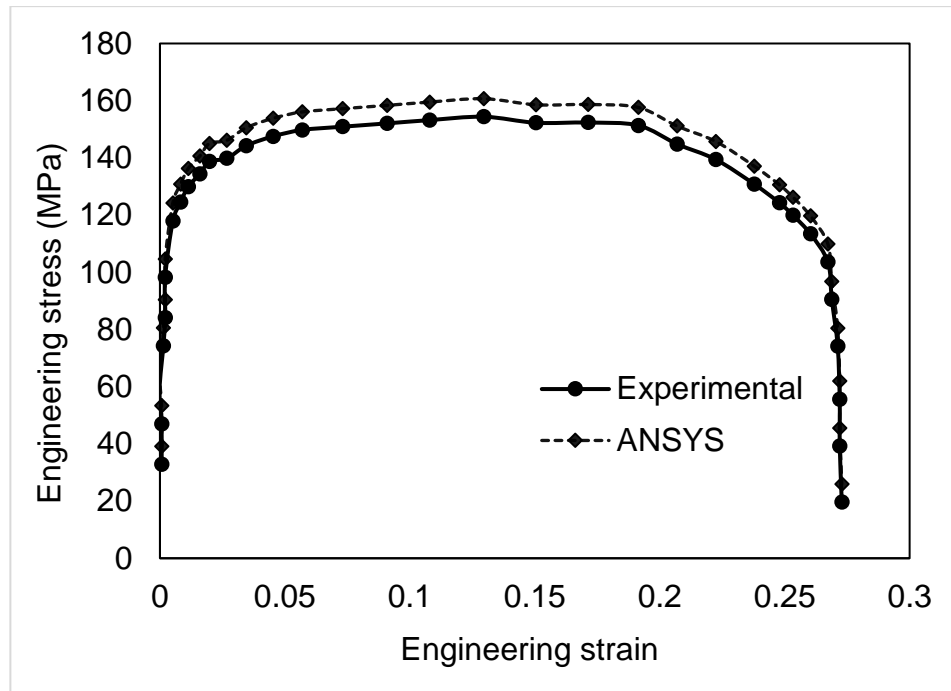


Figure A1.4: Comparison of experimental and simulated values for pure Al. The Verification of ANSYS results with theoretical methods ROM and Bettie's reciprocal theorems are presented in Figure A1.5. For the verification of the results Al matrix at different volume fractions of reinforcement of graphene is considered. The longitudinal Young's modulus of the graphene reinforced Al matrix composites is predicted at various volume fraction of reinforcement and are shown in Figure A1.5 (a) and the plots drawn using simulated values and values calculated from ROM overlap with each other with very good agreement; this could be due to the assumptions made for this analysis that are like the theoretical cases. Whereas, for the verification of the transverse properties of graphene reinforced Al composites, the Bettie's reciprocal theorem was used, and the results are shown in Figure A1.5 (b).

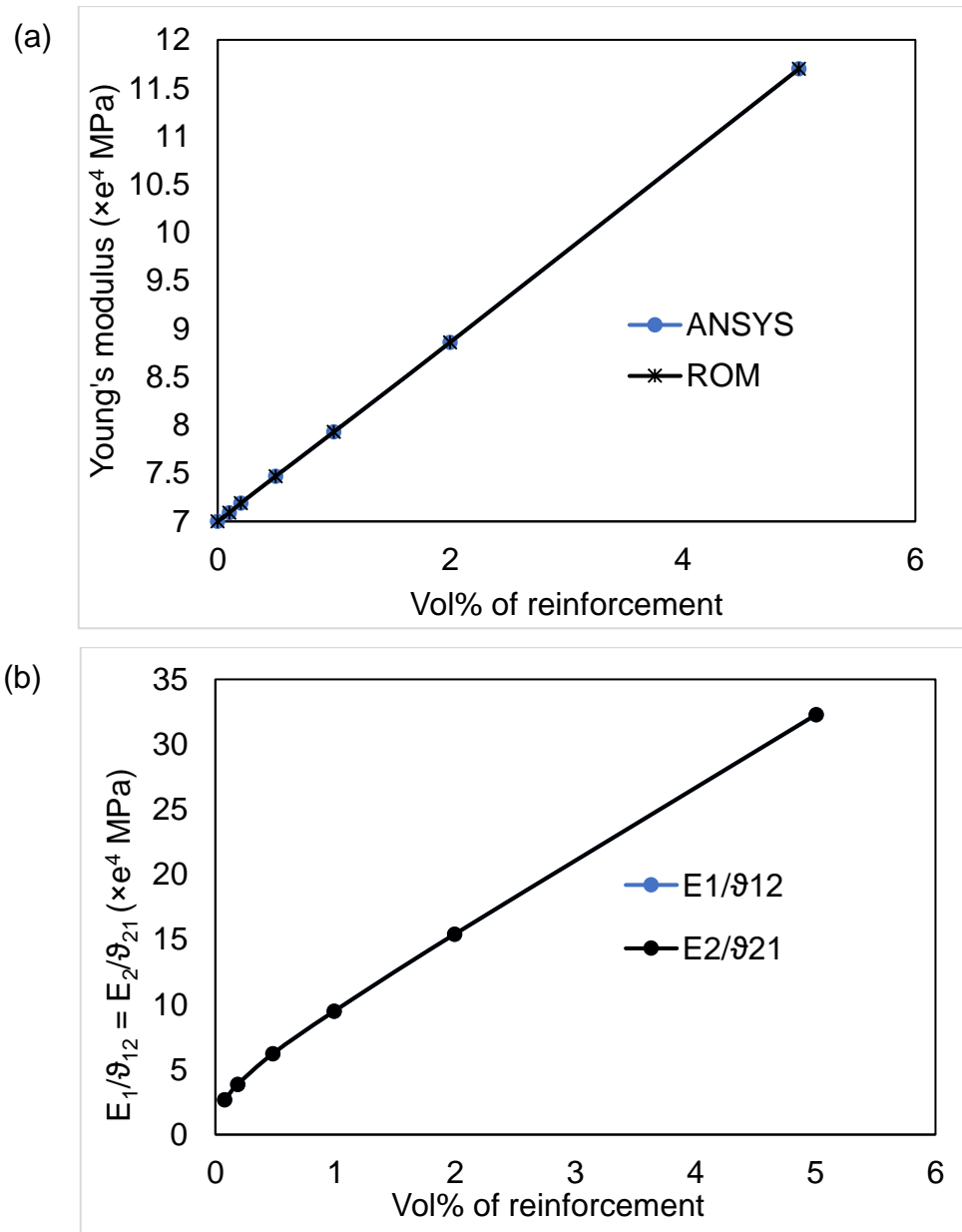


Figure A1.5: Verification of simulation results with theoretical methods (a) ROM, and (b) Bettie's reciprocal theorem.

The transverse Young's modulus, major and minor Poisson's ratio of the composite are obtained from the simulation. The ratios of longitudinal Young's modulus to the major Poisson's ratio and transverse Young's modulus to the major Poisson's ratio are calculated from the values obtained from simulation and the values shows a very good agreement with the Bettie's reciprocal theorem. From Figure A1.5, it can be concluded that the model was well verified against the theoretical model results.

Once the model is validated and verified, the analysis is extended to different matrix materials that include Mg, Ti, Ni, Cu and Fe. The longitudinal Young's modulus of the mentioned matrix materials at different volume fraction of reinforcement is obtained by simulation and a linear increment in values is observed, as shown in Figure A1.6 (a).

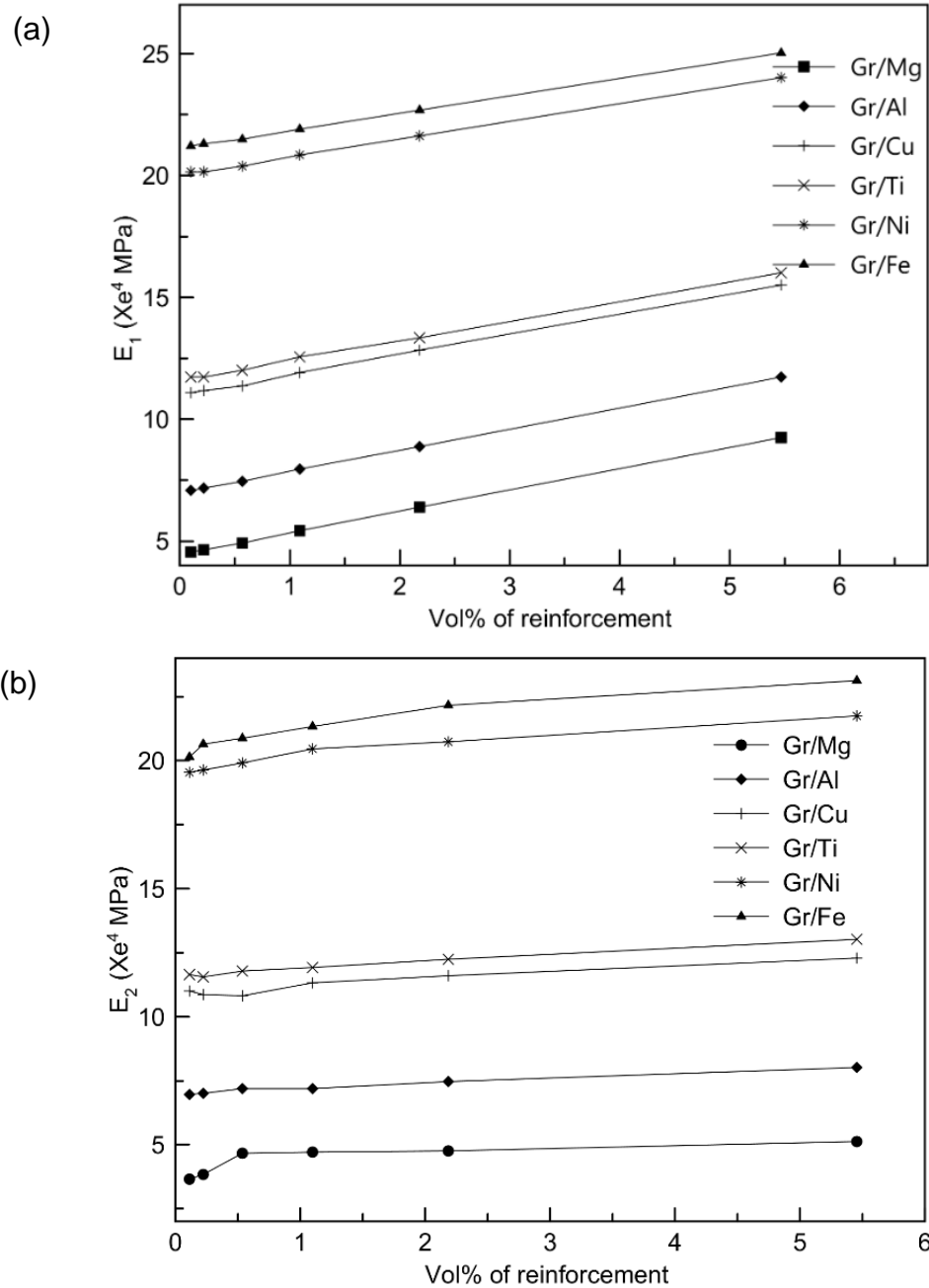


Figure A1.7: Comparison of Young's modulus of different matrix materials with different vol % of graphene reinforcement (0.1%, 0.2%, 0.5%, 1%, 2%, and 5%) (a) longitudinal Young's modulus and (b) transverse Young's modulus.

To observe the effect of reinforcement in transverse direction, transverse Young's modulus of different matrix materials reinforced with at different volume fractions of graphene is simulated. Figure A1.6 (b) shows the increase in transverse Young's modulus of different matrix materials with increase in volume fractions of graphene. It is noted that unlike the longitudinal Young's modulus which increased linearly with volume fractions of graphene, the Young's modulus of the composites in transverse directions are not effected after certain percentage (from 2% onwards) of reinforcement, suggesting that the Young's modulus became almost independent within the range of volume fractions of graphene for all different matrix materials.

Figure A1.7 shows the comparison of tensile strength of two conductor wire materials Al and Cu with graphene as reinforcement. The most striking point to be noted is the improvement in the composite tensile strength for both graphene reinforced Al and Cu. An increase by up to 300% in tensile strength is possible with just 0.3% of graphene reinforcement in Al matrix composites.

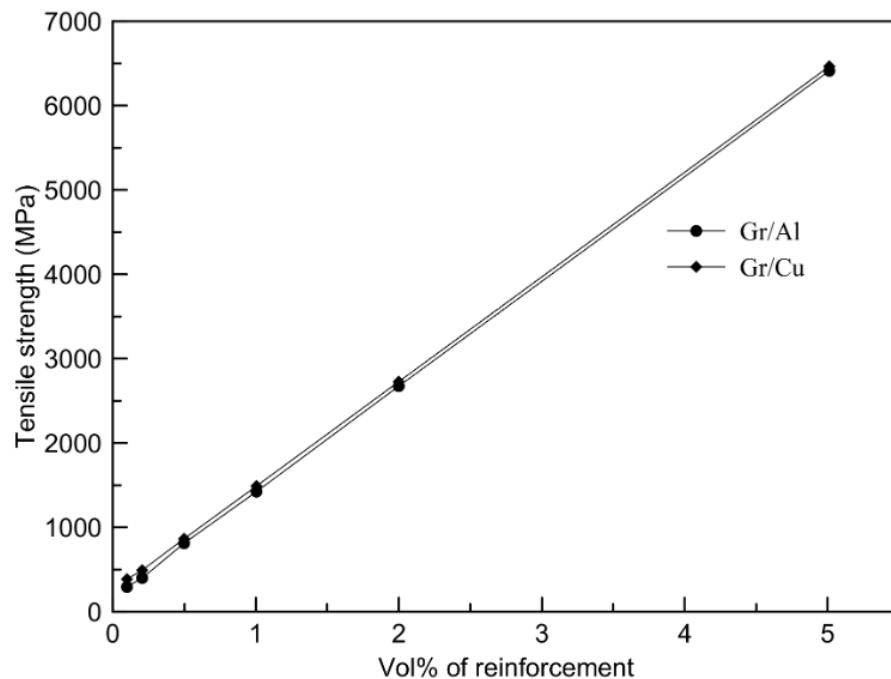


Figure A1.8: Comparison of tensile strength of graphene reinforced Al and Cu matrix composites at different vol % of graphene reinforcement.

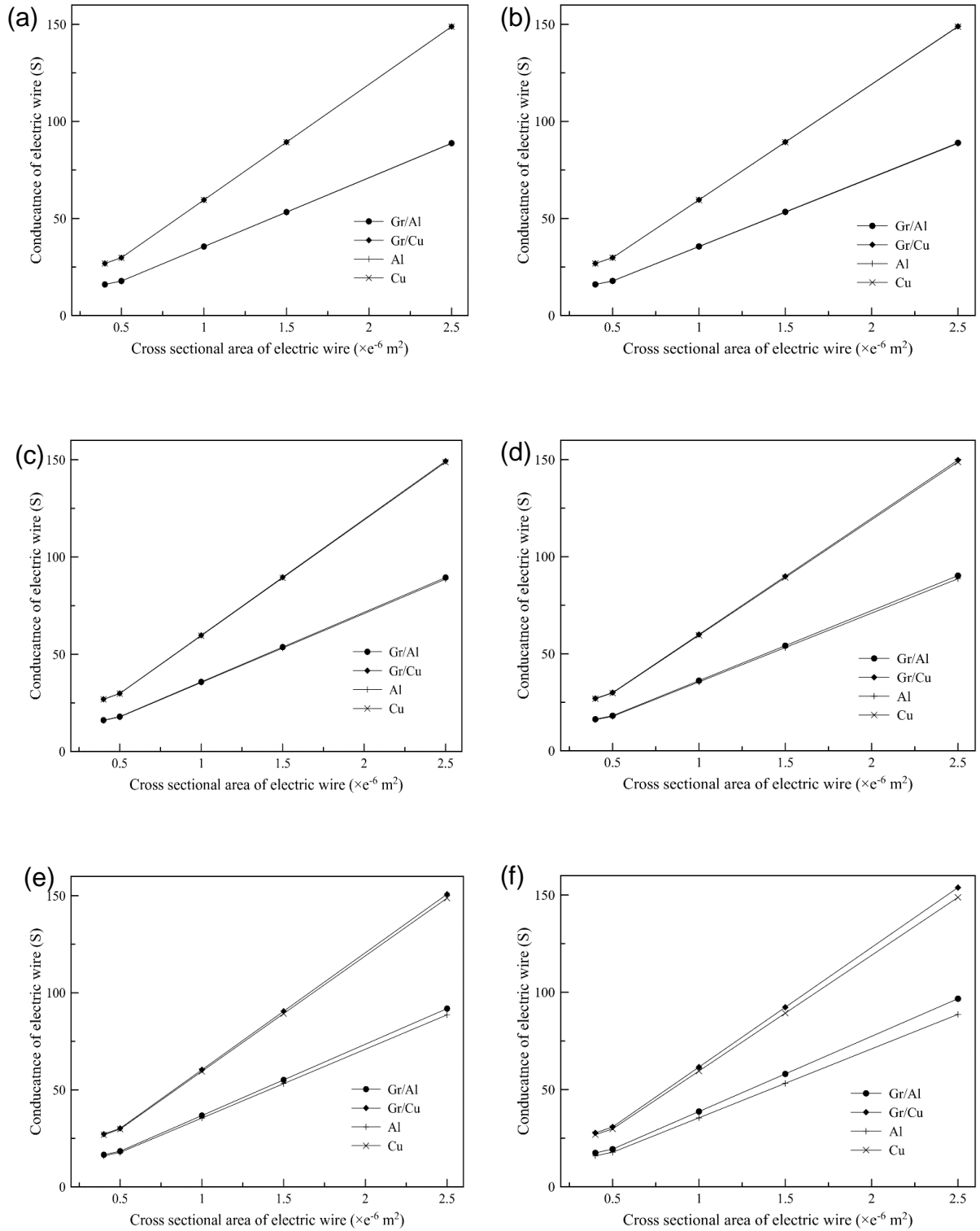


Figure A1.9: Comparison of conductance of Al and Cu as matrix material graphene reinforced composites with different vol % of graphene reinforcement (a) 0.1%vol, (b) 0.2%vol, (c) 0.5%vol, (d) 1%vol, (e) 2%vol and (f) 5%vol.

The effective electrical properties, i.e. conductivity and resistivity of Al and Cu matrix composites reinforced with different volume percentage of graphene, were also predicted. These effective electric properties are used to predict the conductance of different cross-sectional wire areas i.e., 0.4, 0.5, 1.5 and 2.5mm<sup>2</sup> with 1m length at different volume fractions of graphene reinforcement. The results obtained from the analysis are shown in Figure 10. It is noted that there is no improvement on the conductance of the graphene reinforcement of Al and Cu cables for the 0.1, 0.2 and 0.5% of reinforcement with conductance the same as those of pure Al and Cu. This might be due to the smaller cross section area of cables used here. At 1% of graphene the conductance of the Al cable started to increase, and it continues to increase with increase in reinforcement so that at 5% of reinforcement a noticeable increase in conductance is observed, as shown in Figure A1.8(d)-10(f). On the other hand, the conductance of Cu cable reinforced with 2vol% of graphene showed minor increase in conductance, as shown in Figure A1.8(e). From Figure A1.8(f) it can be noted that with 5vol% of graphene reinforcement Al and Cu cables exhibit nearly 9% and 3% increase in conductance at different cross sections. It was well known that Al cables can show conductance as high as copper with increase in cross section, however, increase in cross section increases the volume that requires higher maintenance. From the results shown and considering the percentage of increase in conductance it might be possible to obtain the conductance of Al cable same as that of Cu cable with same cross-sectional area by increasing the volume fractions of graphene reinforcement. Due to high cost and unavailable manufacturing techniques pure graphene reinforced metal matrix composite has not been reported yet. Most of the literatures reported reduce in graphene oxide and also graphene nano sheets reinforced composites. The factors such as highly remained porosities and introduction of longitudinal alignment after manufacturing procedures limits the applications of CNTs in MMCs [11]. This modelling work brings some clear insight of the effect of graphene reinforcement of on metallic matrix with both in terms of mechanical and electrical properties. Theoretically all metallic matrix shows a steady state increase in properties in addition of graphene reinforcement. From the results determined here and the potential applicability to real world applications, aluminium is shown to be a good matrix material of

choice to examine further with graphene reinforcement. From the results presented in this paper, it is shown that graphene reinforcement enhances the properties of composites above those achievable from other conventional aluminium MMCs such as Al/SiC [12]. The dispersion of graphene in the MMC with the existing metallurgical methods is quite challenging due to the huge size differences between graphene nanosheets and metal matrix. Aluminium matrix composites have been used in flywheel enables smaller flywheels compared to polymer composites [13]. The maximum tensile strength of annealed Cu is 200-250MPa. The experimental study of Al matrix composite reinforced with graphene nano sheets have shown that a tensile strength of 249MPa can be achieved with 0.5% of graphene [14]. The full exfoliation of graphene into single or few layer material and good dispersion leads to the production of nanocomposites with low mass density, high strength and stiffness. Unlike the CNTs, which are strong in longitudinal direction, graphene seems to be a processing material that is strong enough across all it's in plane directions. GNPs outperform CNTs in terms of enhancing mechanical properties [15]. The development of accurate theoretical model is a basic issue in designing, to embed and to predict the behaviour of graphene-based composites in some applications. Theoretical predictions of the properties neglect the presence of dislocations, residual stresses and overlapping of the deformed regions, which are quite important parameters to account for in practical cases. Numerous experimental efforts have been made to evaluate the mechanical performance of graphene and composites reinforced by graphene. Trying not only to predict the mechanical properties of graphene reinforced composite but also to account for the basic design of the reinforced composite for the use of practical applications is the motive to develop the present model which is achieved well as the simulated model in this paper predicts the properties that are near to theoretical values calculated. As expected, in all cases higher the reinforcement stronger the composite and highly conductive. The model considered in this study was based on discrete modelling and matrix was assumed as an isotropic continuum element as of Spanos et al. [16]. Their modelling results revealed a dependence of the elastic mechanical properties of a graphene-based composite on the size of the graphene sheets in use, the volume fraction as well as on the stiffness of the

interfacial regions. Interfacial reaction has not been taken into consideration for this study.

#### **A1.4 Conclusions**

The model proposed in this section gave a basic insight on the overall properties of the graphene reinforced Al matrix composite. For the metal matrix compositions examined, significant increases in both properties were observed. The modelling results have shown that both, mechanical and electrical conductivity of MMCs increase with the percentage increase of graphene reinforcement. The main properties that can help reduce the power losses in transmission line electrical power cables are increased in tensile strength, conductivity, thickness and purity. The results presented in this paper examined the effect of graphene reinforced aluminium matrix composite composition on two essential properties of tensile modulus and conductivity. However, this model doesn't account for number of graphene layers and % of graphene reinforced Al particles in the composite. Hence, there is a need to develop a model to incorporate the above mentioned and the model reported in methodology of this thesis was developed.

#### **AR1 References**

1. Chang S.Y, Chen C.F., Lin S.J., and Kattamis T. Z. Electrical resistivity of metal matrix composites. *Acta Mater.* **2003**, 51,6291–6302.
2. Georgios I. G, Ilias G. K. Mechanical properties of graphene based nanocomposites incorporating a hybrid interphase. *Finite Elements in analysis and Design.* **2014**, 10, 31 – 40.
3. Shin S. E., Bae D.H. Deformation behavior of aluminum alloy matrix composites reinforced with fewlayer graphene. *Compos Part A: Appl Sci Manuf* 2015, 42–47.
4. Giannopoulos G. I., Liosatos I. A, and . Moukanidis A. K. Parametric study of elastic mechanical properties of graphene nanoribbons by a new structural mechanics approach. *Phys. E Low-Dimensional Syst. Nanostructures.* **2011**, 44(1), 124–134.
5. Gómez-Navarro. C., Burghard .M, and Kern K. Elastic properties of chemically derived single graphene sheets. *Nano Lett.* **2008**, 8, 2045–2049.
6. Suk J. W., Piner R. D., An J., and Ruoff R. S. Mechanical properties of monolayer graphene oxide. *ACS Nano.* **2010**, 4(11),6557–6564.
7. Rashad M., Pan F., Tang A., and Asif M. Effect of Graphene Nanoplatelets addition on mechanical properties of pure aluminum using

a semi-powder method. *Prog. Nat. Sci. Mater. Int.* **2014**, 24, 101–108.

8. Minnetyan L., Abdi F., Chamis C. C., and Huang D., Prediction/verification of composite electrical properties and nano insertion improvement. *Procedia Eng.* **2009**, 1, 51–54.
9. Prasanthi P., Rao G. S, and Gowd B. U. Effectiveness of Buckminster Fullerene Reinforcement on Mechanical Properties of FRP Composites. *Procedia Mater. Sci.* **2014**, 6, 1243–1252.
10. Wang J., Li Z., Fan G., Pan H., Chen Z., and Zhang D., Reinforcement with graphene nanosheets in aluminum matrix composites. *Scr. Mater.* **2012**, 66(8), 594–597.
11. Neubauer E., Kitzmantel M., Hulman M., and Angerer P., Potential and challenges of metal-matrix-composites reinforced with carbon nanofibers and carbon nanotubes. *Compos. Sci. Technol.* **2010**, 70 (16), 2228–2236.
12. Kumar H. G. P. and Xavior M. A. Graphene Reinforced Metal Matrix Composite (GRMMC): A Review. *Procedia Eng.* **2014**, 97, 1033–1040.
13. Young R. J., Kinloch I. A. Graphene composites. *Wiley Encyclopaedia of Composites.* **2011**, 5, 1218-1222.
14. Hwang J., Yoon T., Jin S. H., Lee J., Kim T.-S, Hong S. H., and Jeon S. Enhanced Mechanical Properties of Graphene/Copper Nanocomposites Using a Molecular-Level Mixing Process. *Adv. Mater.* **2013**, 25, 6724–6729.
15. Rafiee M. A., Rafiee J., Wang Z., Song H., Yu Z. Z., and Koratkar N. Enhanced mechanical properties of nanocomposites at low graphene content. *ACS Nano.* **2009**, 3, 3884–3890.
16. Spanos K. N., Georgantzinis S. K., and Anifantis N. K. Mechanical properties of graphene nanocomposites: A multiscale finite element prediction. *Compos. Struct.* **2015**, 132, 536–544.

## **A2 Powder metallurgy**

### ***A2.1 Introduction***

The powder metallurgical (PM) techniques were in practise from nearly 5000 years. This technique has the capability of producing complex metal shapes to exact dimensions at economical price and even provides better quality product. In brief PM is the process of blending fine metal powders with additives and pressing them into a die of desired shape and then heating the compressed material in a controlled atmosphere to bond the material by sintering. Figure A2.1 shows the flow chart to produce powder metallurgical component.

### ***A2.2 Advantages of PM***

The component obtained from PM route possess high accuracy and smooth surfaces. Voids and porosity with in the component can be reduced to the maximum possible extent and hence highly durable component can be obtained. PM possess the extraordinary advantage of producing uniform structures with excellent reproducibility and enhanced physical properties. This method facilitates the possibility of producing a new material with a combination of metals and non-metals that are impossible to produce using conventional techniques. This also facilitates the freedom to design and consumption of less materials.

### ***A2.3 Limitations of PM***

It will be difficult to secure the high-quality powders while working and there is liability of porous materials to form more oxides. The initial setup required for this process requires high investment as it needs heavy press to make large parts hence this process is not feasible for small scale industries or start-ups. The product obtained from PM route possess poor plastic properties.

### ***A2.4 Applications of PM***

PM components made from tungsten, molybdenum and titanium finds their applications in electric bulbs, florescent lamps etc. Refractory carbides that were made by PM route finds applications in machine construction devices, wire drawing mills, precision tools and mining. Automotive industries use PM components in bearings, screen wipers, clutches, breaks, electrical contacts,

piston rings, connecting rods and brake linings. Metal powders are playing a key role in aerospace and atomic energy industries.

### ***A2.5 Powder preparation and blending***

The efficiency of PM product depends mainly on the chemical and physical characteristics of raw materials. It is a regular practice to test and characterise the metal powders before blending them. The major purpose of performing these tests is to make sure whether the powder is suitable for further processing. Chemical composition and purity (to reveal the percentage of impurities), size of particles and porosity are the basic characteristics of the metal powders that effects the quality of the product. Production of powders can be done by either mechanical processes including machining, milling, crushing, graining, atomization and by physio-chemical processes including condensation, thermal decomposition, reduction, electrodeposition, intergranular corrosion etc. Out of these techniques atomization, electrolysis and reduction of compounds are most frequently used to produce powders.

Atomization is the process of forcing the molten metal stream through an orifice at moderate pressures. To reduce the oxide and carbon content most of the atomized powders will be annealed. In most of the cases the particles produced by this process carry a layer of oxide over them and are of spherical or pear shape. Electrolysis and reduction of compounds are other widely used techniques for production of powders. Electrolysis is used in the preparation of copper, iron, beryllium and nickel powders. By this method the powder with excellent properties and of high purity will be obtained. In some cases, electrolysis is costlier compared to other processes. Reduction of compounds is used in the production of iron, copper, molybdenum and tungsten. The process involves the chemical compounds mostly an oxide or other salt of the metal. The process may be carried out in either from the solid state, from the gaseous state or from the aqueous solution. Powders will be mixed thoroughly with additives using mixers. To facilitate easy ejection and to minimize wear of the compaction tool, lubricants will be added prior to mixing [1].

The powder produced may not possess the desirable physical or chemical properties for further processing to obtain product [2]. The preliminary

treatment of powders before blending usually will be carried out in a reducing environment or vacuum this helps in eliminating work hardening, reducing impurities and effects the apparent density which in turn helps in improving pressing quality of powders. Powder blending or mixing is an important and complex process that needs to be focused while working with PM. It is an operation of intermingling of two different powders of various or same compositions thoroughly. The movement of powder components depends on powder material, particle shape and size and environmental conditions. The major aim of mixing is to achieve uniform distribution; it is indeed difficult to achieve optimum mixing time in advance. Poor blending results in non-homogeneous mixture and weak bonding between two materials which is not suitable for production of product and excessive blending results in partial segregation of powders and produces plastic deformation of particles that leads to work hardening of particles and reduces the compressibility. The mixing of powders should be carried out in a protective environment to avoid oxidation and contamination of powders.

#### *A2.5.1 Powder compaction*

The powders obtained from blending will be compacted to make desired shapes with enough strength to handling tools till the completion of sintering. There are different techniques available to compact powders, i.e., pressure-less shaping technique, cold pressure shaping technique and pressure shaping techniques. Pressure-less shaping techniques involves the imparting desired shape to powder mass without applying external pressure before sintering. Slip casting, loose sintering, slurry casting, clay type moulding techniques fall into the category of pressure-less shaping methods, loose sintering has the scope in PM processing. Cold pressure shaping techniques involves cold die compaction, powder rolling, powder extrusion, explosive forming, high energy rate forming, isostatic pressing, out of these cold die compactions is the most feasible technique in industrial production as it is simple and improves the appearance of surface by eliminating oxidation at room temperature. Pressure shaping techniques such as hot forging, hot isostatic pressing, and hot extrusion are used for large-scale production.

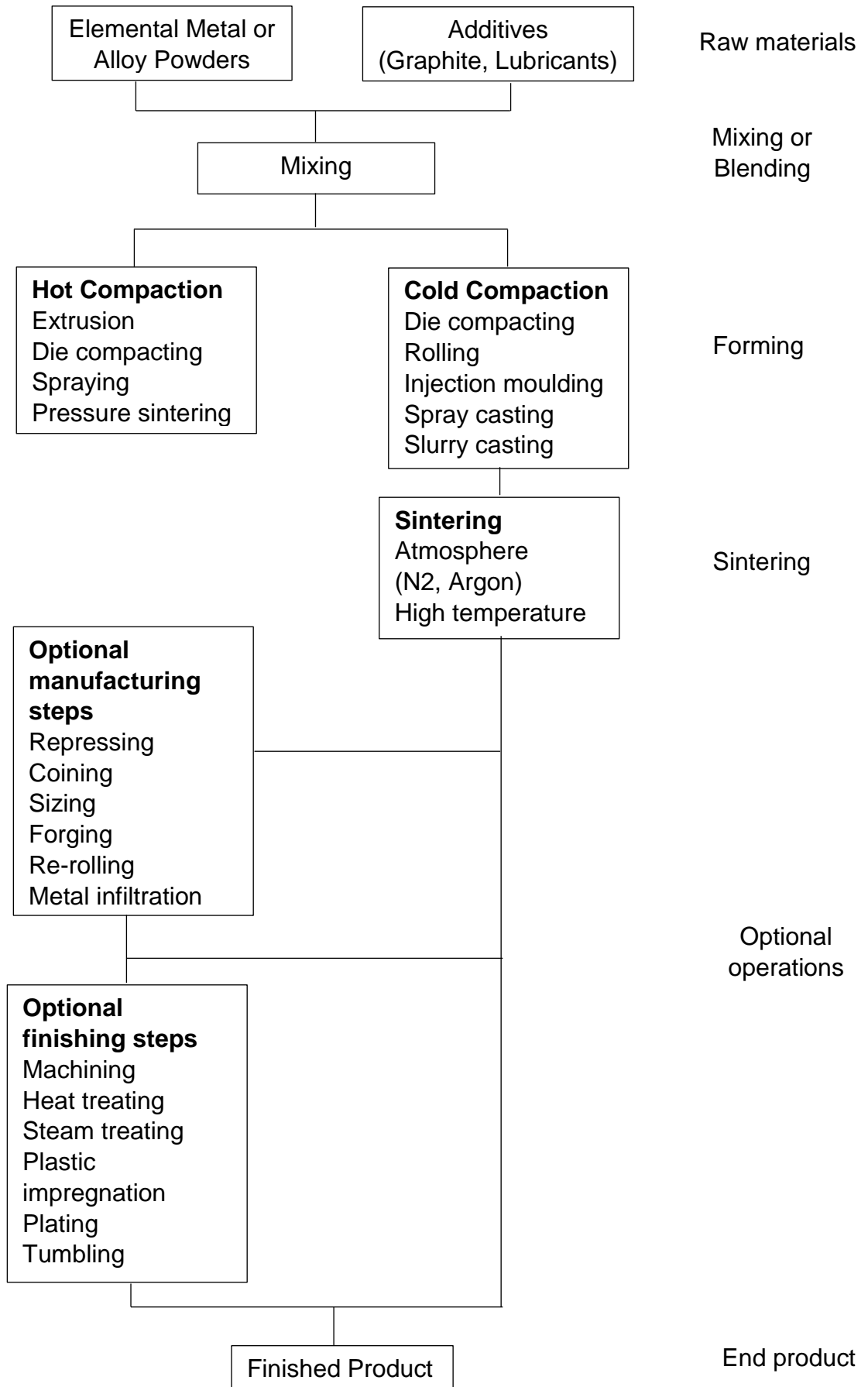


Figure A2.1: Flowchart of powder metallurgical component production [1].

Cold die compaction includes the uniform filling of metal powder into the die cavity, the packing density will be raised and certain bridges will be formed. When the powder is slightly pressed in between the anvils, the packing density will be improved due to the densification by particle movement and the bridges that were formed in previous stages will be distorted. Neither deformation nor adhesion between the particles not occur at this stage. Further increase in compaction pressure leads to deformation of particles, mechanical interlocking of grains and reduction of voids by pressing powder particles. Lubricants are frequently used either on the die surfaces or mixing with powder blend, in either cases lubricant should be removed before sintering. Figure A2.2 and A2.3 shows the schematic representations of the piston – die arrangements and the compaction cycle to press powders.

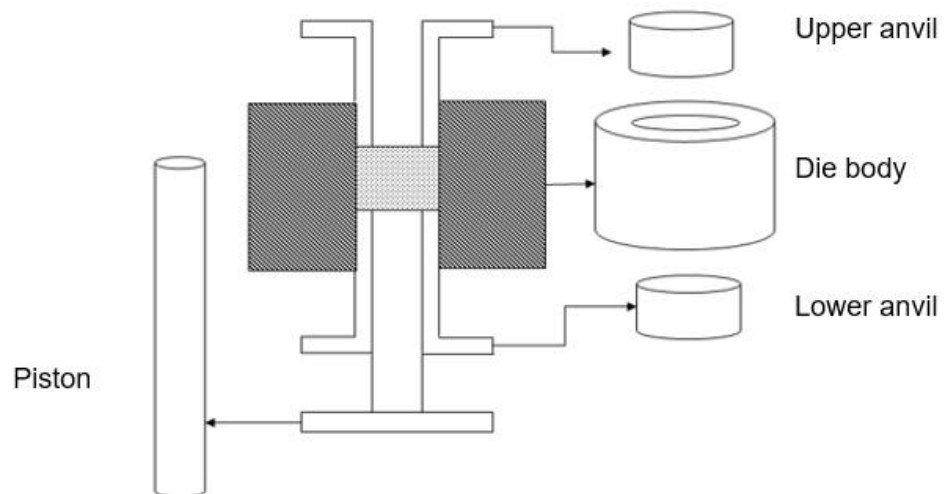


Figure A2.2: Schematic representation of piston-die assembly in press.

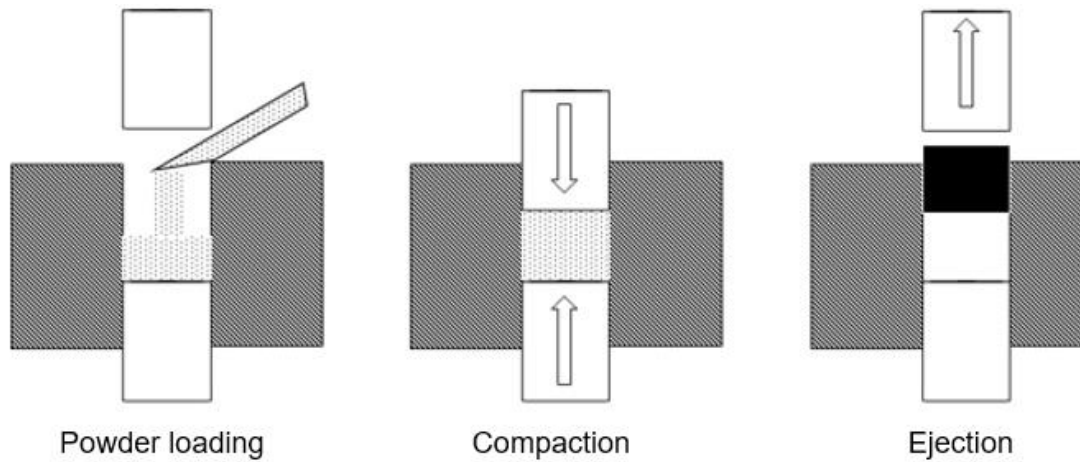


Figure A2.3: Schematic representation of compaction cycle.

### A2.5.2 Sintering

The green compact obtained from the die compaction will be fragile due to weak bonding in between the particles. Sintering is used to attain strength, densification by creating strong bonding in between the particles. Sintering is usually carried out at a temperature range of 70% to 90% of the absolute melting point of the material. Sintering can be defined as the heating of compacted metal powders slightly below the melting point of the base metal without the application of external load. Sintered material will be free from porosity, possess desired mechanical properties. Sintering of material results in dimensional changes, chemical changes, phase changes, reduction of internal stresses. Figure A2.4 shows the schematic representation of sintering process.

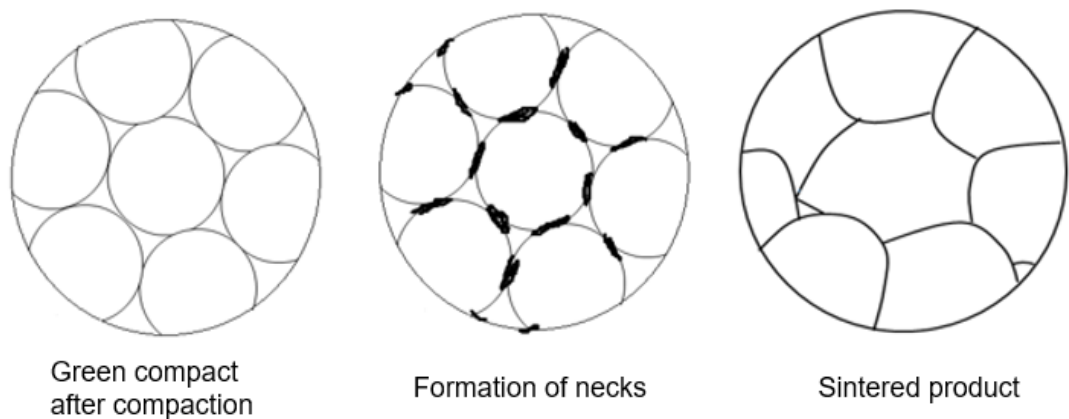


Figure A2.4: Schematic representation of mechanism of sintering.

### ***AR2 References***

1. Angelo P. C., Subramanian R., Powder metallurgy: science, technology and applications, **2008**.
2. Sinha A. K., Powder metallurgy, **1982**.